$CuSbS_2$ and related chalcogenides for sustainable photovoltaics

by **Enzo Peccerillo**

Thesis submitted in accordance with the requirements of the

University of Liverpool for the degree of Doctor in Philosophy

Department of Physics

December 2015

$CuSbS_2$ and related chalcogenides for sustainable photovoltaics

Enzo Peccerillo

Abstract

This thesis presents a systematic investigation of some novel chalcogenides based on Earth abundant elements in order to test their suitability for sustainable photovoltaic (PV) applications. A comprehensive review of sulfo-salts in the family Cu-Sb-Bi-X (X = S, Se) is presented and indicates that $CuSbS_2$ and Cu_3BiS_3 have potential as PV absorbers, showing optical band gaps in the desired range and the p-type conductivity required for PV devices.

A systematic study about the formation of $CuSbS_2$ and Cu_3BiS_3 thin films is presented, including of the experimental steps necessary to ensure the formation of stoichiometric films during the sulfurization of metallic precursor layers. Sulfurized $CuSbS_2$ films (~1.2 µm thick) exhibited absorption coefficients of ~10^5 cm^{-1} and band gaps of ~1.5 eV. The films were p-type with mobilities of ~10 cm^2 V^{-1} s^{-1} and resistivities in the range 10 - 1000 kΩ/□. $CuSbS_2$ films were also deposited in a one-stage process by rf sputtering from a ternary target – they were generally more resistive than those deposited by sulfurization. Cu_3BiS_3 films deposited by sulfurization had band gaps of ~1.4 eV and p-type conductivity, with hole mobilities of ~3 cm^2 V^{-1} s^{-1}. The $CuSbS_2$ films produced by both methods were tested in prototype $CuSbS_2$/CdS heterojunction PV devices, and had efficiencies of ~0.1%. For these devices the dominant transport mechanism was multi-step tunnelling, suggesting that an improvement in the quality of the junction was necessary. Post-growth treatments were trialled, including impurity doping with NaF, Zn and In, and etching the absorber to remove the surface oxides identified by XPS. $CuSbS_2$/CdS devices having efficiencies up to ~1% were achieved by doping the absorber with In and removing unwanted Sb_2O_3 from the layer surfaces with de-ionized water. Their *Voc*s and *FF*s were low and their *Jsc*s were high, as reported by others. Alternative window layer materials were tested, including ZnS and ZnSe, which were expected to have an improved band alignment with $CuSbS_2$ compared to CdS. ZnS gave *Voc* = 0.56 V, the highest yet reported for $CuSbS_2$. However these alternative window layers had reduced photocurrents and their efficiencies were not greater than with CdS. Overall $CuSbS_2$ and Cu_3BiS_3 films displayed the optical and electrical properties required for PV, but further developments will be essential in order to achieve high efficiency PV devices using these materials as absorbers.

Declaration

I declare that with the exception of those procedures listed below all the work presented in this thesis was carried out by the candidate. I also declare that none of this work has been previously submitted for any degree and that it is not being submitted for any other degree.

- X-ray photoelectron spectroscopy (XPS) measurements and in-situ cleaning by means of argon presented in Chapter 5 were conducted by Thomas Whittles at the Stephenson Institute for Renewable Energy, University of Liverpool.
- Fourier-transform infrared spectroscopy (FTIR) analysis presented in Chapter 5 was performed by Max Birkett at the Physics Department of the University of Liverpool.
- Cross-sectional SEM images shown in Chapter 5 were taken by Dr. Kerry Abrams at the Nanoinvestigation Centre at Liverpool (NiCaL), University of Liverpool.
- Transmission electron microscopy reported in Chapter 5 was conducted by Dr. Budhika Mendis and Leon Bowen at the Durham University.
- The experiments with atomic layer deposition (ALD) included in Chapter 6 were performed by Dr. Ian Brunell at the Centre for Materials and Structures, University of Liverpool.
- Ellipsometry measurements mentioned in Chapter 4 were performed by Ayendra Weerakkody at the Electrical Engineering Department of the University of Liverpool.
- The *J-V-T* and impedance analyses presented in Chapter 6 were conducted by Prof. Murat Bayhan and Prof. Habibe Bayhan at the Stephenson Institute for Renewable Energy, University of Liverpool.
- The experiments with chemical bath deposition (CBD) of CdS reported in Chapter 6 were performed by Dr. Guillaume Zoppi at the Northumbria University.
- The Raman analysis included in Chapter 5 was performed by Joseph Roberts at the Centre for Materials and Structures, University of Liverpool.
- The photoluminescence investigation shown in Chapter 5 was conducted by Dr. Douglas Halliday at the Durham University.

Acknowledgments

I would like to acknowledge all the scientists who have contributed to this work from the scientific point of view and all the people who have personally supported me.

Firstly I would like to express my gratitude to my supervisor Prof. Ken Durose for the continuous feedback and assistance to my study. The progress in my research was met also thanks to precious hints from his deep knowledge in the field of photovoltaics. Nevertheless I have always felt comfortable with him, for his cordial and approachable personality.

I am glad to have been working in a group of talented scientists and above all helpful and friendly people. In particular I would like to acknowledge: Dr. Jonathan Major for the assistance with the sulfurization experiments, KCN etching and solar cells fabrication; Dr. Robert Treharne for the demonstrating on optical spectroscopy and assistance with the sputtering kit; Dr. Laurie Phillips for helping with the Hall effect measurements on semiconductor films and electrical characterization of devices. I would like to thank Dr. Benjamin Williams for his appreciated help in the lab when he was concluding his PhD at the University of Liverpool and for his courtesy in doing some depositions of ZnO and ZnO:Al by PECVD and ALD at the Eindhoven University of Technology. Thanks to Peter Yates for his analysis by TEM on my $CuSbS_2$ samples and prototype devices and for his ongoing precious research on copper-bismuth sulfides. Then I would like to mention my beloved friends Silvia Mariotti and Giorgos Papageorgiou and all the other lovely colleagues, including: Annette Pressman, Dr. Oliver Hutter, Dr. Yanina Fedorenko, Tom Baines and the former members of our research group Dr. Mohammed Al-Turkestani and Dr. Atef Rashed. Finally I would like to thank Vincey Vasey for the technical assistance.

Next I would like to express my gratitude to all the other people who gave a scientific contribution to my research. I would like to acknowledge these people from the Stephenson Insitute for Renewable Energy: Dr. Jonathan Alaria for the training session on X-ray diffraction; Thomas Whittles and Dr. Vin Dhanak for the measurements by X-ray photoelectron spectroscopy; Max Birkett and Dr. Tim Veal for the analysis by Fourier-transform infrared spectroscopy. I am very grateful to other scientists from the University of Liverpool, including Dr. Tim Joyce and Dr. Kerry Abrams for their help with SEM/EDX and TEM analyses; Dr. Ian Brunell and Prof. Paul Chalker for their courtesy of using the atomic layer deposition equipment for the deposition of aluminium- and gallium-doped ZnO; Joseph

Roberts for the assistance with Raman spectroscopy; Ayendra Weerakkody for the help with ellispsometry. I would like to acknowledge the expertise on photoluminescence Dr. Douglas Halliday and the microscopists Dr. Budhika Mendis and Leon Bowen from Durham University for their appreciable and important analyses. I am very thankful to Prof. Murat Bayhan and Prof. Habibe Bayhan from Muğla University for their precious investigation by *J-V-T* and impedance spectroscopy on the properties of the $CuSbS_2$/CdS interface of prototype devices. I would like to thank Dr. Guillaume Zoppi for the experiments with chemical bath deposition at the Northumbria University and for his useful tips on device fabrication. I would like to acknowledge Dr. Andriy Zakutayev from the National Renewable Energy Laboratory – one of the few heroes worldwide working on $CuSbS_2$ and related chalcogenides for sustainable photovoltaics. I am glad to have had with him some profitable discussions on the development of these innovative photovoltaic technologies.

Then I would like to show my gratitude to all the people who personally have supported and loved me. After all, before becoming a scientist, I am a human being – when you do a PhD, you sometimes forget about this point. First of all I would like to thank my family, thanks to them I have never felt alone during the last four years despite the distance. My father Gino, my mother Margherita and my brothers Gianluigi and Antonello have always encouraged and adored me, and they are and will be a fundamental point of my life. I would like to thank my childhood friends Matteo D'Aiuto, Giovanni Tortorella and Alberto Mastrogiovanni, simply because I grew up with them and they are still my best friends, luckily the distance did not break our old friendship. I would like to mention my friend from high school Daniele Coda and my friends from my hometown University Ludovico Aiello, Marco Tambasco, Francesco Ventimiglia and Vincenzo Gesa. Liverpool was a very nice place to spend part of my life and I had great time. I was very lucky to meet some very nice people and in particular I am extremely grateful to Salvatore De Rosa and Dr. Tommaso Sgrilli, who were my best friends in Liverpool. I am glad to have been working in a stimulating and friendly environment at the Stephenson Institute for Renewable Energy. In Liverpool I met lots of new friends and I am particularly thankful to: Emiliano, Ivan, Marios, Eva, Marika, Clara, Luigi, Ilaria, Chiara, Sergio, Mario, Simone, Tony, Nikolas, Paula, Pepe, Lorena, Ioritz, Marta, Claudia, Alessandro, Stefano, José, Gaia, Mark, Ian, Ebenezer, Josh, Mar, Filipe, Marco, Davide, Maria, Jon and all the others.

My project was very demanding but also exciting, and I hope that my work will give a small contribution to a crucial topic for the scientific community.

Contents

Appendix

1 Introduction

The world energy demand is growing very rapidly, with a total consumption of 9301 Mtoe[1] – corresponding to ~10^5 TWh – recorded in 2013 [1]. The accelerated increase of the energy consumption had a dramatic impact on the global warming rate last century and can have catastrophic and irreversible repercussions on the climate. The target of the 2015 Paris Climate Conference (COP21) was to rediscuss the international negotiations and policies to limit the global warming by 2100 to no more than 2°C greater than pre-industrial levels [2]. In order to achieve this objective, the expansion of renewable energy sources will play a key role the following decades. As shown in Figure 1.1, the contribution of renewable energies to the global energy supply is at present relatively low.

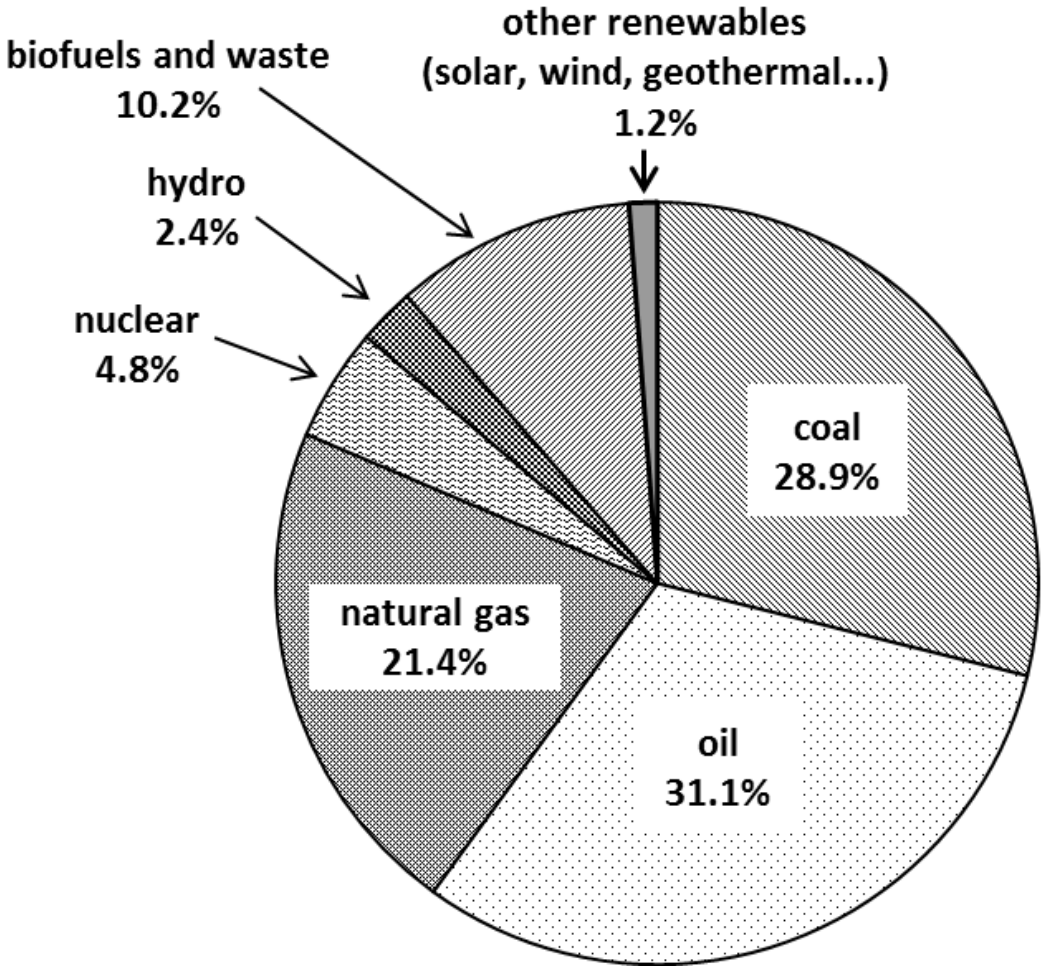

Figure 1.1: Pie chart with the contribution of the various energy sources to the world energy supply (2013) [1].

[1] The tonne of oil equivalent (toe) is an energy units defined as the amount of energy released by burning one tonne of crude oil. 1 toe = 11.63 MWh.

Among the renewable energies, solar photovoltaics (PV) is growing very fast, with more than 40 GWp of photovoltaic systems installed globally in 2014 [3]. However the contribution of solar PV is still low compared to the global demand of energy, and the current commercialized PV technologies – summarized in Table 1.1 – face some challenges in ramping up total PV manufacturing to the terawatt per year level.

Technology	PV market share	Max. cell efficiency	Max. module efficiency	Drawbacks
Silicon	90.7%	25.6%	22.9%	high feedstock costs
CdTe	4.0%	21.0%	17.5%	toxicity of cadmium, scarcity of tellurium
CIGS	3.6%	21.0%	17.5%	high costs of indium and gallium
a-Si	1.7%	13.6%	10.9%	instability, low efficiency

Table 1.1: Commercialized PV technologies (2014) [4].

Silicon is the principal commercialized PV material, having more than 90% of the market, in the single-crystal (c-Si) and multicrystalline (poly-Si) forms. However silicon is an indirect semiconductor, and hence a relatively thick layer is required to absorb the incident light. In addition the high feedstock and refinement costs make silicon intrinsically expensive and in principle other materials may be more suitable for the long term PV production.

Alternatives have emerged in recent years, notably the thin film solar technologies based on direct semiconductors, requiring just a few microns to absorb light and being processable at relatively low temperatures. The two most important are cadmium telluride (CdTe) and copper indium gallium diselenide (CIGS), with laboratory efficiencies above 20%. The main limitations to the expansion of CdTe solar cell manufacturing are the toxicity of cadmium and the scarcity of tellurium. CIGS technology is essentially limited by the high costs of indium and gallium. Finally amorphous silicon (a-Si) is an unstable material and its efficiency in PV devices is low.

The PV research community is therefore exploring novel sustainable technologies, based on Earth abundant, inexpensive and non-toxic elements. The most promising innovative inorganic absorber material is Cu_2ZnSnS_4 (CZTS), with record cell efficiency of 12.6%. However secondary phases and the complexity of the quaternary compound are the main issues of this emerging technology.

Organic and dye-sensitized solar materials are attractive solutions for sustainable PV. In particular the development of solar cells from hybrid organic/inorganic materials having the perovskite lattice has been remarkable, with efficiencies above 20% having been achieved at laboratory scale in just two or three years. However organic compounds and hybrid perovskites are very sensitive to oxygen, moisture and ultraviolet light, hence their properties degrade under atmospheric conditions. Table 1.2 summarizes all the emerging PV technologies and the NREL PV development chart showing all the certified world record efficiencies until 2015 is shown in Figure 1.2.

Technology	First PV publication	Max. efficiency	Drawbacks
CZTS	Ito (1988) [5]	12.6%	secondary phases, complexity
Perovskite	Miyasaka (2009) [6]	20.1%	hysteresis, instability, degradation
Organic	Ghosh (1974) [7]	11.5%	hysteresis, instability, degradation
Dye-sensitized	Tributsch (1972) [8]	11.9%	hysteresis, instability, degradation

Table 1.2: Emerging PV technologies.

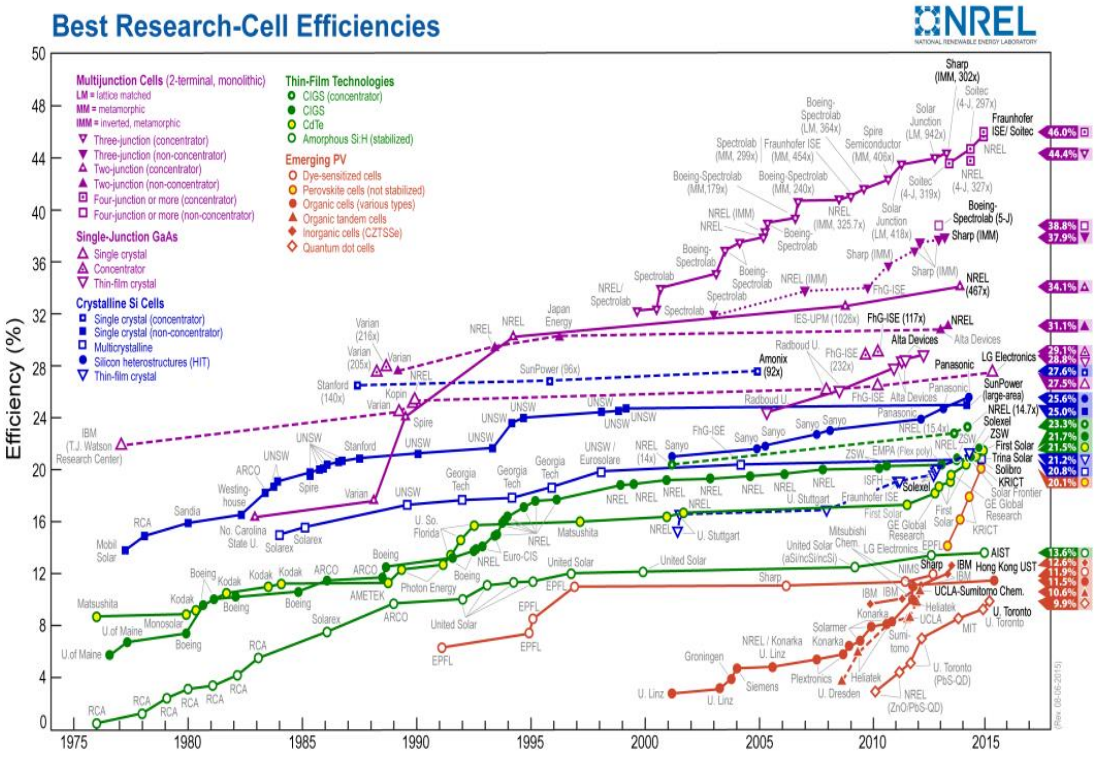

Figure 1.2: NREL chart 2015 showing the certified efficiencies of solar cells for the various PV technologies [9].

Other absorber materials under investigation based on sustainable elements include: Cu_2SnS_3, SnS, Cu_2O, PbS, Zn_3P_2 and FeS_2.

An interesting approach to identify new potential absorber materials was recently proposed by Zunger [10]. The identification of new absorbers used the desired material properties as the starting point, i.e. an inverse design method. In the classical screening approach, the band gap is the only discriminating parameter for potential absorber materials. On the other hand in [10] a set of required optical and electronic properties were predefined (including optical absorption coefficient and electronic structure); then the materials matching the target properties were identified over a large range of elemental combinations by first principle calculations. By this method a significant number of sophisticated compounds were predicted to have potential in PV and lists of candidates are given in references 11 and 12.

This thesis explores the properties of two particular chalcogenides identified to have potential as absorber materials: $CuSbS_2$ and Cu_3BiS_3 – i.e. comprised of Earth abundant, inexpensive and harmless elements. Figure 1.3 shows a comparison of the abundance and raw costs of the constituent elements with those contained in the principal thin film technologies, CdTe and CIGS.

The thesis structure is given as follows. Chapter 2 introduces the basic concepts of semiconductor physics and solar devices. A literature review on the crystallographic, optical and electrical properties of the new chalcogenide materials for PV applications – including $CuSbS_2$ and Cu_3BiS_3 – is presented in Chapter 3. Chapter 4 describes the thin film deposition techniques and characterization methods utilised for this study. Chapter 5 discusses the growth and characterization of $CuSbS_2$ and Cu_3BiS_3 thin films. The deposition approach predominantly investigated in this thesis was sulfurization of metal 'precursor' layers – i.e. a method widely used for the synthesis of chalcogenides (e.g. CIGS, CTZS). $CuSbS_2$ thin films were alternately deposited by radio frequency (rf) sputtering from a ternary target. A thorough study of the structural, optical and electrical characteristics of the as-deposited films is presented. The fabrication and characterization of prototype devices based on the heterojunction $CuSbS_2$/CdS are examined in Chapter 6. Chapter 7 describes the development of alternative window layer materials, including ZnS and ZnSe. Finally Chapter 8 discusses the main issues and perspective of the investigation, and a brief summary is given in Chapter 9.

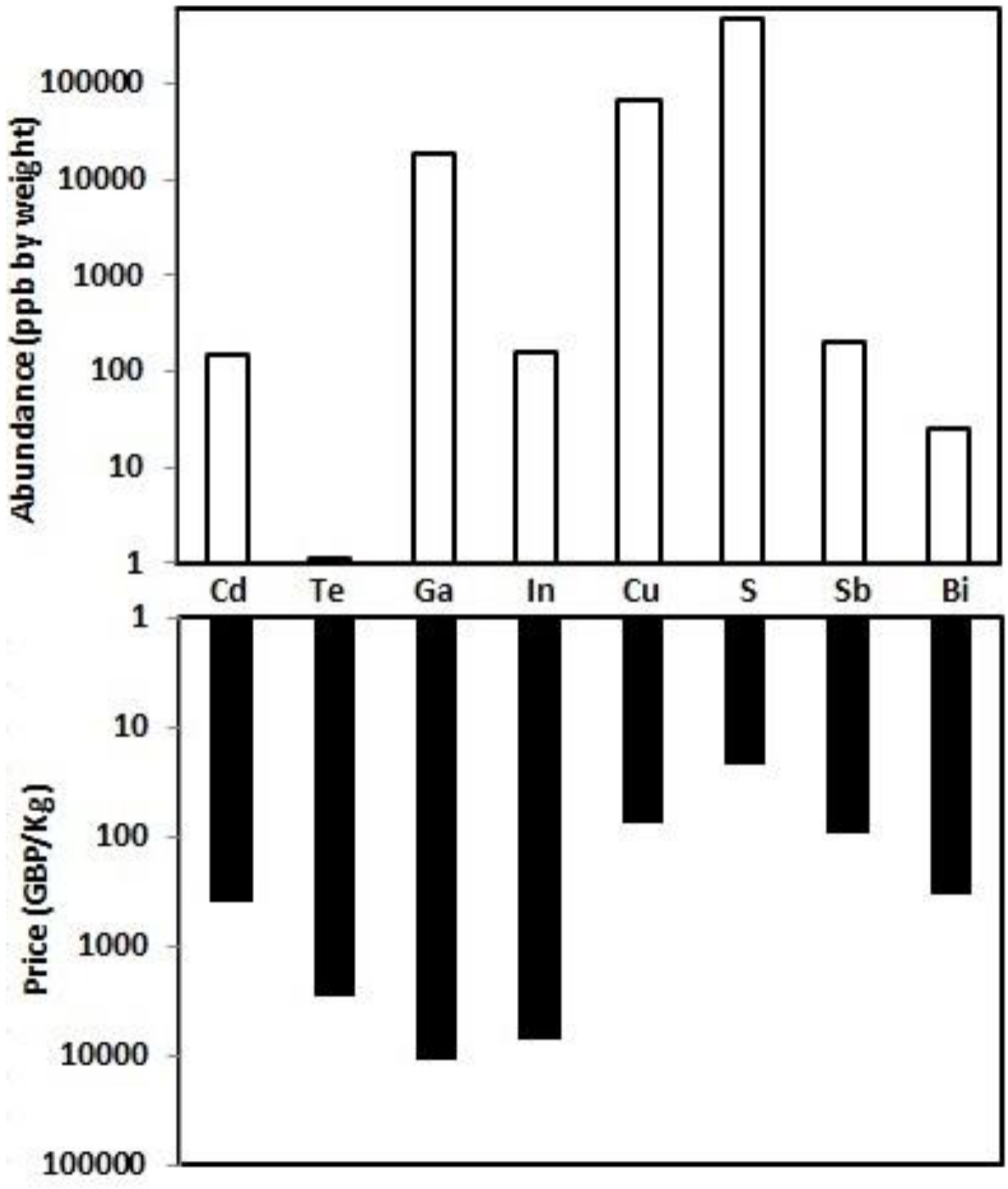

Figure 1.3: Abundance and raw prices of the constituent elements of CdTe and CIGS compared to those of the new chalcogenides under investigation. Chart draw from [13], with additional data.

1.1 References for Chapter 1

[1] International Energy Agency, "World total final consumption from 1971 to 2013 by fuel (Mtoe)", *Key World Energy Statistics 2015*, pp. 1-81, 2015

[2] (2/12/2015) http://www.cop21.gouv.fr/en/2c-target-result-of-state-contributions/

[3] European Photovoltaic Industry Association, "Global solar market: update and prospects", *Global Market Outlook for Solar Power 2015 - 2019*, pp. 1-32, 2015

[4] Fraunhofer Institute for Solar Energy Systems, "PV production by technology", *Photovoltaic Report 2015*, pp. 1-43, 2015

[5] K. Ito and T. Nakazawa, "Electrical and optical properties of stannite-type quaternary semiconductor thin films", *Japanese Journal of Applied Physics*, vol. 27, no. 11, pp. 2094-2097, 1988

[6] A. Kojima, K. Teshima, Y. Shirai and T. Miyasaka, "Organometal halide perovskites as visible-light sensitizers for photovoltaic cells", *Journal of the American Chemical Society*, vol. 131, no. 17, pp. 6050-6051, 2009

[7] A. K. Ghosh, D. L. Morel, T. Feng, R. F. Shaw and C. A. Rowe, "Photovoltaic and rectification properties of Al-Mg phthalocyanine-Ag Schottky-barrier cells", *Journal of Applied Physics*, vol. 45, no. 1, pp. 230-236, 1974

[8] H. Tributsc, "Reaction of excited chlorophyll molecules at electrodes and in photosynthesis", *Photochemistry and Photobiology*, vol. 16, no. 4, pp. 261-269, 1972

[9] (2/12/2015) http://www.nrel.gov/ncpv/

[10] A. Zunger, "The case for design and discovery of functional materials", *40th IEEE Photovoltaic Specialists Conference*, Conference Plenary, p. 53, 2014

[11] R. Gautier, X. Zhang, L. Hu, L. Yu, Y. Lin, T. O. L. Sunde, D. Chon, K. R. Poeppelmeier and A. Zunger, "Prediction and accelerated laboratory discovery of previously unknown 18-electron ABX compounds", *Nature Chemistry*, vol. 7, no. 4, pp. 208-316, 2015

[12] L. P. Yu, R. S. Kokenyesi, D. A. Keszler and A. Zunger, "Inverse Design of High Absorption Thin-Film Photovoltaic Materials", *Advanced Energy Materials*, vol. 3, no. 1, pp. 43-48, 2013

[13] L. M. Peter, "Towards sustainable photovoltaics: the search for new materials", *Philosophical Transactions of the Royal Society A*, vol. 369, no. 1942, pp. 1840-1856, 2011

2 Physics of semiconductors and solar cells

2.1 Introduction

This Chapter introduces the basic principles of semiconductors (Sections 2.2 and 2.3) and solar cells (Section 2.4). The main concepts are extensively reviewed in textbooks (e.g. ref. 1) and so here the emphasis is put on concepts connected to the materials and studies presented in the thesis.

2.2 Fundamentals of semiconductors

2.2.1 Structure and band gap

All conventional solar cells exploit the property of the semiconducting behaviour of materials. Central to this is the existence of the band gap – i.e. the disallowed band of energy levels that is present on account of the behaviour of electrons in the periodic medium of the crystal lattice (it is the promotion of electrons by light over the band gap, or the 'fundamental absorption', that is important in photovoltaic absorber materials). While most technologically important semiconductors (e.g. Si, GaAs) have either the diamond or the closely related zinc-blende structure, there is nothing preventing semiconducting behaviour in materials having other crystal structures. For example, $CuSbS_2$ and Cu_3BiS_3 studied in this work adopt the orthorhombic lattice and have semiconducting properties. A full account of the crystal structure that influences semiconductor behaviour, and the terminology used to describe them (Bravais lattice, crystal system, space groups, Miller indices, etc.) is given in ref. 1. The band structure of solids is conveniently represented on *E* - *k* diagrams plotting energy as a function of the (directionally sensitive) wave vector *k*.

The band gap is temperature (*T*) dependent, and its variation is often described by the empirical relation in Equation 2.1 [1].

$$Eg\ (T)\ \cong\ Eg_0 - \alpha\frac{T^2}{T+\beta} \qquad (2.1)$$

where Eg_0 (eV) , α (eV K^{-1}) and β (K) are typical constants of the semiconductor.

2.2.2 Electrical properties at the thermal equilibrium

The conductivity of semiconductors can be controlled by doping with external impurities. The doping can be either n-type – i.e. when additional electrons are provided to the conduction band from donor species – or p-type – i.e. when electrons are captured from leaving holes in the valence band.

At thermal equilibrium for non-degenerate semiconductors the number of electrons n in the conduction band (electron concentration) is given by Equation 2.2.

$$n = N_c e^{-\frac{E_c - E_f}{kT}} \tag{2.2}$$

where N_c is the density of states in the conduction band, k is the Boltzmann constant, E_c is the conduction band energy and E_f is the Fermi level. Similarly the hole concentration p in the valence band is given from Equation 2.3.

$$p = N_v e^{-\frac{E_f - E_v}{kT}} \tag{2.3}$$

where N_v is the density of states in the valence band and E_v is the valence band energy. For an intrinsic (undoped) semiconductor at thermal equilibrium:

$$n = p = n_i \tag{2.4}$$

Where n_i is the intrinsic carrier concentration. For doped n-type semiconductors the carrier concentration of electrons n at thermal equilibrium is approximately equal to the donor concentration N_D (cm^{-3}). Similarly the hole concentration p of p-type semiconductors is approximately equal to the acceptor concentration N_A (cm^{-3}).

2.2.3 Electron properties under non-equilibrium conditions

In semiconductors under non-equilibrium conditions – i.e. $p \cdot n \neq n_i^2$ – a current can flow as a consequence of different phenomena, including: (a) low electric field (drift), (b) carrier concentration gradient (diffusion), (c) magnetic field (Hall effect), (d) optical absorption, (e) temperature gradient and (f) high electric field (avalanche breakdown). The points (e) and (f) are not discussed in this thesis.

(a) Drift – Under low electric field conditions, the velocity v_d of the carriers is related to the applied electric field E by the carrier mobility μ ($cm^2\ V^{-1}\ s^{-1}$):

$$v_d = \mu E. \tag{2.5}$$

The resistivity ρ of the material is the proportionality constant between the applied electric field E and the generated density current J ($J = \sigma E$, with $\sigma = \rho^{-1}$) and it is related to the material properties by Equation 2.6.

$$\rho = \frac{1}{q(\mu_n n + \mu_p p)} \tag{2.6}$$

where q is the magnitude of the electron charge, μ_n and μ_p correspond to the mobility of electrons and holes respectively.

(b) Diffusion – Current can be generated from a carrier concentration gradient ∇c (either electrons or holes), according to Equation 2.7.

$$J = qD\nabla c \tag{2.7}$$

where D is carrier diffusion coefficient, this being related to the mobility by the Einstein relationship:

$$D = \frac{kT}{q}\mu. \tag{2.8}$$

(c) Hall effect – When a magnetic field B_z is applied perpendicular to a sample with drift current J_x, as shown in the schematic diagram in Figure 2.1, an electric field E_y is generated balancing the Lorentz force. The electric field E_y produced by Hall effect is proportional to the applied magnetic field B_z and the drift current J_x by the Hall coefficient R_H.

$$E_y = R_H J_x B_z \tag{2.9}$$

The Hall coefficient R_H enables calculation of the carrier concentration and mobility for the material. In particular the sign of R_H allows identification of the conductivity type of the semiconductor – i.e. either p-type (+) or n-type (-). For details on the Hall effect measurement setup used in this work the reader is referred to Section 4.4.3.

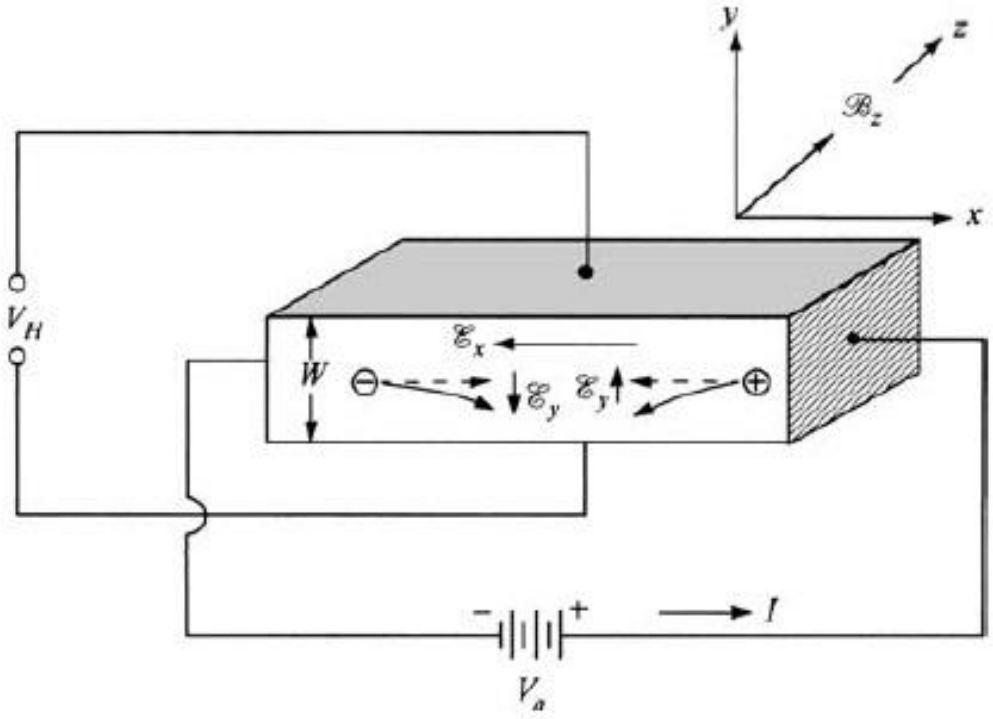

Figure 2.1: Schematic diagram of Hall effect measurement from ref. 1.

(d) Optical absorption – Additional carriers can be generated at rate G ($cm^{-3}\ s^{-1}$) by external excitations, including photon absorption. The absorption coefficient is the principal optical parameter, defined as:

$$\alpha = \frac{4\pi k_e}{\lambda} \tag{2.10}$$

where k_e is the extinction coefficient – i.e. the imaginary part of the refractive index n – and λ is the wavelength of the incident photon. The absorption coefficient is normally calculated from the measurement of the transmission reflection coefficients T and R (for details see ref. 1). The absorption spectrum allows the estimation of the optical characteristics of the semiconductor, including the band gap. As shown in Figure 2.2, there are two types of semiconductors: direct, where the maximum of the valence band and the minimum of the conduction are at the same value of momentum k and indirect, where these points occur at different values of k. The reader is referred to Section 4.4.2 for details on the optical characterization of semiconductors used in this thesis.

E

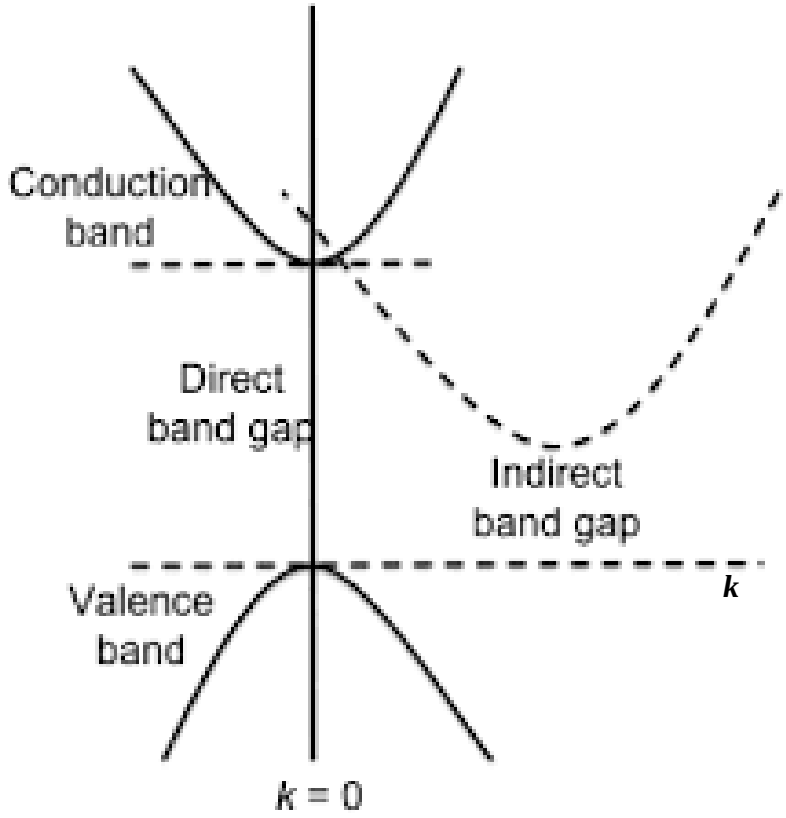

Figure 2.2: Band diagram of direct and indirect semiconductors.

2.3 P-n junction

2.3.1 Basic concepts

Inorganic solar cells are based on the concept of the p-n junction – i.e. the interface of two semiconductors with opposite polarity. A schematic diagram of an abrupt p-n junction and the related band diagram are shown in Figure 2.3.

Figure 2.3 (a) shows the charge distribution within the depletion region arising from the charges on fixed donor and acceptors ions after the carrier diffusion and drift have established equilibrium. It is the field arising from these charges that is responsible for the separation of optically excited charge carriers in the photovoltaic effect.

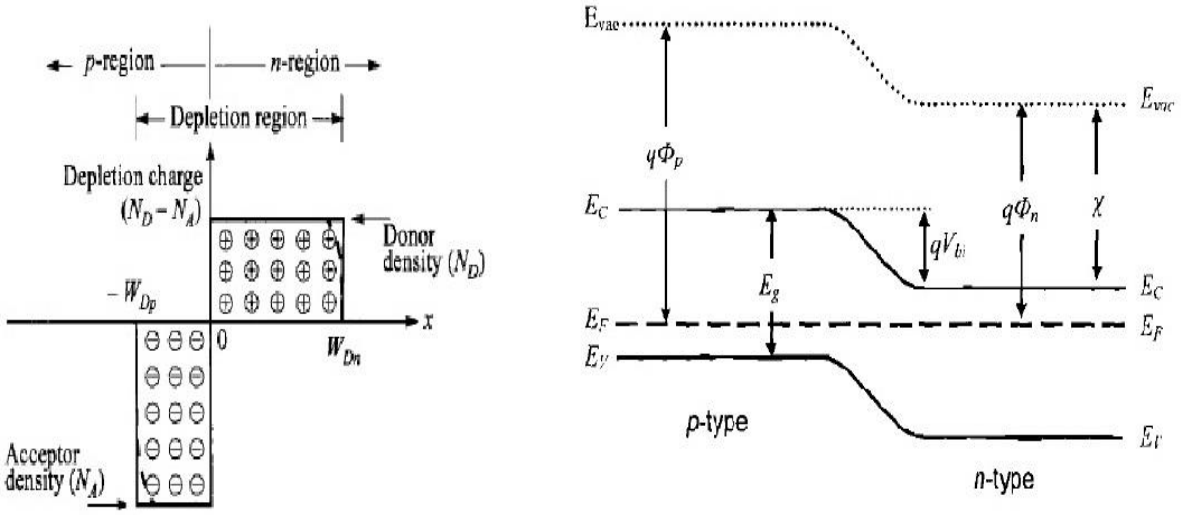

(a) (b)

Figure 2.3: (a) Schematic of p-n junction from ref. 1 and (b) band diagram of homojunction from ref. 2. In (b) ϕ_p and ϕ_n are the work functions of the p-type and n-type semiconductors, whereas χ is the electron affinity.

Important characteristics of the p-n junction are the built-in potential V_{bi} and the depletion region width W, which are given in the ideal case by Equations 2.11 and 2.12.

$$V_{bi} \cong \frac{\mathrm{k}T}{\mathrm{q}} ln\left(\frac{N_A N_D}{{n_i}^2}\right) \tag{2.11}$$

$$W = \sqrt{\frac{2\varepsilon_s}{\mathrm{q}}\left(\frac{N_A+N_D}{N_A N_D}\right) V_{bi}} \tag{2.12}$$

Here $\varepsilon_s = \varepsilon_r \cdot \varepsilon_0$ is the semiconductor permittivity. The reader is referred to ref. 1 for a complete description and derivation of these quantities.

2.3.2 Capacitance

The measurement of the device capacitance allows estimation of the depletion region width W and the doping concentration at the junction $N(W)$. The depletion-layer capacitance C is given from the incremental in charge dQ_c upon applying an infinitesimal voltage dV [1]. It is demonstrable for a p^+-n junction that:

$$\frac{d\left(\frac{1}{C^2}\right)}{dV} = -\frac{2}{q\varepsilon_r\,\varepsilon_0 A^2 N_A(W)} \tag{2.13}$$

where *A* is the device area, and:

$$W = \frac{\varepsilon_s A}{C(V)}. \tag{2.14}$$

2.3.3 Shockley equation

The Shockley equation (Equation 2.15) describes the density current-voltage *J*-*V* characteristics of an ideal p-n junction.

$$J = J_0\left(e^{\frac{qV}{nkT}} - 1\right) \tag{2.15}$$

Here *T* is the temperature, J_0 is the reverse saturation current density, a parameter related to the semiconductor properties, and *n* is the ideality factor. For an ideal p-n junction $n = 1$; in general the ideality factor $n > 1$ takes account of recombination, for example due to impurities and interfaces.

2.4 Fundamentals of solar cells

2.4.1 The photovoltaic effect

A solar cell transforms the incident photon energy by means of the photovoltaic effect – i.e. (a) the photon excites an electron from the valence band to the conduction band, (b) the electric field across the p-n junction ensures the separation of the electron-hole pair and the collection of the current [2]. The photovoltaic effect only takes place when $h\nu \geq Eg$ – i.e. when the incident photon energy $h\nu$ is sufficient to overcome the band gap energy *Eg*. Photons for which $h\nu < Eg$ are lost by transmission.

2.4.2 Solar radiation

The solar irradiance above the Earth's atmosphere (1353 W m^{-2}) is attenuated in the atmosphere by absorption and scattering. The performance parameters of solar devices for

terrestrial applications are evaluated under the standardized solar spectrum AM 1.5[1], as shown in Figure 2.4. Conventional measurements use this spectrum with a total solar irradiance of 1000 W m^{-2}.

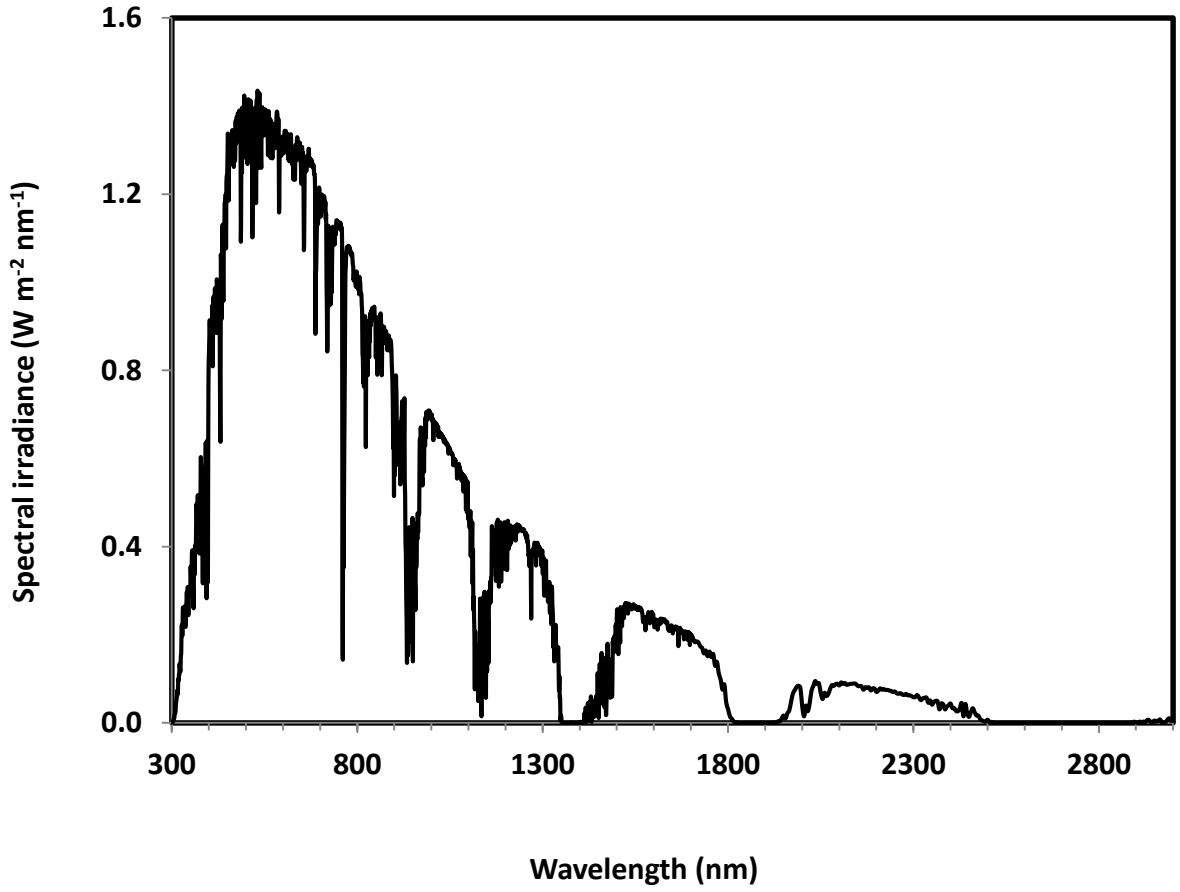

Figure 2.4: AM 1.5 solar spectrum. Data are from ref. 3.

2.4.3 *J-V* characteristics and performance parameters

The equivalent circuit of a single-junction solar cell, shown in Figure 2.5, includes a diode J_D (representative of the p-n junction), a current generator J_L and the parasitic series and shunt resistances *Rs* and *Rsh*.

[1] AM stands for "air mass" – i.e. the path length which light takes through the atmosphere normalized to the shortest possible path length. AM 1.5 implies that the zenith angle is ~48.2°.

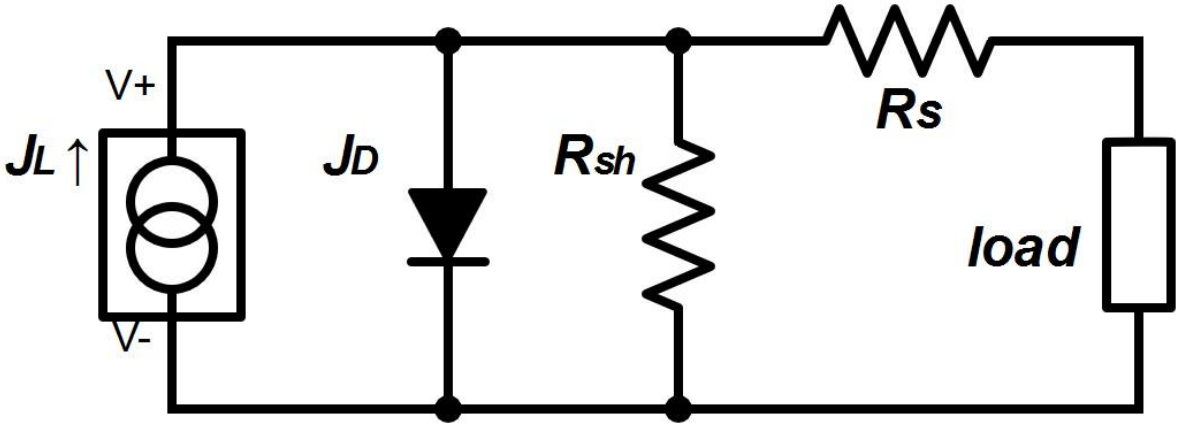

Figure 2.5: Equivalent circuit of a solar cell.

In the ideal case *Rs* = 0 (short-circuit) and *Rsh* → ∞ (open-circuit), in which case the solar cell *J-V* characteristics are described by the Shockley equation (Eq. 2.15). Under illumination an additional density current J_L is generated by photoexcitation as follows:

$$J = J_0\left(e^{\frac{qV}{nkT}} - 1\right) - J_L \qquad (2.16)$$

In the non-ideal case *Rs* and *Rsh* are finite quantities and the corresponding *J-V* characteristics are defined by equation (2.17).

$$J = J_0\left(e^{\frac{q(V-JR_S)}{nkT}} - 1\right) + \frac{V-JR_s}{R_{sh}} - J_L \qquad (2.17)$$

The *J-V* curves of a solar cell in dark conditions and under illumination are displayed in Figure 2.6.

Measurement of the *J-V* characteristic under illumination enables extraction of the performance parameters of the PV device, including [2]:

i. The short-circuit density current *Jsc*, defined as the density current generated from the device without voltage bias; in the ideal case $Jsc = J_L$.
ii. The open-circuit voltage *Voc*, defined as the applied voltage producing zero-current; in the ideal case:

$$Voc = \frac{kTn}{q} ln\left(\frac{J_L}{J_0} + 1\right). \qquad (2.18)$$

iii. Maximum density power point P_m, defined as the maximum point of the generated power density $P = J \cdot V$.

iv. Fill factor *FF*, defined as the ratio of the maximum power density P_m over the product $Jsc \cdot Voc$. The fill factor is a measure of the "squareness" of the *J-V* curve and tends ideally to 1.

$$FF = \frac{P_m}{Jsc \cdot Voc} \tag{2.19}$$

Efficiency η, defined as the ratio of the maximum density power generated P_m over the incident density power P_i.

$$\eta = \frac{P_m}{P_i} \tag{2.20}$$

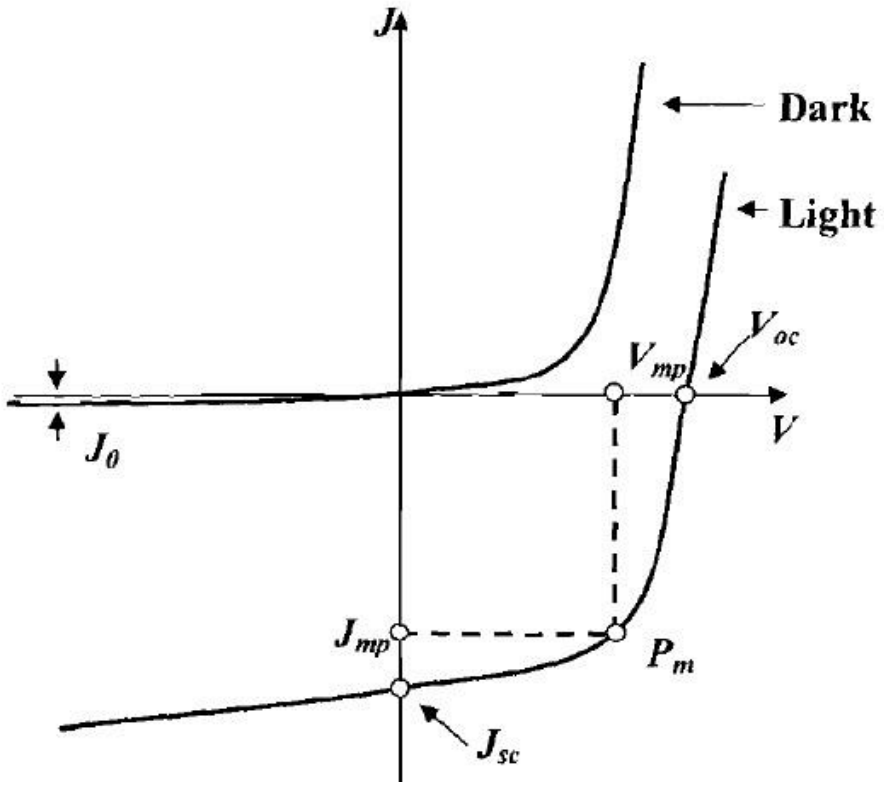

Figure 2.6: *J-V* curve of a solar cell [2].

The theoretical limit to the efficiency η of single-junction solar cells is given by the Shockley-Queisser limit [4], as shown in Figure 2.7, as a function of the absorber material band gap *Eg*. The maximum is nearly 30% for absorber materials having band gaps of ~1.5

eV. Therefore ideal candidates for absorber layers in PV devices should have an optical band gap of around this value.

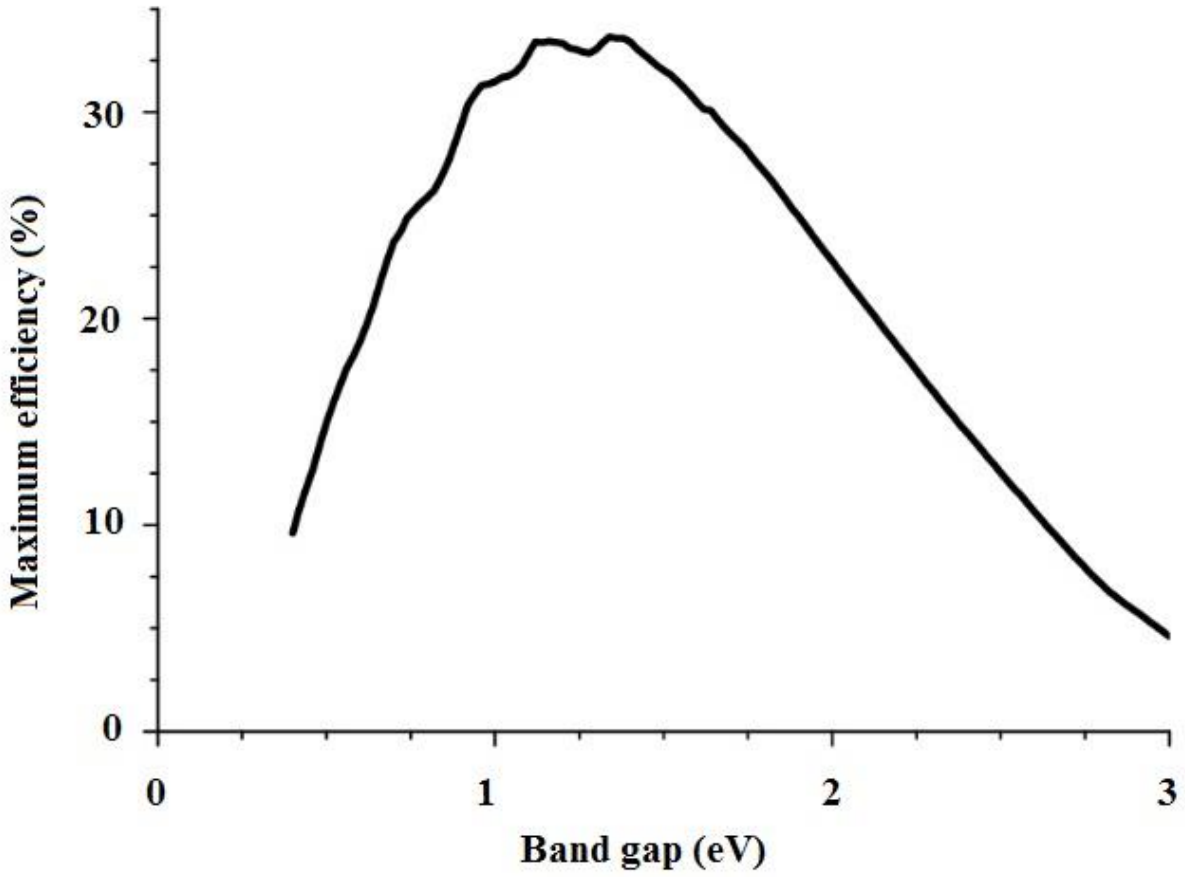

Figure 2.7: Maximum theoretical efficiency for single-junction solar cells as function of the absorber band gap, given from the Shockley-Queisser limit [4].

2.5 References for Chapter 2

[1] S. M. Sze and K. K. Ng, *Physics of Semiconductor Devices (3rd ed.)*, Wiley, 2007

[2] J. Nelson, *The Physics of Solar Cells*, Imperial College Press, 2003

[3] (8/12/2015) http://rredc.nrel.gov/solar/spectra/am1.5/ASTMG173/ASTMG173.html

[4] W. Shockley and H. J. Queisser, "Detailed balance limit of efficiency of p-n junction solar cells", *Journal of Applied Physics*, vol. 32, no. 3, pp. 510-519, 1961

3 Review of new chalcogenide materials for PV applications

3.1 Introduction

This Chapter summarizes the main findings from the literature on some new chalcogenide materials for photovoltaic applications. Generally, chalcogenides are compounds of Group VI element with for example one or more metals, as discussed by Moëlo et al. [1].

The particular subset of chalcogenides examined is based on Earth-abundant, inexpensive and non-toxic elements – i.e. comprising copper as a metallic cation, either antimony or bismuth as the second cation, and either sulfur or selenium as the anion. The generic chemical formula of the group under investigation is:

$$\mathrm{Cu}_x(\mathrm{Sb,Bi})_y(\mathrm{S,Se})_z\,. \tag{3.1}$$

There is an increasing interest in specific compounds of this family of sulfosalts – with above 50 articles having been published in the last three years – due to their potential for photovoltaic applications.

Section 3.2 introduces the Cu-Sb-S and Cu-Bi-S phase diagrams and the crystallographic properties of the principal phases. Sections 3.3 - 3.7 review the published works on thin film formation and PV applications of $CuSbS_2$, Cu_3SbS_3, $CuBiS_2$, Cu_3BiS_3 and the analogous selenides respectively. Each Section includes: (a) the structural, optical and electrical properties predicted from theoretical calculations; (b) the synthesis methods and characterization studies reported for thin films and nanostructures (e.g. nanoparticles, nanowires, nanorods); (c) a review on the photovoltaic devices fabricated from the material. The reader is referred to Chapter 4 for details of the specific deposition techniques and the characterization methods used in this work and relevant to these chalcogenides.

3.2 Phase diagrams

3.2.1 Cu-Sb-S system and principal phases

The Cu-Sb-S phase diagram comprises numerous binary and secondary phases, with complex phase transitions. Several authors have analysed this phase system. Firstly Skinner et al. [2] (1972) reported an exhaustive study of the phase diagram of the ternary system Cu-Sb-S, also summarizing the previous works on the phases occurring in the binary systems Cu-S, Cu-Sb and Sb-S. The authors recognized four ternary phases: (i) famatinite ("fm") Cu_3SbS_4 (tetragonal, space group *I42m*, a = 5.38 Å, c = 10.76 Å, melting congruently at ~627°C), with a large composition field; (ii) tetrahedrite ("td") (cubic, space group *I43m*), with the general formula proposed by the authors: $Cu_{12+x}Sb_{4+y}S_{13}$, where $0 \leq x \leq 1.92$ and $-0.02 \leq y \leq 0.27$; (iii) chalcostibite ("cstb") $CuSbS_2$; (iv) and "phase *B*", Cu_3SbS_3[1], stable at temperatures above 359°C and disappearing at high temperatures by melting congruently at ~607.5°C. The secondary phases recognized by the authors during their experiments, carried out at temperatures above 300°C, are: the Cu-Sb alloy (β), the copper-antimony solid solution ("Cu_{ss}"), covellite CuS ("cv"), the face centred cubic phase ("fcc") and the liquid phase ("L"). The labels in inverted commas were used by Skinner in the phase diagrams, some of which appear in this Chapter.

Lind and Makovicky [4] explored the phase relations in the Cu-Sb-S system for material measured at 200°C and 10^8 Pa under hydrothermal conditions. Diverse phase fields and individual phases were observed and analysed. In particular the authors realized that chalcostibite $CuSbS_2$ is a stable phase at 200°C and 10^8 Pa.

In 1977 Tatsuka and Morimoto [5] re-determined the phase relations for the Cu-Sb-S system with some slight modifications from the earlier work of Skinner et al.: in particular the previous study was partially incomplete, especially in regard to the phase relation of the tetrahedrite ("td ss") and pseudotetrahedrite ("ptd ss") solid solution fields below 400°C (for details the reader is referred to refs. 5 and 6). Figures 3.1 and 3.2 show the stable field of pseudotetrahedrite and the isothermal phase diagram at 400°C from ref. 5. There is a brief list of further secondary phases (labelled using the original author's abbreviations), including:

[1] At the time of the publication [2], the synthetic compound Cu_3SbS_3, had no known mineralogical equivalent in nature, thus Skinner and co-workers named the synthetic phase merely "Phase B". Oddly in the same year (1972), the mineral was discovered in the Ilimaussaq alkaline intrusion in South Greenland, and in 1974 S. Karup-Møller and E. Makovicky published a paper [3] naming this new mineral species skinnerite "*in honor of Professor Brian J. Skinner, Department of Geology and Geophysics, Yale University, who worked out the phase relations in the system Cu-Sb-S, including detailed descriptions of those for synthetic* Cu_3SbS_3".

chalcocite Cu_2S (“cc”), high chalcocite Cu_2S (“hcc”), high digenite $Cu_{1.75}S$ (“hdg”) and stibnite Sb_2S_3 (“stb”).

Braga et al. [7] studied the Cu-Sb-S phase system from synthetic samples prepared by a melting-homogenization approach. In particular Figure 3.3 shows the Cu-Sb-S phase diagram at 300°C extracted from ref. 7. Finally Karup-Møller [8] explored the Cu-Sb-S system at 700°C.

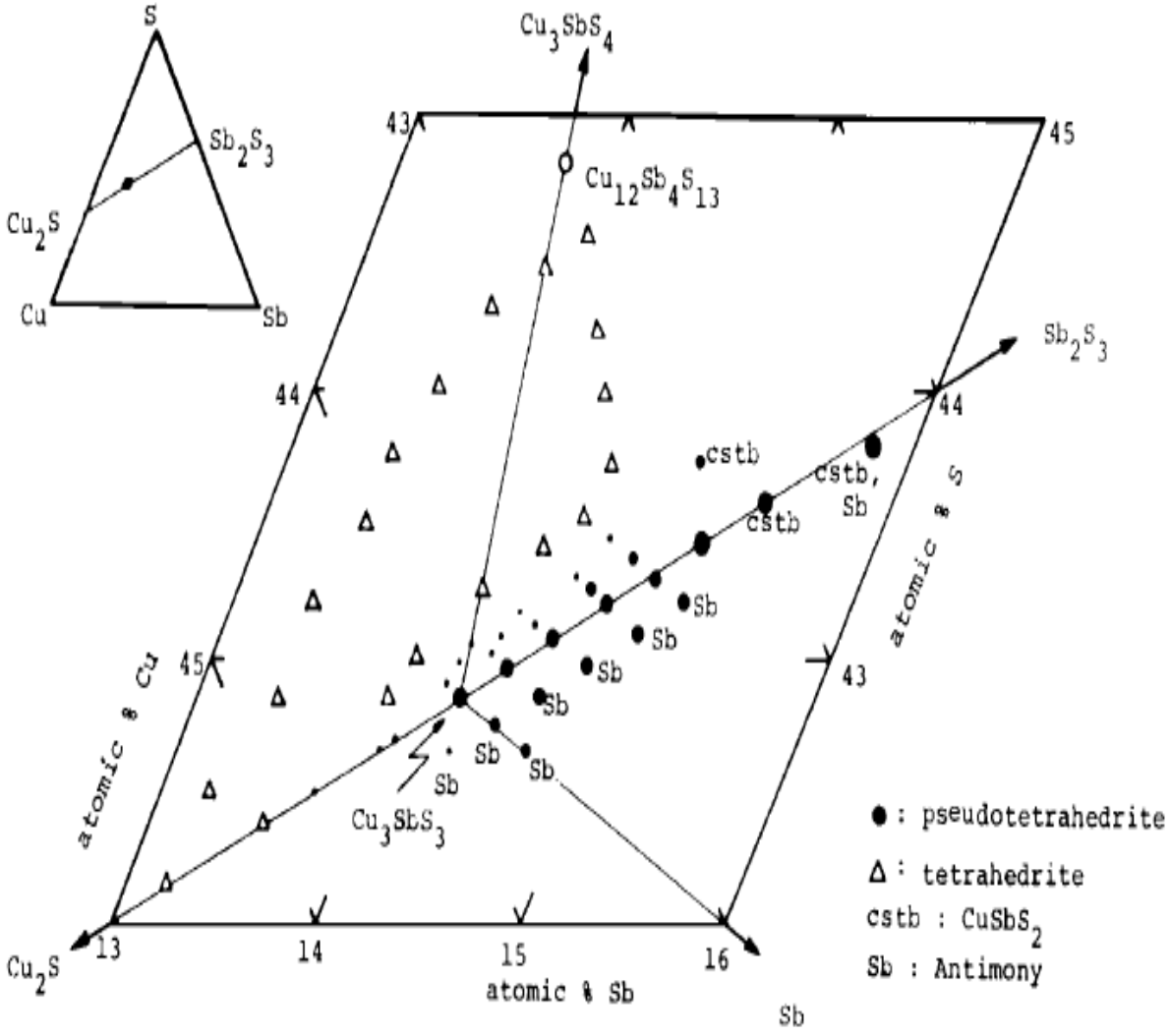

Figure 3.1: Stable field of pseudotetrahedrite, with additional phases displayed. Diagram from ref. 5.

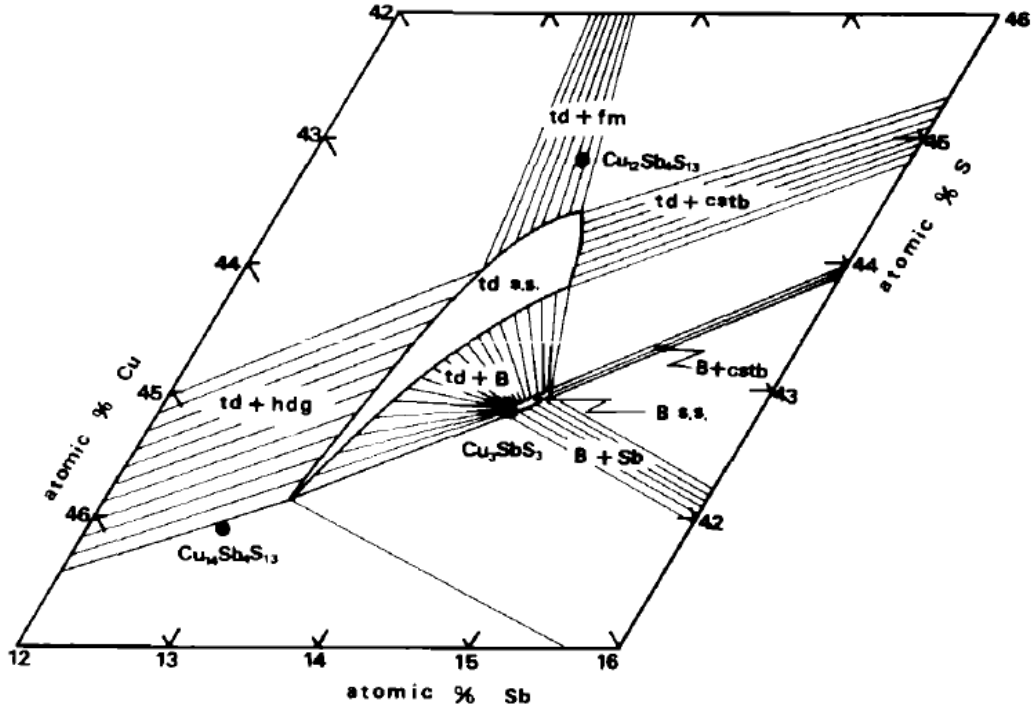

Figure 3.2: Composition field of tetrahedrite and pseudotetrahedrite at 400°C. Diagram from ref 5.

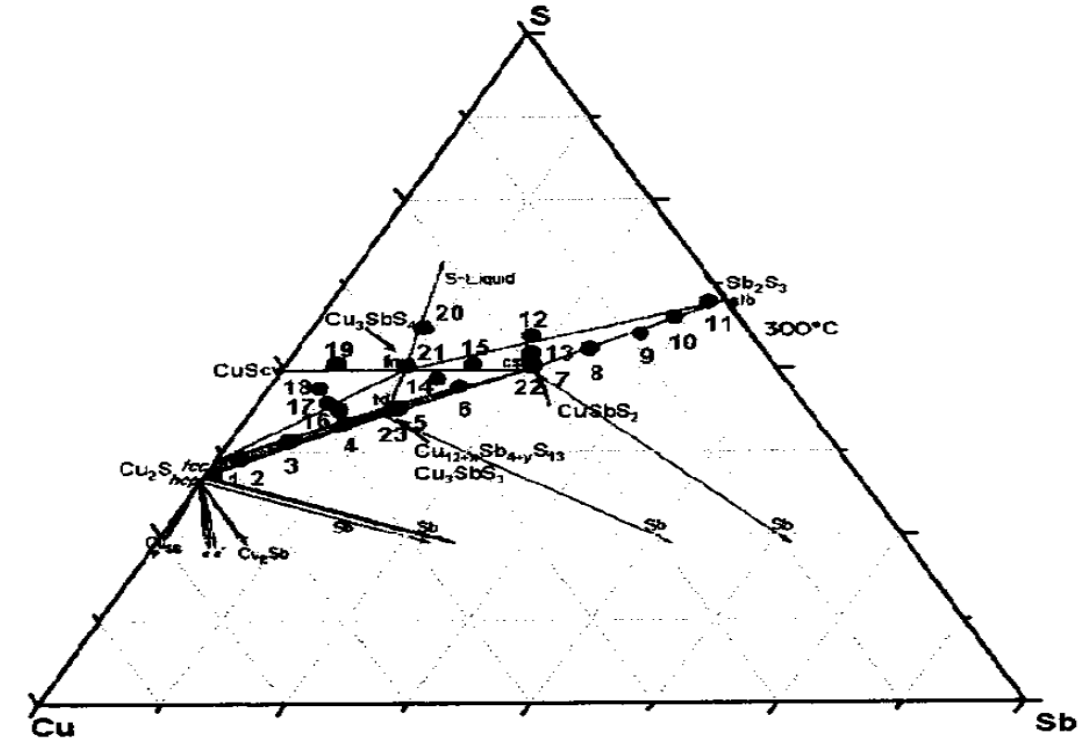

Figure 3.3: Cu-Sb-S phase system at 300°C. Diagram from ref. 7.

Finally Firdu and Taskinen [9] reported the phase equilibria of the Cu-Sb-S system at high temperatures by the pseudo-binary diagram shown in Figure 3.4.

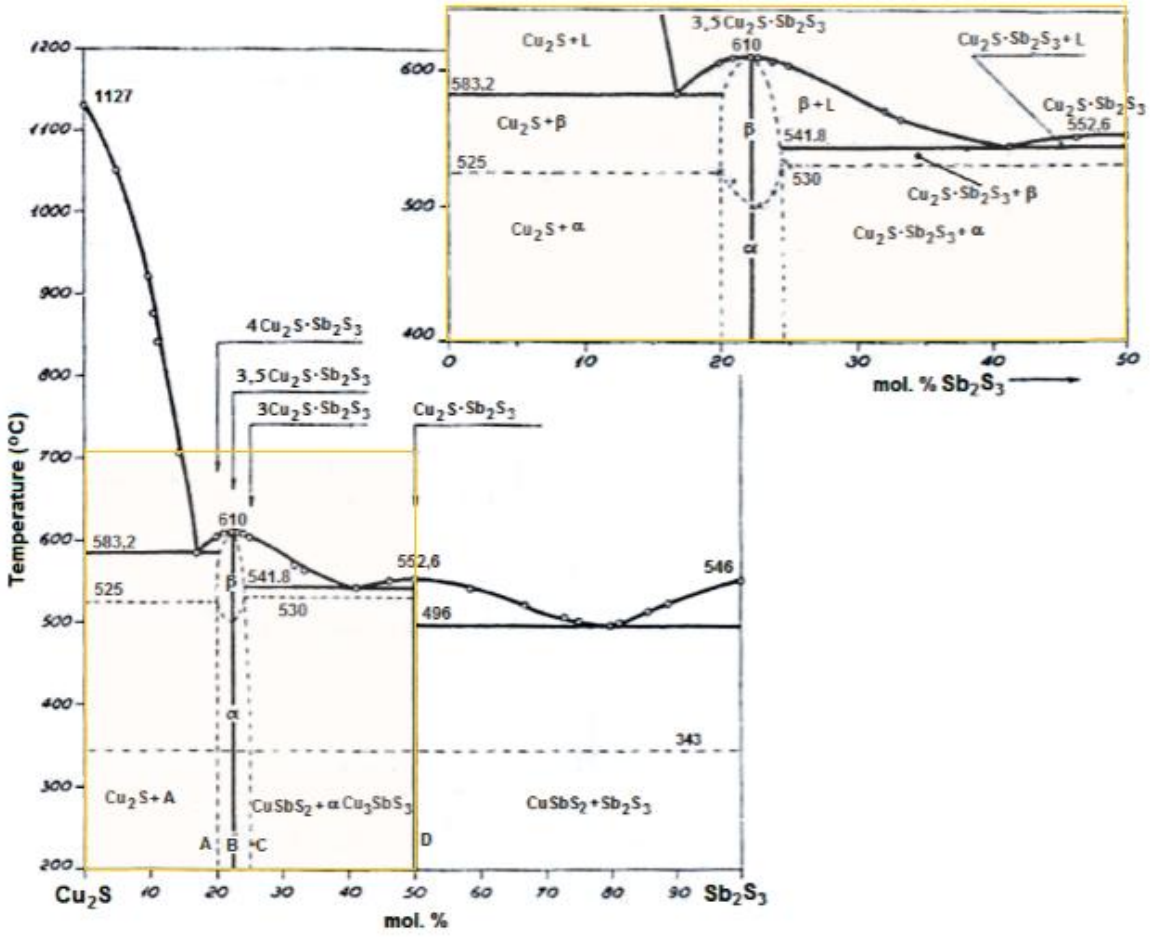

Figure 3.4: Phase diagram of the Cu-Sb-S system at elevated temperatures. Diagram from ref. 9.

The mineralogy and crystallographic properties of the phases of interest from the Cu-Sb-S system – i.e. $CuSbS_2$ and Cu_3SbS_3 – are now introduced.

(a) $CuSbS_2$ – Chalcostibite (from the Greek word "khalkos" meaning copper and the Latin word "stibium" meaning antimony) is a sulfosalt with the chemical formula $CuSbS_2$,

forming in carbonate-rich cavities within antimony and copper deposits [10]. This species is known only in few deposits, including in Bolivia, Canada, Italy, Germany, Slovakia, Morocco and France. The chalcostibite crystals are typically prismatic and elongated in shape, from lead grey to deep grey in colour with some black streaks, normally being opaque and having a metallic lustre.

Razmara et al. [11] described the crystal structure of chalcostibite as "orthorhombic *Pnma* with one antimony atom forming trigonal pyramids linked to three sulfur atoms and with two more sulfur atoms at greater distances forming distorted square pyramids. These pyramids are linked to form chains of SbS_2 parallel to *b*. The Cu-S_4 tetrahedra are corner linked, also forming chains of CuS_3 parallel to *b*. These two types of chains are linked to form sheets perpendicular to *c*" [11].

Kyono and Kimata [12] reported a detailed article updating the crystal parameters of chalcostibite.

(b) Cu_3SbS_3 – The mineral species skinnerite, with the general chemical formula Cu_3SbS_3, was discovered in 1972 in South Greenland and owes its name to Prof. Brian J. Skinner who previously studied the phase relations in the laboratory ternary system Cu-Sb-S and in particular analysed the properties of synthetic Cu_3SbS_3 [3]. The natural species occurs mainly in some mineral deposits in Greenland, including in Kangerdluarssuaq, Ilimaussaq, Narsaq and Kitaa [13]. A typical skinnerite mineral appears silver grey with reddish black streaks, has a metallic lustre and it is brittle; the crystal morphology is granular with irregular grains. A pure skinnerite crystal contains: 46.66% of copper, 29.80% of antimony and 23.54% of sulfur [14], with silver being a common impurity.

The first authors describing the mineralogical and crystallographic properties of this sulfosalt were S. Karup-Møller and E. Makovicky [3]. In their samples they observed a chemical composition very close to the ideal composition 3:1:3 with approximately 2% of silver impurities. The data from the crystal analyses also agreed with the previous studies of Skinner et al. on the synthetic compound [2], in particular concerning the phase transformation *B*-to-*B'*, where in accordance with the formalism of Skinner et al., *B* is the high temperature, and *B'* the low temperature modification. The phase *B'* is identified as monoclinic, space group $P2_1/c$ with lattice constants: $a \cong 7.815$ Å, $b \cong 10.252$ Å, $c \cong 13.270$

Å and β ≅ 90°21'. The synthetic phase *B* is described as orthorhombic, space group *Pnma*, with lattice constants (at 150°C) *a* = 7.81 Å, *b* = 10.25 Å, *c* = 6.61 Å [3]. The lattice constants of the high temperature form of skinnerite Cu_3SbS_3 and wittichenite Cu_3BiS_3 are very similar while the low temperature forms are deeply diverse [3]. From the experimental analysis of Skinner et al. on the Cu-Sb-S system, the phase Cu_3SbS_3 is stable in the temperature range 359 - 607°C; below 359°C it decomposes in a mixture of Sb, $CuSbS_2$ and $Cu_{12+x}Sb_{4+y}S_{13}$ phases, and at about 607°C melts congruently [2]. Karup-Møller and Makovicky hypothesized an analogous behaviour for the natural phase, irrespective of the silver impurities. Finally the co-workers illustrated the conditions for natural crystallization of skinnerite from the geological and mineralogical indications.

Whitfield [15] clarified that Cu_3SbS_3 presents three stable forms at high, room and low temperature respectively. According to the formalism from Pfitzner for the polymorphisms of skinnerite [16], α denotes the high-temperature, β the room temperature (RT) and γ the low-temperature modification.

3.2.2 Cu-Bi-S system and relevant phases

Firdu and Taskinen [9] outlined the phase equilibria in the Cu-Bi-S ternary system. Figure 3.5 shows the Cu-Bi-S phase system at high temperatures by means of a pseudo-binary diagram for Cu_2S-Bi_2S_3. The principal ternary phases and intermetallic compounds are Cu_9BiS_6, $CuBi_3S_5$, $Cu_3Bi_5S_9$, $Cu_{24}Bi_{26}S_{51}$, $CuBiS_2$ and Cu_3BiS_3.

Wang [17] conducted some experiments to investigate the Cu-Bi-S system at low temperatures. The two isothermal phase diagrams at 200 and 300°C shown in Figure 3.6 are extracted from ref. 17.

At 200°C the two stable ternary phases are $CuBiS_2$ and Cu_3BiS_3, and both coexist with metallic bismuth. At 300°C the stable ternary phases are $CuBiS_2$, Cu_3BiS_3 and $Cu_4Bi_4S_9$.

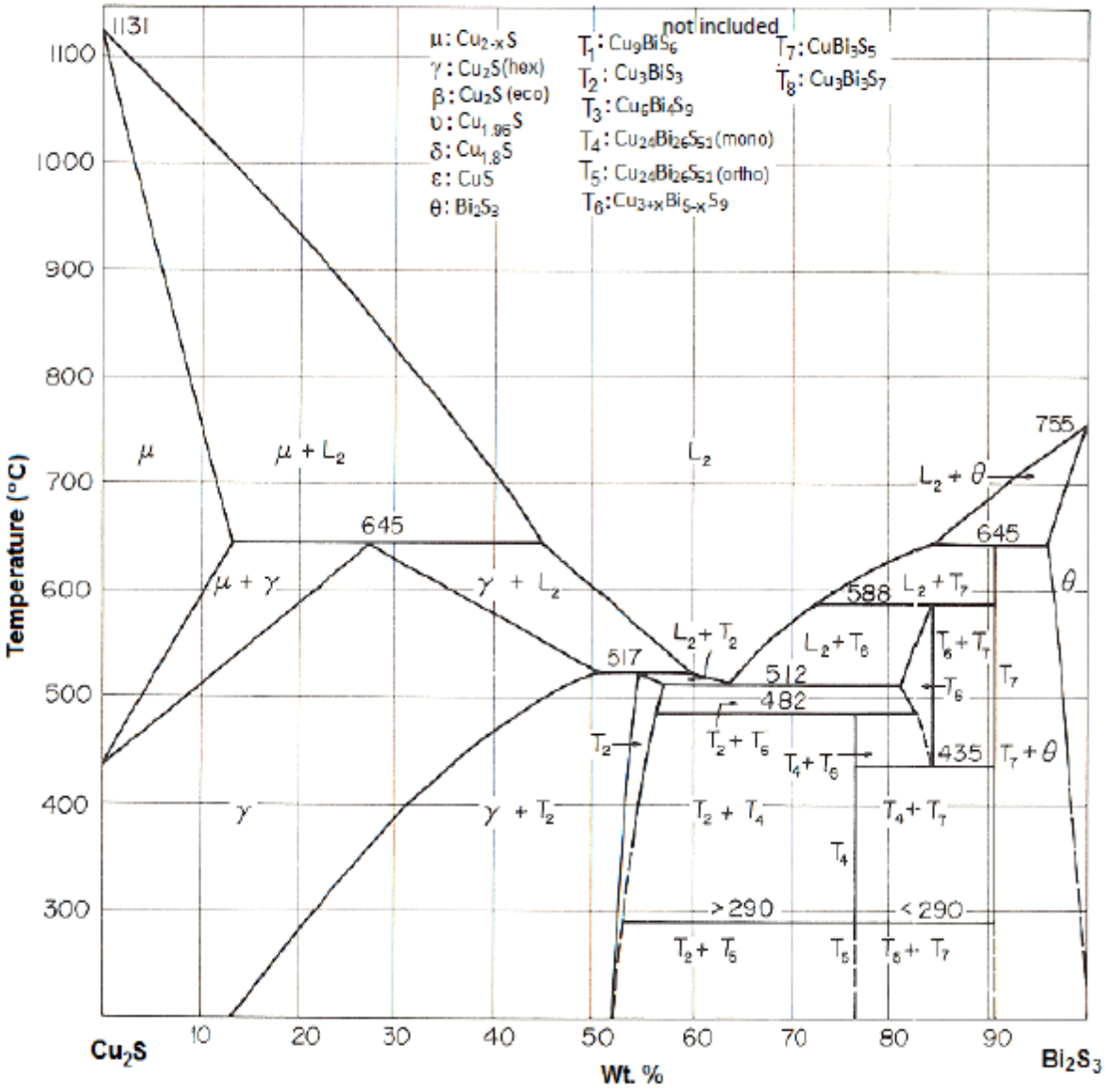

Figure 3.5: Phase diagram of the Cu-Bi-S system at high temperature. Diagram from ref. 9.

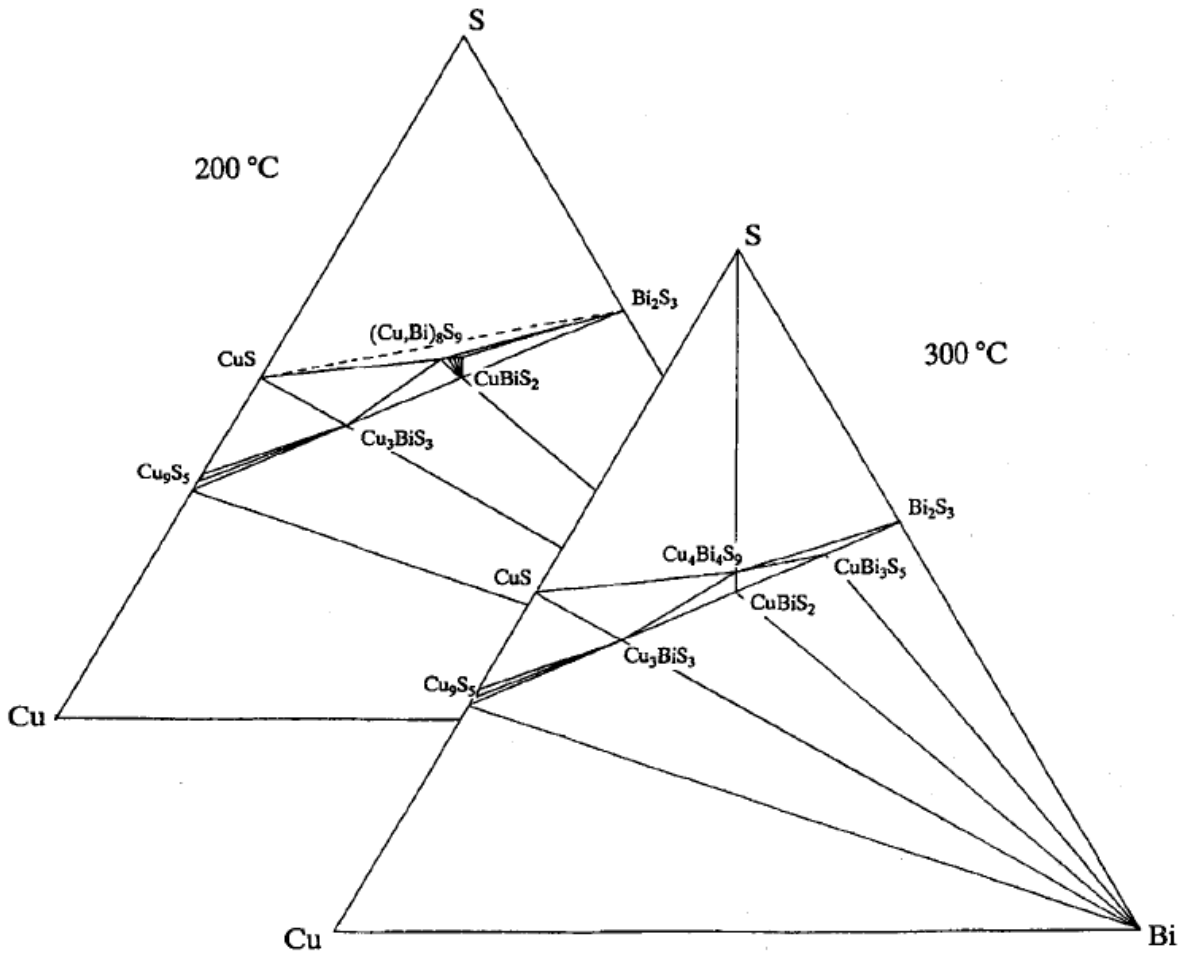

Figure 3.6: Cu-Bi-S phase diagram at 200 and 300°C. Diagram from ref. 17.

The mineralogy and crystallography of the $CuBiS_2$ and Cu_3BiS_3 phases are now presented.

(a) $CuBiS_2$ – Emplectite (from the Greek word "emplektos" meaning interwoven) is a sulfosalt discovered in 1817 with the formula $CuBiS_2$ located typically in moderate temperature hydrothermal veins [18]. This mineral species is brittle, presents a metallic lustre with colour ranging from greyish to tin white. The typical weight composition of emplectite is: 18.88 % of copper, 62.07% of bismuth and 19.05% of sulfur [19].

The crystal structure of emplectite is similar to chalcostibite and has been fully described from Kyono and Kimata [12] – previous studies were conducted from Razmara et al. [11], Portheine and Nowacki [20], Hofmann [21].

(b) Cu_3BiS_3 – Wittichenite (named in 1853 from the discovery locality, Wittichen in Germany) is a mineral species with the generic formula Cu_3BiS_3 exhibiting a variety of colours, from yellow to lead grey and a metallic lustre. This species typically occurs in hydrothermal veins with other bismuth minerals. The weight composition of pure wittichenite is: copper 38.45%, bismuth 42.15%, sulfur 19.40% and a typical impurity is silver [22, 23].

The first exhaustive report on the crystal structure properties of wittichenite measured at ambient conditions is from Kocman and Nuffield [24]. Table 3.1 summarises the crystallographic analysis by Kocman and Nuffield on Cu_3BiS_3 and the lattice properties of $CuSbS_2$ and $CuBiS_2$ [12, 24].

Name	Chalcostibite	Emplectite	Wittichenite
Chemical formula	$CuSbS_2$	$CuBiS_2$	Cu_3BiS_3
Formula weight	249.42	336.65	n.r.
Crystal system	orthorhombic	orthorhombic	orthorhombic
Space group	*Pnma*	*Pnma*	$P2_12_12_1$
***a* (Å)**	6.018(1)	6.134(1)	7.723(10)
***b* (Å)**	3.7958(6)	3.9111(8)	10.395(10)
***c* (Å)**	14.495(7)	14.540(8)	6.716(5)
***V* (Å^3)**	331.1(1)	348.8(2)	539.2(2)
reference	12	12	24

Table 3.1: Lattice parameters and crystallographic properties of $CuSbS_2$, $CuBiS_2$ and Cu_3BiS_3. (n.r. = not recorded). Data from references 11 and 24.

At a later stage Makovicky [25] has studied the phase transformations of Cu_3BiS_3 from 25 to 300°C. The author observed a small rate thermal expansion of the lattice constants *a* and *c* from 25 to 80°C (the so called low polymorph). The first phase transformation occurs

at about 118.5°C from the low polymorph to the intermediate polymorph(s). The latter has space group *Pnma* or *Pn2₁a* with some satellites on the reciprocal lattice. These satellites gradually disappear in the range 170 - 190°C, corresponding to the transition to the high polymorph, which persists up to 290°C and again has the *Pnma* or *Pn2₁a* space group. Above the first phase transformation the author reported a linear contraction of *a* and *c* with rising temperature. On the other hand the lattice constant *b* increased above 118.5°C, so that overall the unit-cell volume remained approximately constant in the range 25 - 350°C. Makovicky argued that the phase transformation is due to a rearrangement of the copper atoms in the lattice and the onset of their mobility. The author analysed this point extensively in a later study [26]. Finally Mariolacos [27] conducted a thermodynamic study on single crystal Cu_3BiS_3 deposited by chemical vapour transport in the gradient temperature.

3.3 $CuSbS_2$ for photovoltaic applications

3.3.1 Fundamental properties

Dufton et al. have conducted the first theoretical study on the structural and electronic properties of $CuSbS_2$ thin films by using the density functional theory (DFT) [28]. From their simulations the authors found for $CuSbS_2$ an indirect band gap of 1.65 eV and having its lowest energy direct gap just 0.1 eV above this – i.e. in practice $CuSbS_2$ has strong direct gap absorption. In addition Dufton emphasized that the $CuSbS_2$ thin films are thermodynamically stable, and present a complex and asymmetrical structure that confirms the findings from X-ray diffraction (XRD).

The calculations conducted by Kumar and Persson on $CuSbS_2$ confirmed the main findings from Dufton. In addition the authors predicted high absorption coefficient – i.e. between 10^5 and 10^6 cm^{-1} in the visible and near infrared – caused from the localized *p*-like states of cation Sb in the conduction band region [29, 30]. From their theoretical investigation Maeda and Wada found slight different values of band gaps for $CuSbS_2$ – i.e. direct transaction of ~1.25 eV and indirect transaction of ~1.16 eV [31].

Perniu et al. have reported an interesting article exploring the defect chemistry of $CuSbS_2$ [32]. Assuming that the point defects have a crucial impact on the fundamental properties of materials, the authors described the formation of different defect mechanisms

using the standard Kröger-Vink notation. The point defects intrinsically present in the $CuSbS_2$ lattice are vacancies (V'_{Cu}, V'''_{Sb}, V'_S) and interstitials (Cu'_i, Sb'''_i, S''_i). Perniu highlighted how these defects influence the properties of the material, in particular how the ionic and electronic defects affect the conductivity. The authors deduced that by using an annealing stage in a reactive atmosphere containing sulfur during the deposition process of $CuSbS_2$ it is possible to tailor the p-type conductivity of the compound.

Yang et al. underlined that $CuSbS_2$ is an intrinsically p-type semiconductor from the Cu vacancy defects. From DFT simulations Yang et al. also found that the forbidden band gap of $CuSbS_2$ does not include recombination center defects [33].

All these theoretical works on the fundamental properties of $CuSbS_2$ emphasized the potential of the material as an absorber in photovoltaic devices. In particular Tablero estimated a maximum efficiency of ~41% for a solar device based on ~10 µm $CuSbS_2$ absorber layer under maximum light concentration – i.e. 46200 suns, where 1 sun = 1 kW m^{-2} [34].

Finally the DFT study conducted from Gudelli et al. suggested the viability of p-type $CuSbS_2$ for thermoelectric applications at low temperature – i.e. below the melting point ~825 K [35].

3.3.2 Synthesis approaches for $CuSbS_2$ thin films and nanostructures

$CuSbS_2$ thin films for PV applications have been deposited by numerous techniques, including thermal evaporation, spray pyrolysis, chemical bath deposition, sulfurization of the metal precursors, rf sputtering and spin coating. The properties of the films depend strongly on the method adopted and the growth conditions. A summary is presented in Table 3.2.

Compound	Author	Growth technique	ref.	*Eg* (eV)	σ type
$CuSbS_2$	Rabhi	thermal evaporation	36	0.91 - 1.89	p-type
	Soliman	thermal evaporation	39	nr	p-type
	Suriakarthick	thermal evaporation	40	1.62 - 2.18	p-type
	Manolache	spray pyrolysis deposition	41	1.10 - 1.80	nr
	Liu	spray pyrolysis deposition	43	1.72 - 1.75	nr
	Nair	chemical bath deposition	44	1.53	p-type
	Garza	chemical bath deposition + thermal evaporation	46	1.54	p-type
	Ornelas	chemical bath deposition + thermal evaporation	47	1.55	p-type
	Colombara	sulfurization of metal precursors	49	1.5	p-type
	Ikeda	sulfurization of metal precursors	51	1.5	p-type
	Welch	rf sputtering	53	1.5	p-type
	Al-Saab	rf sputtering	54	nr	nr
	Al-Saab	atmospheric plasma chemical vapour deposition	54	nr	nr
	Rastogi	electrodeposition	55	1.65	p-type
	Choi	spin coating	56	1.5	p-type
	Tian	spin coating	57	nr	nr
	Yang	spin coating	33	1.4	p-type
	Yan	drop-casting	58	1.4	p-type
Cu_3SbS_3	Maiello	sulfurization of metal precursors	75	1.84	p-type
	Rodriguez	chemical bath deposition	77	1.6	nr
$CuBiS_2$	Pawar	spray pyrolysis deposition	87	1.65	n-type
	Sonawane	chemical bath deposition	88	1.8	n-type
	Colombara	sulfurization of metal precursors	92	nr	nr
	Wubet	reactive sintering	93	nr	p-type
Cu_3BiS_3	Nair	chemical bath deposition	95	nr	p-type
	Estrella	chemical bath deposition + thermal evaporation	96	1.2	p-type
	Gerein	sulfurization of metal precursors	97	nr	nr
	Colombara	sulfurization of metal precursors	100	1.4	nr
	Gerein	rf sputtering	101	1.4	p-type
	Mesa	two-stage co-evaporation	103	1.41	p-type
	H. Hu	screen printing method	109	nr	nr
$CuSbSe_2$	Tang	Electrodeposition + RTA	120	1.1	p-type
	Colombara	selenization of metal precursors	49	1.2	p-type
	Welch	rf sputtering	122	1.1	p-type
$CuBiSe_2$	Bari	chemical bath deposition	124	1.84 - 2.10	n-type

Table 3.2: Experimental works on the film deposition of the novel chalcogenides by different methods. The optical band gap and conductivity-type measured are reported. (nr = not recorded).

(a) Thermal evaporation – Rabhi et al. have deposited $CuSbS_2$ thin films by thermal evaporation. Crushed powder of an ingot of $CuSbS_2$ used as the source material was evaporated in high vacuum from a resistively heated molybdenum crucible. The substrate temperature during the deposition was held in the range 100 - 200°C. The deposition lasted

two hours, and the thin films exhibited the following properties [36]: strong adhesion to the substrates; crystallinity increased with the substrates temperature *Ts*, for *Ts* > 170°C; whereas, for *Ts* < 170°C, the films were amorphous; absorption coefficient between 10^5 cm^{-1} and 10^6 cm^{-1} in the visible and near-infrared range, with a sharp fall at the band edge, especially for those films deposited at lower *Ts*; direct band gap in the range 0.91 - 1.89 eV, this being dependent on the growth temperature; resistivity in the range 0.03 - 0.96 Ω cm, again depending on *Ts*; and p-type conductivity. Rabhi and co-workers recently reported the effects of post-growth annealing in vacuum on the structural, optical and electrical properties of thermally evaporated $CuSbS_2$ films [37]. They found the the annealing improved the crystallinity, increased the optical band gap (annealing temperature dependent) and the samples assumed p-type conductivity. Fadhli et al. reported similar work with annealing in air [38].

Soliman et al. have analysed the transport properties of $CuSbS_2$ thin films prepared by thermal evaporation [39]. The crystal structure determined by X-ray diffraction and the calculated lattice parameters were in good agreement with the data reported by theoretical papers. From transmission electron microscopy the authors concluded that heat treatment changes the nature of the thin films from amorphous to crystalline. Soliman et al. also found that the electrical conductivity increases with the temperature – i.e. as expected in semiconductors. Finally the films exhibited p-type conductivity and were non-degenerate semiconductors.

Suriakarthick et al. deposited $CuSbS_2$ films by thermal evaporation from a bulk material grown by solvothermal method [40] in the *Ts* range RT - 400°C. The films were generally p-type, with carrier concentration increasing with *Ts*. The optical band gap decreased from 2.18 eV, for the films grown at RT, to 1.62 eV for those deposited at *Ts* = 400°C.

(b) Spray pyrolysis deposition (SPD) – Manolache et al. report the growth of $CuSbS_2$ thin films by spray pyrolysis deposition technique. For details on the specific precursors used, the precursor weight ratios and other growth information the reader is referred to ref. 41. By analysing the films grown under different precursor weight ratios, the authors found that the porosity and the crystallite size of the films deposited increased with

the relative concentration of the antimony precursor $(CH_3COO)_3Sb$ in the spray solution. The optical band gap was between 1.1 and 1.8 eV increasing with the grain size of the films, this resulting directly proportional to the antimony precursor relative concentration [41].

Popovici and Duta have investigated the effects of polymeric additives into the spray solution of the SPD precursors to control the stability of the reactant species, which influence the reaction rate, and in turn the morphology of $CuSbS_2$ films [42].

Liu et al. deposited $CuSbS_2$ films by SPD from a methanol solution in the range 280 - 400°C [43]. The as-grown samples exhibited band gap of ~1.75 eV

(c) Chemical bath deposition (CBD) – Nair et al. fabricated $CuSbS_2$ thin films by chemical bath deposition. The samples were produced by the heating of a CBD prepared Sb_2S_3-CuS bi-layer in nitrogen at 350 - 400°C. The detailed growth information is reported in ref. 44. The films presented some interesting properties – i.e. the films were orthorhombic, had uniform atomic composition through the depth of the film, had a direct band gap of 1.53 eV, and p-type photoconductivity.

Ezugwu et al. examined the effects of the deposition time on the optical properties of $CuSbS_2$ thin films deposited by CBD at room temperature [45]. In particular the authors found that the deposition time had a strong impact on the optical properties of the films, with measured energy band gaps apparently varying in the range 1.3 - 2.3 eV. (This would of course be unexpected for the deposition of a homogeneous film having controlled composition).

Garza et al. reported a novel two-step method to deposit $CuSbS_2$ thin films. Firstly the authors grew antimony sulphide Sb_2S_3 layers (300 nm thick) onto glass substrates by CBD. Then Cu thin films (of thickness between 20 and 50 nm) were thermally evaporated onto the Sb_2S_3 layers under high vacuum and finally the samples were heated at either 300 or 380°C in vacuum [46]. From their preliminary study the authors found that the optical properties and conductivity type of the samples were suitable for PV applications – i.e. they had a band gap of ~1.54 eV and p-type conductivity. Ornelas-Acosta et al. used a similar deposition approach to produce photoactive $CuSbS_2$ films having a band gap of 1.55 eV [47, 48].

(d) Sulfurization of metal precursor – Thin films of $CuSbS_2$ have been grown by a number of authors using the method of sulfurization of a metal 'precursor' stack comprising copper and antimony. Different methods are reported for the deposition of the metal precursor, including electrodeposition, thermal evaporation and dc sputtering.

Colombara et al. deposited the metal precursor by either evaporation of a Cu/Sb stack or electrodeposition of a Sb-Cu alloy [49]. The annealing of the precursors was performed in atmosphere containing sulfur, in the temperature range 200 - 400°C. The authors produced single-phase $CuSbS_2$ films at temperatures above 350°C, with band gap of ~1.5 eV and p-type conductivity. Maiello et al. employed dc sputtering for the deposition of the metal precursor to produce Cu-Sb based sulfides [50].

Ikeda et al. sulfurized the electrodeposited metal stack by a multi-step temperature process – i.e. (a) the metal stack was preheated at 510°C in argon atmosphere for 60 minutes, (b) the sample was then sulfurized at 450°C by using 5% H_2S for 30 minutes, (c) finally the sample was cooled down to room temperature in-situ [51, 52]. The authors produced single-phase $CuSbS_2$ films from stoichiometric precursors, whereas Cu-rich or Cu-poor stacks contained secondary phases after sulfurization, such as Sb_2S_3 and $Cu_{12}Sb_3S_{14}$.

(e) Rf sputtering – Welch et al. reported a combinatorial approach for the growth of chalcogenide films by rf sputtering from one Cu_2S and two Sb_2S_3 binary targets to control the composition [53]. In particular $CuSbS_2$ films were deposited by a three-stage process, with: (a) co-sputtering from both Cu_2S and Sb_2S_3 sources during the heating of the substrate, (b) co-sputtering at the desired *Ts* temperature – i.e. normally 400°C, (c) cooling down with the Sb_2S_3 sources open. $CuSbS_2$ single-phase films exhibited absorption coefficients of ~10^5 cm^{-1}, with band gaps of ~1.5 eV, and p-type conductivity with the carrier concentration being tunable from 10^{16} to 10^{18} cm^{-3} by changing the sputtering conditions.

Al-Saab produced $CuSbS_2$ thin films by rf sputtering from a ternary target [54]. The films were sputtered on molybdenum-coated glass at room temperature and subsequently annealed by rapid thermal process in the temperature range 250 - 325°C from 5 to 60 minutes. The structure and composition of the samples were characterized by XRD and secondary emission microscopy and energy-dispersive X-ray spectroscopy (SEM/EDX). The author observed loss of antimony at temperatures above 300°C.

(f) Atmospheric plasma chemical vapour deposition (APCVD) – Al-Saab fabricated also $CuSbS_2$ films by atmospheric plasma chemical vapour deposition [54] on glass substrates by using $SbCl_5$, CuCl and H_2S as precursor species. This technique yielded very high growth rates (e.g. 35 μm deposited in 1 hour).

(g) Electrodeposition – Rastogi and Janardhana [55] produced chalcogenide films by electrodeposition from ionic liquid electrolyte. Single-phase $CuSbS_2$ films were grown from a stoichiometric precursor ratio at 80°C and showed a band gap of ~1.66 eV and p-type conductivity.

(h) Spin-coating – The deposition of chalcogenide films by spin-coating is reported by Choi et al. [56]. The authors used a Cu-Sb-thiourea complex precursor solution with post-growth annealing in argon atmosphere in the range 300 - 500°C. Single-phase $CuSbS_2$ were deposited at 500°C and exhibited a band gap of ~1.5 eV, with absorption coefficient generally increasing with the number of cycles.

Tian et al. report the deposition of $CuSbS_2$ nanocrystal thin films by spin coating from a metal-organic homemade precursor solution [57].

Yang et al. grew $CuSbS_2$ films by spin coating from a hydrazine based solution [33]. Optimal samples exhibited large grain sizes, optical band gaps of ~1.4 eV and p-type conductivity with hole concentrations of $\sim 10^{18}$ cm^{-3} and mobilities of 49 cm^2 V^{-1} s^{-1}.

(i) Drop-casting – A novel method developed with the intention of producing large-area solar cells at low cost is the nanoparticle-ink painting approach for the deposition of the absorber layer. Yan et al. reported the successful synthesis of $CuSbS_2$ brick-like nanoparticles, or 'nanobricks', by using a hot-injection technique. An ink was then formed by dispersing the nanobricks in toluene. The authors deposited $CuSbS_2$ thin films by drop-casting the ink onto indium tin oxide (ITO) substrates [58]. The resulting samples exhibited a band gap of ~1.40 eV, had p-type conductivity and were stable under AM 1.5 light-soaking. The study reported by Yan et al. in ref. 57 was based on the previous work from Zhou et al.

on the synthesis of $CuSbS_2$ particles in millimetre scale by solvothermal method. Each experiment was performed by mixing the reagents in a sealed tube heated 160°C for 10 days [59].

(j) Nanostructures – The deposition of spherical $CuSbS_2$ nanoparticles by solvothermal technique is reported by Su et al. [60], whereas Ikeda et al. employed a hot-injection method [61]. The latter approach is widely used for the synthesis of $CuSbS_2$ nanocrystals [62 - 65], nanobricks (see section i above) [58] and nanoplates [66]. Finally the growth of $CuSbS_2$ nanorods by a low temperature hydrothermal approach is reported from An et al. [67].

3.3.3 $CuSbS_2$-based photovoltaic devices

An increasing number of research groups have recently reported the fabrication of prototype solar cells based on $CuSbS_2$. A summary is given in Table 3.3.

Author	Structure	Absorber technique	ref.	η (%)	*Voc* (mV)	*Jsc* (mA/cm^2)	*FF* (%)
Manolache	TCO/TiO_2/**$CuSbS_2$**/graphite	SPD	68	nr	90	nr	28.6
Rodriguez	glass/SnO_2/CdS/Sb_2S_3/**$CuSbS_2$**/Ag	CBD	69	0.017	345	0.2	25
Ornelas	glass/FTO/CdS/**$CuSbS_2$**/C/Ag	CBD + thermal evaporation	48	0.26	294	1.55	57
Ikeda	glass/Mo/**$CuSbS_2$**/CdS/ZnO:Al	sulfurization	52	3.1	490	14.73	44
Welch	glass/Mo/**$CuSbS_2$**/CdS/i-ZnO/ZnO:Al/Al	rf sputtering	70	0.86	309	8.91	31
Al-Saab	TCO/CdS/**$CuSbS_2$**/Mo	rf sputtering	54	0.007	90	0.07	25
Rastogi	glass/FTO/ZnO/**$CuSbS_2$**/Ag	electrodeposition	55	0	0	0	0
Choi	TiO_2/**$CuSbS_2$**/PCPDTBT/Au	spin coating	56	3.1	304	21.5	46.8
Yang	FTO/**$CuSbS_2$**/CdS/ZnO/ZnO:Al/Au	spin coating	33	0.5	440	3.65	31
Suehiro	glass/ITO/ZnO/CdS/**$CuSbS_2$ NC**/Au	spin coating	64	0.01	220	0.16	26
Mesa	glass/Al/**Cu_3BiS_3**/ZnS or In_2S_3/ZnO	co-evaporation	119	nr	nr	nr	nr
Welch	glass/Mo/**$CuSbSe_2$**/CdS/i-ZnO/ZnO:Al/Al	rf sputtering	122	3.08	350	20	44

Table 3.3: Performance of the prototype devices based on the new chalcogenide absorbers (nr = not recorded).

Manolache and Duta fabricated prototype devices having the structure TCO/TiO_2/$CuSbS_2$/graphite, with the absorber synthesized by spray pyrolysis deposition (Section 3.3.2 b) [68]. Under optimized conditions the authors produced cells with diode behaviour but poor photoactivity – i.e.: *Voc* = 90 mV, *Isc* = $2.39 \cdot 10^{-2}$ mA (the authors did not specify the device area) and *FF* = 28.6%.

Rodriguez-Lazcano et al. created solar cells in the p-i-n configuration glass/SnO_2/CdS/Sb_2S_3/$CuSbS_2$/Ag, with the absorber and the intrinsic layer Sb_2S_3 being synthetized by chemical bath deposition (Section 3.3.2 c) [69]. The authors reported devices with performance as follows: ŋ ≅ 0.017%, *Voc* = 345 mV, *Jsc* = 0.2 mA/cm^2 and *FF* ≅ 25%.

Ornelas-Acosta et al. produced solar cells with the structure glass/FTO/CdS/$CuSbS_2$/C/Ag [48]. The absorber layer was grown by heating a precursor stack comprising Sb_2S_3 and Cu – these being deposited by CBD and thermal evaporation respectively (Section 3.3.2 c). Under optimal conditions the authors produced cells with ŋ ≅ 0.26%, *Voc* = 294 mV, *Jsc* = 1.55 mA/cm^2 and *FF* ≅ 57%.

Ikeda et al. fabricated solar cells in the substrate configuration glass/Mo/$CuSbS_2$/CdS/ZnO:Al, with the absorber produced by sulfurization of electrodeposited metal precursor (Section 3.3.2 d) [52]. The authors reported a maximum efficiency of ~3.1%, with *Voc* = 490 mV, *Jsc* = 14.73 mA/cm^2 and *FF* ≅ 44%.

Welch et al. developed photovoltaic devices having the substrate structure glass/Mo/$CuSbS_2$/CdS/i-ZnO/ZnO:Al/Al, with the absorber fabricated by rf sputtering (Section 3.3.2 e) [70]. Optimized devices included a thin MoO_x charge selective layer between the absorber and the back contact and exhibited the following average performance: ŋ = 0.86%, *Voc* = 309 mV, *Jsc* = 8.91 mA/cm^2 and *FF* ≅ 31%.

Al-Saab fabricated prototype devices based on $CuSbS_2$ sputtered from single target (Section 3.3.2 e) in the superstrate configuration TCO/CdS/$CuSbS_2$/Mo [54]. The best cell exhibited: ŋ ≅ 0.007%, *Voc* = 90 mV, *Jsc* = 0.07 mA/cm^2 and *FF* ≅ 25%.

Rastogi and Janardhana made devices in the superstrate configuration glass/FTO/ZnO/$CuSbS_2$/Ag, based on the electrodeposition of the absorber layer (Section 3.3.2 g) [55]. The resulting samples showed diode behaviour but were not photoactive.

Choi et al. produced hybrid solar cells in the configuration TiO_2/$CuSbS_2$/PCPDTBT/Au, where absorber layer was grown by spin coating (Section 3.3.2 h) and PCPDTBT is a polymer employed as hole transport material. The authors produced cells exhibiting maximum efficiency ŋ = 3.1%, with *Voc* = 304 mV, *Jsc* = 21.5 mA/cm^2 and *FF* = 46.8% [56].

Yang et al. fabricated devices based on spin-coated $CuSbS_2$ layers (Section 3.3.2 h) in the structure FTO/$CuSbS_2$/CdS/ZnO/ZnO:Al/Au [33]. The best devices recorded from the authors showed: ŋ = 0.5%, with *Voc* = 440 mV, *Jsc* = 3.65 mA/cm^2 and *FF* = 31%.

Yan et al. tested the photovoltaic performance of $CuSbS_2$ layers deposited by drop-casting of nanoparticle-ink on ITO (Section 3.3.2 i) in photoelectrochemical cells [58]. The authors observed photoactive response with Jsc ≅ 0.09 mA/cm^2 at -0.02 V potential.

Suehiro et al. developed solar cells in the structure glass/ITO/ZnO/CdS/$CuSbS_2$/Au based on $CuSbS_2$ nanocrystals prepared by spin coating [64]. The best performance reported as follows: ŋ = 0.01%, with *Voc* = 220 mV, *Jsc* = 0.16 mA/cm^2 and *FF* = 26%.

Finally Ramasamy et al. reported the use of $CuSbS_2$ nanocrystals as the counter electrode for dye-sensitized photovoltaic devices [71].

Overall, while $CuSbS_2$ has p-type conductivity, an optical band gap in the required range and strong optical absorption, current practice has failed to achieve the expected potential for this material in terms of PV device performance.

3.4 Cu_3SbS_3 properties and materials

3.4.1 Fundamental studies

Kehoe et al. undertook a DFT study on the structural, optical and electrical properties of Cu_3SbS_3 for photovoltaic applications [72]. The calculations (of room temperature properties) were based on the γ-polymorphism of Cu_3SbS_3 – i.e. stable below 263 K and crystallizing in the orthorhombic structure, space group $P2_12_12_1$, with: *a* = 7.884(1) Å, *b* = 10.221(1) Å, *c* = 6.624(1) [73]. According to their simulations Cu_3SbS_3 is expected to have p-type conductivity and an optical band gap of 2.13 eV – i.e. rather high for application as a PV absorber.

Tablero has presented a theoretical study on the electronic and optical properties of oxygen-doped Cu_3SbS_3 layers [74]. The author postulated that the introduction of intermediate states within the band gap of a semiconductor may favour further optical transitions, potentially improving the optical properties of the absorber. Tablero analysed the effects of substitutional O_S on the characteristics of polymorphic Cu_3SbS_3 crystals by a first-principles methodology. The conclusion was that the material is attractive for concentrator applications: with sunlight intensity above 100 suns, the efficiency of the O-doped Cu_3SbS_3 absorber turns out to be higher than that of the undoped compound.

3.4.2 Deposition and characterization of Cu_3SbS_3 thin films and nanostructures

Only a few authors have examined the photovoltaic properties of Cu_3SbS_3 films as a possible low cost and sustainable alternative absorber material.

Maiello et al. created Cu_3SbS_3 thin films by a two-stage process – i.e.: (a) Cu-Sb metallic precursors with a thickness of ~300 nm were first deposited by dc magnetron sputtering (from an alloy Cu_3Sb target) onto molybdenum/glass substrates or onto simple glass substrates; (b) the precursors were then sulfurized under vacuum in the temperature range 250 - 550°C. Maiello et al. performed the sulfurization step in two different ways: (i) by placing the precursors in a sealed graphite box with sulfur powder as the sulfurization agent, and (ii) by depositing elemental sulfur by means of evaporation onto the precursors and subsequently putting them into the annealing furnace [75]. Absorber layers sulfurized in the range 250 - 300°C and at 500°C showed good adhesion but at 550°C the films evaporated during processing. Most of the sulfurized samples had rough surfaces. From XRD analysis the authors concluded that for the samples deposited on glass substrates a sulfurization temperature of 500°C was necessary to create single phase Cu_3SbS_3 films. The films sulfurized by controlled evaporation of sulfur (method ii above) presented improved adhesion and exhibited the single orthorhombic phase Cu_3SbS_3. The only photoactive film found was a 1.2 µm thick sample annealed at 500°C under sulfur vapour. It exhibited p-type conductivity and a direct band gap of 1.84 eV.

The band gap was tuned in the range 1.38 - 1.84 eV by including selenium in the growth process, with the formation of the $Cu_3Sb(Se_xS_{1-x})_3$ alloy, where $0 < x < 0.49$ [76]. The authors attempted to produce devices however these showed poor photoactivity.

Rodriguez et al. published a full article reporting the various conditions (e.g. thickness of the precursors, time, pressure, gas carrier flow and annealing temperature) required to make $Cu_xSb_yS_z$ thin films by annealing Sb_2S_3-CuS stacked precursor films, these having been deposited by chemical bath technique [77]. In particular, Cu_3SbS_3 thin films were obtained by annealing stacked precursors comprising 0.20µm Sb_2S_3 and 0.07µm CuS at 400°C for 30 minutes in medium vacuum. The as-deposited Cu_3SbS_3 films exhibited a band gap of 1.60 eV.

Finally the deposition and characterization of Cu_3SbS_3 nanostructures is reported from several authors, including Ikeda [61], Ramasamy [63, 81], Hao [78], Qiu [79], Xu [80], Chen [82], Wang [83], Zhong [84] and Li [85].

The author is not aware of any PV devices that have been fabricated from Cu_3SbS_3.

3.5 $CuBiS_2$ materials and properties

3.5.1 Fundamental studies

From theoretical studies $CuBiS_2$ is predicted to have a large absorption coefficient [29], and an indirect band gap of ~1.55 eV, this being only 0.1 eV below a direct gap [28]. Hence it is expected $CuBiS_2$ to have potential for high-efficiency solar cells [34] since direct absorption is possible in the appropriate part of the spectrum. In addition a theoretical study on the elastic and thermodynamic properties of $CuBiS_2$ has been recently reported from Zhang et al. [86].

3.5.2 Deposition and characterization of $CuBiS_2$ thin films

There is limited literature about the deposition techniques used for thin films of $CuBiS_2$ (emplectite) for PV applications. A few articles are reported on spray pyrolysis, chemical bath deposition and more recently on sulfurization of metal precursors.

Pawar et al. have developed a series of experiments on the deposition of $CuBiS_2$ thin films by SPD [87]. The films were deposited on ultrasonically cleaned glass substrates, kept at *Ts* in the range 150 - 400°C. The precursors utilized were CuCl, $BiCl_3$ and thiourea. The

films deposited by SPD exhibited the following properties: good adhesion to the substrate; high uniformity; a thickness decrease upon raising *Ts*; a powdery and porous nature at low *Ts*; secondary phases were negligible in the range *Ts* 250 - 300°C; a direct band gap of 1.65 eV; n-type conductivity and resistivity in the range 10^4 - 10^7 Ω cm.

Emplectite thin films have also been deposited by CBD [88, 89]. Sonawane et al. have prepared the films by dipping ultrasonically cleaned glass substrates in an acid bath at room temperature for 3 hours. The solution contained copper nitrate, bismuth nitrate and sodium thiosulfate (NaS_2O_3), used as the sulfur precursor species. The disodium salt of EDTA was added to the solution to improve the adhesion of the as-deposited films [88]. In order to enhance the quality and the characteristics of the films, the authors have investigated the effects of the various deposition parameters – i.e.: concentration of the chemicals, bath temperature, reaction mechanism, deposition time, annealing temperature. Optimized $CuBiS_2$ films were photosensitive and displayed a band gap of 1.8 eV and n-type conductivity. Hall effect investigation and photoluminescence study on $CuBiS_2$ films deposited by CBD were reported from Balasubramanian et al. [90, 91].

Colombara reported thorough work on the deposition of antimony and bismuth chalcogenides, including $CuBiS_2$ thin films by sulfurization of the metal precursors. Diverse techniques were investigated to grow the metal precursor layers Cu and Bi, including evaporation, rf sputtering and co-electrodeposition [92]. Colombara has studied two different approaches to the chalcogenisation of the precursors – by rapid thermal processing (RTP), and in a conventional tube furnace, with either elemental sulfur or H_2S as the sulfurization agent. The reader is referred to ref. 92 for full details of the complex chalcogenisation reaction and the structural characteristics of the resulting films.

Wubet et al. produced bulk $CuBiS_2$ by reactive sintering of Cu_2S and Bi_2S_3 powder mixtures [93]. The annealing temperature was varied from 300 to 450°C and the deposition time was varied from 1 to 3 hours. Under optimal deposition conditions, the samples exhibited p-type conductivity – this contradicting the previous works on $CuBiS_2$ (see above). Wubet reports p-carrier concentrations of ~$2.4 \cdot 10^{18}$ cm^{-3} and mobilities of ~11 $cm^2\ V^{-1}\ s^{-1}$.

3.6 Cu_3BiS_3 for photovoltaic applications

3.6.1 Fundamental studies

Kumar and Persson have calculated the structural, electronic and optical properties of Cu_3BiS_3 by DFT [94]. The authors estimated an indirect band gap at about 1.69 eV with the lowest direct band gap *Eg* only ~0.1 eV above – i.e. at ~1.79 eV – therefore the material essentially behaves as a direct semiconductor. In addition Kumar and Persson calculated the absorption coefficient α (Figure 3.7), showing a strong absorption coefficient $>10^5$ cm^{-1} above the optical band gap. Kumar and Persson explained that the strong absorption is caused by localized Bi 6*p* states in the lowest conduction band which form a flat energy band enhancing the value of α in the low-energy region.

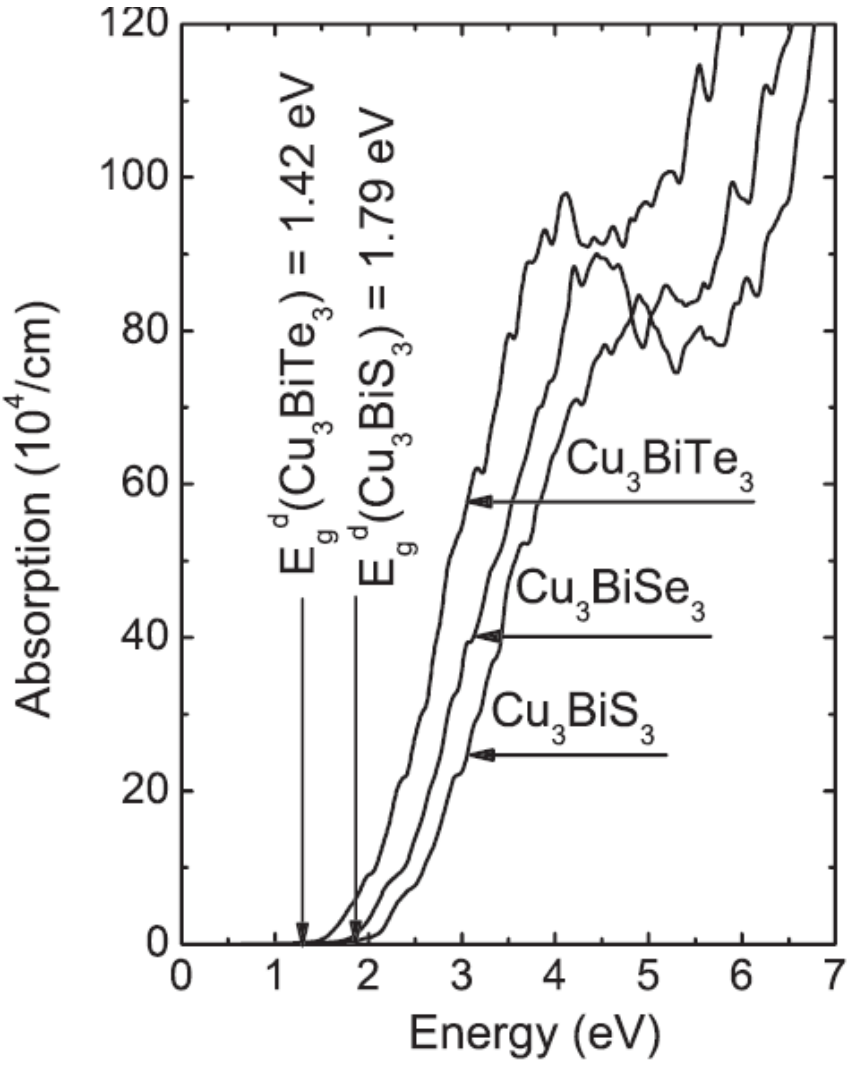

Figure 3.7: Absorption coefficient of Cu_3BiS_3, Cu_3BiSe_3 and Cu_3BiTe_3 from DFT calculation. Figure from ref. 94. "E_g^d" is the direct gap energy.

These characteristics make Cu_3BiS_3 suitable as potential absorber in thin film solar cells. However the band gap is slightly higher than the optimal range for photovoltaics. Kumar and Persson argued that as may be expected, it can be decreased by replacing sulfur with selenium or tellurium – i.e. with Cu_3BiSe_3 and Cu_3BiTe_3.

3.6.2 Synthesis methods and characterization of Cu_3BiS_3 thin films and nanostructures

Thin films of Cu_3BiS_3 have been synthesized and analysed by various techniques, including chemical bath deposition, sulfurization of metal precursors, rf sputtering, co-evaporation and the screen-printing method.

(a) Chemical bath deposition – Nair et al. report the growth of Cu_3BiS_3 thin films by annealing of CuS and Bi_2S_3 precursor film prepared by CBD [95]. Details of the chemistry and growth conditions are given in ref. 95. The authors annealed the samples in an air for 1 hour at 100 - 350°C. The resulting films exhibited an optical absorption coefficient in the order of 10^4 cm^{-1} in the visible spectrum and p-type conductivity. Nair et al. contrast the thermal stability of the compound Cu_3BiS_3 to temperatures above 300°C, with that of CuS films, which undergo decomposition above 220°C.

An alternative approach was reported from Estrella et al. and consisted of two steps: (a) the deposition of a thin film of CuS onto the substrate by CBD, and (b) thermal evaporation of a bismuth layer [96]. CuS thin films of ~300 nm were obtained by placing the glass substrates in a chemical bath mixture for 5 hours at 60°C. A ~100 nm bismuth layer was then evaporated onto them (40 mg of bismuth powder placed into a tungsten crucible heated at 800 - 900°C for 30 seconds). Finally an annealing process took place in 'medium vacuum' in a furnace for 1 hour at 300°C. The resultant Cu_3BiS_3 films had grain sizes of about 40 nm, optical absorption coefficients of ~10^5 cm^{-1}, a direct band gap of ~1.2 eV and electrical conductivity of ~ 10^{-4} - 10^{-2} Ω^{-1} cm^{-1}. The authors indicated a low value of the free carrier mobility-lifetime product and suggested that it would be beneficial the optimization of the annealing process to enhance this important parameter.

(b) Sulfurization of metal precursor layers – For the synthesis of Cu_3BiS_3, Gerein and Haber have investigated a two-step method with preliminary deposition of the copper and bismuth layers by dc sputtering (either as a multilayer stack or co-sputtering), followed by the annealing process in a reactive atmosphere, using H_2S as sulfur source [97 - 99]. The annealing temperature ranged from 175 - 400°C and the annealing time from 2 - 30 hours. The characteristics of the resulting films depended strongly on the sputtering and annealing conditions. Secondary phases such as $Cu_{1.8}S$ and Bi were observed in the samples annealed at temperatures above 300°C or with times below 16 hours [97]. However, these samples were generally not smooth and continuous and hence not suitable for photovoltaic applications.

A similar two-step approach was reported by Colombara et al., with (a) the deposition by sequential or simultaneous electrodeposition of copper and bismuth layers, and (b) sulfurization of the precursor sample, placed in a graphite box containing elemental sulfur [100]. The annealing treatments were performed in the temperature range 270 - 550°C and the sulfurization time varied from 5 minutes to 16 hours. At 500°C the sulfurization of the precursors to Cu_3BiS_3 was complete and no binary sulphide peaks coexisted with the main phase peaks in the XRD patterns. As underlined by the authors, these outcomes are very different from those obtained by Gerein and Haber, probably due to the different sulfurization agent. Good quality films fabricated from Colombara et al. exhibited a band gap of ~1.4 eV, but low photoresponse.

(c) Rf sputtering – Gerein and Haber reported an alternative one-step synthesis process for the deposition of Cu_3BiS_3 films onto hot substrates by rf sputtering [101, 102]. Gerein and Haber used fused silica substrates cleaned in an ultrasonic bath. The deposition of the thin films took place in a sputtering chamber from a CuS (rf) and a Bi target (dc), with argon at a pressure of 5 mTorr. The substrate temperature was varied from 250 to 300°C. Further details are reported in ref. 101. In order to achieve the desired 3:1:3 stoichiometry, Gerein and Haber used the technique of continuously sputtering the CuS target and cycling the Bi target. Finally some samples were post-growth annealed in a furnace for 2 hours in the temperature range 250 - 300°C in a reactive atmosphere. This process yielded high quality Cu_3BiS_3 films, displaying: (i) dense morphology with mirror-like surfaces – the samples deposited at 300°C were more homogeneous than those grown at 250°C which retained the

layered structure; (ii) crystalline and single-phase structure, with some differences in the XRD patterns for the as-grown samples; the crystallites were smaller and randomly oriented for those samples deposited at lower temperature; the annealing enhanced the crystallinity and the orientation of the films; (iii) high absorption coefficient (~10^5 cm^{-1} at 1.9 eV); (iv) direct band gap of 1.4 eV; (v) electrical resistivity of 9.6 Ω cm for samples post-growth annealed at 300°C; (vi) p-type conductivity.

(d) Co-evaporation – An advanced growth technique for Cu_3BiS_3 films was presented from Mesa and Gordillo [103]. The authors created the samples by co-evaporation of metal precursors onto a glass substrate by a two-stage process. The process took place in a high-vacuum chamber, with bismuth and copper evaporated from separate tungsten boats, and sulfur introduced by a tantalum effusion cell. In the first stage only bismuth and sulfur were evaporated; in the second stage only copper in a sulfur atmosphere, while the substrate temperature was kept in the range 280 - 320°C. By analysing the transmittance of the as-grown samples, the authors found the optimum substrate temperature was 300°C. The best quality Cu_3BiS_3 thin films showed absorption coefficients above 10^4 cm^{-1}, band gaps of 1.41 eV and p-type conductivity. Further exhaustive analyses of the electrical conductivity and photoconductivity are reported in the refs. 104 - 108.

(e) Screen-printing method – H. Hu et al. deposited thermally stable ~10 μm thick Cu_3BiS_3 coatings by screen-printing [109]. The characteristics of the films depended on the temperature, the precursors and the annealing atmosphere. Phase-pure films with good quality were obtained at temperatures ≥ 250°C.

(f) Nanostructures – Cu_3BiS_3 nanostructures in different forms have been deposited and characterized by numerous authors, including J. Hu [110], Chen [111], Shen [112], Zhong [113], Zeng [114], Aup-Ngoen [115], C. Yan [116], J. Yan [117] and Murali [118].

3.6.3 Cu_3BiS_3-based prototype devices

Mesa et al. reported the characterization by TEM and HRTEM of prototype solar cells based on Cu_3BiS_3 with the substrate structure glass/Al/Cu_3BiS_3/buffer/ZnO [119]. The aluminium back contact was deposited on glass by dc sputtering and then the Cu_3BiS_3 absorber layer by the two-step co-evaporation method (Section 3.6.2 d). Mesa et al. tested two different materials as heterojunction partner layers – i.e.: In_2S_3, grown by co-evaporation, and ZnS, deposited by CBD. The authors did not report any performance characterization of the device fabricated.

3.7 $CuSbSe_2$ and $CuBiSe_2$ for PV applications

3.7.1 Fundamental studies

Kumar and Persson identified $CuSbSe_2$ and $CuBiSe_2$ as potential alternative absorber materials [29]. From their DFT simulations both of these selenides are expected to have absorption coefficient above $3 \cdot 10^5$ cm^{-1} in the visible, and indirect band gaps of 1.36 eV for $CuSbSe_2$ and 1.14 eV for $CuBiSe_2$.

Additionally, Maeda and Wada calculated an indirect band gap of 0.93 eV and direct transition of 1.04 eV for $CuSbSe_2$ [31].

3.7.2 Synthesis and characterization of $CuSbSe_2$ and $CuBiSe_2$ films

$CuSbSe_2$ thin films for photovoltaic applications have been deposited by rapid thermal annealing (RTA) of electrodeposited films, selenization of the metal precursors and rf sputtering.

Tang et al. have examined the optical and electrical properties of $CuSbSe_2$ thin films grown on SnO_2-coated glass substrates by a one-step electrodeposition process followed by RTA stage of 5 minutes at 330°C in an argon atmosphere [120, 121]. Under the best conditions the authors reported samples exhibiting properties as follows: the films were polycrystalline having the orthorhombic structure; the films were smooth, compact and had a uniform and dense film morphology with strong adhesion to the substrate; the films had

absorption coefficients greater than $7 \cdot 10^4$ cm^{-1}; band gaps of 1.1 eV; p-type conductivity; a Hall coefficient of +11.0 cm^3 C^{-1}; carrier concentration of $5.8 \cdot 10^{17}$ cm^{-3}; resistivities of 9.3 Ω cm; and mobilities of 1.2 cm^2 V s^{-1}.

Colombara et al. demonstrated the preparation of $CuSbSe_2$ thin films by selenization at 400°C of a Sb-Cu electroplated alloy precursor by means of selenium powder [49]. The films displayed a band gap of 1.2 eV and p-type conductivity, but poor photoresponse.

Welch et al. produced $CuSbSe_2$ thin films by a combinatorial approach using rf sputtering [122]. Optimized films deposited at ~400°C exhibited large absorption coefficients with band gaps of 1.1 eV and p-type conductivity with carrier concentrations of $\sim 10^{17}$ cm^{-3}.

Takei et al. formed solid solutions of $CuSb(S_{1-x}Se_x)_2$ ($0.0 \leq x \leq 1.0$) by a mechano-chemical growth technique [123]. Powder samples with good $CuSbSe_2$ crystallinity were produced with a post-growth treatment at 400 - 450°C. The indirect band gap of the solid solution linearly decreased from 1.40 eV of $CuSbS_2$ ($x = 0$) to 1.04 eV for $CuSbSe_2$ ($x = 1$).

Bari and Patil reported a work on the deposition of $CuBiSe_2$ thin films on glass substrates by chemical bath deposition [124]. Good quality films were fabricated from one hour depositions at 60 °C. The resulting samples were polycrystalline, uniform and with good adhesion to the substrates. The samples exhibited n-type conductivity and a band gap ranging from 1.84 to 2.10 eV depending on the Cu:Bi ratio. However the films generally contained secondary phases (e.g. Bi_2Se_3 and Cu_2Se).

3.7.3 $CuSbSe_2$-based prototype devices

Welch et al. produced prototype cells with the absorber $CuSbSe_2$ grown by rf sputtering and having the structure glass/Mo/$CuSbSe_2$/CdS/i-ZnO/ZnO:Al/Al [122]. The authors reported devices with best average performance as follows: ŋ = 3.08%, *Voc* = 350 mV, *Jsc* = 20 mA/cm^2 and *FF* = 44%. There have been significantly fewer attempts to make PV devices with $CuSbSe_2$ than with $CuSbS_2$. Nevertheless, the outcome from Welch's work is a device with significantly higher efficiency than that for $CuSbS_2$ which was generally < 1% (the single exceptions being Ikeda [52] and Choi [56]).

There are no reports of $CuBiSe_2$ devices.

3.8 Summary

This Chapter reviews the theoretical and experimental studies on the novel chalcogenide compounds for photovoltaic applications. Table 3.2 summarizes the principal optical and electrical properties of chalcogenide thin films deposited by various synthesis methods.

$CuSbS_2$ films grown by different techniques were usually found p-type, in agreement with how expected from the dominant presence in the lattice of copper vacancies. Many authors detected an absorption coefficient in the range 10^4 - 10^5 cm^{-1} in the visible. The measured optical band gaps range from ~0.9 to ~2.2 eV. However the majority of authors agreed that the band gap of single-phase $CuSbS_2$ films deposited under standard conditions is ~1.5 eV – i.e. in the ideal range for absorber applications. Deviations from this value can be attributed to either coexisting secondary phases or quantum effects, due to variation of the grain structure of the films with the growth conditions. Mobilities in the range 10 - 50 cm^2 V^{-1} s^{-1} have been reported for $CuSbS_2$ films, i.e. relatively high values for polycrystalline materials for photovoltaic applications. $CuSbS_2$ films were in included in solar cells by several authors with efficiencies up to ~3.1%, as shown in Table 3.3. Therefore $CuSbS_2$ has good prospects for further investigation in photovoltaics and is the principal theme explored in this thesis.

Cu_3SbS_3 samples with good properties for PV – i.e. high absorption coefficient, band gap of 1.6 - 1.8 eV and p-type conductivity – have been reported from a restricted number of authors, due to the challenge to synthetize single-phase films.

$CuBiS_2$ films present absorption coefficient of 10^4 - 10^5 cm^{-1} in the visible and optical band gap of ~1.65 - 1.8 eV. However the reported n-type conductivity limits the application of this material in thin film solar cells.

Cu_3BiS_3 films with high absorption, band gap of ~ 1.4 eV and p-type conductivity have been fabricated by different methods. This material is also promising for PV applications and the growth of Cu_3BiS_3 films is secondly discussed in this thesis.

$CuSbSe_2$ is also a promising chalcogenide candidate for absorber applications, having high absorption, band gap of ~1.1 eV and p-type conductivity. Prototype devices based on

$CuSbSe_2$ with efficiency of ~3% have been reported. However the synthesis of $CuSbSe_2$ was not considered in this study, due to the toxicity of selenium.

3.9 References

[1] Y. Moëlo, E. Makovicky, N. N. Mozgova, J. L. Jambor, N. Cook, A. Pring, W. Paar, E. H. Nickel, S. Graeser, S. Karup-Møller, T. Balic-Žunic, W. G. Mumme, F. Vurro, D. Topa, L. Bindi, K. Bente and M. Shimizu, "Sulfosalt systematics: a review. Report of the sulfosalt sub-committee of the IMA Commission on Ore Mineralogy Yves", *European Journal of Mineralogy*, vol. 20, no. 1, pp. 7-46, 2008

[2] B. J. Skinner, F. D. Luce and E. Makovicky, "Studies of the sulfosalts of copper III. Phases and phase relations in the system Cu-Sb-S", *Economic Geology*, vol. 67, no. 7, pp. 924-938, 1972

[3] S. Karup-Møller and E. Makovicky, "Skinnerite, Cu_3SbS_3, a new sulfosalt from Ilímaussaq alkaline intrusion, South Greenland", *American Mineralogist*, vol. 59, no. 9-10, pp. 889-895, 1974

[4] I. L. Lind and E. Makovicky, "Phase relations in the system Cu-Sb-S at 200°C, 10^8 Pa by hydrothermal synthesis – microprobe analyses of tetrahedrite – a warning", *Neus Jahrbuch fur Mineralogie-Abhandlungen*, vol. 145, no. 2, pp. 134-156, 1982

[5] K. Tatsuka and N. Morimoto, "Tetrahedrite stability relations in the Cu-Sb-S system", *Economic Geology*, vol. 72, no. 2, pp. 258-270, 1977

[6] K. Tatsuka and N. Morimoto, "Composition variation and polymorphism of tetrahedrite in Cu-Sb-S system below 400°C", *American Mineralogist*, vol. 58, no. 5-6, pp. 425-434, 1973

[7] M. H. Braga, J. A. Ferreira, C. Lopes and L. F. Malheiros, "Phase transitions in the Cu-Sb-S system", *Materials Science Forum*, vols. 587-588, pp. 435-439, 2008

[8] S. Karup-Møller, "The Cu-Sb-S phase system at 700°C", *Neus Jahrbuch für Mineralogie-Monatshefte*, no. 7, pp. 333-336, 2000

[9] F. Tesfaye Firdu and P. Taskinen, "Thermodynamics and phase equilibria in the (Ni, Cu, Zn)-(As, Sb, Bi)-S systems at elevated temperatures (300 - 900°C)", *Aalto University Publications in Materials Science and Engineering*, pp. 1-60, 2010

[10] (14/12/2015) http://www.handbookofmineralogy.org/pdfs/chalcostibite.pdf

[11] M. Razmara, C. M. B. Henderson, R. A. D. Pattrick, A. M. T. Bell and J. M. Charnock, "The crystal chemistry of the solid solution series between chalcostibite ($CuSbS_2$) and emplectite ($CuBiS_2$)", *Mineralogical Magazine*, vol. 61, no. 1, pp. 79-88, 1997

[12] A. Kyono and M. Kimata, "Crystal structures of chalcostibite ($CuSbS_2$) and emplectite ($CuBiS_2$): structural relationship of stereochemical activity between chalcostibite and emplectite", *American Mineralogist*, vol. 90, no. 1, pp. 162-165, 2005

[13] (14/12/2015) http://www.mindat.org/min-3679.html

[14] (14/12/2015) http://www.webmineral.com/data/Skinnerite.shtml

[15] H. J. Whitfield, "Polymorphism in skinnerite, Cu_3SbS_3", *Solid State Communications*, vol. 33, pp. 747-748, 1980

[16] A. Pfitzner, "Disorder of Cu^+ in Cu_3SbS_3: structural investigations of the high- and low-temperature modification", *Zeitschrift fur Kristallographie*, vol. 213, no. 4, pp. 228-236, 1998

[17] N. Wang, "The Cu–Bi–S system: results from low temperature experiments", *Mineralogical Magazine*, vol. 58, no. 391, pp. 201-204, 1994

[18] (14/12/2015) http://www.mindat.org/min-1378.html

[19] (14/12/2015) http://webmineral.com/data/Emplectite.shtml

[20] J. C. Portheine and W. Nowacki, "Refinement of crystal structure of emplectite, $CuBiS_2$", *Zeitschrift fur Kristallographie*, vol. 141, no. 5-6, pp. 387-402, 1975

[21] W. Hofmann, "Structural and morphological correlations in ores of formula type ABC_2. I. The structure of wolfsbergite $CuSbS_2$ and emplectite $CuBiS_2$ and their relationships to the structure of antimonite Sb_2S_3", *Zeitschrift fur Kristallographie*, vol. 84, no. 3-4, pp. 177-203, 1933

[22] (14/12/2015) http://www.mindat.org/min-4300.html

[23] (14/12/2015) http://webmineral.com/data/Wittichenite.shtml

[24] V. Kocman and E. W. Nuffield, "The crystal structure of wittichenite, Cu_3BiS_3", *Acta Crystallographica Section B-Structural Science*, vol. 29, no. 15, pp. 2528-2535, 1973

[25] E. Makovicky, "The phase transformations and thermal expansion of the solid electrolyte Cu_3BiS_3, between 25 and 300°C", *Journal of Solid State Chemistry*, vol. 49, no. 1, pp. 85-92, 1983

[26] E. Makovicky, "Polymorphism in Cu_3SbS_3 and Cu_3BiS_3: the ordering schemes for copper atoms and electron microscope observations", *Neus Jahrbuch fur Mineralogie-Abhandlungen*, vol. 108, no. 2, pp. 185-212, 1994

[27] K. Mariolacos, "Single crystal synthesis of ternary mineral phases in the temperature gradient: wittichenite, Cu_3BiS_3, dolerophanite, $CuO{\cdot}CuSO_4$, bismoclite, BiOCl", *Neus Jahrbuch für Mineralogie-Monatshefte*, no. 4, pp. 164-170, 1998

[28] J. T. R. Dufton, A. Walsh, P. M. Panchmatia, L. M. Peter, D. Colombara and M. S. Islam, "Structural and electronic properties of $CuSbS_2$ and $CuBiS_2$: potential absorber materials for thin-film solar cells", *Physical Chemistry Chemical Physics*, vol. 14, no. 20, pp. 7229-7233, 2012

[29] M. Kumar and C. Persson, "$Cu(Sb,Bi)(S,Se)_2$ as indium-free absorber material with high optical efficiency", *Proceedings of E-MRS spring meeting 2013 Symposium D*, vol. 44, pp. 176-183, 2014

[30] M. Kumar and C. Persson, "$CuSbS_2$ and $CuBiS_2$ as potential absorber materials for thin-film solar cells", *Journal of Renewable and Sustainable Energy*, vol. 5, no. 3, pp. 1-6, 2013

[31] T. Maeda and T. Wada, "First-principles study of electronic structure of $CuSbS_2$ and $CuSbSe_2$ photovoltaic semiconductors", *Thin Solid Films*, vol. 582, pp. 401-407, 2015

[32] D. Perniu, A. Duta and J. Schoonman, "Defect chemistry of $CuSbS_2$", *International Semiconductor Conference, 2006*, vol. 2, pp. 245-248, 2006

[33] B. Yang, L. Wang, J. Han, Y. Zhou, H. Song, S. Chen, J. Zhong, L. Lv, D. Niu and J. Tang, "$CuSbS_2$ as a promising earth-abundant photovoltaic absorber material: a combined theoretical and experimental study", *Chemistry of Materials*, vol. 26, no. 10, pp. 3135-3143, 2014

[34] C. Tablero, "Microscopic analysis and applications of the $Cu(Sb,Bi)S_2$ high optical absorption", *Journal of Physical Chemistry C*, vol. 119, no. 16, pp. 8857-8863, 2015

[35] V. K. Gudelli, V. Kanchana, G. Vaitheeswaran, A. Svane and N. E. Christensen, "Thermoelectric properties of chalcopyrite type $CuGaTe_2$ and chalcostibite $CuSbS_2$", *Journal of Applied Physics*, vol. 114, no. 22, pp. 1-8, 2013

[36] A. Rabhi, M. Kanzari and B. Rezig, "Optical and structural properties of $CuSbS_2$ thin films grown by thermal evaporation method", *Thin Solid Films*, vol. 517, no. 7, pp. 2477-2480, 2009

[37] A. Rabhi, Y. Fadhli and M. Kanzari, "Investigation on dispersive optical constants and microstructural parameters of the absorber $CuSbS_2$ thin films", Vacuum, vol. 112, pp. 59-65, 2015

[38] Y. Fadhli, A. Rabhi and M. Kanzari, "Effect of annealing time and substrates nature on the physical properties of $CuSbS_2$ thin films", *Journal of Materials Science - Materials in Electronics*, vol. 25, no. 11, pp. 4767-4773, 2014

[39] L. I. Soliman, A. M. A. El Soad, H. A. Zayed and S. A. El Ghfar, "Structural and electrical properties of $CuSbTe_2$, $CuSbSe_2$ and $CuSbS_2$ chalcogenide thin films", *Fizika A*, vol. 11, no. 4, pp. 139-152, 2002

[40] R. Suriakarthick, V. N. Kumar, T. S. Shyju and R. Gopalakrishnan, "Effect of substrate temperature on copper antimony sulphide thin films from thermal evaporation", *Journal of Alloys and Compounds*, vol. 651, pp. 423-433, 2015

[41] S.A. Manolache, L. Andronic, A. Duta and A. Enesca, "The influence of the deposition condition on crystal growth and on the band gap of $CuSbS_2$ thin film absorber used for solid state solar cells (SSSC)", *Journal of Optoelectronics and Advanced Materials*, vol. 9, no. 5, pp. 1269-1272, 2007

[42] I. Popovici and A. Duta, "Tailoring the composition and properties of sprayed $CuSbS_2$ thin films by using polymeric additives", *International Journal of Photoenergy*, article ID 962649, 2012

[43] S. Liu, L. Chen, L. Nie, X. Wang and R. Yuan, "The influence of substrate temperature on spray-deposited $CuSbS_2$ thin films", *Chalcogenide Letters*, vol. 11, no. 12, pp. 639-644, 2014

[44] M. T. S. Nair, Y. Rodriguez-Lazcano, Y. Pena, S. Messina, J. Campos and P. K. Nair, "Absorber films of antimony chalcogenides via chemical deposition for photovoltaic application", *Materials for Photovoltaics*, vol. 836, pp. 167-172, 2005

[45] S. C. Ezugwu, F. I. Ezema and P. U. Asogwa, "Synthesis and characterization of ternary $CuSbS_2$ thin films: effect of deposition time", *Chalcogenide Letters*, vol. 7, no. 5, pp. 341-348, 2010

[46] C. Garza, S. Shaji, A. Arato, E. P. Tijerina, G. A. Castillo, T. K. Das Roy and B. Krishnan, "P-type $CuSbS_2$ thin films by thermal diffusion of copper into Sb_2S_3", *Solar Energy Materials and Solar Cells*, vol. 95, no. 8, pp. 2001-2005, 2011

[47] R. E. Ornelas-Acosta, S. Shaji, D. Avellaneda, G. A. Castillo, T. K. Das Roy and B. Krishnan, "Thin films of copper antimony sulfide: a photovoltaic absorber material", *Materials Research Bulletin*, vol. 61, pp. 215-225, 2015

[48] R. E. Ornelas-Acosta, D. Avellaneda, S. Shaji, G. A. Castillo, T. K. Das Roy and B. Krishnan, "$CuSbS_2$ thin films by heating Sb_2S_3/Cu layers for PV applications", *Journals of Materials Science-Materials in Electronics*, vol. 25, no. 10, pp. 4356-4362, 2014

[49] D. Colombara, L. M. Peter, K. D. Rogers, J. D. Painter and S. Roncallo, "Formation of $CuSbS_2$ and $CuSbSe_2$ thin films via chalcogenisation of Sb-Cu metal precursors", *Thin Solid Films*, vol. 519, no. 21, pp. 7438-7443, 2011

[50] P. Maiello, G. Zoppi, K. Hutchings, S. Roncallo and I. Forbes, "Cu-Sb based library for solar cell absorber material identification", *Proceedings of 8th Photovoltaic Science Applications and Technology (PVSAT-8)*, pp. 137-140, 2012

[51] S. Ikeda, Y. Iga, W. Septina, T. Harada and M. Matsumura, "$CuSbS_2$-based thin film solar cells prepared from electrodeposited metallic stacks composed of Cu and Sb layers", *Proceedings of the 2013 IEEE 39th Photovoltaic Specialist Conference (PVSC)*, pp. 2598-2601, 2013

[52] W. Septina, S. Ikeda, Y. Iga, T. Harada and M. Matsumura, "Thin film solar cell based on $CuSbS_2$ absorber fabricated from an electrochemically deposited metal stack", *Thin Solid Films*, vol. 550, pp. 700-704, 2014

[53] A. W. Welch, P. P. Zawadzki, S. Lany, C. A. Wolden and A. Zakutayev, "Self-regulated growth and tunable properties of $CuSbS_2$ solar absorbers", *Solar Energy Materials and Solar Cells*, vol. 132, pp. 499-506, 2015

[54] F. Al-Saab, "Chalcogenides for solar applications", PhD thesis, Faculty of Physical and Applied Sciences, University of Southampton, 2015, Southampton, United Kingdom

[55] A. C. Rastogi and N. R. Janardhana, "Properties of $CuSbS_2$ thin films electrodeposited from ionic liquids as p-type absorber for photovoltaic solar cells", *Thin Solid Films*, vol. 565, pp. 285-292, 2014

[56] Y. C. Choi, E. J. Yeom, T. K. Ahn and S. Il Seok, "$CuSbS_2$-sensitized inorganic-organic heterojunction solar cells fabricated using a metal-thiourea complex solution", *Angewandte Chemie-International Edition*, vol. 54, no. 13, pp. 4005-4009, 2015

[57] Q. Tian, G. Wang, W. Zhao, Y. Chen, Y. Yang, L. Huang and D. Pan, "Versatile and low-toxic solution approach to binary, ternary, and quaternary metal sulfide thin films and its application in $Cu_2ZnSn(S,Se)_4$ solar cells", *Chemistry of Materials*, vol. 26, no. 10, pp. 3098-3103, 2014

[58] C. Yan, Z. Su, E. Gu, T. Cao, J. Yang, J. Liu, F. Liu, Y. Lai, J. Lia and Y. Liu, "Solution-based synthesis of chalcostibite ($CuSbS_2$) nanobricks for solar energy conversion", *RSC Advances*, vol. 2, no. 28, pp. 10481-10484, 2012

[59] J. Zhou, G.Q. Bian, Q.Y. Zhu, Y. Zhang, C.Y. Li and J. Dai, "Solvothermal crystal growth of $CuSbQ_2$ (Q = S, Se) and the correlation between macroscopic morphology and microscopic structure", *Journal of Solid State Chemistry*, vol. 182, no. 2, pp. 259-264, 2008

[60] H. Su, Y. Xie, S. Wan, B. Li and Y. Qian, "A novel one-step solvothermal route to nanocrystalline $CuSbS_2$ and Ag_3SbS_3", *Solid State Ionics*, vol. 123, no. 1-4, pp. 319-324, 1999

[61] S. Ikeda, S. Sogawa, Y. Tokai, W. Septina, T. Harada and M. Matsumura, "Selective production of $CuSbS_2$, Cu_3SbS_3, and Cu_3SbS_4 nanoparticles using a hot injection protocol", *RSC Advances*, vol. 4, no. 77, pp. 40969-40972, 2014

[62] M. Hao, Y. Liu, F. Zhou, L. Jiang, F. Liu and J. Li, "$CuSbS_2$ nanocrystals applying in organic-inorganic hybrid photodetectors", *ECS Solid State Letters*, vol. 3, no. 9, pp. 41-43, 2014

[63] K. Ramasamy, H. Sims, W. H. Butler and A. Gupta, "Selective nanocrystal synthesis and calculated electronic structure of all four phases of copper-antimony-sulfide", *Chemistry of Materials*, vol. 26, no. 9, pp. 2891-2899, 2014

[64] S. Suehiro, K. Horita, M. Yuasa, T. Tanaka, K. Fujita, Y. Ishiwata, K. Shimanoe and T. Kida, "Synthesis of copper-antimony-Sulfide nanocrystals for solution-processed solar cells", *Inorganic Chemistry*, vol. 54, no. 16, pp. 7840-7845, 2015

[65] Y. Zou and J. Jiang, "Colloidal synthesis of chalcostibite copper antimony sulfide nanocrystals", *Materials Letters*, vol. 123, pp. 66-69, 2014

[66] K. Ramasamy, H. Sims, W. H. Butler and A. Gupta, "Mono-, few-, and multiple layers of copper antimony sulfide ($CuSbS_2$): a ternary layered sulfide", *Journal of the American Chemical Society*, vol. 136, no. 4, pp. 1587-1598, 2014

[67] C. An, Q. Liu, K. Tang, Q. Yang, X. Chen, J. Liu and Y. Qian, "The influences of surfactant concentration on the quality of chalcostibite nanorods", *Journal of Crystal Growth*, vol. 256, no. 1-2, pp. 128-133, 2003

[68] S. A. Manolache and A. Duta, "The influence of the spray deposition parameters in the photovoltaic response of the three-dimensional (M) solar cell: TCO/dense TiO_2/$CuSbS_2$/graphite", *Journal of Optoelectronics and Advanced Materials*, vol. 9, no. 10, pp. 3219-3222, 2007

[69] Y. Rodriguez-Lazcano, M. T. S. Nair and P. K. Nair, "Photovoltaic p-i-n structure of Sb_2S_3 and $CuSbS_2$ absorber films obtained via chemical bath deposition", *Journal of the Electrochemical Society*, vol. 152, no. 8, pp. 635-638, 2005

[70] A. Welch, L. Baranowski, P. Zawadzki, C. DeHart, S. Johnston, S. Lany, C. Wolden and A. Zakutayev, "Accelerated development of $CuSbS_2$ thin film photovoltaic device prototypes", *Progress in Photovoltaics: Research and Applications, in press*

[71] K. Ramasamy, B. Tien, P. S. Archana and A. Gupta, "Copper antimony sulfide ($CuSbS_2$) mesocrystals: a potential counter electrode material for dye-sensitized solar cells", *Materials Letters*, vol. 124, pp. 227-230, 2014

[72] A. B. Kehoe, D. J. Temple, G. W. Watson and D. O. Scanlon, "Cu_3MCh_3 (M = Sb, Bi; Ch = S, Se) as candidate solar cell absorbers: insights from theory", *Physical Chemistry Chemical Physics*, vol. 15, no. 37, pp. 15477-15484, 2013

[73] A. Pfitzner, "Disorder of Cu^+ in Cu_3SbS_3: structural investigations of the high- and low-temperature modification", *Zeitschrift fur Kristallographie*, vol. 213, no. 4, pp. 228-236, 1998

[74] C. Tablero, "Electronic property analysis of O-doped Cu_3SbS_3", *Solar Energy Materials and Solar Cells*, vol. 104, pp. 180-184, 2012

[75] P. Maiello, G. Zoppi, R. Miles, N. Pearsall and I. Forbes, "Investigations of ternary Cu_3SbS_3 thin films as absorber in photovoltaic devices", *The 7th Photovoltaic Science Applications and Technology Conference and Exhibition (PVSAT-7)*, 2011

[76] P. Maiello, G. Zoppi, R. Miles, N. Pearsall and I. Forbes, "Chalcogenisation of Cu-Sb metallic precursors into $Cu_3Sb(Se_xS_{1-x})_3$", *Solar Energy Materials and Solar Cells*, vol. 113, pp. 186-194, 2013

[77] Y. Rodriguez-Lazcano, M. T. S. Nair and P. K. Nair, "$Cu_xSb_yS_z$ thin films produced by annealing chemically deposited Sb_2S_3-CuS thin films", *Modern Physics Letters B*, vol. 15, no. 17-19, pp. 667-670, 2001

[78] Z. Hao, D. Zeng, L. Chen and F. Huang, "Synthesis and characterization of Cu_3SbS_3 nanocrystallites: effect of reaction time", *Materials Letters*, vol. 122, pp. 338-340, 2014

[79] X. Qiu, S. Ji, C. Chen, G. Liu and C. Ye, "Synthesis, characterization, and surface-enhanced Raman scattering of near infrared absorbing Cu_3SbS_3 nanocrystals", *CrystEngComm*, vol. 15, no. 48, pp. 10431-10434, 2013

[80] D. Xu, S. Shen, Y. Zhang, H. Gu and Q. Wang, "Selective synthesis of ternary copper-antimony sulfide nanocrystals", *Inorganic Chemistry*, vol. 52, no. 22, pp. 12958-12962, 2013

[81] K. Ramasamy, R. K. Gupta, H. Sims, S. Palchoudhury, S. Ivanov and A. Gupta, "Layered ternary sulfide $CuSbS_2$ nanoplates for flexible solid-state supercapacitors", *Journal of Materials Chemistry A*, vol. 3, no. 25, pp. 13263-13274, 2015

[82] D. Chen, G. Shen, K. Tang, X. Jiang, L. Huang, Y. Jin and Y. Qian, "Polyol mediated synthesis of nanocrystalline M_3SbS_3 (M = Ag, Cu)", *Materials Research Bulletin*, vol. 38, no. 3, pp. 509-513, 2003

[83] M. X. Wang, G. H. Yue, X. Y. Fan and P. X. Yan, "Properties and characterization of Cu_3SbS_3 nanowires synthesized by solvothermal route", *Journal of Crystal Growth*, vol. 310, no. 12, pp. 3062-3066, 2008

[84] J. Zhong, W. Xiang, H. Jin, W. Cai, L. Liu, X. Yang, X. Liang and H. Liu, "A simple L-cystine-assisted solvothermal approach to Cu_3SbS_3 nanorods", *Materials Letters*, vol. 64, no. 13, pp. 1499-1502, 2010

[85] Z. Li, J. Zhong, Z. Chen, Q. Cai, X. Liang and W. Xiang, "Preparation and formation mechanism of Cu_3SbS_3 nanorods", *Rare Metal Materials and Engineering*, vol. 41, no. 2, pp. 1-5, 2012

[86] S. R. Zhang, D. P. Zeng, L. H. Xie, X. P. Deng and K. H. Song, "First-principles study of the elastic and thermodynamic properties of $CuBiS_2$ photovoltaic absorber material", *Chalcogenide Letters*, vol. 11, no. 12, pp. 661-670, 2014

[87] S. H. Pawar, A. J. Pawar and P. N. Bhosale, "Spray pyrolytic deposition of $CuBiS_2$ thin-films", *Bullettin of Material Science*, vol. 8, no. 3, pp. 423-426, 1986

[88] P. S. Sonawane, P. A. Wani, L. A. Patil and T. Seth, "Growth of $CuBiS_2$ thin films by chemical bath deposition technique from an acidic bath", *Materials Chemistry and Physics*, vol. 84, no. 2-3, pp. 221-227, 2004

[89] V. Balasubramanian, N. Suriyanarayanan, S. Prabahar and S. Srikanth, "Structural and optical properties of chemically deposited $CuBiS_2$ thin films", *Chalcogenide Letters*, vol. 8, no. 10, pp. 637-648, 2011

[90] V. Balasubramanian, N. Suriyanarayanan, S. Prabahar, S. Srikanth and P. Ravi, "Temperature- and time- dependent Hall effect studies on chemically deposited $CuBiS_2$ thin

films", *Optoelectronics and Advanced Materials - Rapid Communications*, vol. 6, no. 1-2, pp. 104-106, 2012

[91] V. Balasubramanian, N. Suriyanarayanan, S. Prabahar, S. Srikanth and P. Ravi, "Photoluminescence study on chemically deposited $CuBiS_2$ thin films", *Journal of Ovonic Research*, vol. 8, no. 1, pp. 1-8, 2012

[92] D. Colombara, "Investigation of chalcogenide absorber materials for photovoltaic applications", PhD thesis, Department of Chemistry, University of Bath, 2012, Bath, United Kingdom

[93] W. Wubet, D. H. Kuo and H. Abdullah, "Effects of sintering temperature and duration on the structural and electrical properties of $CuBiS_2$ bulks", *Journal of Solid State Chemistry*, vol. 230, pp. 237-242, 2015

[94] M. Kumar and C. Persson, "Cu_3BiS_3 as a potential photovoltaic absorber with high optical efficiency", *Applied Physics Letters*, vol. 102, no. 6, 2013

[95] P. K. Nair, L. Huang, M. T. S. Nair, H. L. Hu, E. A. Meyers and R. A. Zingaro, "Formation of p-type Cu_3BiS_3 absorber thin films by annealing chemically deposited Bi_2S_3-CuS thin films", *Journal of Material Research*, vol. 12, no. 3, pp. 651-656, 1997

[96] V. Estrella, M. T. S. Nair and P. K. Nair, "Semiconducting Cu_3BiS_3 thin films formed by the solid-state reaction of CuS and bismuth thin films", *Semiconductor Science and Technology*, vol. 18, no. 2, pp. 190-194, 2003

[97] N. J. Gerein and J. A. Haber, "Synthesis of Cu_3BiS_3 thin films by heating metal and metal sulfide precursor films under hydrogen sulfide", *Chemistry of Materials*, vol. 18, no. 26, pp. 6289-6296, 2006

[98] N. J. Gerein and J. A. Haber, "Physical vapor deposition synthesis of Cu_3BiS_3 for application in thin film photovoltaics", *Thin-Film Compound Semiconductor Photovoltaics*, vol. 865, pp. 119-124, 2005

[99] N. J. Gerein and J. A. Haber, "Cu_3BiS_3, Cu_3BiS_4, Ga_3BiS_3 and $Cu_5Ga_2BiS_8$ as potential solar absorbers for thin film photovoltaics", *Conference Record of the Thirty-First IEEE Photovoltaic Specialists Conference*, pp. 159-162, 2005

[100] D. Colombara, L. M. Peter, K. Hutchings, K. D. Rogers, S. Schafer, J. T. R. Dufton and M. S. Islam, "Formation of Cu_3BiS_3 thin films via sulfurization of Bi-Cu metal precursors", *Thin Solid Films*, vol. 520, no. 16, pp. 5165-5171, 2012

[101] N. J. Gerein and J.A. Haber, "One-step synthesis and optical and electrical properties of thin film Cu_3BiS_3 for use as a solar absorber in photovoltaic devices", *Chemistry of Materials*, vol. 18, no. 26, pp. 6297-6302, 2006

[102] N. J. Gerein and J.A. Haber, "Synthesis and optical and electrical properties of thin film Cu_3BiS_3 - a potential solar absorber for photovoltaic devices", *Conference Record of the 2006 IEEE 4th World Conference on Photovoltaic Energy Conversion*, vol. 1-2, pp. 564-566, 2006

[103] F. Mesa and G. Gordillo, "Effect of preparation conditions on the properties of Cu_3BiS_3 thin films grown by a two-step process", *Journal of Physics*, vol. 167, no. 1, 2009

[104] F. Mesa, A. Dussan and G. Gordillo, "Evidence of trapping levels and photoelectric properties of Cu_3BiS_3 thin films", *Physica B-Condensed Matter*, vol. 404, no. 23-24, pp. 5227-5230, 2009

[105] F. Mesa, G. Gordillo, T. Dittrich, K. Ellmer, R. Baier and S. Sadewasser, "Transient surface photovoltage of p-type Cu_3BiS_3", *Applied Physics Letters*, vol. 96, no. 8, 2010

[106] F. Mesa, W. Chamorro, W. Vallejo, R. Baier, T. Dittrich, A. Grimm, M.C. Lux-Steiner and S. Sadewasser, "Junction formation of Cu_3BiS_3 investigated by Kelvin probe force microscopy and surface photovoltage measurements", *Beilstein Journal of Nanotechnology*, vol. 3, pp. 277-284, 2012

[107] A. Dussan, J.M. Murillo and F. Mesa, "Thermally stimulated conductivity of Cu_3BiS_3 thin films deposited by co-evaporation: determination of trap parameters related to defects in the gap", *Journal of Materials Science*, vol. 47, no. 18, pp. 6688-6692, 2012

[108] F. Mesa, A. Dussan, B. A. Paez-Sierra and H. Rodriguez-Hernandez, "Hall Effect and transient surface photovoltage (SPV) study of Cu_3BiS_3 thin films", *Universitas Scientiarum*, vol. 19, no. 2, pp. 99-105, 2014

[109] H. Hu, O. Gomez-Daza and P.K. Nair, "Screen-printed Cu_3BiS_3-polyacrylic acid composite coatings", *Journal of Material Research,* vol. 13, no. 9, pp. 2453-2456, 1998

[110] J. Hu, B. Deng, C. Wang, K. Tang and Y. Qian, "Convenient hydrothermal decomposition process for preparation of nanocrystalline mineral Cu_3BiS_3 and $Pb_{1-x}Bi_{2x/3}S$", *Materials Chemistry and Physics*, vol. 78, no. 3, pp. 650-654, 2003

[111] D. Chen, G. Shen, K. Tang, X. Liu, Y. Qian and G. Zhou, "The synthesis of Cu_3BiS_3 nanorods via a simple ethanol-thermal route", *Journal of Crystal Growth*, vol. 253, no. 1-4, pp. 512-516, 2003

[112] G. Shen, D. Chen, K. Tang and Y. Qian, "Synthesis of ternary sulfides Cu(Ag)-Bi-S coral-shaped crystals from single-source precursors", *Journal of Crystal Growth*, vol. 257, no. 3-4, pp. 293-296, 2003

[113] J. Zhong, W. Xiang, Q. Cai and X. Liang, "Synthesis, characterization and optical properties of flower-like Cu_3BiS_3 nanorods", *Materials Letters*, vol. 70, pp. 63-66, 2012

[114] Y. Zeng, H. Li, B. Qu, B. Xiang, L. Wang, Q. Zhang, Q. Li, T. Wang and Y. Wang, "Facile synthesis of flower-like Cu_3BiS_3 hierarchical nanostructures and their electrochemical properties for lithium-ion batteries", *CrystEngComm*, vol. 14, no. 2, pp. 550-554, 2012

[115] K. Aup-Ngoen, S. Thongtem and T. Thongtem, "Cyclic microwave-assisted synthesis of Cu_3BiS_3 dendrites using L-cysteine as a sulfur source and complexing agent", *Materials Letters*, vol. 65, no. 3, pp. 442-445, 2011

[116] C. Yan, E. Gu, F. Liu, Y. Lai, J. Li and Y. Liu, "Colloidal synthesis and characterizations of wittichenite copper bismuth sulphide nanocrystals", *Nanoscale*, vol. 5, no. 5, pp. 1789-1792, 2013

[117] J. Yan, J. Yu, W. Zhang, Y. Li, X. Y. Yang, A. Li, X. K. Yang, W. Wang and J. Wang, "Synthesis of Cu_3BiS_3 and $AgBiS_2$ crystallites with controlled morphology using hypocrellin template and their catalytic role in the polymerization of alkylsilane", *Journal of Materials Science*, vol. 47, no. 9, pp. 4159-4166, 2012

[118] B. Murali and S. B. Krupanidhi, "Tailoring the band gap and transport properties of Cu_3BiS_3 nanopowders for photodetector applications", *Journal of Nanoscience and Nanotechnology*, vol. 13, no. 6, pp. 3901-3909, 2013

[119] F. Mesa, A. Dussan, J. Sandino and H. Lichte, "Characterization of Al/Cu_3BiS_3/buffer/ZnO solar cells structure by TEM", *Journal of Nanoparticle Research*, vol. 14, no. 9, 2012

[120] D. Tang, J. Yang, F. Y. Liu, Y. Q. Lai, J. Li and Y. X. Liu, "Growth and characterization of $CuSbSe_2$ thin films prepared by electrodeposition", *Electrochimica Acta*, vol. 76, pp. 480-486, 2012

[121] D. Tang, J. Yang, F. Y. Liu, Y. Q. Lai, M. Jia, J. Li and Y. X. Liu, "One-step electrodeposition and annealing of $CuSbSe_2$ thin films", *Electrochemical and Solid State Letters*, vol. 15, no. 2, pp. 11-13, 2012

[122] A. W. Welch, L. L. Baranowski, P. P. Zawadzki, S. Lany, C. A. Wolden and A. Zakutayev, "$CuSbSe_2$ photovoltaic devices with 3% efficiency", *Applied Physics Express*, vol. 8, no. 8, pp. 1-4, 2015

[123] K. Takei, T. Maeda and T. Wada, "Crystallographic and optical properties of $CuSbS_2$ and $CuSb(S_{1-x}Se_x)_2$ solid solution", *Thin Solid Films*, vol. 582, pp. 263-268, 2015

[124] R. H. Bari and L. A. Patil, "Preparation and characterization of nanostructured copper bismuth diselenide thin films from a chemical route", *Bulletin of Materials Science*, vol. 33, no. 6, pp. 663-670, 2010

4 Experimental methods

4.1 Introduction

The experimental methods adopted in this thesis are described in this Chapter. Section 4.2 presents the various deposition techniques for thin films. The post-growth processes, including doping and etching of the absorber layers are introduced in Section 4.3. Section 4.4 gives detailed information on the growth conditions of the absorber materials $CuSbS_2$ and Cu_3BiS_3 adopted in this thesis. Section 4.5 focuses on the characterization techniques for the study of the thin film properties.

Prototype devices based on $CuSbS_2$ were fabricated under the conditions described in Section 4.6. The analysis and characterisation methods used to evaluate the prototype $CuSbS_2$ solar cell devices produced in this work are described in Section 4.7.

4.2 Thin film growth techniques

4.2.1 Sputtering

Sputtering is a widely known deposition technique used for thin films. A schematic diagram is shown in Figure 4.1 (a). Plasma is created in the chamber from an ionized inert gas (i.e. typically argon at pressures of 1 - 10 mTorr), excited by an applied potential – either direct current (dc) or radio frequency (rf). The argon ions bombard the material source (i.e. the sputtering target) with consequent ejection of the atoms from the surface. The ejected atoms move in the chamber and deposit onto the substrate to form the thin film. In magnetron sputtering sources, a magnetic field confines the plasma close to the target, hence giving a more efficient sputtering process.

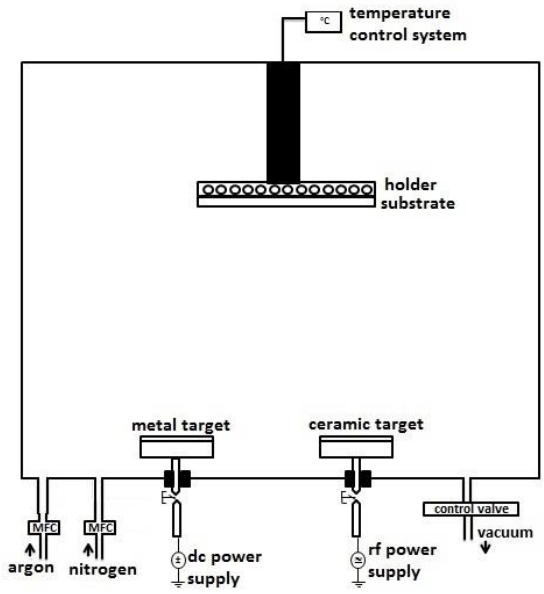

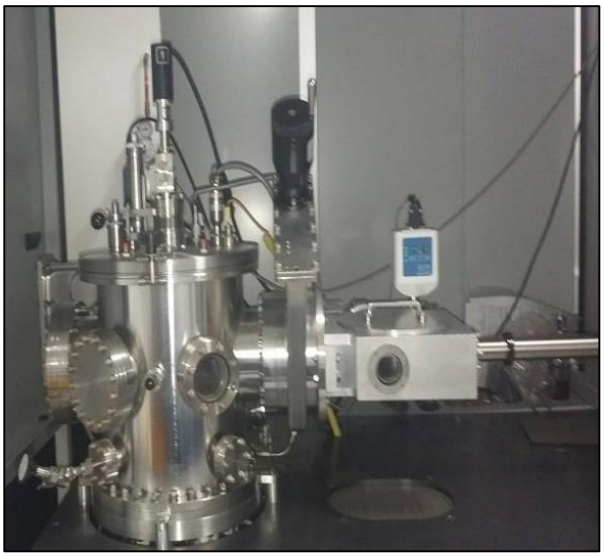

(a) (b)

Figure 4.1: (a) Schematic diagram of the sputtering chamber and (b) photograph of the AJA International Orion Phase II sputtering system used in the present study.

The sputtering deposition process offers many advantages, including: (a) deposition of uniform thin films from large-area targets, (b) easy and fine control of the film thickness, (c) deposition of alloys and multi-layer samples, (d) control of several film properties – i.e. adhesion, coverage, grain structure, (e) option to clean the substrate in vacuum before the film deposition, (f) numerous depositions can be performed from a single sputtering target [1]. It is possible to deposit a huge variety of materials by sputtering, including both metals (generally by means of dc power source) and semiconductors (by rf power). However some materials (e.g. organic compounds) degrade in the sputtering environment. The main drawbacks of sputtering are: (a) high equipment costs and (b) inefficiency in terms of energy consumption – i.e. 70% of the input energy is thermally dissipated in the target source and 25% is dissipated by emission of secondary electrons and photons from the target surface.

In this work the coatings were routinely deposited using an AJA International Orion Phase II sputtering system, shown in Figure 4.1 (b), designed in the 'sputter-up' configuration and comprising five 'ST20-O low profile' magnetron sputtering sources. The chamber pressure is controllable and the base pressure is ~10^{-7} Torr. The substrate can be

heated with two halogen lamps (up to 800°C) and is normally rotated in order to achieve uniform depositions. For further details on the sputtering system the reader is referred to ref. 2.

Dc sputtering was used to deposit the metal layers, including: molybdenum, copper, antimony, bismuth and aluminium. Rf sputtering was used to grow semiconductor films, such as: CdS, ZnO, AZO and ITO. In addition $CuSbS_2$ films were deposited by rf sputtering from a ternary target – i.e. in a one-step process as alternative to the sulfurization method described below.

4.2.2 Sulfurization

Sulfurization is a growth technique commonly used in chalcopyrite and kesterite materials for the conversion by reactive annealing of a metal 'precursor' layer into the sulfide film.

In this study sulfurization was largely used for the formation of $CuSbS_2$ and Cu_3BiS_3 layers from a sputtered metal stack. Sulfur powder (99.5% Alfa Aesar) was used as chalcogenization agent. Figure 4.2 shows a schematic diagram of the apparatus.

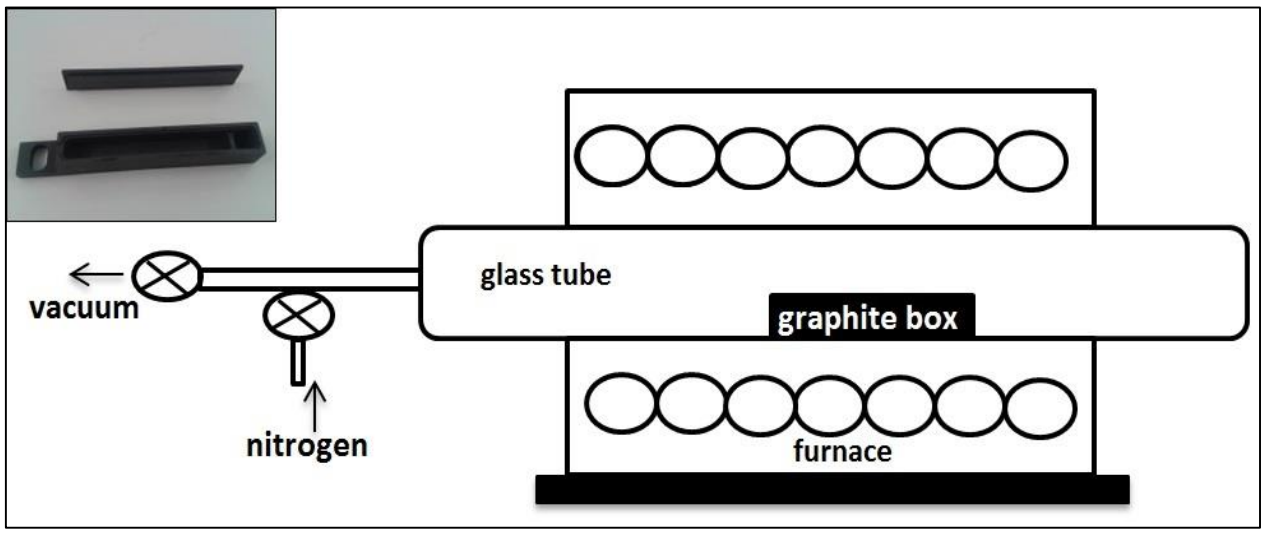

Figure 4.2: Schematic diagram of the home-built sulfurization apparatus. Inset: photograph of the graphite box utilised for the chalcogenization.

The metal precursor film – generally either 1 cm^2 or 5 cm^2 – was placed in a 16 mm x 100 mm x 16 mm sulfurization box, with the sulfur powder added in a well at one end. The closed graphite box was then loaded in a quartz tube having 30 mm internal diameter and placed in an Elite Thermal Systems TSH 12/38/250 furnace. The glass tube was evacuated for about 15 minutes with a rotary pump and subsequently filled with nitrogen at the required pressure. The reactive annealing was finally performed at specific temperatures and times, as described in Section 4.4.

4.2.3 Thermal evaporation

Thermal evaporation, or physical vapour deposition, is generally used for the deposition of metals having significant vapour pressures at temperatures achievable by resistive heating of a source boat. The boats are often tungsten, molybdenum or tantalum. In high vacuum (~10^{-5} Torr) the vaporized atoms transfer to the substrate for the formation of the film. High growth rates are achievable and the incorporation of impurities is minimized [1]. Coatings deposited by thermal evaporation however present limited uniformity and step coverage and the method has limited applicability to compounds.

In this work two thermal evaporators have been used. In particular the Univex 300 Oerlikon system was dedicated for the deposition of gold back contacts using ~0.3 mm^2 evaporation mask apertures. A multisource evaporator (Minilab 080 from Moorfield Nanotechnology Limited) was used to deposit indium, zinc and sodium fluoride thin films. The specifics of the system are reported in ref. 3.

4.2.4 Chemical bath deposition

Chemical bath deposition (CBD) is a thin film growth method based on the reaction of precursor chemicals in aqueous solution. It allows the growth of high quality films at low temperature [4]. The main drawback of CBD is the formation of particles which affect the morphological properties of the films.

The experiments with CBD of cadmium sulfide (CdS) layers were conducted at Northumbria University. For the growth of CdS films firstly 0.1456 g of $CdSO_4$ were mixed with 31.8 g of ammonia, then after 5 minutes and 30 seconds 0.333 g of thiourea were added

to the solution. The glass substrates were then placed in the precursor solution for about 20 minutes. Nitrogen gas was bubbled over the substrate surface every 20 seconds to prevent gas bubbles from building up on it and to ensure homogeneous deposition. The resulting CdS layers were about 100 nm thick, uniform and had rough surfaces. In order to create Cd-rich CdS films the step with the solution comprising $CdSO_4$ and ammonia (i.e. prior to the addition of thiourea) was extended to 10 minutes rather than the standard 5 minutes and 30 seconds.

4.2.5 Atomic layer deposition

Atomic layer deposition (ALD) is a growth technique based on cycled self-saturating reactions. The precursors are injected in the chamber one at a time in short pulses with the help of a carrier gas (e.g. argon or nitrogen). The precursor reacts on the substrate surface allowing the formation of a monolayer film. Each deposition period is followed by a purging period. A full single ALD cycle is defined by the deposition of the precursors alternate with the purge periods. The film thickness is controlled by the number of ALD cycles. ALD ensures the deposition of pinhole-free, uniform and smooth films [5].

In this work a Cambridge ALD reactor at the Centre for Materials and Structures, University of Liverpool, was utilised for the deposition of aluminium- and gallium-doped zinc oxide layers. Thin films of aluminum-doped zinc oxide (AZO) were deposited by ALD by using di-ethyl zinc (DEZ) with H_2O as precursors for ZnO and tri-methylaluminum (TMA) as precursor for Al [6]. For gallium-doped zinc oxide (GZO) triethlylgallium (TEG) was used as gallium precursor [7].

4.3 Post-growth processing of thin films

4.3.1 Doping

The electrical conductivity and carrier concentration of semiconductors can be altered by doping the material with impurities intentionally injected during the growth process. Different strategies and techniques are used for doping semiconductors. In thin film solar cells having the substrate structure three approaches are generally adopted: (i) the dopant element is included in the substrate or back contact material (e.g. from a combined Mo/Na

sputtering target in the case of CIGS) [8], (ii) the dopant is deposited onto the substrate (i.e. back contact in the case of substrate-geometry cells) before the growth of the absorber layer, or (iii) the absorber is covered with a thin layer comprising the dopant and is post-growth heated [9]. In this work the method investigated to dope $CuSbS_2$ films consisted of depositing a thin layer of the dopant (either NaF or In or Zn) on the back contact (Mo) by thermal evaporation (Section 4.2.3) before the deposition of the absorber layer.

4.3.2 Etching

In thin film solar cell fabrication etching treatments are often performed in order to remove impurities and secondary phases from the surface of the absorber (as is sometimes found for CIGS to remove unwanted phases) or else to modify the stoichiometry of a surface (e.g. in contacting CdTe). Removal of unwanted phases has the capacity to improve the quality of the p-n junction by eliminating recombination sites. Two principal approaches are used: (i) wet etching – i.e. the absorber is dipped in a specific solution and the impurities are removed by chemical reaction, (ii) dry etching – i.e. the material is cleaned in a plasma environment by exposing the surface to accelerated ions of a heavy and inert element (e.g. argon).

In this study both dry etching and a series of different wet etching methods were investigated for use in the preparation of chalcogenides. Details are given in Section 4.4.1 c, and their effects on the properties of the absorbers are discussed in Section 5.4.1

4.4 Deposition conditions of the absorber layers

This Section describes the details of thin film deposition and post-growth used in the investigation of the growth and properties of both $CuSbS_2$ and Cu_3BiS_3 films described in this thesis, while the general experimental methods were described in Section 4.3.

4.4.1 'Two-step' growth of $CuSbS_2$ and Cu_3BiS_3

The general principles of 'two-step' growth of chalcogenide films and the apparatus used to sputter metal 'precursor' films and to sulfurize were described in Section 4.3.

a) Metal films sputtering and calibration curves

All films were sputtered using an AJA International Orion Phase II sputtering system: 2" x 0.25" targets of copper (99.995%), antimony (99.999%) and bismuth (99.999%) were obtained from PI-KEM Ltd. The substrates were 5 x 5 cm^2 soda-lime glass (SLG) plates cleaned with de-ionized water. Additional samples were prepared on molybdenum films that had been sputtered onto SLG plates (Mo 99.999% PI-KEM). The sputtering conditions were generally as follows: the working distance was 112 mm; the sample was rotated at 80 rpm (unless stated otherwise, in this thesis these two conditions were applied for all the materials deposited by sputtering); the plasma starting conditions were 20 mTorr of argon flowing at 10 sccm. The pressures and dc powers were as follows: Cu - 60 Wdc, 5mTorr; Sb - 60 Wdc, 10 mTorr; and Bi - 20 Wdc, 5 mTorr. These operating conditions were found by experiment to give uniform surface coverage and smooth films.

Calibration curves for the sputtered thicknesses vs. time for Cu, Sb and Bi grown under the conditions above were generated with the aid of stylus thickness profiler (Ambios XP – 200, see Section 4.5.1 a) for thicknesses above 100 nm. The thicknesses of the thinner films – i.e. below 100 nm - were obtained by optical techniques (see Section 4.5.2). The calibration curves are shown in Figure 4.3. For each of the metals was possible to fit the data to a straight line. The linear fit is reasonably accurate for thick metal films. The non-zero intercepts reflect the possibility of nucleation phenomena and also errors. However since these intercepts were in the range -16 to +27 nm and the films used in experiments were ~1000 nm in thickness, the errors were negligible.

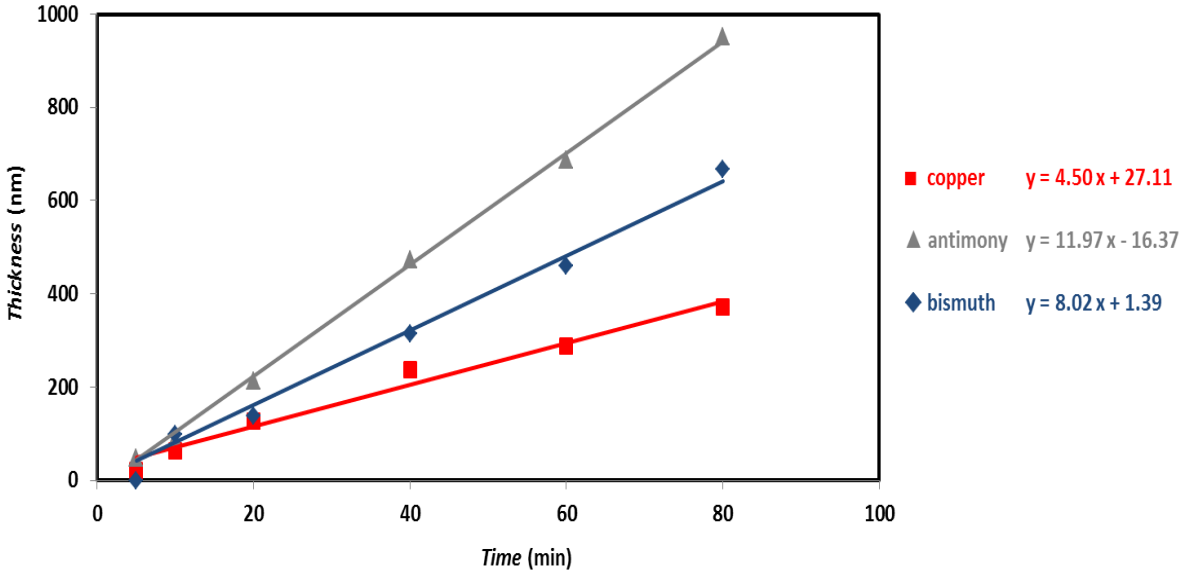

Figure 4.3: Calibration curves for copper, antimony and bismuth films. The equations are for the linear fits. The films were sputtered with powers and pressures as follows: Cu - 60 Wdc, 5mTorr; Sb - 60 Wdc, 10 mTorr; and Bi - 20 Wdc, 5 mTorr. The thickness values above 100 nm were obtained by profilometer and below 100 nm by optical methods (see Section 4.5). The measurement error is typically ±1 nm.

The lines in Figure 4.3 were used to calibrate an in-situ quartz microbalance thickness monitor in the sputter chamber. Readings from this were subsequently used in the control of film deposition for the metal precursors used in the sulfurization experiments that follow.

A range of precursor layer stack designs were investigated. For Cu-Sb these were 1 µm (total thickness) with i) Cu/Sb bilayers, ii) 2 periods of Cu/Sb and iii) multistacks comprising 5 periods of Cu/Sb bilayers. The precursor ratio was varied from Cu:Sb 1:1 to Cu:Sb 1:3 – i.e. Sb-rich, this being chosen since Sb-loss became an issue during initial experiments. For Cu-Bi fewer precursor stack designs were investigated since the experience from Cu-Sb was helpful in limiting the number of experiments necessary.

b) Post-growth sulfurization

Equipment for the post-growth sulfurization of Cu-Sb and Cu-Bi metal films was described in Section 4.2.2. Here, the conditions for the fabrication of high quality thin films of $CuSbS_2$ and Cu_3BiS_3 were explored. Temperatures in the range 200 - 550°C, times up to

360 minutes, nitrogen pressures in the range 0.1 - 760 Torr and a mass of sulfur in the range 5 mg to 0.5 g were investigated.

For the sulfurization runs the heating rate was ~50°C min^{-1} and cooling was done in-situ in the tube furnace simply by switching off the power (cooling down at ~1.67°C min^{-1}) until a temperature of < 150°C was achieved.

A limited number of experiments were conducted by including up to 50% elemental selenium in the graphite chalcogenization box with the sulfur.

c) Post-growth etching

Etching was deployed for two reasons: i) To remove unwanted phases, notably Cu_xS which is a common impurity phase in the growth of $Cu(In,Ga)Se_2$ and which was also expected here. This was achieved using KCN etching as described in Section 4.3.2. ii) For the removed of oxides. During the investigation it was found that the $CuSbS_2$ films were often covered by an oxide. A range of etching solutions were therefore tested as means of removing oxides, these being chosen by analogy with treatments described elsewhere for use with CIGS [10]. They were:

- HCl : HNO_3 solution for 1 minute (‘*etch 1*’ in ref. 10);
- NaOH : H_2O_2 solution for 1 minute (‘*etch 2*’ in ref. 10);
- NH_4OH solution for 5 minutes (‘*etch 3*’ in ref. 10).

The following methods were also used:

- soaking in de-ionized water for up to 4 hours;
- etching in NaOH as described in ref. 11. Solutions of 1%, 10% and 20% by weight were tested.

Finally the use of argon ion cleaning was tested with an energy of 500 eV.

The chemical state of the surfaces was investigated by XPS as described in Section 4.5.1 f.

d) Post-growth doping

Many of the $CuSbS_2$ films were highly resistive. A range of impurity doping strategies were therefore tested by evaporating dopant materials onto the SLG substrates prior to the deposition of the Cu-Sb metal precursor films. Dopant films of ~10 nm thickness of sodium fluoride, zinc and indium were tested. A thin layer of the dopant was normally deposited on the substrate by thermal evaporation. The absorber layer was subsequently grown as described above.

4.4.2 One-step sputtering of $CuSbS_2$ films

The one-step approach with the deposition of $CuSbS_2$ films from single sputtering target was introduced in Section 4.2.1.

Thin films were grown by rf sputtering from 2" x 0.125" ternary target of $CuSbS_2$ (99.9%) supplied from Plasmaterials Inc. The SLG 5 x 5 cm^2 substrates were cleaned by de-ionized water. A limited number of samples were grown on Mo-coated SLG. The substrates were loaded in the AJA International Orion Phase II sputtering chamber at base pressure of 10^{-7} Torr with working distance of 107 mm and rotated at 80 rpm. The plasma starting conditions were 20 mTorr of argon flowing at 10 sccm.

The power was limited at 36 Wrf and the working pressure was fixed at 5 mTorr. The substrate temperature was normally kept at RT and for some experiments was set at 400°C. The thickness calibration was obtained by varying the sputtering time from 10 minutes to 12 hours.

Table 4.1 summarizes the deposition conditions of the samples grown by rf sputtering from single target for the calibration. Characterization results are given in Section 5.5.

Sample ID	*thickness* (nm)	*rf power* (Wrf)	*pressure* (mTorr)	*temperature* (°C)	*time* (min)	*working distance* (mm)
A	20	24	5	25	10	117
B	80	24	5	25	30	117
C	180	24	5	25	120	117
D	220	36	5	25	180	112
E	300	36	5	400	180	112
F	1000	36	5	400	720	112
G	1000	36	5	25	720	112

Table 4.1: Deposition conditions of films deposited from the $CuSbS_2$ single target for thickness calibration. The samples were grown by rf sputtering under similar conditions with increasing deposition time.

4.4.3 Deposition conditions of Cu-Bi films

Thin films of copper and bismuth were deposited by dc sputtering on SLG as explained in Section 4.4.1 a. A smaller number of experiments were conducted compared to Cu-Sb since the main findings on the sulfurization process helped the development of films from the Cu-Bi system – e.g. the sulfurization stage was generally conducted under nitrogen at atmospheric pressure.

The precursor layer was normally deposited in the multistack configuration with 10 alternate thin layers of copper and bismuth (~1 μm total thickness). In the Cu-Bi-S system the target phase for PV applications is Cu_3BiS_3, hence the precursor stack was usually sputtered with Cu:Bi ratio 3:1. In the development of sulfurized films, metal precursors with Cu:Bi ~14:5 – i.e. slightly Bi-rich – were also tested, bismuth being the more volatile element.

Samples for the XRD analysis were prepared with the sulfurization conditions varied as follows: temperature – 300 to 550°C; sulfurization time – 5 to 360 minutes; sulfur mass: 6 to 100 mg. For the electrical characterization presented in Section 5.6 c the sulfurization time was fixed at 40 minutes and the sulfur mass at 20 mg.

4.5 Characterization methods of thin films

This Section describes the techniques used to investigate the structural characteristics of thin films (Section 4.5.1) and the methods for the analysis of the optical (Section 4.5.2) and electrical (Section 4.5.3) properties.

4.5.1 Methods for the analysis of the structural properties

(a) Stylus profilometer – An Ambios XP-200 stylus profilometer was used to measure the thicknesses of the films. A profilometer is a contact technique measuring the step height from the substrate to the film surface. The sensor can be either capacitive, inductive or piezoelectric [12] and the method is appropriate for films ranging in thickness from several tens of nm to several microns. However, the accuracy of profilometer measurement is generally limited for thicknesses below 100 nm, especially for films on rough

substrates. For film thicknesses < 100 nm other options for thickness measurement include ellipsometry and optical spectroscopy.

(b) XRD – An X-ray diffractometer measures the scattering pattern produced from a sample for the analysis of the structural properties of the material. As shown in the schematic diagram in Figure 4.4, XRD was used in the θ-2θ mode for composition analysis and crystal structure identification of the samples fabricated in this work. The X-rays were emitted from a Cu Kα1 source (having wavelength of 1.5405952 Å).

The system employs a goniometer to adjust the placement of the sample and the X-ray detector. The diffracted intensity as function of θ generally exhibits a series of peaks – these being associated with the particular angles θ_p at which the X-ray beam is diffracted from specific (*h k l*) planes of the crystal (Bragg condition). Libraries from the X'pert HighScore Plus software were used for the analysis of the measured XRD patterns. The XRD technique presents two main limitations for phase detection: (i) amorphous phases cannot be detected, (ii) diverse phases presenting overlapping peaks cannot be discriminated.

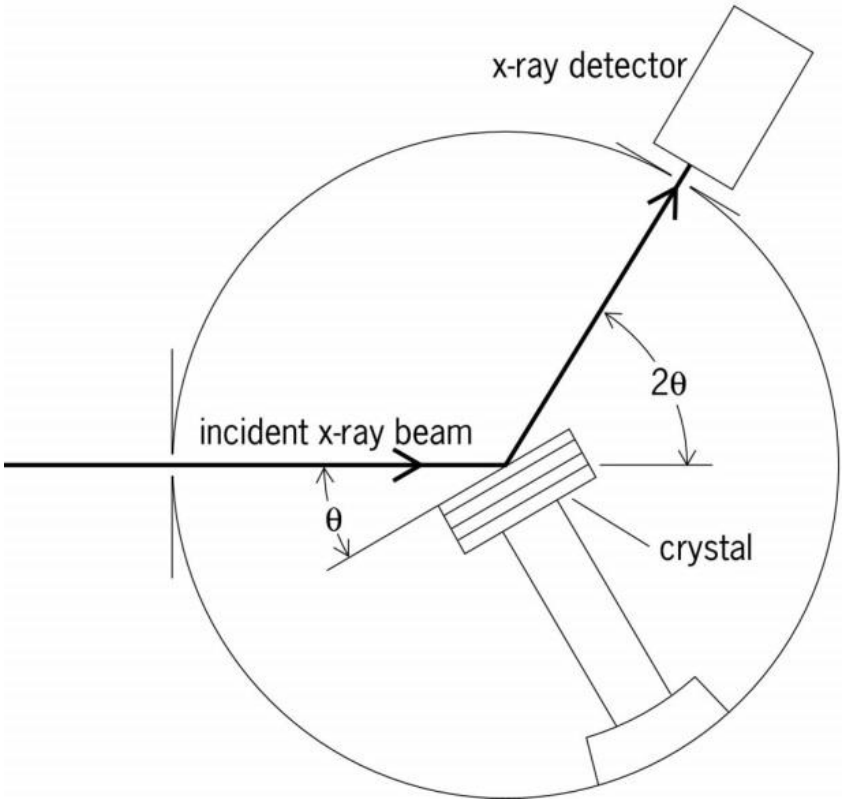

Figure 4.4: XRD schematic diagram in θ-2θ mode.

(c) Raman spectroscopy – Raman spectroscopy is a technique for the analysis of the structure and composition of materials based on the interaction of light with the low-frequency and vibrational modes of the material (e.g. phonons) [13]. The monochromatic light coming from a laser source (either NIR or VIS or UV) interacts with the material in two ways:

- the photon scatters elastically, hence conserves its energy – i.e. Rayleigh scattering.
- the photon exchanges energy with the lattice for inelastic scattering – i.e. Raman scattering or Raman effect.

The Raman spectrum displays the intensity of the scattered light as function of the shift in wavelength of the incident light. The Raman spectrum consists of two regions:

- Stokes region – where the photons are scattered at lower energies than the Rayleigh energy.
- Anti-Stokes region – where the photons are scattered at higher energies than the Rayleigh energy.

Raman spectroscopy can be used as a complementary technique to XRD for phase identification. The measurements were undertaken at the Centre for Materials and Structures, University of Liverpool. Libraries from the RRUFF database [16] were used for phase analysis.

(d) SEM/EDX – Scanning electron microscopy (SEM) and energy dispersive X-ray (EDX) analysis were conducted at the Nanoinvestigation Centre at Liverpool (NiCaL) by the JEOL 6610 and the high resolution JEOL 7001F SEM systems. SEM is a microscopy technique using a focused electron beam to image the topography and structure of the samples. The electron energy generally can be varied from 100 eV to 30 keV. The higher resolution limit of the SEM can be as low as several nanometers. As shown in Figure 4.5, when an electron strikes the sample surface different phenomena can occur [13], these being:

- 'Backscattering' of electrons out of the sample, these electrons having energies comparable to the incident energy.

- Electrons from the sample are ejected – these are the low energy 'secondary' electrons. These electrons are used in the normal imaging mode of the SEM.
- Auger electrons are emitted, but are not used in SEM.
- X-ray radiation is produced, and may be used in elemental analysis.

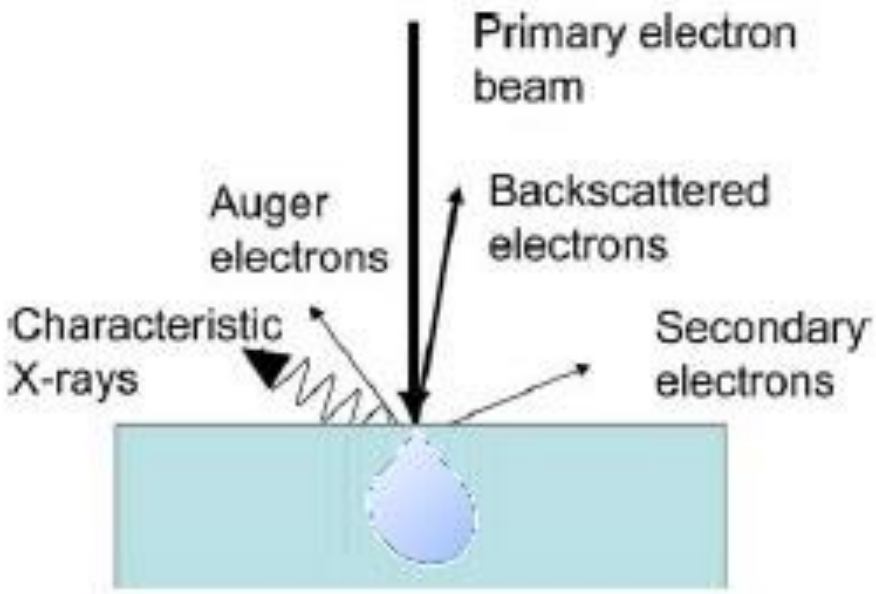

Figure 4.5: Schematic diagram showing electron beam-solid interactions and the 'signals' emitted from the solid that may be used in microscopy and analysis [13].

The SEM/EDX equipment typically comprises dedicated detectors for the various signals in order to acquire different types of images and data. In particular the X-ray radiation provides information about the elemental composition of the sample, since each element of the periodic table emits X-rays at specific energies. Uncertainty in the EDX analysis can occur in inhomogeneous samples if there is chemical variation within the generation volume shown in Figure 4.5.

In this thesis SEM/EDX was used for the surface and cross-sectional imaging and analysis of the fabricated and processed samples.

(e) Transmission electron microscopy (TEM) – Transmission electron microscopy (TEM) is a high resolution microscopy technique used for imaging and analyzing the micro-structural characteristics of thin films, including grain structure, composition distribution and defects. The TEM apparatus comprises of an electron source, a condenser lens, an objective lens and a data acquisition system [14]. TEM in transmission operates similarly to optical microscopy but an electron source is used instead of light – i.e. this yields to considerably higher imaging resolution. The electron beam is focused by a condenser lens onto a thin specimen. The incident beam is transmitted through the specimen and then focused by the objective lens onto the screen for the imaging. The resolution of TEM measurements is typically in the order of 1 nm. In this work TEM analyses were conducted at Durham University by a JEOL 2100F FEG TEM system and a JEOL 3010 at NiCaL in Liverpool.

(f) X-ray Photoelectron Spectroscopy (XPS) – X-ray Photoelectron Spectroscopy (XPS) is a characterization method used for analysis of the compositional and chemical states of surfaces [15]. XPS is based on the photoelectric effect – i.e. X-rays bombard the sample surface with consequent emission of photoelectrons. Measurements of the binding energies of the detected photoelectrons enable quantification of the composition of the sample surface. All the elements of the periodic table can be identified by XPS except hydrogen and helium.

In this work the XPS equipment comprised a vacuum chamber, an 'X-ray Specs XR 50 M' Al Kα monochromated source and a 'PSP' Hemispherical Electron Analyser. XPS analysis was principally used to estimate the phases present on the surface of as-grown $CuSbS_2$ absorber layers. The XPS apparatus was used also for in-situ cleaning (see Section 5.4.1 e) by means of a Sputter Gun Ar^+ PSP ISIS 2000.

4.5.2 Methods for optical characterization of thin films

(a) Optical spectroscopy – Optical spectroscopy is a technique based on the interaction between light and matter for the analysis of the optical properties of the materials. A light beam of intensity I_o strikes the sample and dedicated detectors can measure the intensity of the light transmitted through the sample or reflected from the surface (N.B. the actual sensors detect powers).

The transmittance T is defined as the ratio between the intensities of the transmitted light I_T and the incident light I_o:

$$T = \frac{I_T}{I_0} \tag{4.1}$$

The reflectance R is the ratio between the intensities of the reflected light I_R and the incident light I_o:

$$R = \frac{I_R}{I_0} \tag{4.2}$$

The transmittance spectrum and the reflectance spectrum are the representation of T and R respectively as functions of the wavelength λ. In this study the transmittance and reflectance spectra of thin films were generally recorded in the wavelength range 250 - 2600 nm by a SolidSpec-3700 UV-VIS-NIR Spectrophotometer Shimadzu. The system employs two lamp sources and three detectors for the different portions of the spectrum. An integrating sphere, producing uniform distribution of the scattered light, was used to obtain uniform and reproducible measurements

The absorption coefficient α of a thin film with thickness d (cm) can be calculated from the transmittance and reflectance by the approximate Equation 4.3 [17].

$$\alpha\ (\mathrm{cm}^{-1}) = \frac{1}{d} ln \left[\frac{(1-R)^2}{T}\right] \tag{4.3}$$

The absorption coefficient is a measure of the critical distance within the light is absorbed in the material. In semiconductors the band gap Eg can be estimated from the absorption coefficient spectrum α(λ). The two following empirical methods are the principal approaches used for the band gap estimation of semiconductors:

i. Fundamental method [18] – For direct semiconductors the absorption coefficient squared α^2 is plotted as function of photon energy hν and the optical band gap is given by the x-axis intercept of the tangent to the linear region of the graph. For indirect semiconductors the procedure is the same by plotting $\alpha^{1/2}$ instead of α^2.
ii. Tauc plot [19] – The optical band gap of a direct semiconductor is estimated from the x-axis intercept of the tangent to the linear region of the $(\alpha h\nu)^2$ curve

as function of the photon energy hν. For indirect semiconductors the optical band gap is estimated from the graph of $(\alpha h\nu)^{1/2}$ vs. hν graph.

These methods are prone to uncertainty since the graphs do not always contain clear linear regions with which to perform the extrapolation. While method (i) is based on fundamental relations, method (ii) is an empirical modification that works well in practice and which is widely used.

In this work optical spectroscopy was also used for the thickness calibration of very thin films of copper. The thickness was estimated by matching the transmittance spectra of the metal layers with the fit to modeled spectra from the "Code" software that uses dispersion relation data and the transfer matrix method to generate spectra [20]. Thickness is used as a fitting parameter and gives an estimate of actual film thickness when the model converges with experiment. The thickness estimation of other materials not included in the libraries database of the "Code" software – e.g. Sb, In and ZnO – was performed by ellipsometry (see Section 4.5.2 c).

(b) FTIR – In Fourier transform infrared (FTIR) spectroscopy the radiation is sent to the sample – generally placed in a cryostat – though an interferometer. The detector measures the energy variation as a function of time. Using the Fourier transform theory the intensity as a function of frequency is extracted [21]. In this thesis the absorption coefficient $\alpha(\lambda)$ was calculated from the measured transmittance and reflectance measured in the temperature range 3.7 - 300 K by a Bruker Vertex 70v FTIR spectrometer.

(c) Ellipsometry – Ellipsometry is an optical technique generally used to measure the thickness of semi-transparent coatings [22]. Polarized light incident on the sample with angle Φ is reflected and collected from the detector placed at the same angle Φ. The polarization change of the reflected light is described by Ψ (proportional to the amplitude variation) and Δ (proportional to the phase shift). The analysis of Ψ and Δ enables calculation of the complex refractive index of the material, and permits extraction of the thickness, roughness, composition and conductivity of the film.

Ellipsometry is a very sensitive and accurate technique method to measure the thickness of semi-transparent films with nanometer resolution. In this work ellipsometry measurements were conducted at the Department of Electrical Engineering of the University of Liverpool for the thickness calibration of ultrathin Sb, ZnO and In layers. The thicknesses were estimated by fitting the measured Ψ and Δ vs. λ spectra with the appropriate models by the software "CompleteEase".

(d) Photoluminescence spectroscopy – Photoluminescence (PL) is a spectroscopy method for the analysis of impurities and defects in semiconductors. A photoluminescent material emits photons as a consequence of photo-excitation of electron-hole pairs. In the PL process, the excited electrons recombine, usually but not always via defect states, and when the recombination process is radiative, the luminescence energy (and intensity) gives information about the defect states and the recombination process.

The PL measurements on as-grown samples were undertaken at the Durham University. The system has an argon ion laser source (514.5 nm) with maximum power of 397 mW and the samples were analysed at 3 K.

PL analysis at different power levels and temperatures is a powerful method of investigating the recombination mechanisms, including via defects and impurities in the semiconductor [23].

4.5.3 Methods for electrical characterization of thin films

(a) Four-point probe method – The measurement of the resistivity of thin films is based on the van der Pauw method. In case of square probe arrangement a current I_{12} is injected through two probes and the voltage V_{34} is measured across two other probes placed at the opposite edge of the sample, hence the resistance $R_{34,12}$ according to the Ohm's law is given by Equation 4.4.

$$R_{34,12} = \frac{V_{34}}{I_{12}} \tag{4.4}$$

The measured resistance $R_{34,12}$ is related to the sheet resistance $R_{\square}$ of the material by the particular geometry of the sample. In general the relationship is complex and must be solved by numerical techniques.

In this work an "Advanced Instrument Technology CMTSR2000N" four-point probe equipment was used to measure the resistivity of the films. This system employs a simple linear probe arrangement. In this case the relationship between the resistance of the material and the measured sheet resistance is given from the simplified Equation 4.5.

$$R_{\square} = \frac{\pi}{ln2} R \tag{4.5}$$

Finally Equation 4.6 allows calculation of the resistivity ρ of the material from the sheet resistance $R_{\square}$, known the film thickness d.

$$\rho(\Omega\, cm) = R_{\square}(\Omega/\square) * d\ (\text{cm}) \tag{4.6}$$

The main advantage of the van der Pauw method over the classic ohmmeter measurement is that the four-point probes arrangement prevents the systematic measurement errors caused by the series resistances of the electrodes.

(b) Hall effect measurement – A home-built Hall effect apparatus was used to measure the electrical parameters of semiconductor films, including: conductivity type, resistivity, carrier concentration and mobility. The sample was first scribed in a square area and four small dot contacts are made at the corners with either carbon paste or silver paste. The sample connected to the four-point probes in the van der Pauw configuration was then placed in magnetic field of typically 0.8 T. The measurement of the electrical features is based on the Hall effect. In particular the calculation of the Hall coefficient R_H (Equation 2.9 – see Section 2.2.3 c) enables the determination of the conductivity type of the semiconductor, the carrier concentration and the mobility. The apparatus has a cryostat for the temperature-dependence measurement of the electrical parameters of the films. This investigation tool is useful for the physical analysis of the material [24].

(c) White light photoconductivity measurement – A photoconductivity test of the absorber films (e.g. $CuSbS_2$) was conducted under white light. The films were deposited on transparent conductive substrates (e.g. SnO_2-coated glass being the front contact) and

contacted with high work function metal (e.g. Au deposit by thermal evaporation being the back contact). The resistance of the film was measured by the "Keithley 2400" source meter both in dark conditions and under light AM 1.5, by placing the sample in the "TS-Space Systems class AAA" solar simulator. A potential drop in the resistance from dark conditions to light indicates that a photocurrent is generated, hence the film is photoconductive.

4.6 Fabrication of solar cells based on $CuSbS_2$

4.6.1 Device configurations

For the development of prototype devices based on the heterojunction $CuSbS_2$/CdS the two typical configurations for thin film solar cells were considered: the superstrate structure glass/TCO/CdS/$CuSbS_2$/Au and the substrate structure Mo/$CuSbS_2$/CdS/TCO – the latter being the most investigated device type in this thesis. The investigation of alternative window layer materials is discussed in Chapter 7.

a) Superstrate $CuSbS_2$ devices

Figure 4.6 shows the superstrate configuration $CuSbS_2$ device as grown in this work. The substrate used was generally commercial TEC 8, either 5 cm^2 or 25 cm^2. The substrates were cleaned in an ultrasonic bath with isopropyl alcohol (IPA), then rinsed with DI water and dried with nitrogen. A ~80 - 100 nm thick layer of cadmium sulfide was deposited on the substrate by either rf sputtering or chemical bath deposition (CBD). CdS is the most common window layer material used in thin film solar cells – being an n-type semiconductor with optical band gap of ~2.42 eV. The $CuSbS_2$ absorber layer was grown either by sulfurization of metal precursor films or rf sputtering from single source. A thin layer of about 200 nm of gold was normally deposited by thermal evaporation for back contact. For these prototype devices small area contacts – i.e. 0.8 - 3 mm^2 – were generally adopted.

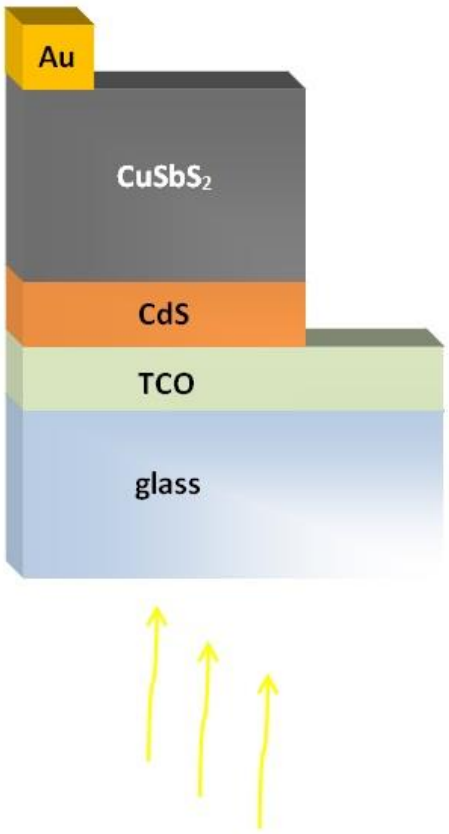

Figure 4.6: Diagram of the substrate device configuration used for $CuSbS_2$. The window layer was CdS and the back contact was gold while the glass/TCO was commercial 'TEC 8' from Pilkington/NSG.

b) Substrate $CuSbS_2$ devices

Figure 4.7 shows the substrate structure of $CuSbS_2$-based device. The substrate was usually soda-lime glass (SLG), either 5 cm^2 or 25 cm^2. The substrates were cleaned in an ultrasonic bath with IPA, then rinsed with de-ionized water and dried with nitrogen.

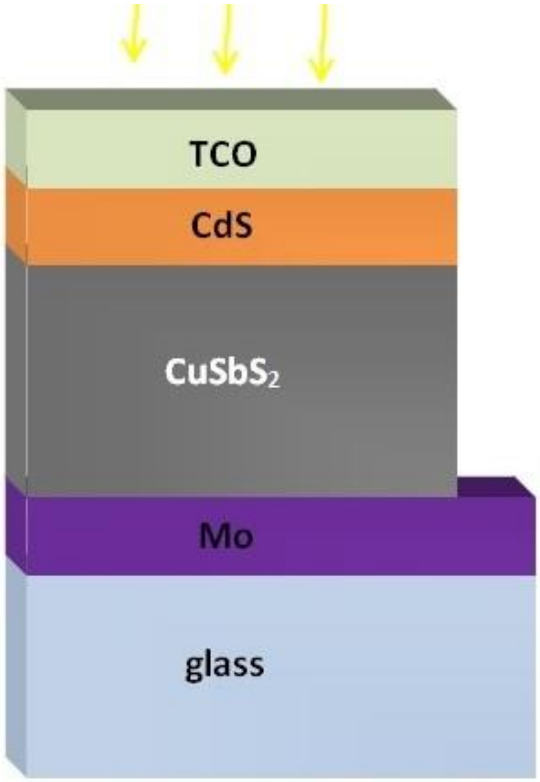

Figure 4.7: Diagram of the substrate geometry used for the $CuSbS_2$/CdS heterojunction. The absorber layers were generally deposited on Mo-coated glass. Different materials and deposition techniques were investigated for the front contact.

The back contact material used in the substrate structure was molybdenum, normally grown on the SLG substrates by dc sputtering. For a limited number of trials, devices were grown on molybdenum foils. A large variety of back contact materials are reported for use in thin film solar cells are reported, including W, Mo, Cr, Ta, Nb, V, Ti, Mn, Au, Cu, Al, Pt [25]. Mo exhibits optimal characteristics as a back contact material, including: high conductivity; high melting point (2623°C) – i.e. processable at high temperature; being relatively inert to oxygen and during sulfurization or selenization; a relatively high work function (nearly 4.6 eV) and it is an inexpensive and abundant element. Hence molybdenum was used throughout this work. The deposition conditions of Mo layers by dc sputtering are reported in Section 4.6.2 a. The absorber layer $CuSbS_2$ was deposited on molybdenum by either sulfurization of metal films or by direct rf sputtering. The window layer CdS was grown above the absorber either by CBD or rf sputtering. Several materials and deposition techniques were explored for the front transparent contact, including:

- aluminum-doped zinc oxide (AZO) deposited by either rf sputtering or atomic layer deposition (ALD);
- gallium-doped zinc oxide grown by ALD;
- indium tin oxide (ITO) deposited by rf sputtering.

Aluminum-doped zinc oxide (AZO) is the most common TCO material employed as front contact in the substrate configuration for thin film solar cells. It is a highly conductive n-type semiconductor and having a band gap of of ~3.5 eV is highly transparent. For PV applications it is desirable to fabricate TCO films with sheet resistance below 15 Ω/□ [26], and this is achievable with AZO. However, indium tin oxide (ITO) is the TCO material with the highest performance for thin film solar cells.

The devices were scribed into small contact areas – generally ~4 - 6 mm^2. In some experiments small modifications to the structure shown in Figure 4.7 were made.

(i) For some devices a thin intentionally created layer of $MoSe_2$ was included between the back contact and the absorber layer. In CIGS a thin layer of $MoSe_2$ normally grows between the back contact and the absorber layer from the selenization process and this minimizes the effects of the Schottky barrier between the back contact and the absorber layer [27]. Here the $MoSe_2$ was formed by the selenization of molybdenum.

(ii) For some devices the CdS window layer was omitted in order to study the $CuSbS_2$/AZO junction.

(iii) Finally for the best devices a thin layer of intrinsic ZnO was included between the window layer and the front contact. This strategy is commonly used in the commercial thin film solar cell technologies [28].

Details of the formation of individual layers are deferred to Section 4.6.2.

4.6.2 Preparation of the various layers of the device

This Section describes the deposition conditions of the individual layers for the production of full devices. Table 4.2 summarizes the growth parameters of the main materials used for device fabrication deposited by sputtering - alternative growth methods in some cases were evaluated and are shown in the comments column. The films grown by sputtering were

normally calibrated on 5 x 5 cm^2 SLG. The substrates were generally loaded in the sputtering chamber at a base pressure of ~10^{-7} Torr with a working distance of 112 mm from the source and rotated at 80 rpm.

Material	Power (W)	Pr. (mTorr)	Temp. (°C)	time (min)	Alternative deposition methods
Mo	50 - 300 (dc)	2 -20	25 - 400	10 - 180	/
CdS	25 (rf)	5	25 - 200	60	chemical bath deposition
AZO	20 - 46 (rf)	1.8 - 10	25 - 400	30 - 180	atomic layer deposition
ITO	20 - 46 (rf)	1.8 - 10	25 - 400	30 - 180	/

Table 4.2: Deposition conditions of the principal layers used for the fabrication of solar devices based on the heterojunction $CuSbS_2$/CdS.

(a) Molybdenum

Mo films were deposited by dc sputtering. The deposition conditions influence the structural and electrical properties of the sputtered Mo thin films and in turn the performance of the device [29]. The primary requirements are for good substrate coverage and high conductivity.

The Mo films were grown by using a 2" x 0.25" thick 99.95% Mo target supplied from PI-Kem. The sputtering parameters were varied over a large range in order to obtain films with high conductivity. In particular for the electrical calibration of the Mo films the power was varied from 50 to 300 Wdc, the chamber pressure from 2 to 20 mTorr, the substrate temperature from RT to 400°C and the deposition time from 10 minutes to 3 hours.

(b) $MoSe_2$

As an alternative to the accidental formation of a MoS_2 interlayer during the formation of the $CuSbS_2$ film, $MoSe_2$ was intentionally introduced prior to deposition of the absorber. The selenization was performed in the sulfurization apparatus described in Section 4.2 by using a dedicated graphite box. In order to obtain single-phase $MoSe_2$ films, the

sputtered Mo precursor layers were normally selenized at temperature above 500°C in accordance with the procedures in ref. 30.

(c) Cadmium sulfide

CdS was deposited by rf sputtering. However due to the kit downtime for the first experiments on the development of the prototype devices, CdS films were grown by chemical bath deposition (CBD) – details of the deposition conditions are given in Section 4.2.4.

Thin films of CdS were deposited by rf sputtering from a 2" x 0.25" thick 99.99% CdS target supplied from Pi-Kem. Uniform CdS films about 110 nm thick were produced with 25 Wrf and 5 mTorr for about 1 hour; the substrate temperature being normally set at 200°C.

(d) Aluminum-doped zinc oxide and gallium-doped zinc oxide

In this work AZO films were mainly deposited by rf sputtering. The films were grown by using 2" x 0. 25" thick 99.99% ZnO:Al (98:2 at%) target supplied from Pi-Kem. The sputtering conditions were varied in order to produce transparent AZO films with high conductivity.

Alternative deposition techniques were explored, including atomic layer deposition (ALD). For the ALD deposition of AZO the following growth conditions were explored: substrate temperature – 150, 200 and 300°C; ZnO:Al ratio – 17:1 or 20:1; number of ALD cycles – 648, 1296 or 1365. The properties of the films are described in Section 6.2 d.

An alternative material to aluminum-, gallium-doped zinc oxide (GZO) was also used, with the GZO films also being deposited by ALD.

(e) Indium tin oxide

In the present study ITO films were deposited by rf sputtering. The samples were calibrated from 2" x 0.25" thick 99.99% ITO (90:10 at%) target fabricated from Pi-Kem. In order to produce transparent ITO films with high conductivity the sputtering parameters were

varied as follows: power from 20 to 46 Wrf; chamber pressure from 1.8 mTorr to 10 mTorr; substrate temperature from RT to 400°C; deposition time from 30 minutes to 3 hours.

(f) Intrinsic zinc oxide

In this work the i-ZnO films were deposited by either ALD or rf sputtering. It is desirable to produce thin layers of ZnO with high resistivity – i.e. sheet resistance > 1 MΩ/□. 30 nm layers of ZnO were grown by rf sputtering from 2" x 0.25" thick 99.99% pure ZnO target supplied from Pi-Kem. ZnO thin films were also deposited by ALD using similar conditions to those described above for AZO.

(g) Front grid

In the development of prototype devices based on the substrate configuration very small contact areas below 10 mm^2 were normally scribed. A front grid is generally deposited in thin film solar cells in the substrate structure to ensure uniform sheet resistance across the TCO layer. For these small samples it was not necessary to grow a metal grid. For few experiments a 1μm thick dot of aluminum was grown as front grid by dc sputtering in order to evaluate possible improvements in the device performance.

4.7 Characterization techniques of photovoltaic devices

(a) *J-V* measurement – Current density-voltage (*J-V*) analysis is the standard characterization technique used to extract the performance parameters of photovoltaic devices – i.e. efficiency ŋ, fill factor *FF*, open-circuit voltage *Voc* and short-circuit current density *Jsc*. In this work two equivalent solar simulator systems were used – i.e. a "TS-Space Systems class AAA" system and an "Oriel Instruments 81160" solar simulator.

The samples were placed on the holder at RT in the solar simulator under AM 1.5 radiation having an intensity of 100 mW cm^{-2}. A "Keithley 2400" source meter controlled from LabView software biased the cell and measured the current density. Details on the program are given in ref. 31. The *J-V* measurements were conducted from -1V to +1V unless otherwise stated.

(b) *J-V-T* measurement – The temperature-dependent analysis of the current density-voltage response enables determination of the transport mechanisms in the solar device. In the present study the samples were placed in a "Janis CCS-450" cryostat and analysed in dark conditions in the range 120 - 300 K controlled by a Lake Shore 331 system with the *J-V* measurements being made by a "Keithley 2400" source meter.

(c) *EQE* analysis – The spectral performance of the solar cells is obtained from the external quantum efficiency (*EQE*) measurement. *EQE* is defined as the ratio of the number of charge carriers collected and the number of incident photons – i.e. $0 \leq EQE \leq 100\%$ [32]. In this work a "Bentham PVE300" *EQE* system remote controlled by BenWin+ software was utilised for the *EQE* spectrum measurement in the range 300 - 1000 nm.

The radiation emitted from a xenon lamp is chopped and filtered to ensure monochromatic light incident on the device. The system employs also a light bias source to perform the *EQE* measurement under stimulated conditions.

(d) Impedance spectroscopy – Impedance spectroscopy is an analysis method of the electrical characteristics of devices used for the investigation of the p-n junction properties. From the impedance study by appropriate circuit models, the equivalent capacitance and conductance of the device can be determined. The simplest impedance model for a solar cell is a parallel resistor-capacitor *Rsh-Csh* network connected with a series resistor *Rs*, as shown in Figure 4.8.

The impedance is the generalized resistance for alternating currents (ac), as defined by Equation 4.7.

$$Z(\omega) = \frac{V(\omega)}{I(\omega)}, \tag{4.7}$$

where $\omega = 2\pi f$. For the circuit in Figure 4.8 it can be demonstrated that the impedance magnitude is given by Equation 4.8 [33].

$$|Z| = \{[Rs + \frac{Rsh}{1+2\pi f^2 Rsh^2 Csh^2}]^2 + [\frac{2\pi f Rsh^2 Csh^2}{1+2\pi f^2 Rsh^2 Csh^2}]^2\}^{1/2} \tag{4.8}$$

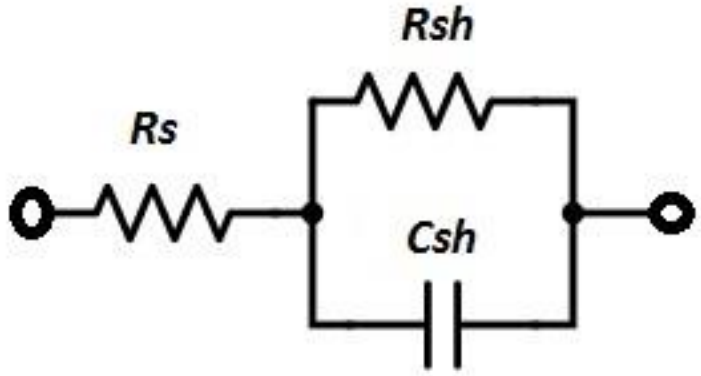

Figure 4.8: Equivalent circuit model of the device impedance, where *Rs* represents the series resistance, *Rsh* the shunt resistance and *Csh* the equivalent capacitance.

$$Z(\omega) = \frac{V(\omega)}{I(\omega)}, \tag{4.9}$$

At low frequencies $|Z|$ tends to $Rsh + Rs$ and at high frequencies it tends to Rs. Hence the analysis of $|Z|$ at low frequencies f is strictly related to the series resistance of the device. In particular there are two possible scenarios: (i) *Rs* does not vary with the voltage V – i.e. the applied voltage acts mainly on the p-n junction, (ii) *Rs* depends on the applied bias, this meaning that potentially there is a Schottky barrier between the absorber and one electrode.

The analysis of the impedance phase gives information on the equivalent capacitance of the device and therefore on the nature of the p-n junction [34].

Finally from the temperature-dependence measurement of the capacitance as function of the frequency, details on the deep trap levels at the junction can be acquired, including: activation energy, trapping frequency, density of states and capture cross section [35], although this was not attempted here. In this work a Solartron SI 1260 impedance/gain-phase analyzer with a Solartron 1296 dielectric interface was used for the impedance analysis of $CuSbS_2$-based prototype devices.

4.8 References for Chapter 4

[1] S. Wolf and R. Tauber, *Silicon Processing for the VLSI Era, Vol. 1*, Lattice Press, 1986

[2] (20/11/2015) http://www.ajaint.com/atc-orion-series-sputtering-systems.html

[3] (20/11/2015) http://www.moorfield.co.uk/minilab/minilab-080.php

[4] I. Kaur, D. K. Pandya and K. L. Chopra, "Growth-kinetics and polymorphism of chemically deposited CdS films", *Journal of the Electrochemical Society*, vol. 127, no. 4, pp. 943-948, 1980

[5] A. Pakkala and M. Putkonen, "Chapter 8: Atomic layer deposition", *Handbook of Deposition Technologies for Films and Coatings (3rd ed.)*, Elsevier, 2009

[6] B. Y. Oh, J. H. Kim, J. W. Han, D. S. Seo, H. S. Jang, H. J. Choi, S. H. Baek, J. H. Kim, G. S. Heo, T. W. Kim and K. Y. Kim, "Transparent conductive ZnO:Al films grown by atomic layer deposition for Si-wire-based solar cells", *Current Applied Physics*, vol. 12, pp. 273-279, 2012

[7] P. R. Chalker, P. A. Marshall, S. Romani, M. J. Rosseinsky, S. Rushworth, P. A. Williams, J. Buckett, N. McSporran and J. Ridealgh, "Atomic layer deposition of gallium-doped zinc oxide transparent conducting oxide films*", Transparent Conducting Oxides and Applications*, vol. 1315, pp. 39-44, 2011

[8] P. M. P. Salomé, A. Hultqvist, V. Fjällström, M. Edoff, B. G. Aitken, K. Zhang, K. Fuller and C. Kosik Williams, "Incorporation of Na in Cu(Ga,In)Se_2 thin film solar cells: a statistical comparison between Na from soda lime glass and from a precursor layer of NaF", *IEEE Journal of Photovoltaics*, vol. 4, no. 6 pp. 1659-1664, 2014

[9] D. Rudmann, D. Brémaud, H. Zogg, and A. N. Tiwari, "Na incorporation into Cu(In,Ga)Se_2 for high-efficiency flexible solar cells on polymer foils", *Journal of Applied Physics*, vol. 97, 2005

[10] T. Delsol, M. C. Simmonds and I. M. Dharmadasa, "Chemical etching of Cu(In, Ga)Se_2 layers for fabrication of electronic devices", *Solar Energy Materials and Solar Cells*, vol. 77, pp. 331-339, 2003

[11] H. Katagiri, K. Jimbo, S. Yamada, T. Kamimura, W. Maw, T. Fukano, T. Ito and T. Motohiro, "Enhanced conversion efficiencies of Cu_2ZnSnS_4-based thin film solar cells by using preferential etching technique", *Applied Physics Express*, vol. 1, 2008

[12] G. Franceschinis, "Surface profilometry as a tool to measure thin film stress, a practical approach", *RIT MicroE*, 2006

[13] D. R. Baer and S. Thevuthasan, "Characterization of thin films and coatings", *Handbook of Deposition Technologies for Films and Coatings* (3rd ed.), Elsevier, 2009

[14] R. F. Egerton, "The transmission electron microscope", *Physical Principles of Electron Microscopy*, Springer, 2005

[15] J. F. Watts and J. Wolstenholme, "Electron spectroscopy: some basic concepts", *An Introduction to Surface Analysis by XPS and AES*, John Wiley & Sons, 2003

[16] (20/11/2015) http://rruff.info/

[17] A. Rabhi, M. Kanzari and B. Rezig, "Optical and structural properties of $CuSbS_2$ thin films grown by thermal evaporation method", *Thin Solid Films*, vol. 517, no. 7, pp. 2477-2480, 2009

[18] J. I. Pankove, *Optical Processes in Semiconductors*, Englewood Cliffs, N.J.: Prentice-Hall, 1971

[19] J. Tauc, "Optical properties and electronic structure of amorphous Ge and Si", *Materials Research Bulletin*, vol. 3, pp. 37-46, 1968

[20] (01/05/2016) http://www.mtheiss.com/download/software_brochure.pdf

[21] B. C. Smith, "Introduction to infrared spectroscopy", *Fundamentals of Fourier Transform Infrared Spectroscopy*, CRC Press, 2011

[22] H. Fujiwara, "Introduction to spectroscopic ellipsometry", *Spectroscopic Ellipsometry: Principles and Applications*, John Wiley & Sons, 2007

[23] S. Perkowitz, "Cases studies: photoluminescence characterization", *Optical Characterization of Semiconductors*, Academic Press, 1993

[24] L. A. Kazakevich, V. I. Kuznetsov, P. F. Lugakov and A. R. Salmanov, "Influence of transition-metal impurities on accumulation of radiation defects in p-type silicon", *Semiconductors*, vol. 27, no. 3, pp. 268-270, 1993

[25] K. Orgassa, H. W. Schock and J. H. Werner, "Alternative back contact materials for thin film Cu(In,Ga)Se_2 solar cells", *Thin Solid Films*, vol. 431, pp. 387-391, 2003

[26] R. W. Birkmire and E. Eser, "Polycrystalline thin film solar cells: present status and future potential", *Annual Review of Materials Science*, vol. 27, pp. 625-653, 1997

[27] K. Hsiao, J. Liu, H. Hsieh and T. Jiang, "Electrical impact of $MoSe_2$ on CIGS thin-film solar cells", *Physical Chemistry Chemical Physics*, vol. 15, no. 41, pp. 18174-18178, 2013

[28] A. H. Jahagirdar, A. A. Kadam and N. G. Dhere, "Role of i-ZnO in optimizing open circuit voltage of $CIGS_2$ and CIGS thin film solar cells", *Conference Record of the 2006 IEEE 4th World Conference on Photovoltaic Energy Conversion*, vols. 1 and 2, pp. 557-559, 2006

[29] G. Zoppi, N. S. Beattie, J. D. Major, R. W. Miles and I. Forbes, "Electrical, morphological and structural properties of RF magnetron sputtered Mo thin films for application in thin film photovoltaic solar cells", *Journal of Materials Science*, vol. 46, no. 14, pp. 4913-4921, 2011

[30] D. Abou-Rasa, G. Kostorz, D. Bremaud, M. Kälin, F. V. Kurdesau, A. N. Tiwari and M. Döbeli, "Formation and characterisation of $MoSe_2$ for Cu(In,Ga)Se_2 based solar cells", *Thin Solid Films*, vol. 480, pp. 433-438, 2005

[31] M. D. Archbold, "Polycrystalline CdS thin films and their role in CdS/CdTe photovoltaic devices", PhD thesis, Department of Physics, Durham University, 2007, Durham, United Kingdom

[32] J. Major, "CdTe solar cells: growth phenomena and device performance", PhD thesis, Department of Physics, Durham University, 2008, Durham, United Kingdom

[33] A. S. Sedra and K. C. Smith, *Microelectronic Circuits (6th ed.)*, Oxford University Press, 2009

[34] S. Özden, H. Bayhan, A. Dönmez and M. Bayhan, "Measurement and comparison of silicon p-i-n photodiodes with ac impedance at different voltages", *Semiconductors*, vol. 42, no. 7, pp. 834-837, 2008

[35] G. Zoppi, "Studies of CdTe thin films and solar cells grown by MOCVD", PhD thesis, Department of Physics, Durham University, 2005, Durham, United Kingdom

5 Growth and characterization of $CuSbS_2$ and Cu_3BiS_3 films

5.1 Introduction

The subject of this Chapter is the growth and characterization of thin films of $CuSbS_2$ and Cu_3BiS_3 that were identified in Chapter 3 as being promising candidates for solar cell absorber layers. An evaluation of the growth methods and the resulting properties of the films are presented with emphasis on the preparation of phase-pure films having the optical absorption and electrical conductivity characteristics that are desirable for photovoltaic applications – i.e. band gap in the optimal region and p-type conductivity.

As discussed in Chapter 4, two different approaches to the growth of the films were attempted, these being: a) growth of metal "precursor" films followed by post-growth sulfurization (see Section 4.2.2 for the experimental methods) and b) by sputtering of the complete films directly from a single target (see Section 4.2.1).

Both methods were investigated for $CuSbS_2$ while only method (a) was attempted for Cu_3BiS_3. Specific details of the growth and sulfurization conditions are given in Section 4.4.

Sections 5.2 and 5.3 describe the growth outcomes and characterization of $CuSbS_2$ films made using the post-growth sulfurization method including the conditions necessary to prevent the loss of antimony. The successively refined experimental protocols for the formation of the most phase pure $CuSbS_2$ films are described in preliminary experiments (5.2) with a first series of films (5.2 – sample set 'A') and higher quality films (5.3 – sample set 'B'). Both sets of samples A and B were taken forward for the fabrication of devices in Chapter 6. Aspects of the surface chemistry of the films [1, 2] and their doping with impurities – both of which are relevant to device making – are described in Section 5.4. Section 5.5 focuses on films prepared by the one-step sputtering method – i.e. from a single target. In Section 5.6 the properties of films of Cu_3BiS_3 prepared by post-growth sulfurization are reported. Discussion and conclusions are presented in Sections 5.7 and 5.8.

Table 5.1 summarizes the principal categories of samples grown and analysed in this Chapter. Overall a total of ~1000 samples were grown for material characterization.

Material	Preparation method	Sample sequence	Section
$CuSbS_2$	sulfurization of metal layers	preliminary study and series A	5.2
$CuSbS_2$	sulfurization of metal layers	series B (improved process)	5.3
$CuSbS_2$	single-step by rf sputtering	/	5.5
Cu_3BiS_3	sulfurization of metal layers	/	5.6

Table 5.1: Summary of the samples described in the various Sections of Chapter 5.

5.2 Fabrication of $CuSbS_2$ films by the two-step process: initial trial

5.2.1 Initial considerations and composition control

This Section presents a lengthy set of experiments to determine the optimum conditions for the two-stage synthesis of $CuSbS_2$ films by the sulfurization of Cu-Sb metal multilayers. Indeed at the start of the investigation very little was known about the conditions that would be required, i.e. temperatures, composition, times, gas pressure for the sulfurization process and so a very wide process variables was explored by experiment. Hence Section 5.2 presents the results of successively refined range of processing conditions for the preparation of precursor films and their subsequent sulfurization.

A major concern was the control of the elemental composition during heating with sulfur: since Sb has a much higher vapour pressure than Cu [3] it was expected that Sb would be lost from the films and that measures would have to be taken to prevent this. Two approaches were investigated:

a) The use of non-stoichiometric Cu:Sb ratios in the precursor films. It would be expected that the use of excess Sb would compensate for its loss and hence allow stoichiometric films to be formed. This was tested in Section 5.2.2.
b) The use of over-pressure of nitrogen gas during the sulfurization in order to prevent the loss of the volatile Sb. This was evaluated theoretically by Colombara [4]. Ref. 4 provides the equation that may be used to predict the fraction of sulfur F_{eqm} reacting in a given experiment

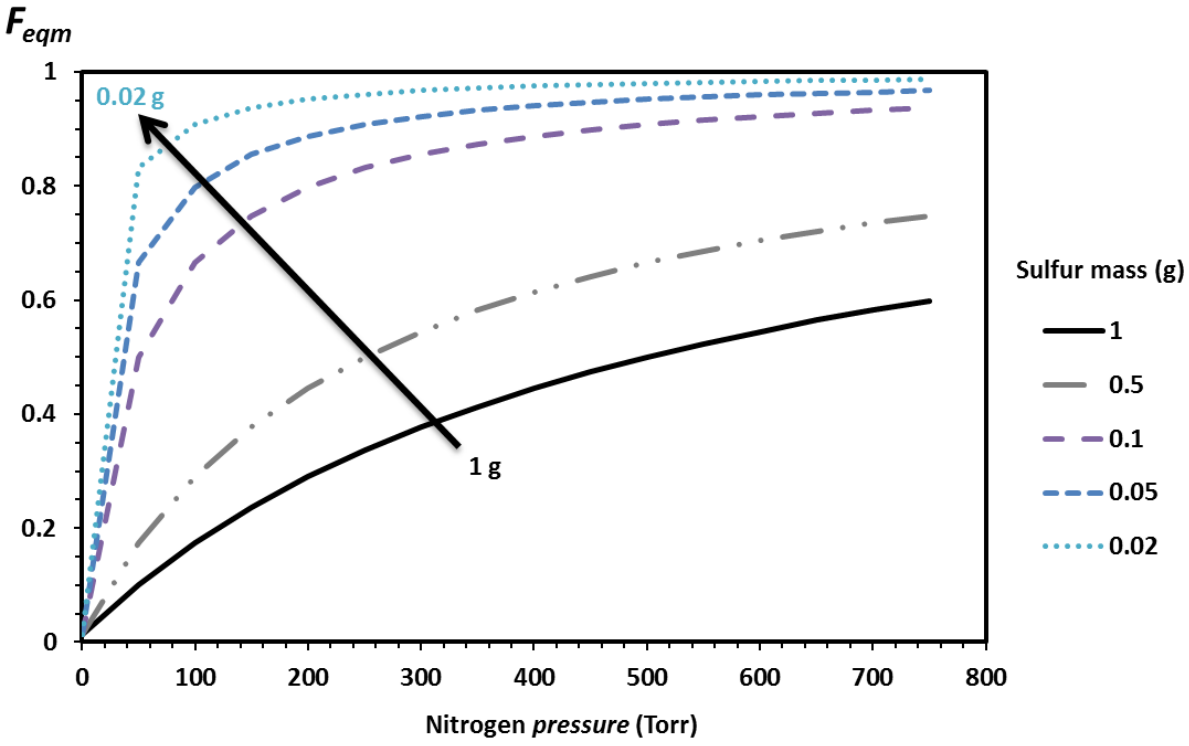

Figure 5.1: Fraction of sulfur molecules (*Feqm*) reacting in the graphite box as function of the nitrogen pressure. *Feqm* was calculated at different sulfur mass values from the equation provided in ref. 4 for the case of the specific sulfurization apparatus deployed in this work.

Figure 5.1 shows the variation of this fraction as function of both the mass of sulfur and the background pressure in the experiment. It is seen that both the use of appropriate amounts of sulfur and – more important – the use of a relatively high background pressure of inert gas encourage full reaction. This method was used in the later sulfurization experiments described in Sections 5.2.3 and 5.3.

5.2.2 Preliminary experiments for two-stage synthesis of $CuSbS_2$

A wide range of precursor designs and sulfurization conditions were explored in these preliminary experiments (a fuller description is given in the author's paper ref. 5).

These included:

a) precursor designs such as multilayers; Cu:Sb ratios in the range 1:9 to 9:1; the substrates comprised SLG and SLG coated with either SnO_2 or TiO_2.

b) sulfurization conditions in the range 200 - 550°C, 1 - 6 hours and pressures in the range 10 mTorr - 100 Torr. The use of higher pressure as indicated by Figure 5.1 was explored in Sections 5.2.3 and 5.3.

It was found that conversion in the lower temperature ranges (i.e. 200 - 300°C) produced films that were largely blue in colour. This is characteristic of CuS and indicates incomplete conversion. The optimum temperature range was 350 - 450°C with ~400°C giving continuous grey films. Higher temperatures yielded discontinuous holey films, presumably due to evaporative losses.

Of the substrates tested, the most adherent and continuous films were obtained on SnO_2-coated glass, e.g. "TEC 8". Use of plain glass gave very poor adhesion, and films grown on it were not usable. Growth on glass coated with TiO_2 gave more pinholes than for SnO_2. The preferred substrate was therefore SnO_2-coated glass.

Variation of the precursor layer stack design from a simple bilayer to a 5 period multistack had an effect on the optical band-edge and XRD, with the latter encouraging both clearer absorption behaviour and more single-phase films. Characterization results were similar to those presented in the next Section for the case of more refined growth parameters and will not repeated here. Hence further experiments mostly used precursors comprising 5 period multistack Cu/Sb layers.

It was found that the Cu:Sb ratio in the precursor had profound effect on the final composition of the sulfurized films. Figure 5.2 shows a graph of the film Cu:Sb ratio plotted as a function of that for the precursor. The precursor compositions were determined from thicknesses while those for the sulfurized films were from SEM/EDX.

Indeed EDX was not used to evaluate the composition of the multistack precursors – i.e. comprising alternate metal layers – due to the inaccuracy of this technique for the composition measurement of inhomogeneous samples (see Section 4.5.1 d).

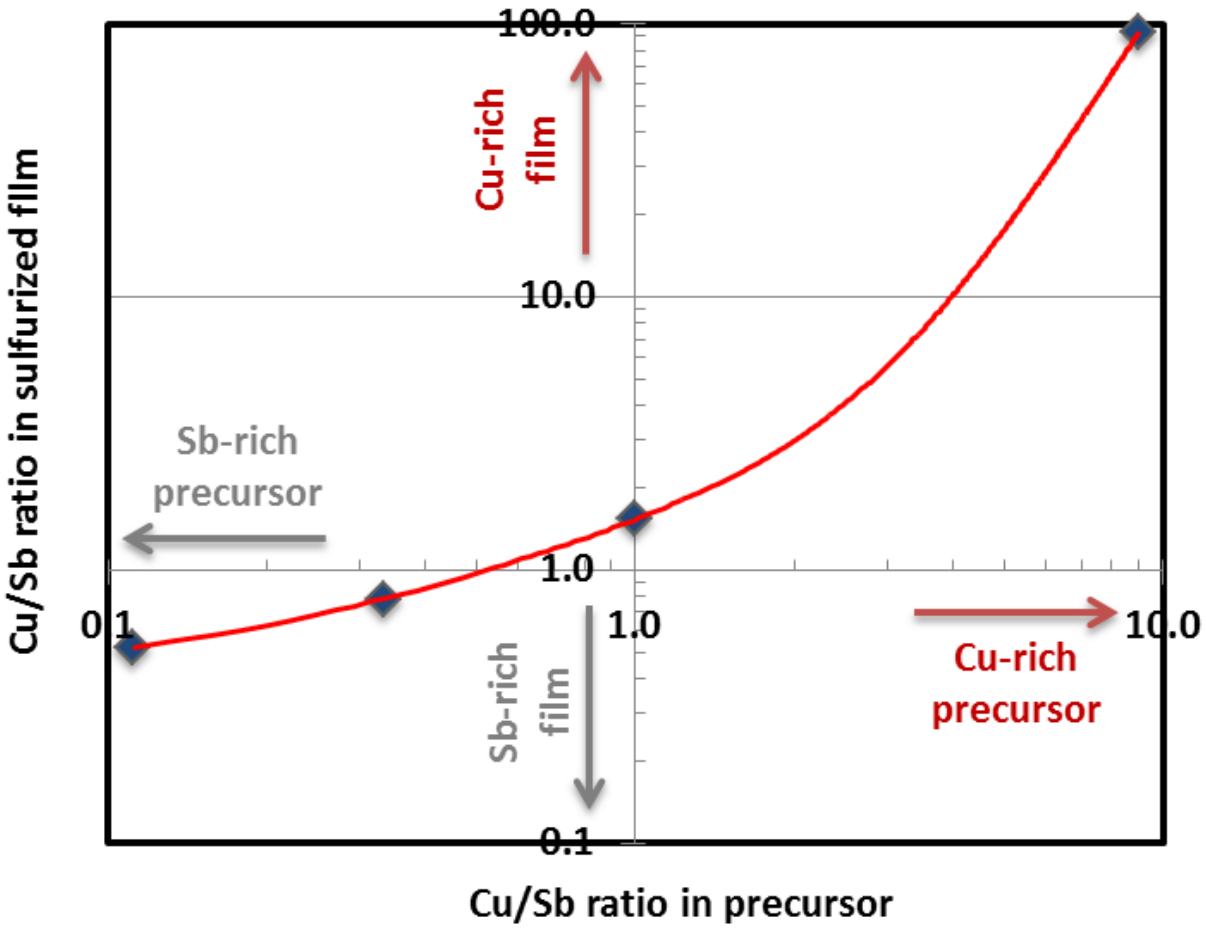

Figure 5.2: Cu/Sb ratio of the sulfurized film as function of Cu/Sb in the precursor stack. The compositions of the sulfurized films were determined by SEM/EDX, while those for the precursor layers were determined from the thicknesses. The EDX measurement error of a single measurement is typically of ±0.1%.

The point at which the curve crosses the *x* axis indicates the Cu:Sb ratio required to generate $CuSbS_2$ films with 1:1 metal stoichiometry. For the conditions used this was ~1:2, i.e. to compensate Sb loss, an excess of Sb metal is required.

5.2.3 Further experiments on the two-stage growth of $CuSbS_2$ films (sample series 'A')

A refined set of fabrication parameters determined from the outputs of the preliminary study were subsequently explored. Higher pressures of nitrogen buffer gas were used in the sulfurization tubes in order to take advantage of the composition control identified Section 5.2.1. Typically reaction at atmospheric pressure was found to be effective. 5-period multilayers were generally used, with a narrow range of compositions (Cu:Sb from 1:1 to

1:3) being explored. Both short annealing times (10 minutes) and low temperatures (< 350°C) led to the formation of blue CuS films. Hence sulfurization experiments were conducted in the range 375 - 450°C with 10 - 80 mg of sulfur for 1 hour. Generally it was found that two-stage heating – i.e. with a low temperature (~100°C) anneal followed by heating at the process temperature in the sulfurization box – yielded films with stronger adhesion than otherwise.

The full characterization of the $CuSbS_2$ films is presented in this Section. At a later stage the growth process was refined, and the characterization of the improved samples is discussed in Section 5.3. The $CuSbS_2$ films analysed in this Section are defined 'series A' samples to distinguish from the optimized samples – i.e. 'series B' samples.

(a) XRD and Raman spectroscopy

The main phase identified by XRD of the samples annealed either at low temperature (< 350°C) or short times generally was CuS. For several sulfurized films it was found that ternary phases coexisted with the target phase $CuSbS_2$, such as Cu_3SbS_4, Cu_3SbS_3 and $Cu_{12}Sb_4S_{13}$.

Samples sulfurized at 400°C for 1 hour with low sulfur mass (< 80 mg) normally were single-phase $CuSbS_2$. As shown in Figure 5.3 most of the peaks of the XRD pattern matched the $CuSbS_2$ phase (JCPDS code 00-44-1417, orthorhombic, *Pbnm*, 62).

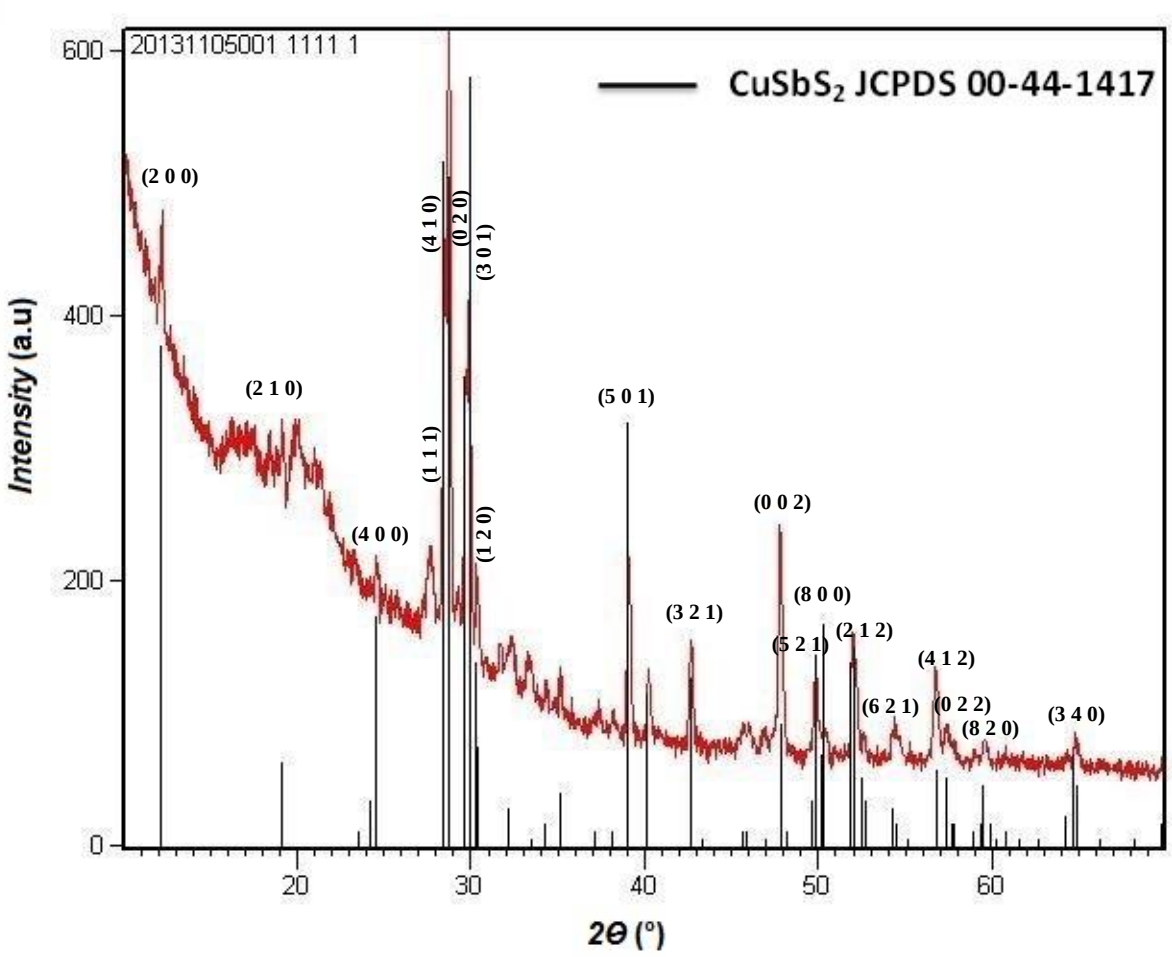
20131105001 1111 1
CuSbS2 JCPDS 00-44-1417
Intensity (a.u)
2θ (°)
(2 0 0)
(2 1 0)
(4 0 0)
(1 1 1)
(4 1 0)
(0 2 0)
(3 0 1)
(1 2 0)
(5 0 1)
(3 2 1)
(0 0 2)
(8 0 0)
(5 2 1)
(2 1 2)
(4 1 2)
(6 2 1)
(0 2 2)
(8 2 0)
(3 4 0)

(a)

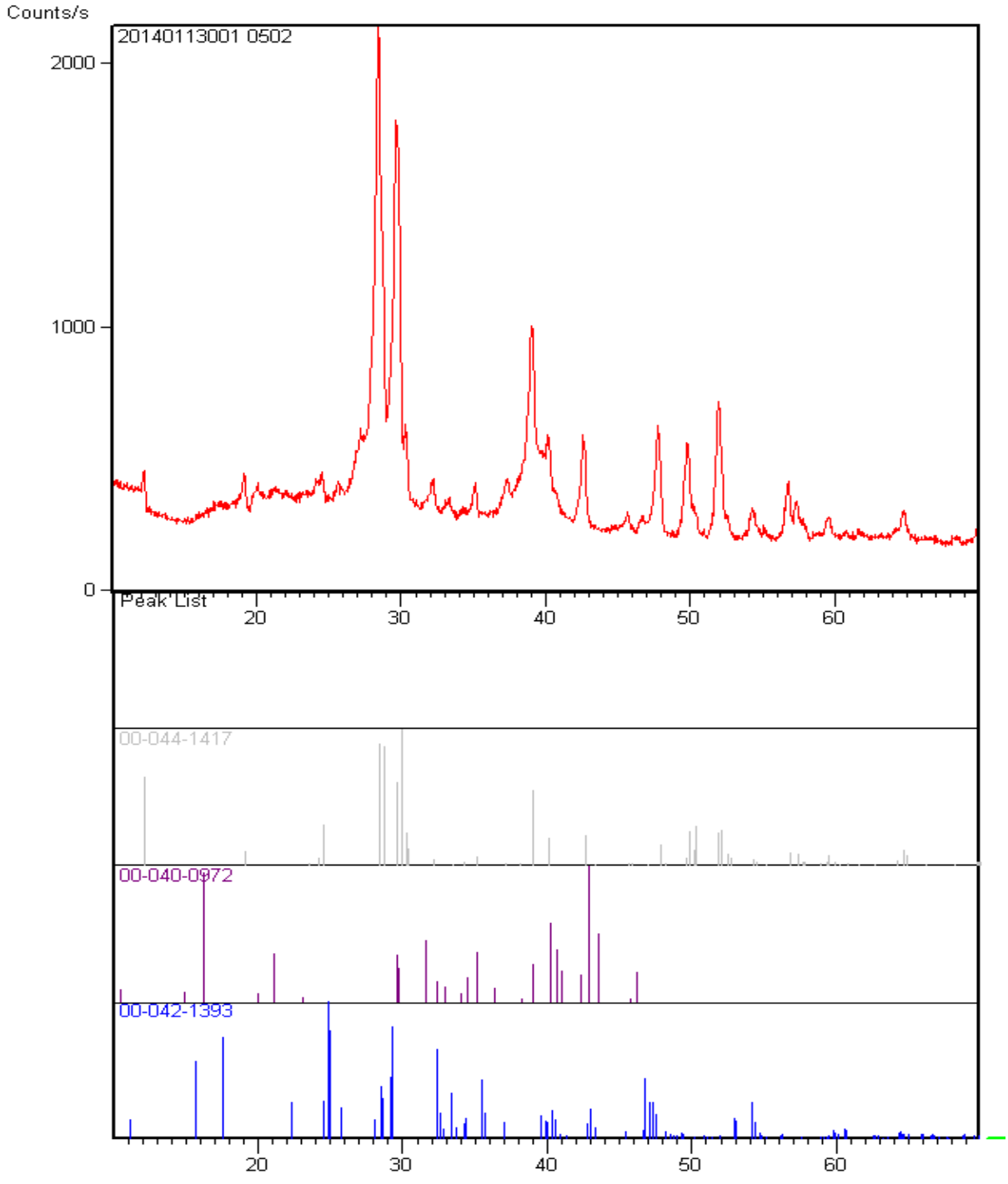

(b)

Figure 5.3: (a) XRD pattern of good quality sample grown from sulfurization at 400°C for 1 hour. The black lines are the reference peaks of the orthorhombic phase $CuSbS_2$ (JCPDS code: 00-044-1417). For comparison in (b) XRD pattern of a sample deposited under non-optimal conditions, where secondary phases coexist with the target phase $CuSbS_2$.

It is recognized that peaks of some possible secondary phases – including Sb_2S_3, $Cu_{12}Sb_4S_{13}$ and Cu_3SbS_4 – are at 2θ angles close those of the $CuSbS_2$ main peaks, and that any amorphous phases cannot be detected by XRD. The possible presence of additional phases may not therefore be excluded by XRD.

Raman spectroscopy is a complementary characterization technique to identify secondary phases [6]. Figure 5.4 shows the Raman spectrum (at RT) of a $CuSbS_2$ sample sulfurized under the optimal conditions. Residues of Sb_2S_3 were found from Raman spectroscopy in the as-grown samples of type A.

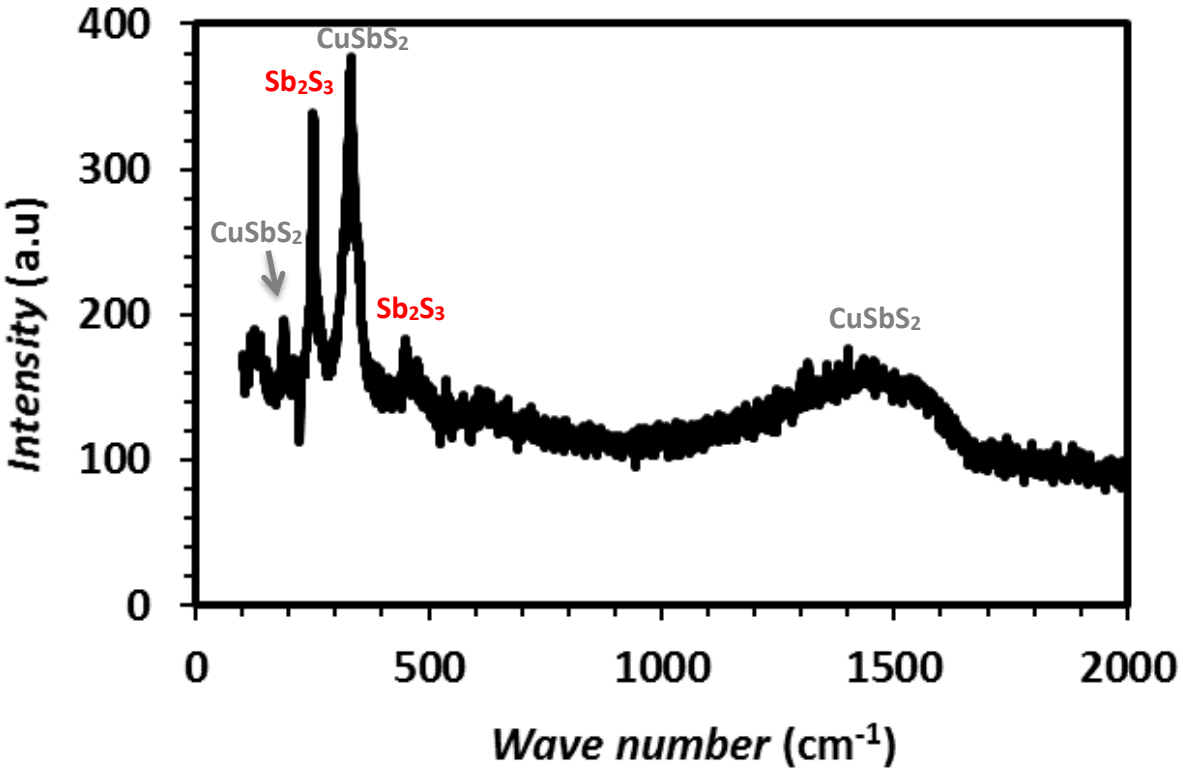

Figure 5.4: Raman spectrum at RT of sample series A deposited by sulfurization at 400°C for 1 hour. Residues of Sb_2S_3 were detected (ref. RRUFFID: R120137 from the rruff online database – see Chapter 4) coexisting with the main phase $CuSbS_2$ (ref. RRUFF ID: R060262.2).

(b) Optical characterization

The transmittance and reflectance spectra of the sulfurized samples were measured by optical spectroscopy. For the samples with incomplete phase conversion the optical analysis indicated metallic behaviour with either no or a very weak band edge in the transmittance spectrum.

According to the optical spectroscopy analysis the $CuSbS_2$ films deposited under the optimal conditions showed semiconductor-like behaviour with high absorption in the visible and a band edge in the optimal range at approximately 800 nm, as shown in Figure 5.5.

The transmittance spectra of the samples series A were generally high in the near infrared and zero in the visible, having edges at ~1000 nm. The reflectance spectra normally exhibited interference peaks in the near infrared and decayed in the visible – this being characteristic for semiconductors.

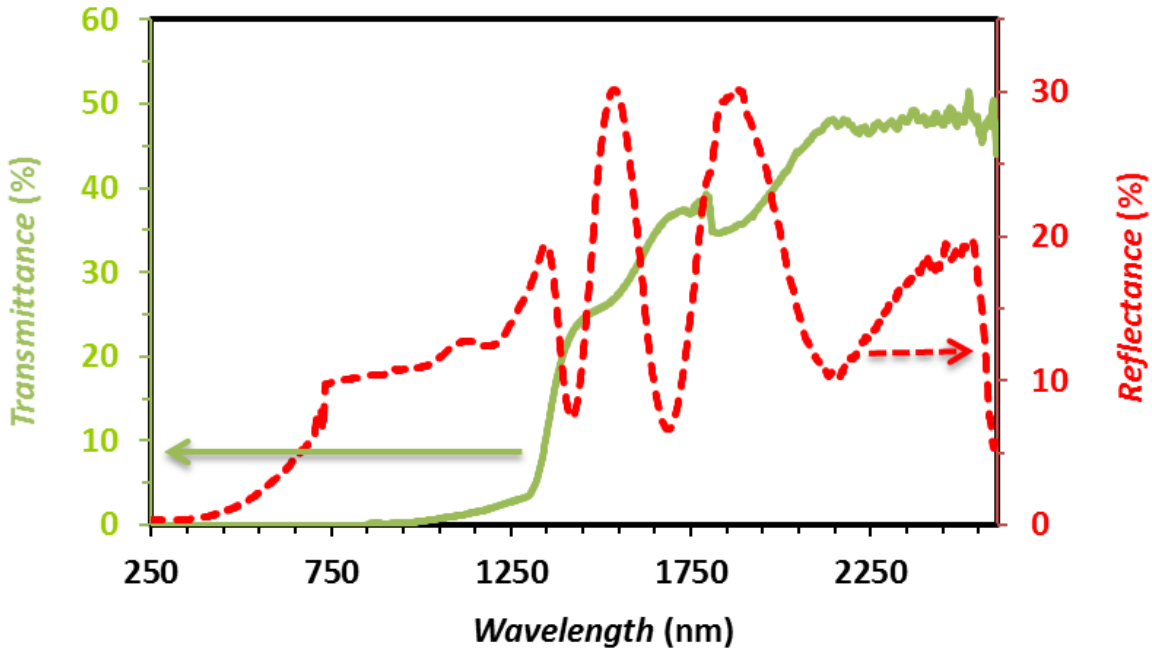

Figure 5.5: Transmittance and reflectance spectra of good quality $CuSbS_2$ sample sulfurized at 400°C for 1 hour with 20 mg of sulfur mass (sample type A). Green line - transmittance; red dashed line - reflectance.

From the transmittance and reflectance spectra the absorption coefficient α was calculated according to Equation 4.3 and is shown as a function of wavelength in Figure 5.6 (a). The band gap position was estimated by the fundamental method described in Section 4.5.2 a – i.e. by plotting α^2 vs. photon energy, as shown in Figure 5.6 (b). From this method the optical band gap was ~1.45 eV. The absorption coefficient in Figure 5.6 (a) is high above the band gap energy and exceeds 10^5 cm^{-1}. From its optical performance, this material may therefore be considered as possible candidate for PV applications.

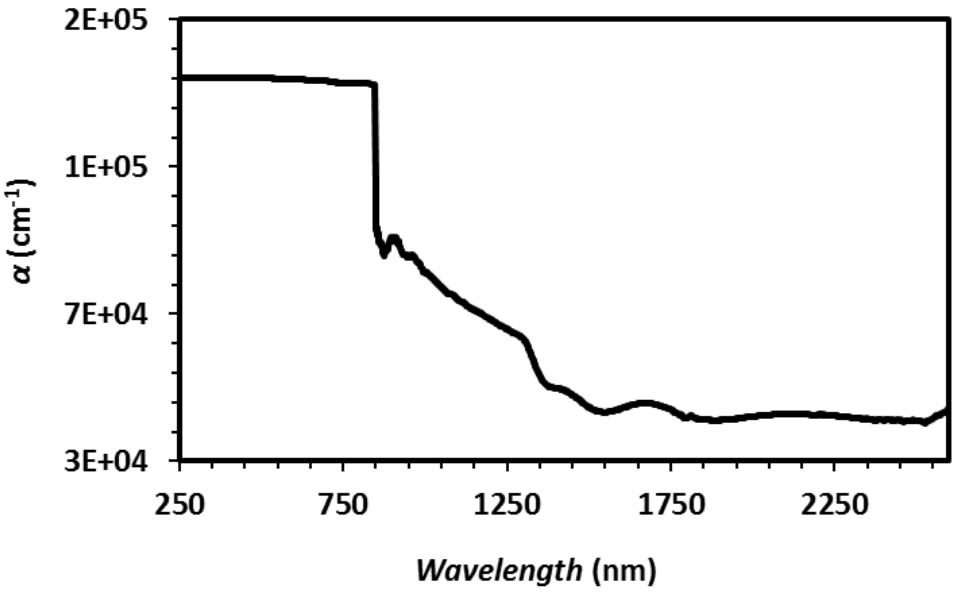

(a)

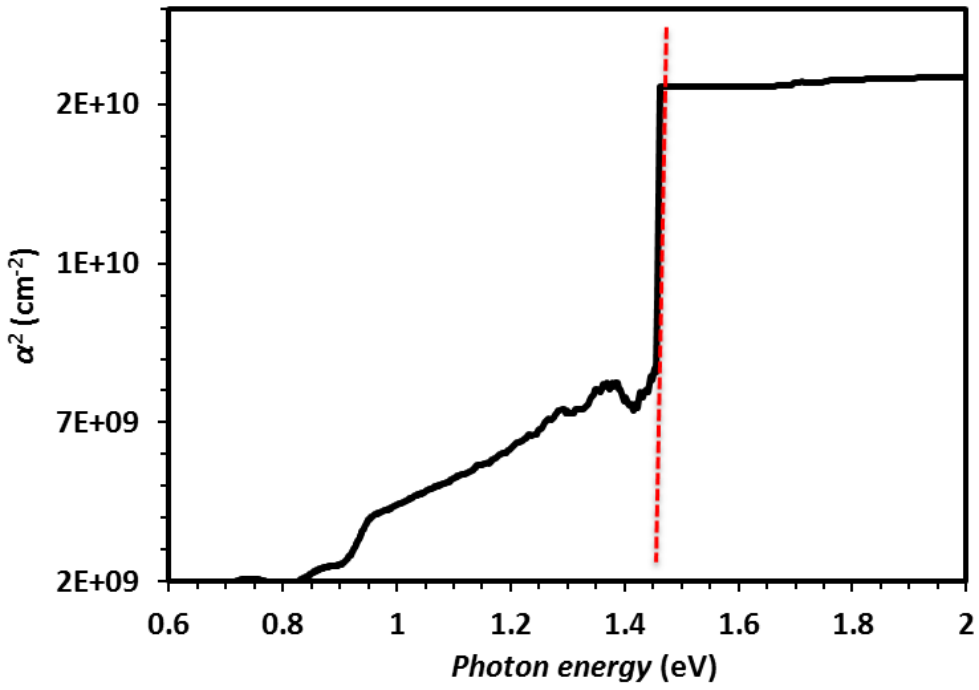

(b)

Figure 5.6: (a) Absorption coefficient α (cm^{-1}) of $CuSbS_2$ sulfurized sample 1.2 μm thick (sample type A) as a function of wavelength and (b) graph for the band gap determination. The absorption coefficient α was calculated from Equation 4.3 from the transmittance and reflectance spectra. The flat patterns on the curves represent the instrumental limit. A band gap of ~1.45 eV was estimated.

(c) FTIR

Further optical characterization was conducted by FTIR analysis at 7 temperatures in the range 3.7 - 300 K. Figure 5.7 shows the absorption coefficient squared (α^2) as function of photon energy determined by FTIR at two different temperatures – i.e. 300 K and 3.7 K. Data for the other temperatures tested fell within these limits and varied systematically, as shown by the arrow in the diagram.

The FTIR analysis on samples of type A confirmed the high absorption coefficient, the band gap of ~ 1.45 eV at RT and strong band tailing from secondary phases or impurities.

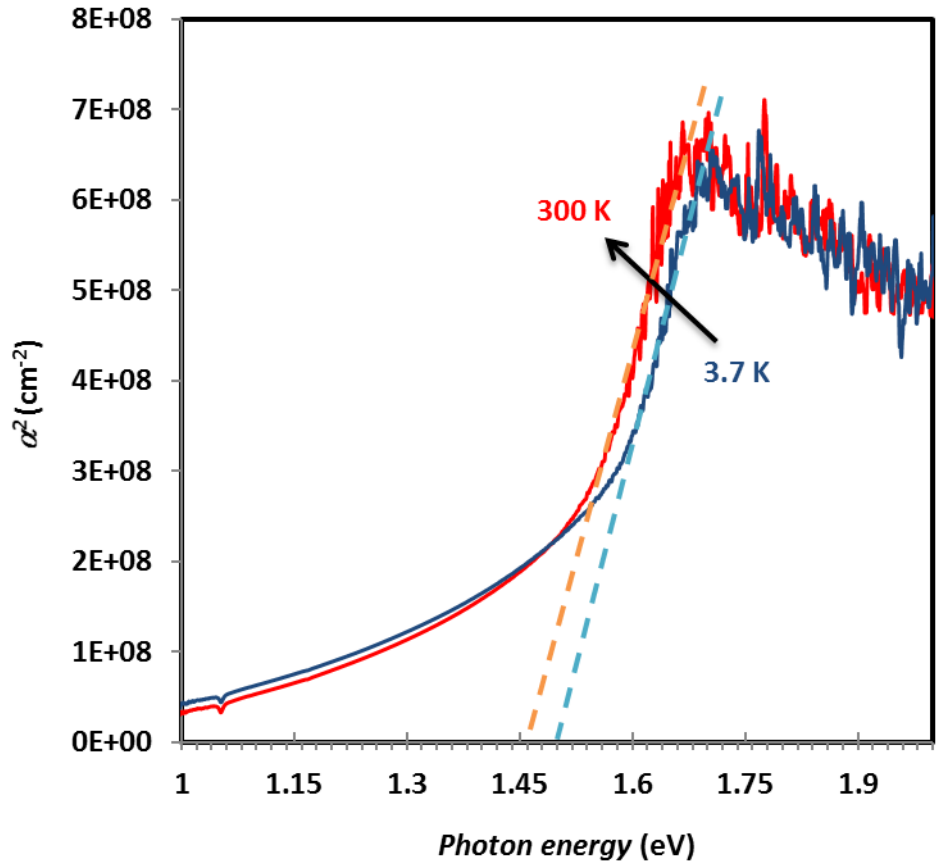

Figure 5.7: Analysis by FTIR at 3.7 K and 300 K of $CuSbS_2$ sulfurized sample grown at 400°C (sample type A).

(d) Electrical characterization

The electrical properties of samples from series A were determined by van der Pauw and Hall measurements.

The as-grown samples typically showed p-type conductivity with carrier concentration of ~10^{17} cm^{-3} and mobility of ~10 cm^2 V^{-1} s^{-1}. The sheet resistance of the films was in the range 10 - 30 kΩ/□. A reproducibility test of the Hall effect analysis was undertaken on samples grown under the same conditions. From Hall effect all the samples analysed were p-type with carrier concentration in the order of 10^{17} cm^{-3} and mobility around 10 cm^2 V^{-1} s^{-1}. The data from 8 samples shown in Table 5.2 demonstrates the consistency and reproducibility of the deposition process.

Sample ID	Conductivity	Resistivity (Ω cm)	Hall coefficient (cm^3 C^{-1})	Mobility (cm^2 V^{-1} s^{-1})	Carrier concentration (cm^{-3})
0611	p-type	3.09 ± 0.01	40.4 ± 0.1	13.1 ± 0.1	$(1.54 \pm 0.01)\cdot10^{17}$
0711	p-type	4.20 ± 0.01	30.8 ± 0.1	7.3 ± 0.1	$(2.03 \pm 0.01)\cdot10^{17}$
1111 4	p-type	2.35 ± 0.01	26.5 ± 0.1	11.3 ± 0.1	$(2.35 \pm 0.01)\cdot10^{17}$
1111 1	p-type	2.47 ± 0.01	32.8 ± 0.1	13.3 ± 0.1	$(1.90 \pm 0.01)\cdot10^{17}$
1111 2	p-type	2.86 ± 0.01	36.3 ± 0.1	12.7 ± 0.1	$(1.72 \pm 0.01)\cdot10^{17}$
1111 3	p-type	4.67 ± 0.01	29.1 ± 0.1	6.2 ± 0.1	$(2.14 \pm 0.01)\cdot10^{17}$
1111 5	p-type	2.10 ± 0.01	25.3 ± 0.1	12.0 ± 0.1	$(2.47 \pm 0.01)\cdot10^{17}$
1111 6	p-type	2.02 ± 0.01	17.8 ± 0.1	8.8 ± 0.1	$(3.51 \pm 0.01)\cdot10^{17}$

Table 5.2: Reproducibility test of the Hall effect parameters of 8 similar sulfurized samples. All the samples were deposited on 1 cm^2 glass by a multistack precursor configuration with Cu:Sb 1:1 and sulfurized at 400°C for 1 hour (sample series A).

Figure 5.8 shows the temperature-dependence trends of the resistivity, carrier concentration and mobility determined from Hall effect measurements. The resistivities of samples decreased logarithmically with temperature while the carrier concentration increased with temperature. The mobility was almost temperature invariant in the range studied.

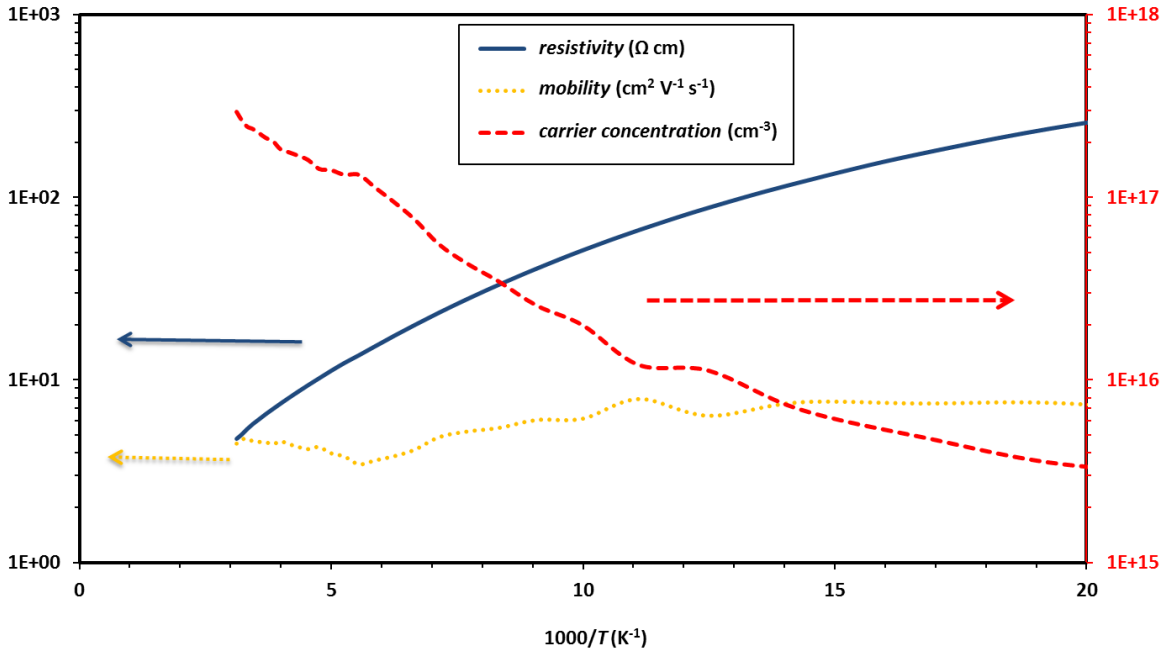

Figure 5.8: Temperature-dependence of the resistivity (Ω cm), carrier concentration (cm^{-3}) and mobility ($cm^2\ V^{-1}\ s^{-1}$) of $CuSbS_2$ sulfurized film at 400°C for 1 hour (sample series A). The analysis was performed from 50 K to RT.

Finally it was seen that relatively small increases in the mass of sulfur used acted to yield more resistive films with more distinct optical band edges – e.g. with 40 mg S_2 the resulting sulfurized sample presented a sheet resistance of ~76 k kΩ/□ and sharper band gap.

(e) SEM/EDX and TEM analyses

A microscope study by SEM/EDX and TEM was undertaken on samples of type A in order to investigate the surface morphology and structure of $CuSbS_2$ sulfurized as shown in Figure 5.9. For the surface analysis several samples were analysed and typically exhibited the morphology shown in Figures 5.9 (a) and (b).

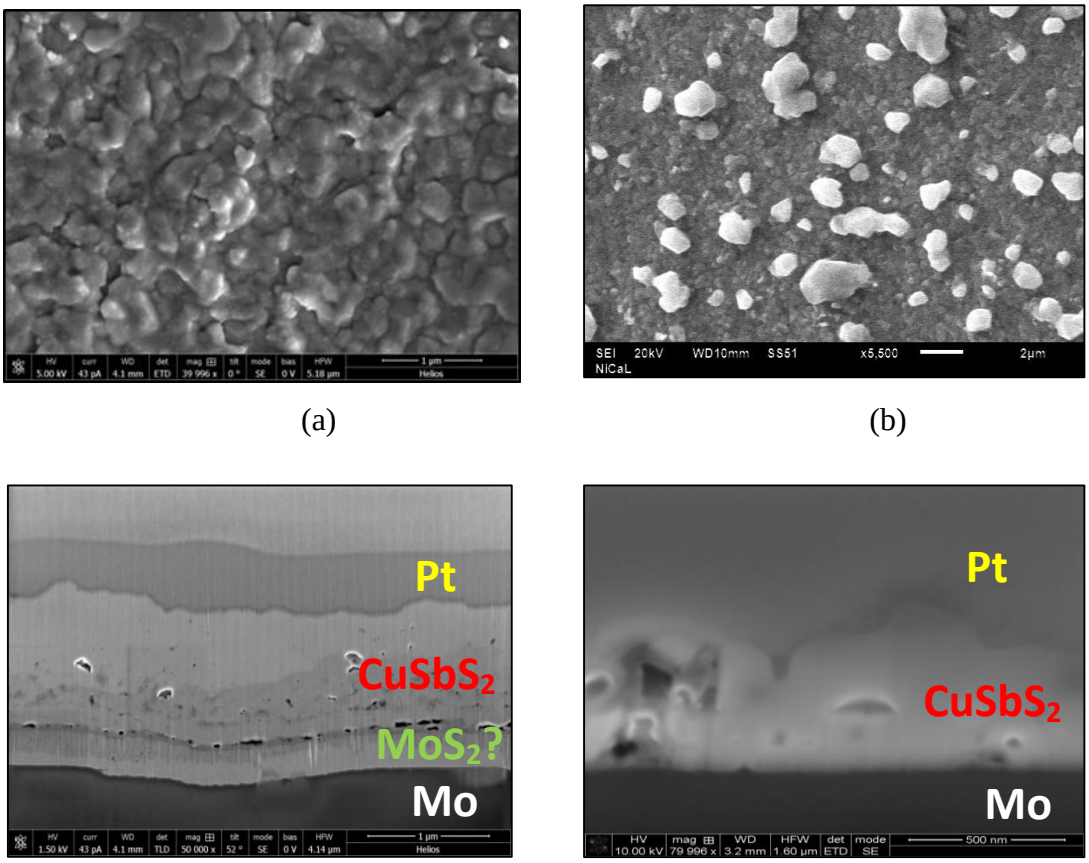

Figure 5.9: Electron microscope images of $CuSbS_2$ films. (a,b) Surface and (c) cross-sectional images from the SEM analysis and (d) TEM image. The samples were grown by sulfurization at 400°C for 1 hour from a multistack precursor configuration with Cu:Sb 1:1 (i.e. sample series A). For the cross-sectional analysis the samples were deposited on Mo-coated glass for better adhesion and then were coated with Pt in the measurement preparation.

Initially the composition of the as-deposited samples was determined by EDX as follows: Cu ~25%; Sb ~22%; S ~53%. Within the accuracy of the EDX measurement this confirmed the expected elemental ratio for $CuSbS_2$.

The surface SEM images in Figures 5.9 (a) and (b) show the presence of impurity particles or residues of secondary phases on the surface of the as-grown samples (e.g. the light particles in (b)). The cross-sectional image in Figure 5.9 (c) shows a compact $CuSbS_2$ film grown on molybdenum-coated glass. The darker spots in the SEM cross-sectional image

are thought to be impurities. The features with bright rings are voids and are typical for films grown by sulfurization. They are also visible in the TEM image in Figure 5.9 (d).

From the cross-sectional SEM image in Figure 5.9 (c) two different shades are visible in the absorber layer and they are potentially associated to two different phases. Furthermore a thin layer of material between the back contact and the absorber layer is discernible. This could be MoS_2 which is regularly seen for sulphides grown on Mo.

(f) Photoluminescence

The photoluminescence analysis was conducted on a few selected samples grown under the optimal conditions. Figure 5.10 shows the PL spectrum of an as-grown sample. It is expected that all the transitions should occur at energies less than or equal to the semiconductor band gap – i.e. $\leq$ 1.45 eV for $CuSbS_2$. However as shown in Figure 5.10 several sharp peaks and a broad background were observed in the PL spectrum at energies greater than this. This confirmed the outcomes from the SEM/EDX analysis in Section 5.2.3 e – i.e. that there are secondary phases in the as-deposited $CuSbS_2$ films and that these have a higher band gap than the main phase.

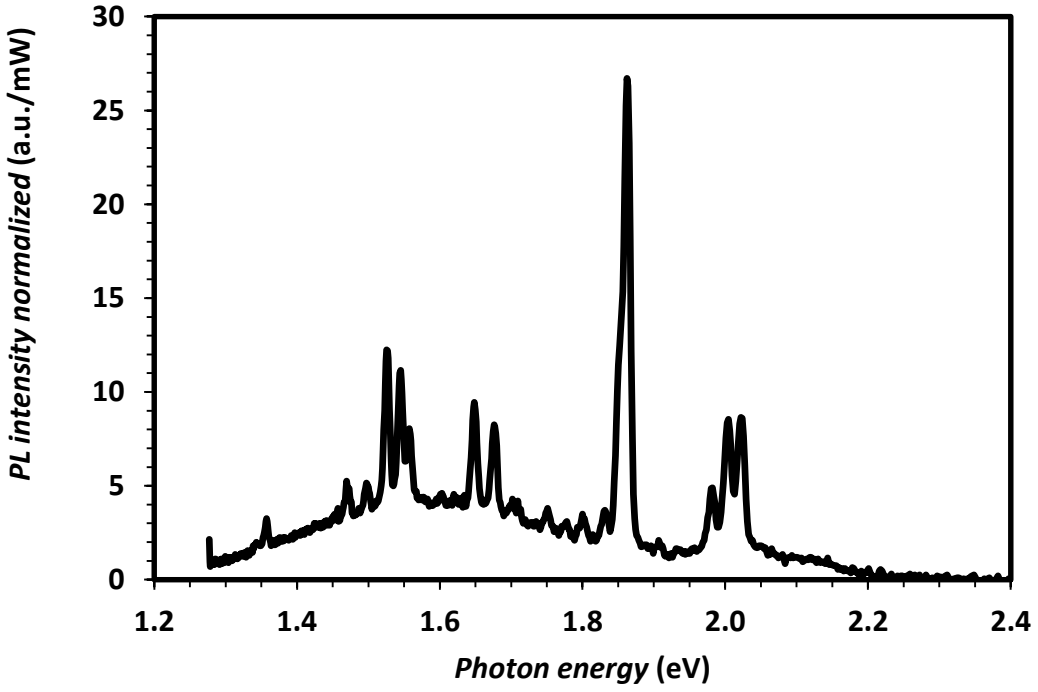

Figure 5.10: Photoluminescence spectrum normalized to the incident power at 3 K of the $CuSbS_2$ sample sulfurized at 400°C. The sample was excited with an argon ion laser (514.5 nm) at 20 mW input power.

5.3 $CuSbS_2$ two-step process B: refined process

The $CuSbS_2$ films analysed in Section 5.2.3 displayed promising characteristics for absorber applications. However the presence of impurities, most likely in the form of secondary phases, indicated that the material quality should ideally be improved for inclusion in devices.

Consequently different strategies were adopted to minimize the incorporation of impurities in the $CuSbS_2$ films. Primarily the control of the sputter deposition of the metal layers and the chamber vacuum were improved. In addition the time between the sputtering of the precursor multistack and the reactive annealing was generally minimized in order to prevent oxidation of the metal stack.

Also it was found experimentally that an improvement in the optical response was possible for samples grown from a precursor stack with Cu:Sb ~4:5 – i.e. slightly antimony-rich. It is reasonable to assume that the Sb-rich precursor compensated the loss of antimony and prevented the formation of secondary phases. Hence all the samples in this Section were grown from a metal multistack with Cu:Sb ≅ 4:5. The sulfurization conditions were kept as described in Section 5.2.3 – i.e. temperature = 400°C, time = 1 hour, N_2 pressure ≅ 750 Torr and sulfur mass ≅ 20 mg.

The characterization of $CuSbS_2$ films grown from this refined process – i.e. sample series B – is now presented with emphasis on the differences with the properties of the samples discussed in Section 5.2.3 – i.e. sample series A.

(a) XRD

The XRD analysis undertaken on several samples was consistent and showed that the main phase of samples of type B was the target phase $CuSbS_2$ – this being consistent with the findings from Section 5.2.3 a on the XRD of samples type A. The XRD patterns shown in Figure 5.11 were similar to the earlier ones shown in Figure 5.3.

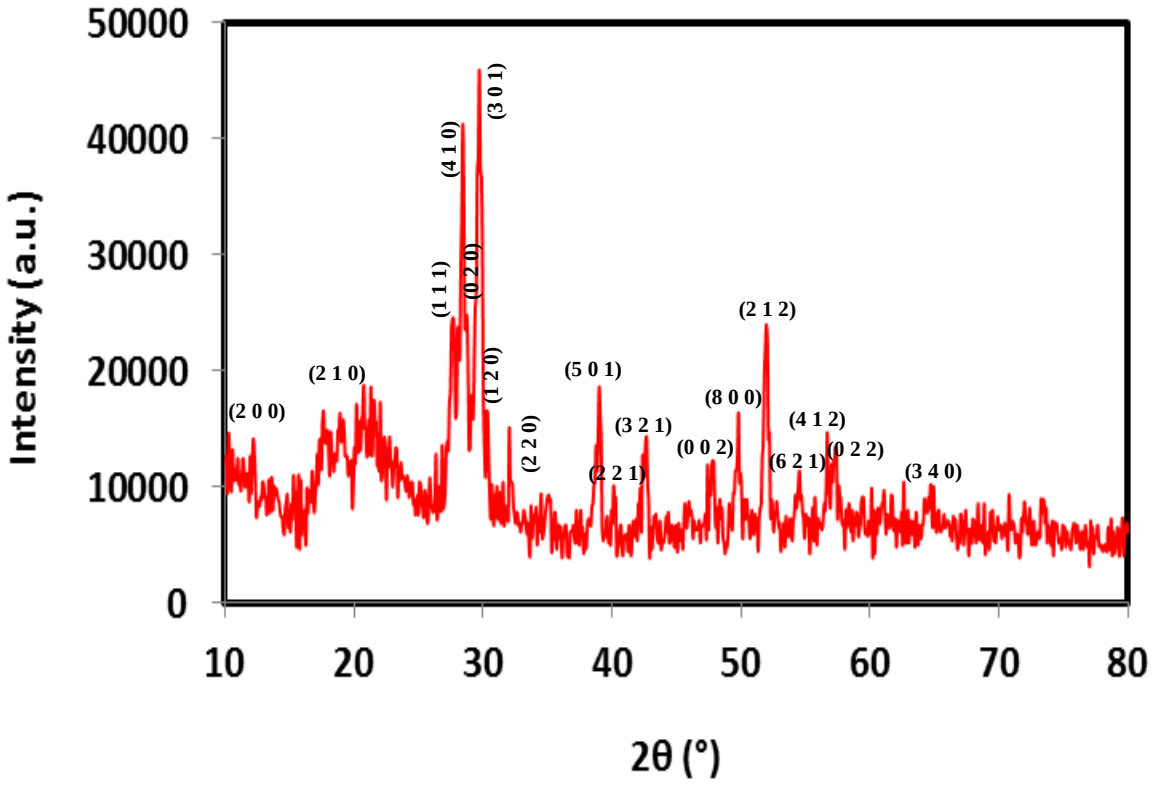

Figure 5.11: XRD on sulfurized sample series B. The pattern was very similar to that measured for sample of type A (see Figure 5.3). The main phase was $CuSbS_2$ (JCPDS 00-44-1417) with preferred orientation (301), rather than the (410) orientation seen for sample series A.

(b) Optical characterization

Typical transmittance and reflectance spectra are shown in Figure 5.12. Figure 5.13 (a) shows the absorption coefficient α of sample series B as function of wavelength. In Figure 5.13 (b) the absorption coefficient squared α^2 is represented as function of the photon energy in order to determine the band gap of the material.

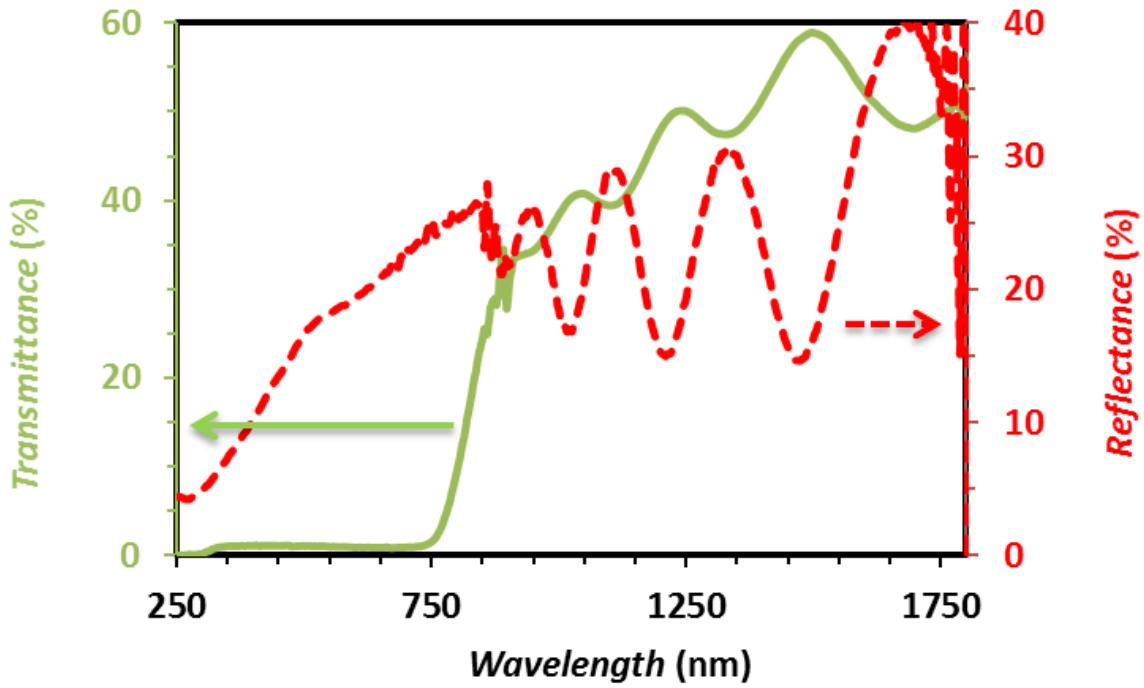

Figure 5.12: Transmittance and reflectance spectra of an optimized 1.2 µm thick $CuSbS_2$ layer grown from the refined process (sample type B). The green line represents the transmittance and the red dashed line represents the reflectance with values reported on the secondary axis. The sample had some pinholes and therefore the transmittance was not exactly zero in the visible.

The samples in series B had a more distinct band edge than for series A, this being at 1.5 eV. Indeed samples from series A exhibited larger band tailing from 0.8 eV to 1.4 eV, as shown in Figure 5.6 (b). The above-gap absorption coefficient of samples from series B was slightly lower (~$7 \cdot 10^4$ compared to ~$1 \cdot 10^5$ cm^{-1}) and significant below-gap absorption still remains. These measurements therefore indicate that while at sensitivity of XRD measurements the samples were phase-pure $CuSbS_2$, some other phases remain.

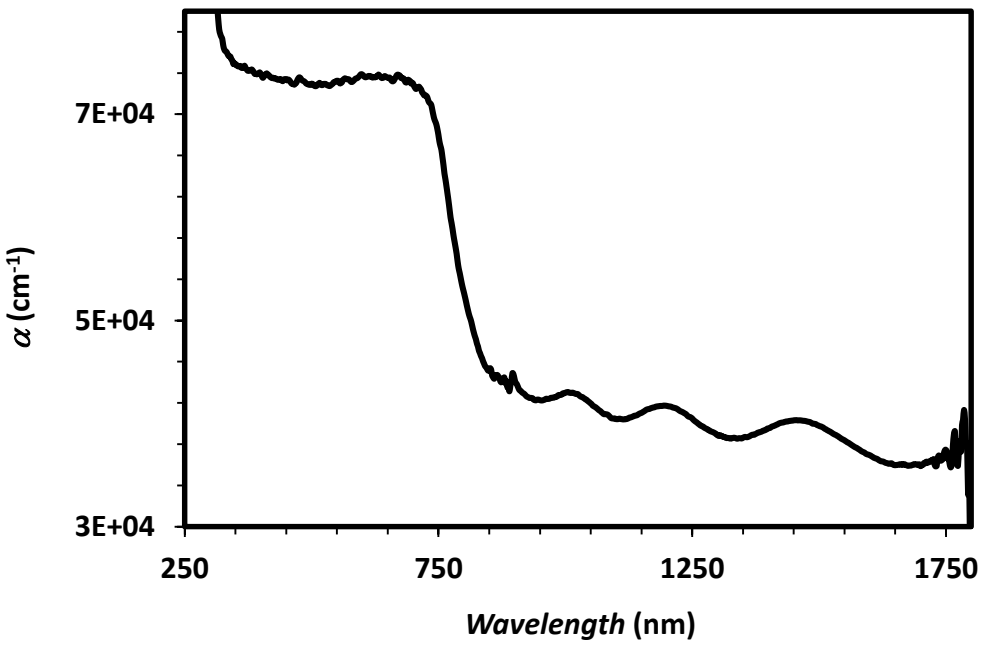

(a)

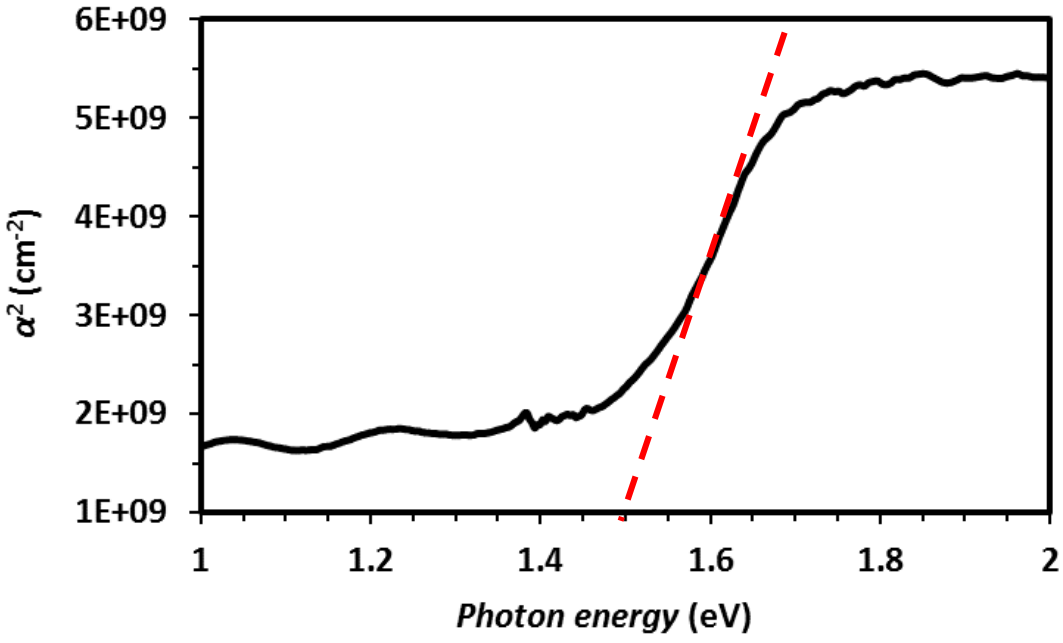

(b)

Figure 5.13: a) Absorption coefficient α (cm^{-1}) of $CuSbS_2$ sulfurized from the refined process (sample type B) with (b) graph for the determination of the band gap. The absorption coefficient α was calculated using Equation 4.3 from the measured transmittance and reflectance. The absorption coefficient squared gave an estimation of the band gap of samples B at 1.5 eV.

(c) Electrical characterization

From the van der Pauw measurements the type B samples typically had sheet resistances in the range 0.5 - 1 MΩ/□ – i.e. approximately one order of magnitude more resistive than samples of type A. For such samples Hall effect measurement was therefore impracticable.

(d) SEM/EDX and XPS analyses

Several samples of type B were analysed by SEM/EDX. The SEM image in Figure 5.14 shows the presence of particles on the surface of a typical as-grown sample of type B.

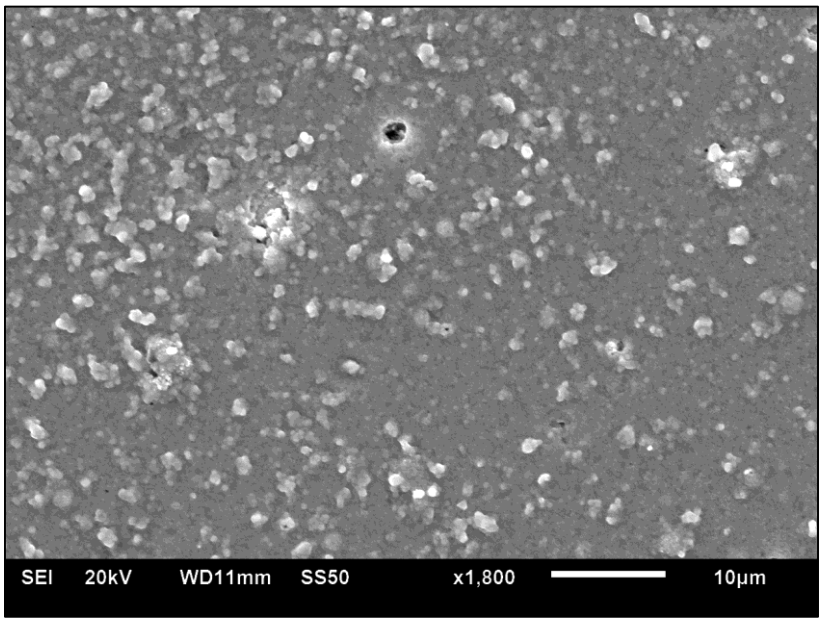

Figure 5.14: SEM surface image of $CuSbS_2$ grown from the refined sulfurization process (sample type B).

XPS analysis showed mixed sulfur and oxygen-bonded states for both Cu and Sb. For example the Sb3d region in Figure 5.15 (a) shows the Sb3d3/2 peak and components associated with the Sb-O and Sb-S environments. As shown in Figure 5.15 (b), the Cu2p3/2 region had a dominant peak at 931.9 eV (due to Cu-S) and a weaker peak at 934.2 eV that was attributed to Cu-O. Overall, the XPS analysis demonstrated the presence of antimony oxides – i.e. Sb_2O_3 – and copper oxides on the surface of as-deposited $CuSbS_2$ films.

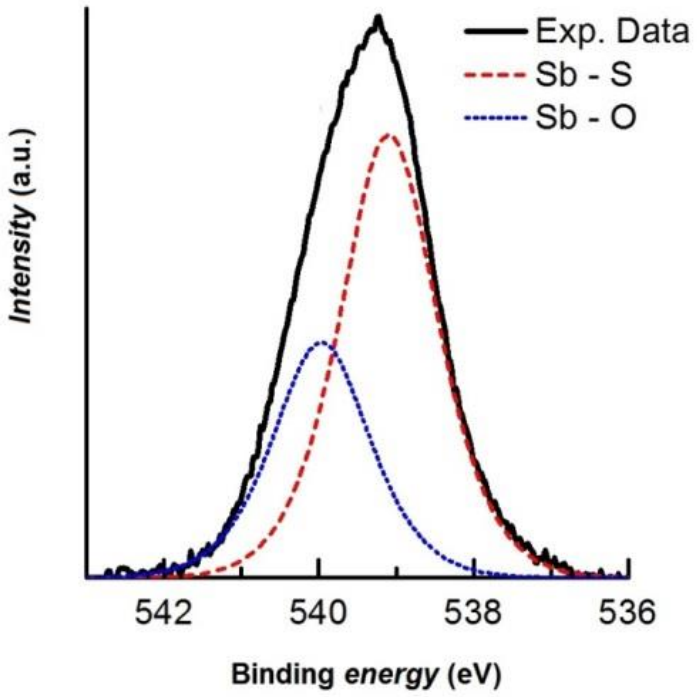

(a)

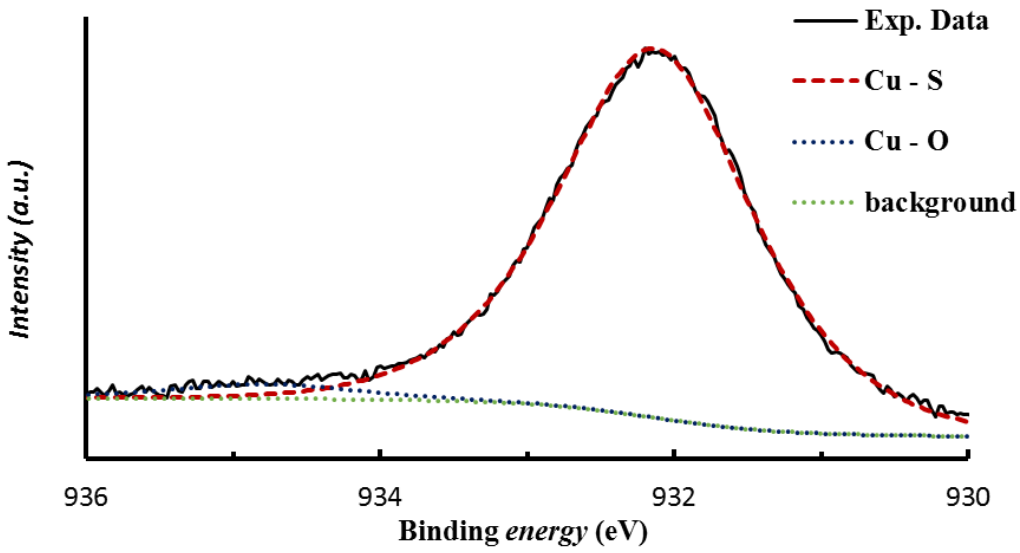

(b)

Figure 5.15: XPS fits on the as-grown $CuSbS_2$ sulfurized sample from the refined process (sample type B). The Sb3d region analysis (a) demonstrated the existence of antimony oxide particles on the surface of the as-grown samples.

(e) Photoluminescence

A few samples of type B grown under the best conditions were analysed by photoluminescence. The PL spectra of type B samples presented peaks above the estimated band gap (~1.5 eV), as shown in Figure 5.16.

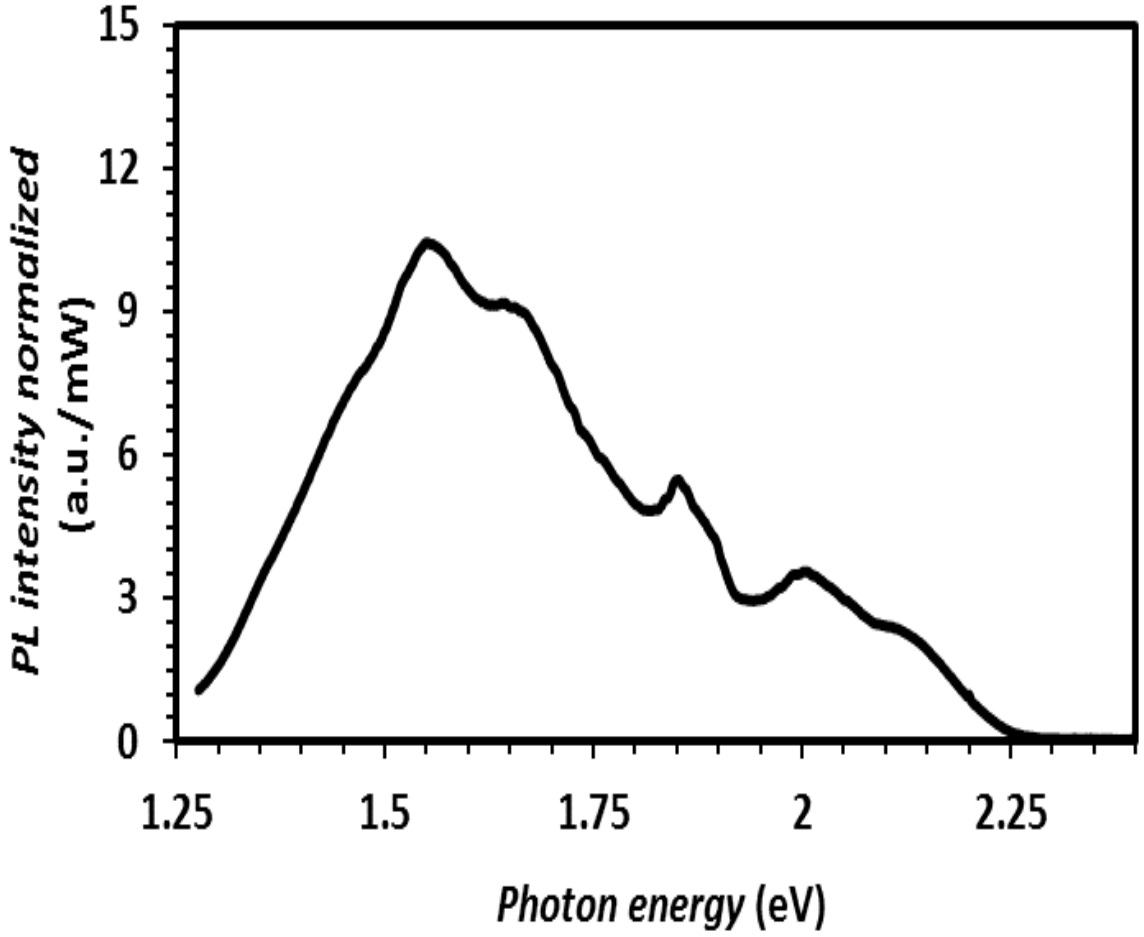

Figure 5.16: Photoluminescence spectrum (3 K) normalized to the incident power of $CuSbS_2$ sulfurized in the refined process (sample type B). For the analysis an argon ion laser was used at maximum input power (397 mW) as the material displayed low PL efficiency.

This indicated the presence of secondary phases in the films. However, the impurity phase PL peaks for sample series B were significantly less pronounced than those for sample series A (see Figure 5.10). Hence the refinement of the growth was effective in reducing – but not in removing – the impurities in the as-grown $CuSbS_2$ films.

In the previous Section the surface impurities were identified with Sb_2O_3 particles by XPS. Antimony trioxide presents band gap of ~3.8 eV [7]. Therefore some peaks above 1.5 eV in Figure 5.16 may be related to the surface phase Sb_2O_3.

5.4 Effects of post-growth treatments on the properties of $CuSbS_2$ sulfurized films

5.4.1 Evaluation of the etching treatments

The analysis conducted in Sections 5.2.3 and 5.3 on both samples from series A and B indicated the presence of residual of secondary phases and oxides – e.g. Sb_2O_3 – on the surface of the as-grown $CuSbS_2$ films. Hence a series of etching treatments were investigated in order to clean the surface of the as-deposited $CuSbS_2$ films. The various methods adopted are listed in Section 4.4.1 c and this Section explores their effects.

(a) KCN etching

The initial experiments with 10% KCN solutions were destructive and led to partially or completely delaminated samples. This issue was avoided by dipping the as-grown samples for very short time (about 10 seconds) in 1% dilute KCN solutions. However the latter etching treatment on samples A was not very effective for removing the surface particles, as shown in Figure 5.17 (a). Etching treatments for 2 minutes with high concentrated 10% KCN were more effective but generally led to micro-cracks and delamination, as seen by SEM analysis (Figure 5.17 (b)).

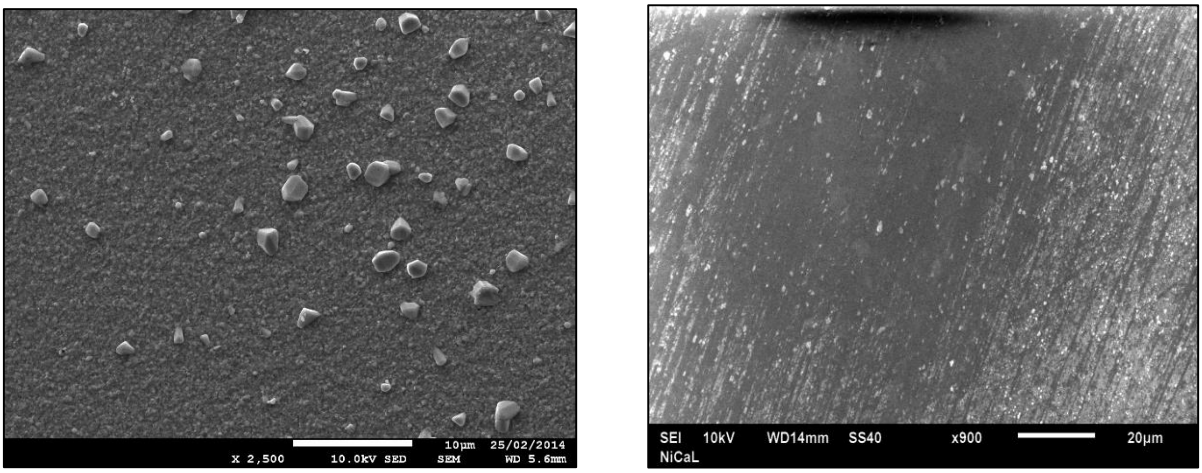

(a) (b)

Figure 5.17: SEM images of the surface morphology of $CuSbS_2$ samples type A (a) after 1% KCN etching treatment for 10 seconds; (b) after 10% KCN etching treatment for 2 minutes.

(b) Etching with HCl : HNO_3, NaOH : H_2O_2 and NH_4OH – from ref. 1

The effects of these alternative etching treatments on the surface properties of the films were evaluated by SEM/EDX. All acted to change the surface morphology as seen by SEM in Figure 5.18, but none of them completely removed the surface particles that are presumed to be secondary phases.

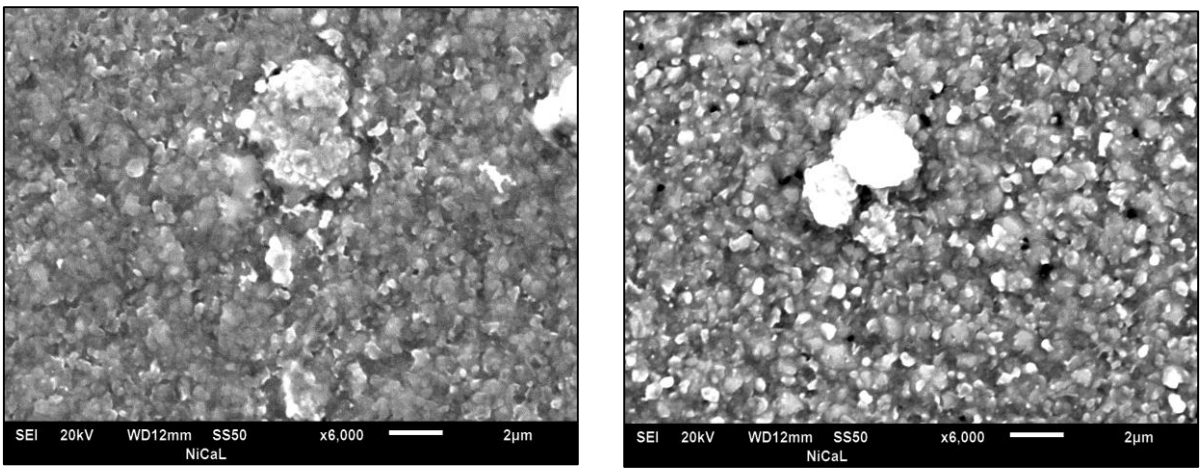

(a) (b)

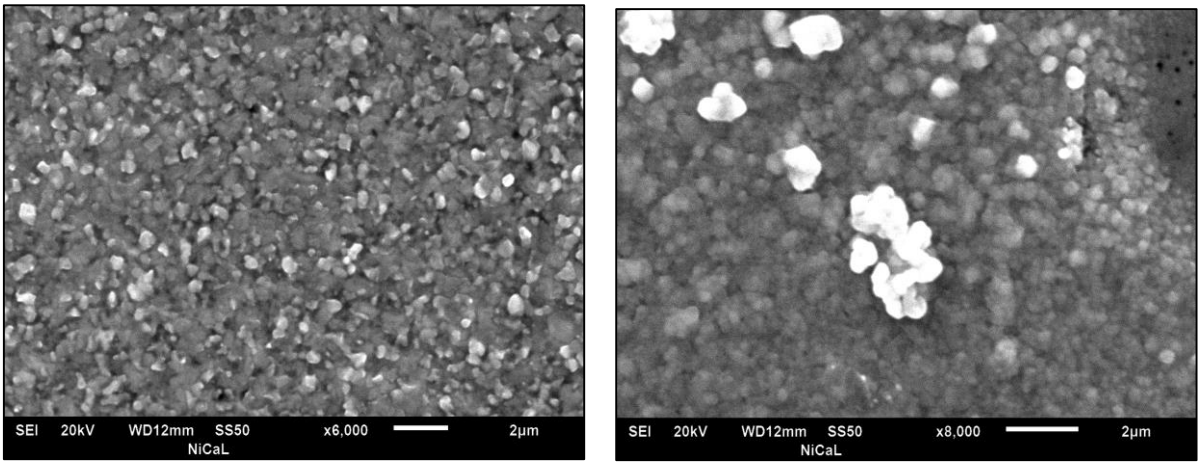

(c) (d)

Figure 5.18: SEM images of the surface morphology of $CuSbS_2$ samples type A, (a) as-grown, and after: (b) HCl : HNO_3 solution for 1 minute ('*etch 1*' introduced in Chapter 4); (c) NaOH : H_2O_2 solution for 1 minute ('*etch 2*'); (d) NH_4OH solution for 5 minutes ('*etch 3*').

(c) Soaking in de-ionized water

From the analysis by SEM the de-ionized water soaking was effective in removing the particles on the surface even for a short immersion time (10 min), as seen in Figure 5.19.

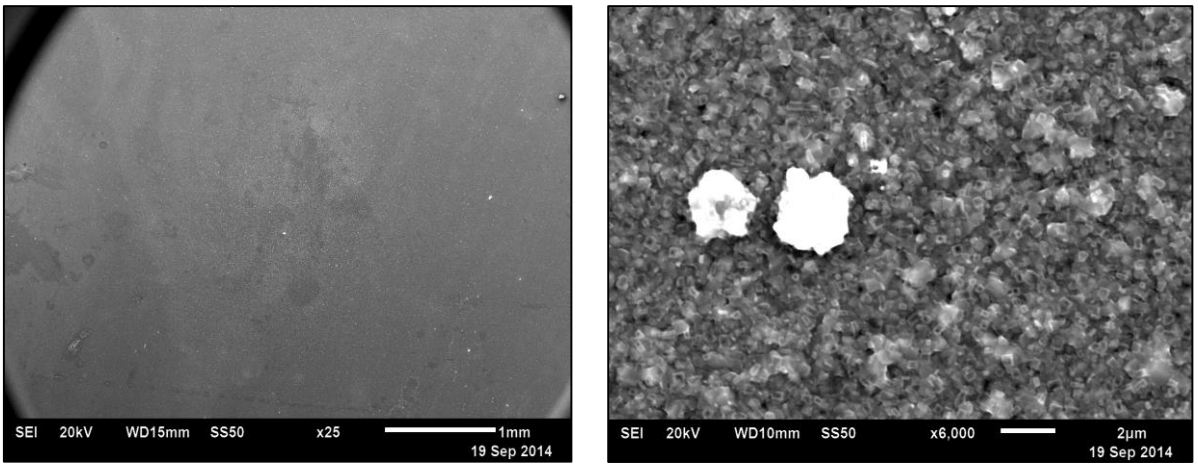

(a) (b)

Figure 5.19: SEM images of the surface morphology of $CuSbS_2$ samples type A after soaking in de-ionized water for 10 minutes. The top view image (a) shows low concentration of oxide particles.

However, an increase of the oxygen content in the films soaked in de-ionized water was detected by EDX – in particular for long time treatments (4 hours) at which 2% (atomic percentage) was detected.

(d) NaOH etching

The samples generally became darker after the etching treatment. The most effective experiment in cleaning the surface was the 20% dilute NaOH solution, as shown in Figure 5.20. From EDX the oxygen content in the etched samples dropped from ~1% to zero.

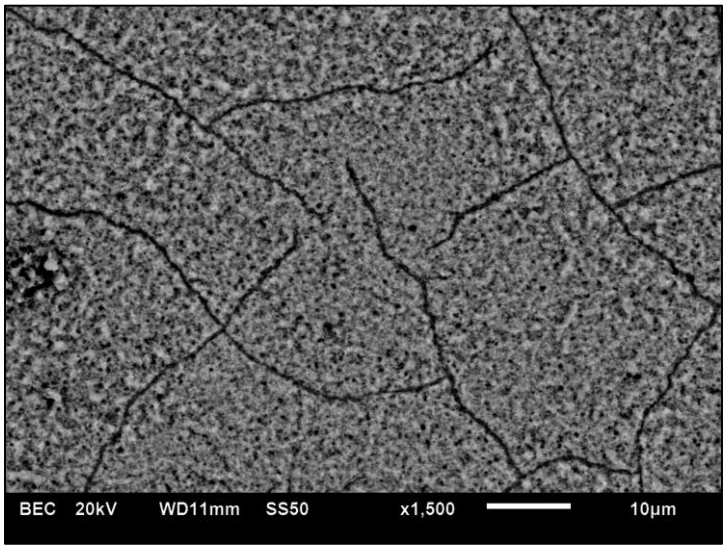

Figure 5.20: Top view SEM image in backscattering mode (BEC) of $CuSbS_2$ sample type B after etching with 20% NaOH for 3 minutes. The 20% solution resulted to be more effective in removing the oxide particles.

(e) Argon ion beam

Argon ion cleaning (with an energy of 500 eV) was undertaken in-situ in the ultra-high vacuum (UHV) analysis apparatus. As shown in Figure 5.21, it was found to be very effective in removing Sb_2O_3, more so than the wet chemical methods.

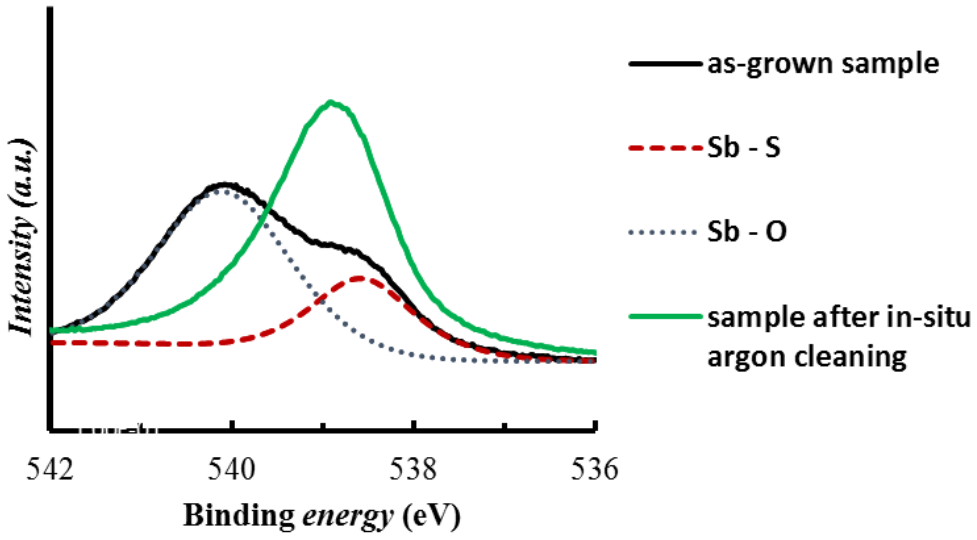

Figure 5.21: Effect of the in-situ cleaning by argon ions. The oxide particles were effectively removed, according to the XPS analysis.

5.4.2 Analysis of the doping treatments

As discussed in Section 5.3 c the sulfurized samples from series B were very resistive, having sheet resistances of the order of 1 MΩ/□. This Section explores the effects of the dopants listed in Section 4.4.1 d on the electrical and optical properties of the sulfurized films.

The doping effects of these elements on the properties of sulfurized $CuSbS_2$ films were first tested on $1cm^2$ samples from series A. From the XRD measurement dopants had no significant effect on the crystal structure of the sulfurized films. All the three elements were effective in increasing the conductivity of the films – in particular indium and zinc. The conductivity of the indium-doped samples increased of one order of magnitude from ~500 to ~7000 Ω^{-1} m^{-1}. However, while NaF did not change the optical transmission, both zinc and indium doping acted to significantly decrease above-gap transmission, as shown in Figure 5.22.

The optimization of the dopant layers and their effects on the device performance are described in Chapter 6.

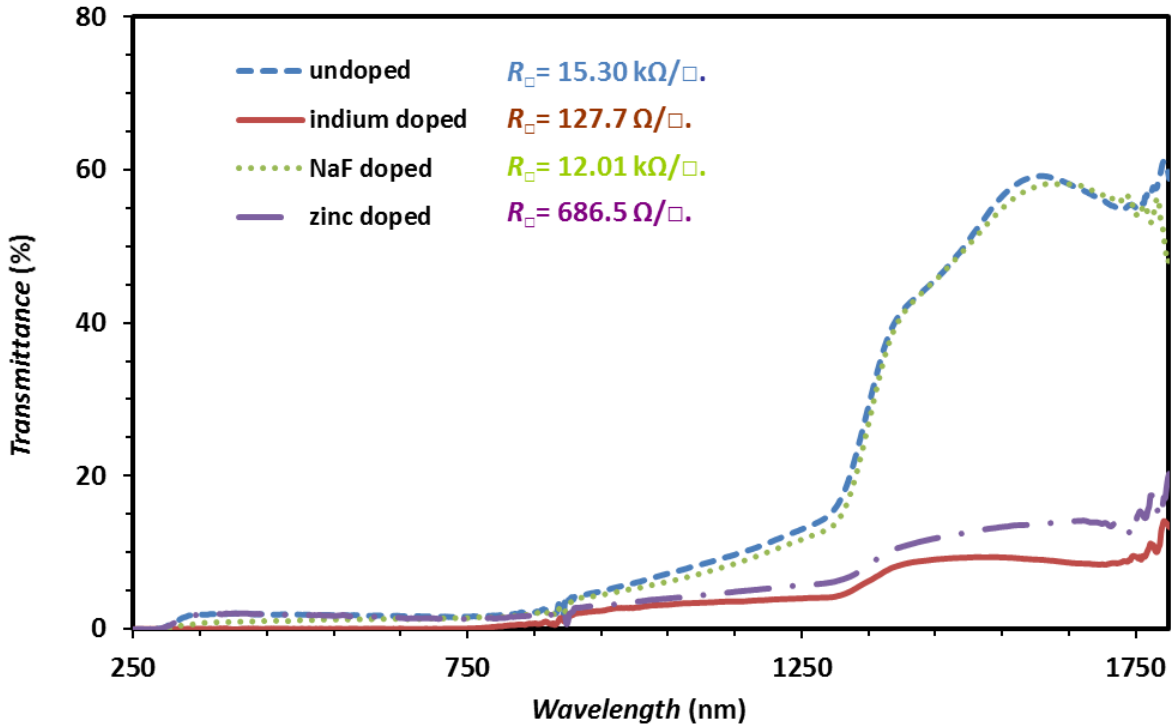

Figure 5.22: Effects of doping by either sodium fluoride (NaF) or indium (In) or zinc (Zn) on the electrical and optical properties of $CuSbS_2$ sulfurized samples from process A. All the elements – in particular indium – increased the conductivity of the $CuSbS_2$ sample. However in this test only NaF did not affect the transmittance of the material.

5.5 Characterization of films grown from the $CuSbS_2$ single target

This Section discusses the properties of films grown by the one-step process described in Section 4.4.2. The samples listed in Table 4.1 were characterized by XRD, optical spectroscopy and the van der Pauw method. The as-deposited samples were generally homogeneous with excellent substrate coverage. A peculiar characteristic of the samples was the change in colour from light yellow for the thinner layers to grey for the thickest films.

5.5.1 Properties of the films deposited by one-step process

(a) XRD

The XRD patterns of samples B, C, D, E and F (see Table 4.1) are reported in Figure 5.23. The thinnest sample A was grown only for thickness calibration and it was not

considered in this analysis. According to the XRD analysis the thinner films – i.e. samples B, C, D and E – were amorphous while the 1 µm thick films (i.e. samples F and G) were crystalline, having a main phase of $CuSbS_2$. Samples F and G exhibited similar XRD patterns and Figure 5.23 shows only that for sample F.

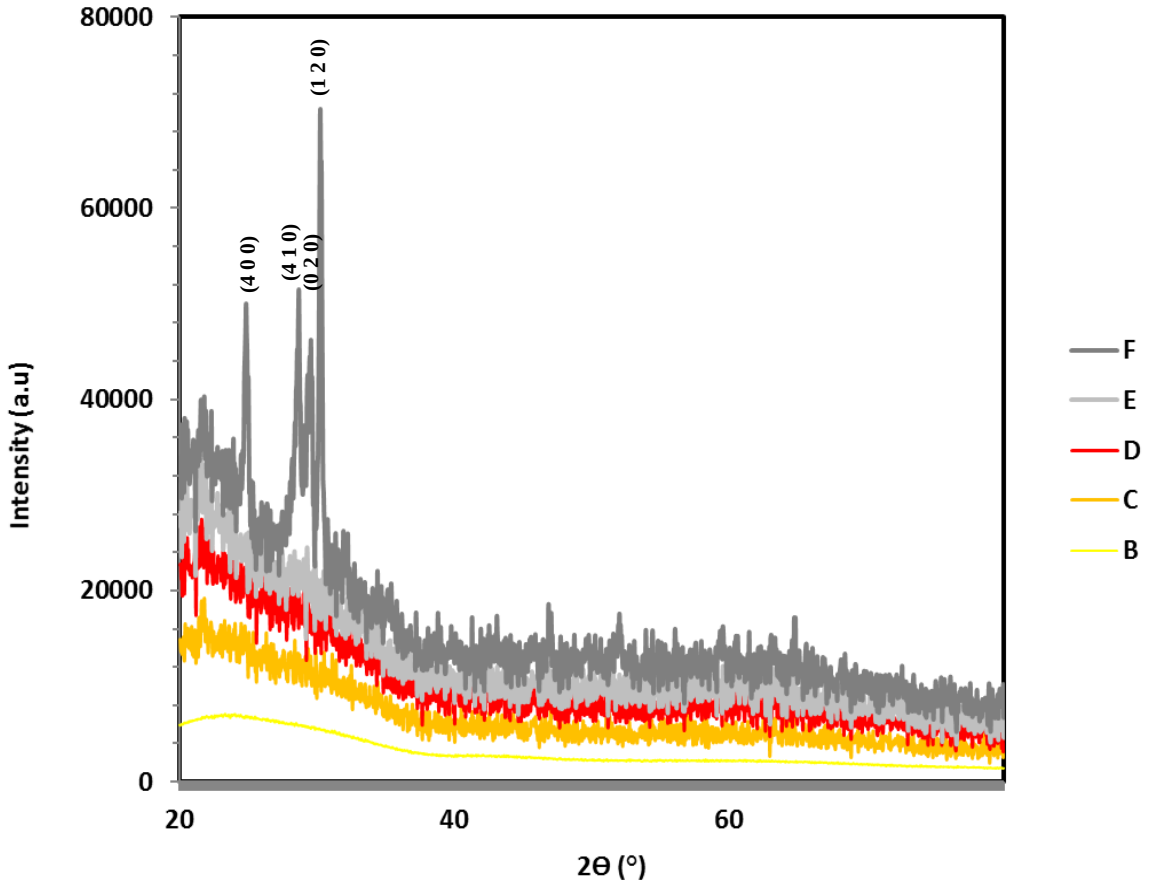

Figure 5.23: XRD patterns of the films listed in Table 4.1 deposited by single step rf sputtering from a $CuSbS_2$ target. Only the thickest film (sample F, 1 µm) was crystalline, the others being amorphous.

(b) Optical characterization

The samples listed in Table 4.1 were characterized by optical spectroscopy. Figure 5.24 shows the transmittance for the various samples.

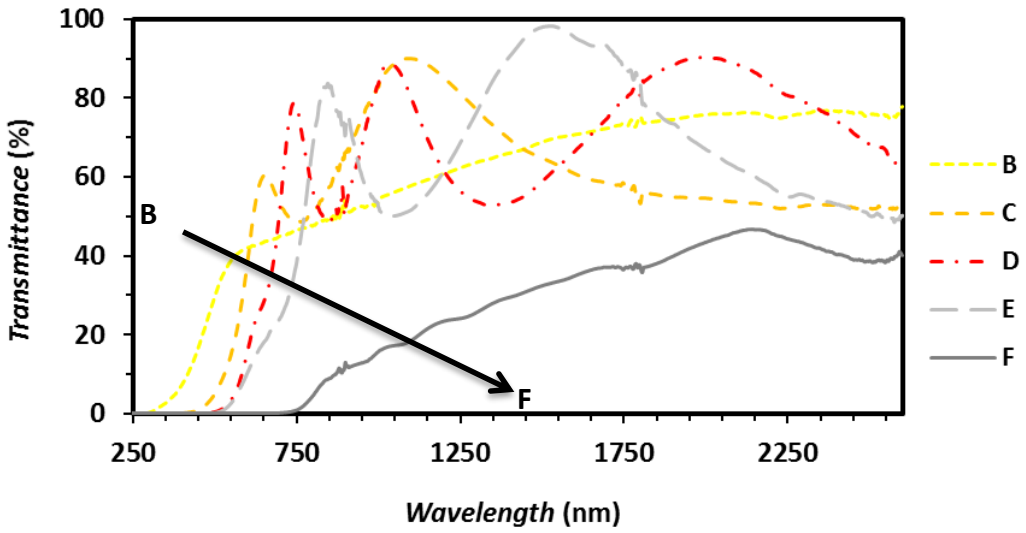

Figure 5.24: Transmittance spectra for the $CuSbS_2$ samples (B-F from Table 4.1) deposited by the one-step process.

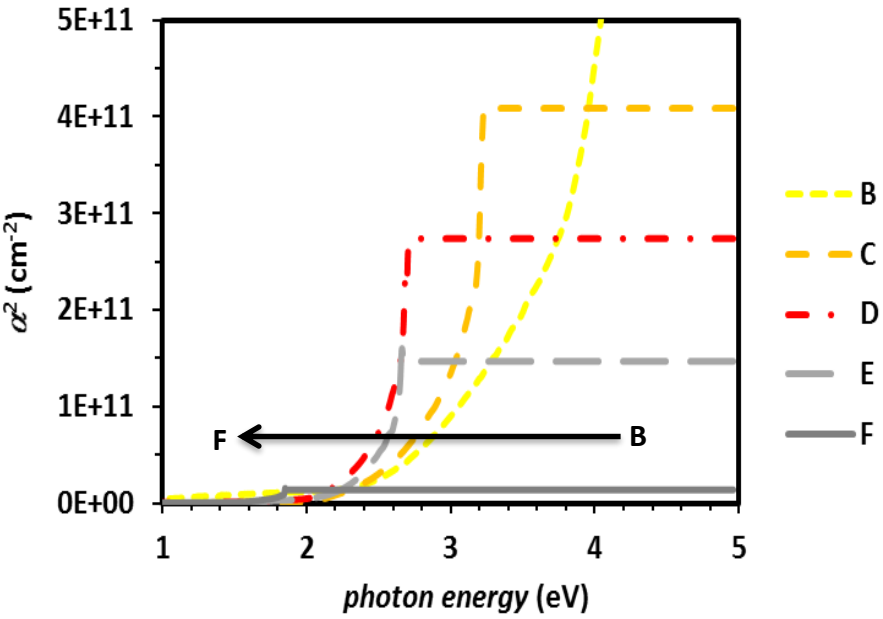

Figure 5.25: Absorption coefficient squared as function of the photon energy for the nominally $CuSbS_2$ samples sputtered from a single source. The flat part of the patterns represents the instrumental limit.

An interesting outcome from the optical characterization was the shift of the band edge with the thickness. This property is highlighted in Figure 5.25 and Figure 5.26 showing respectively the absorption coefficient squared and the absorbance squared of the films as

functions of the photon energy. Figure 5.26 (b) shows the graph of the band gap energy as a function of the film thickness.

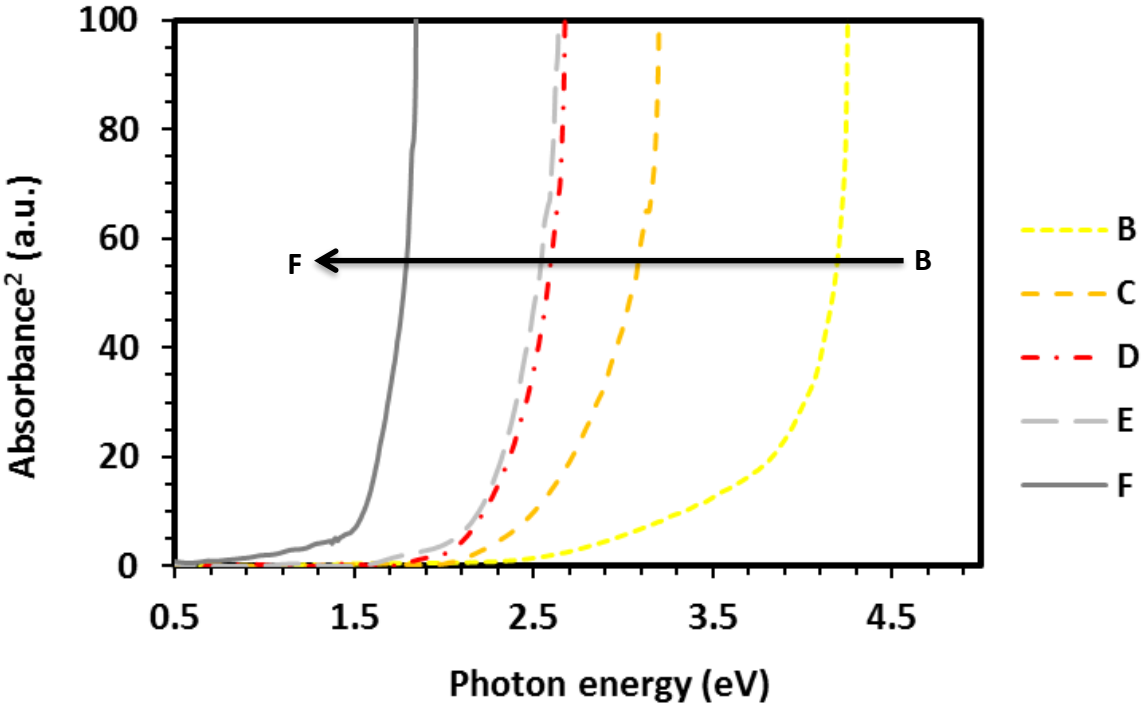

(a)

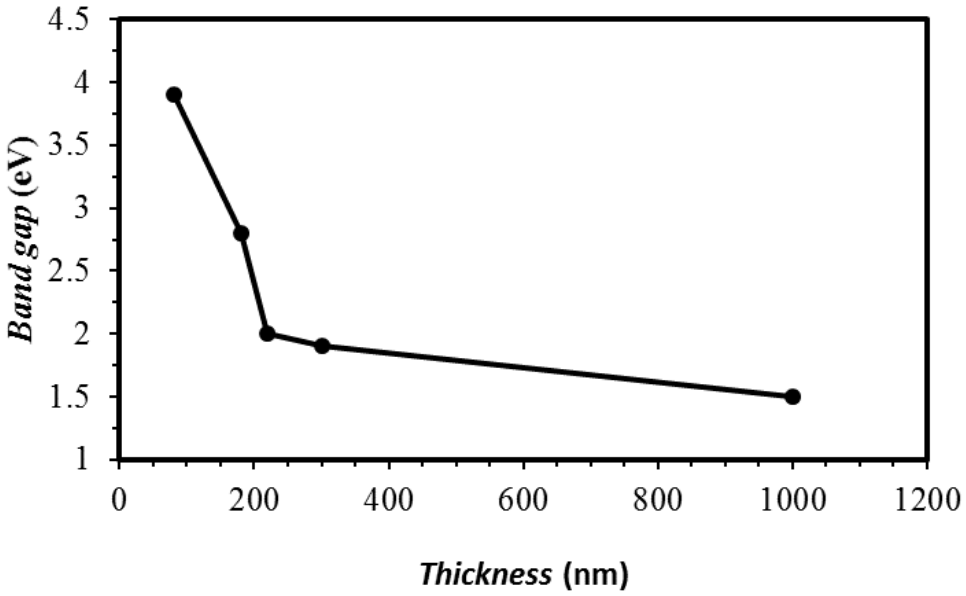

(b)

Figure 5.26: (a) Absorbance squared vs. photon energy for the $CuSbS_2$ samples sputtered from a ternary target. This graph shows an apparent shift in the band gap with increasing thickness of the sputtered films. The interpretation is provided in Section 5.7 [8]. (b) Band gap vs. thickness graph.

Figure 5.27 shows: (a) the absorption coefficient as a function of wavelength and (b) the absorption coefficient squared as a function of the photon energy for the band gap determination of $CuSbS_2$ sample F (1µm thick and sputtered at 400°C).

The 1 µm film sputtered at 400°C exhibited an absorption coefficient of ~$9.5 \cdot 10^4$ cm^{-1} and band gap of ~1.5 eV. Similar results were obtained with film sputtered at RT (sample G). Hence the optical properties of the thicker films grown by the one-step process were very similar to those observed for the sulfurized $CuSbS_2$ films in samples series B described earlier.

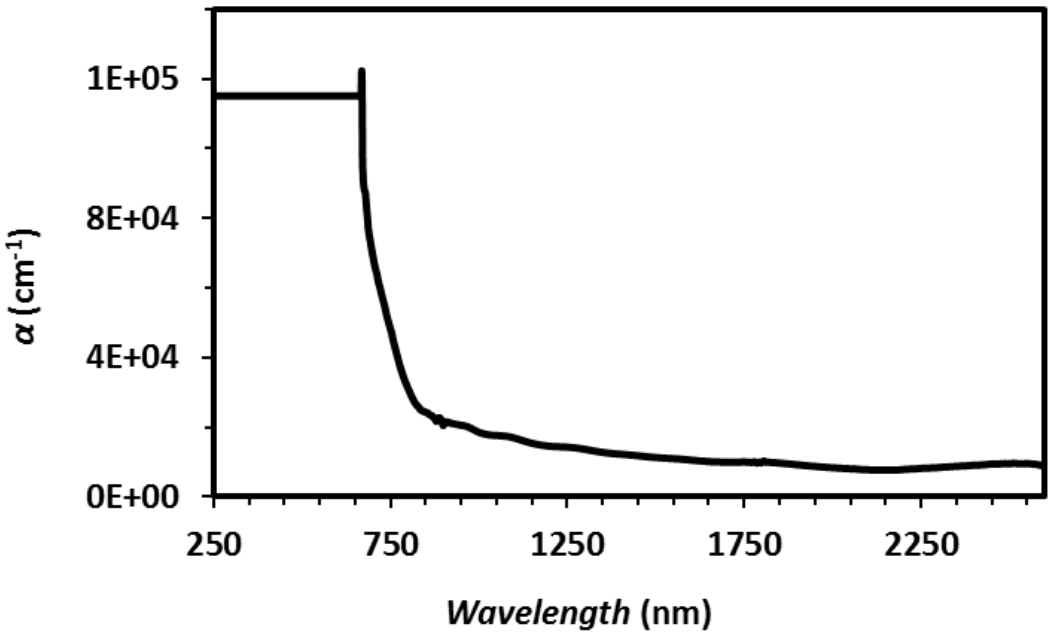

(a)

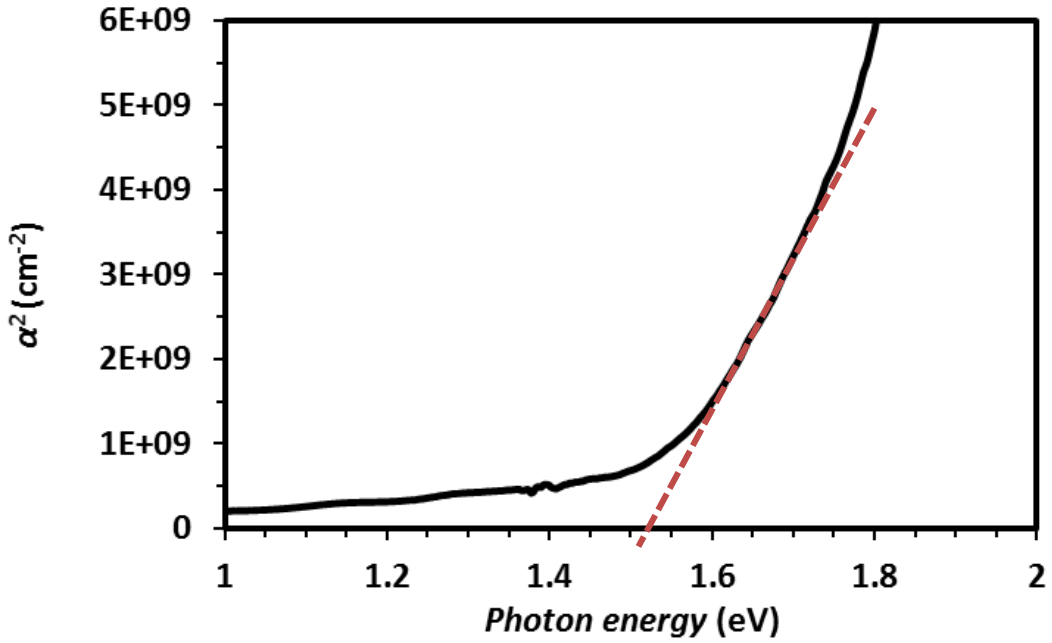

(b)

Figure 5.27: (a) Absorption coefficient and (b) plot for the band gap determination of 1 µm thick $CuSbS_2$ film deposited by rf sputtering from the ternary target (sample F).

(c) Electrical characterization

According to the van der Pauw measurement, sample F had a sheet resistance of 866 kΩ/□. For the thinner layers the sheet resistance was above 1 MΩ/□. The high resistivity of the films could be a constraint for their application in solar cells.

(d) Photoconductivity test

A photoconductivity test was conducted under white light as described in Section 4.5.3 c. A film ~1µm thick grown by rf sputtering on SnO_2-coated glass at RT under the same conditions of sample G was examined.

A drop in the resistance of the sample from about 10 kΩ in dark to about 2 kΩ under light was observed. This experiment proved that there was a photoactive response from the 1 µm thick $CuSbS_2$ film sputtered at room temperature from the single sputtering source.

Therefore the material could be included as absorber layer in a PV device and has the potential benefit of low temperature deposition.

5.5.2 Post-growth treatments of single step sputtered $CuSbS_2$ films

Since the conductivity of the as-grown films was low, post-growth treatments on the as-grown samples both in vacuum, in an oxygen atmosphere and by sulfurization were tested as possible means of achieving higher conductivity material. A limited number of experiments were conducted.

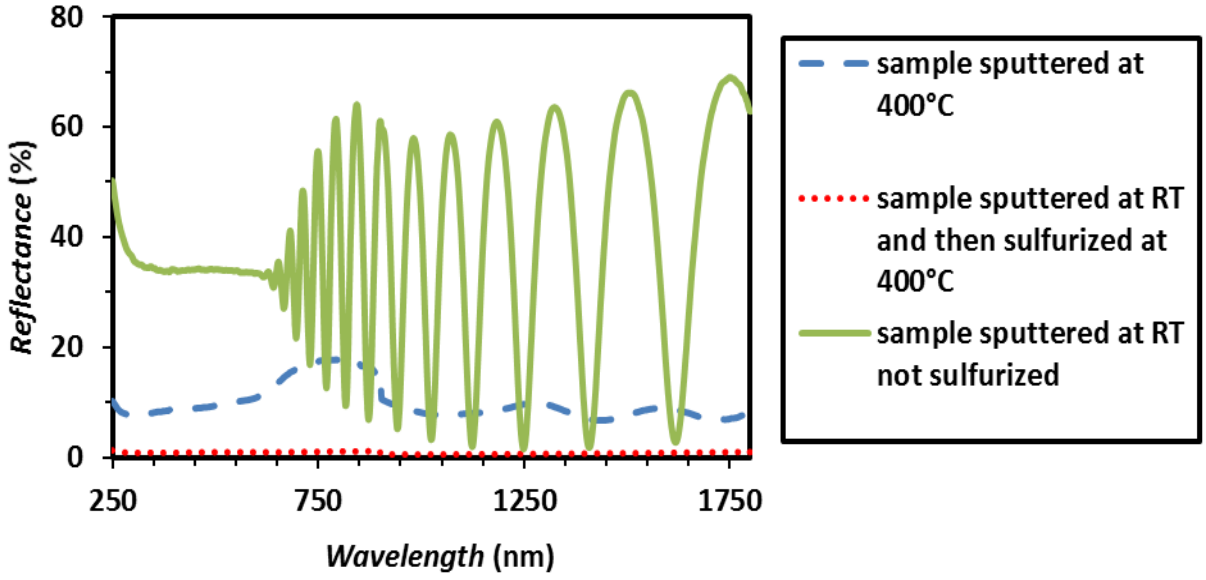

Figure 5.28: Reflectance spectra of some samples deposited on Mo-coated from the $CuSbS_2$ single source. The figure shows the interference fringes typical for semiconductors (from multiply reflected rays) for the as-grown samples. This was particularly evident for the samples sputtered at RT (green solid curve).

However none of these procedures were effective in improving the performance of the films – e.g. the samples annealed in oxygen atmosphere oxidized; annealing in the sputtering chamber produced little change but this did not change the optical and electrical properties of the samples; post-growth sulfurization generally introduced pinholes and deteriorated the optical response of the films. Figure 5.28 shows the reflectance spectra of some samples deposited under the same conditions as samples F and G on molybdenum-

coated glass together with the effect of sulfurizing. The procedure causes the samples to become opaque at all wavelengths.

5.6 Properties of Cu_3BiS_3 sulfurized films

This Section describes the characterization of sulfurized Cu_3BiS_3 films. The experimental method was introduced in Section 4.4. The structural, optical, electrical and surface properties of the films are presented.

(a) XRD

The samples sulfurized at 300°C appeared blue and contained metallic phases – i.e. unreacted metals – and CuS. According to the XRD measurements samples annealed at 350 and 400°C normally presented secondary phases, including $CuBiS_2$, CuS, $Cu_6Bi_4S_9$ and Bi_2S_3. However, as shown in Figure 5.29 Cu_3BiS_3 single-phase films were obtained by sulfurizing the metal stack at 450°C with relatively low sulfur mass and times greater than 20 minutes. Figure 5.29 shows the presence of additional small peaks that are unmatched from the target phase, i.e. these being related to the presence of residues of secondary phases.

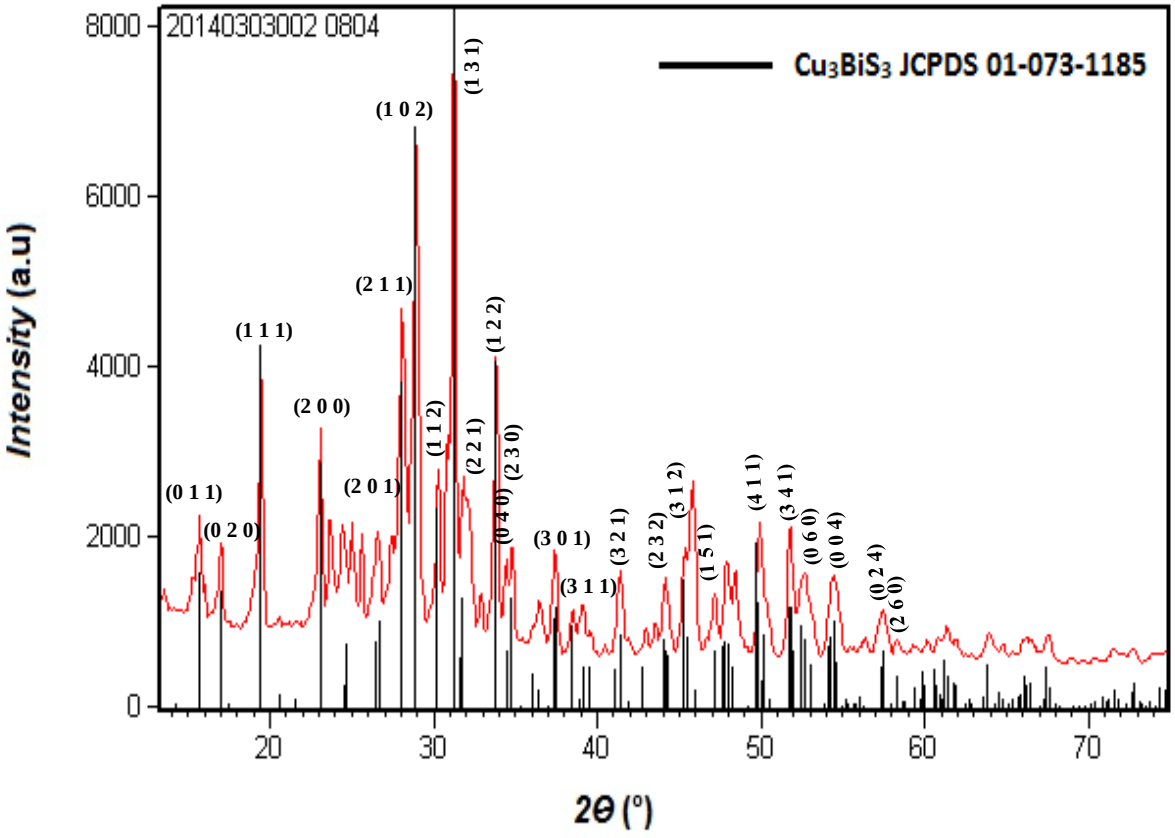

Figure 5.29: XRD pattern of Cu_3BiS_3 sample sulfurized at 450°C. The XRD analysis showed that most of the peaks matched the reference lines of the target phase Cu_3BiS_3 (JCPDS 01-073-1185, orthorhombic, $P2_12_12_1$, 19). The unmatched peaks are related to residues of secondary phases.

(b) Optical characterization

The best optical responses were generally observed in samples sulfurized for times greater than 20 minutes and with low sulfur content annealed at temperature between 350°C and 450°C. As shown in Figure 5.30, samples with an improved optical response were fabricated from Bi-rich precursor layers (Cu:Bi ~14:5). These samples exhibited absorption coefficients of ~$9 \cdot 10^4$ cm^{-1} and band gaps of ~1.4 eV.

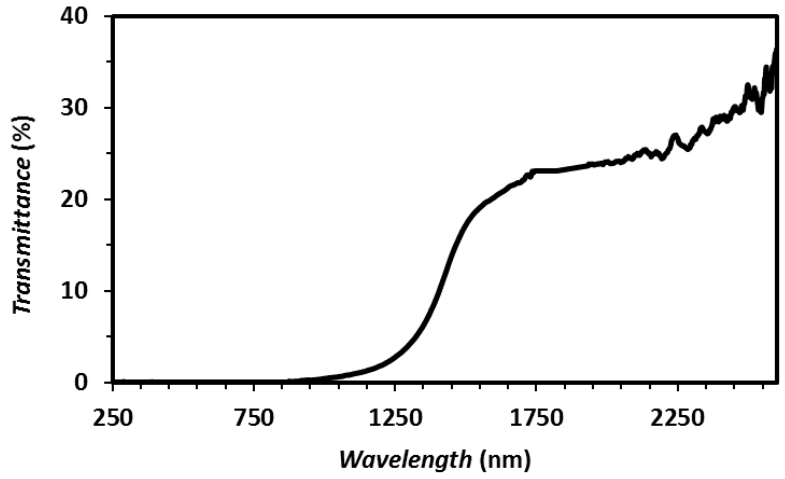

(a)

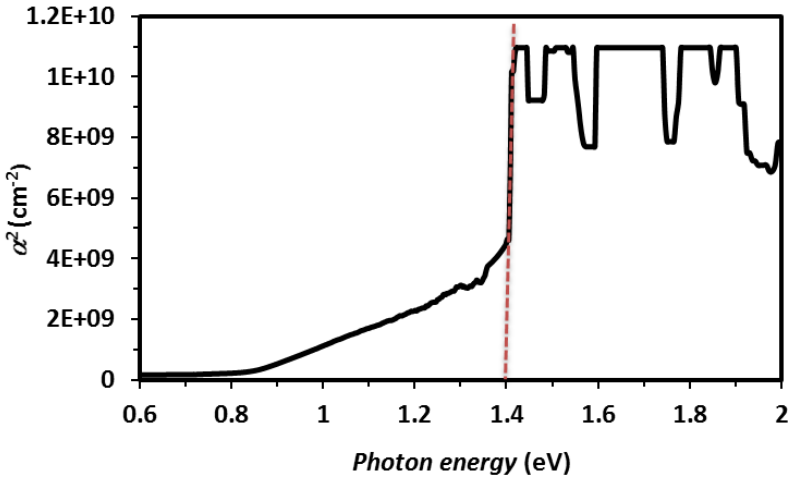

(b)

Figure 5.30: (a) Transmittance spectrum and (b) plot for the band gap determination of an optimized Cu_3BiS_3 sample sulfurized at 450°C and grown from a metal precursor multistack layer with Cu:Bi ~14:5. In (b) the noisy pattern at energies above 1.4 eV represents the instrumental limit.

(c) Electrical characterization

A variation in the electrical properties with the sulfurization temperature was observed from conductivity and Hall measurements. Samples sulfurized at 300°C generally exhibited metallic behaviour. The samples sulfurized at temperature above 350°C appeared generally light grey and were p-type with conductivity and carrier concentration increasing with the sulfurization temperature. In particular the sample sulfurized at 350°C had a sheet

resistance of 63.51 kΩ/□ and carrier concentration of $5 \cdot 10^{16}$ cm^{-3}. Conversely the sample sulfurized at 500°C was more conductive with sheet resistance of 18.80 kΩ/□ and carrier concentration of $2 \cdot 10^{18}$ cm^{-3}. Further increase in the conductivity was observed in the sample sulfurized at 550°C. However this sample delaminated from its substrate making it unsuitable for PV applications.

The samples grown from copper-poor precursors – i.e. Cu:Bi ~14:5 – were generally more resistive with sheet resistances in the order of 100 kΩ/□.

Figure 5.31 shows the resistivity (Ω cm), carrier concentration (cm^{-3}) and mobility (cm^2 V^{-1} s^{-1}) as functions of the temperature for the sample sulfurized at 350°C. These parameters were analysed from 25 K to RT. Three regimes are visible: one with low carrier concentration and high mobility at very low temperature, one with high carrier concentration and lower mobility at high temperature and in between an "intrinsic" region with the Hall effect parameters being invariant with temperature.

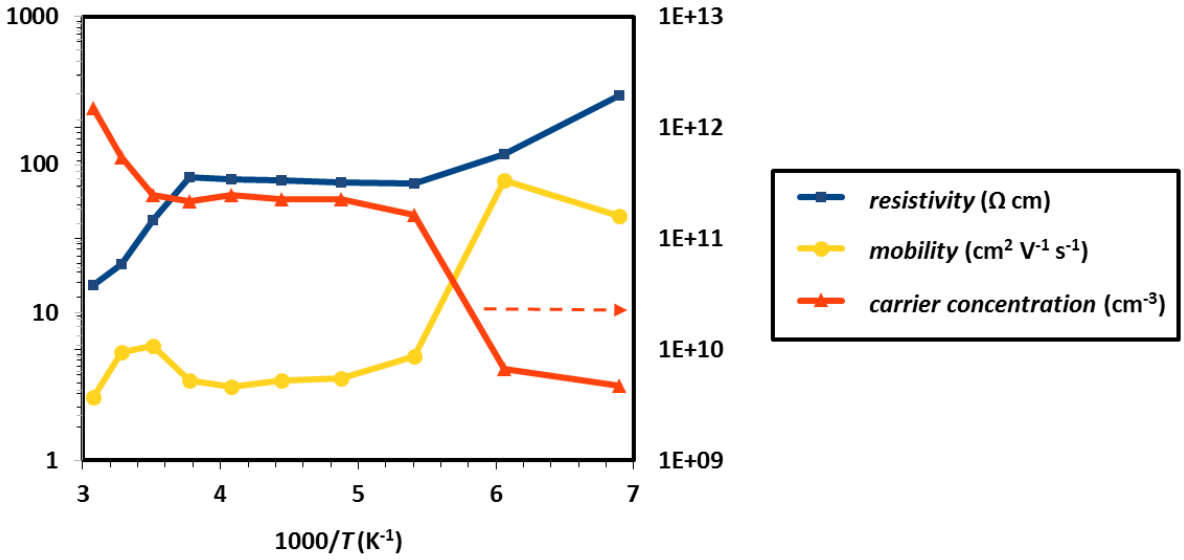

Figure 5.31: Temperature-dependence plot of the Hall effect parameters for a Cu_3BiS_3 sample sulfurized at 350°C. The respective units are reported in the legend.

(d) SEM/EDX analysis

Figure 5.32 shows the (a) surface and the (b) cross-sectional SEM of as-deposited films. The plan view image shows a granular holey film with areas of light contrast that may

be secondary phases. The cross section indicates the holes do not penetrate through the whole film but that the films contain pores.

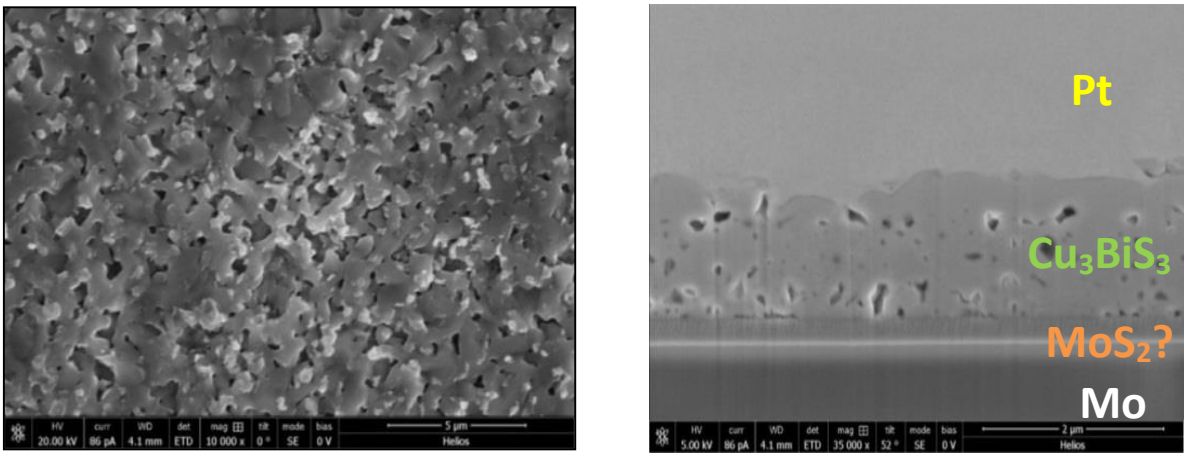

(a) (b)

Figure 5.32: (a) Surface and (b) cross-sectional SEM images of as-grown Cu_3BiS_3 sample sulfurized at 450°C on Mo-coated glass (the samples deposited on Mo-coated glass exhibited better adhesion and were more suitable for SEM analysis). Residual secondary phases are visible on the surface in (a). Voids and impurities in the bulk of the film are observed in the cross-sectional image (b), and there is an interfacial phase that is presumed to be MoS_2.

5.7 Discussion

5.7.1 $CuSbS_2$ films prepared by sulfurizing metal precursor layers

Results in Sections 5.2 and 5.3 showed the properties of $CuSbS_2$ films grown by sulfurization. The synthesis of phase-pure films was challenging due to the complexity of the Cu-Sb-S system, with several binary and ternary phases being possible. In the initial as-grown films the main issue was the loss of antimony. This was ascribed to volatile species forming with the excess of sulfur – e.g. Sb_2S_4 [4]. As explained in Sections 5.2 and 5.3, loss of antimony was minimized by depositing a Sb-rich precursor layer and sulfurizing under atmospheric nitrogen pressure. The high pressure encouraged sulfur to react on the surface of the precursor layer while the antimony excess included in the precursor layer compensated the potential loss of antimony.

$CuSbS_2$ single-phase films exhibited absorption coefficients of ~10^5 cm^{-1}, this being in agreement with what found from a DFT theoretical study [9]. Optimized samples had band

gaps of ~1.5 eV – i.e. consistently with other works on $CuSbS_2$ thin films grown by sulfurization of a metal precursor layer [10].

However, as shown in Section 5.2.3, FTIR analysis showed marked band tailing in the below-gap absorption coefficient of the first samples. This was attributed to the presence of residues of secondary phases in the material. From FTIR the temperature-dependence of the $CuSbS_2$ band gap was described using an equation of the form of Equation 2.1, the coefficients being from the fit approximately as follows.

$$Eg\ (T)\ =\ 1.505 - 0.0007\frac{T^2}{T+900}\ ,\quad 3.7\ \text{K}\ \leq\ T\ \leq\ 300\ \text{K} \tag{5.1}$$

Figure 5.33 is the plot of Equation 5.1

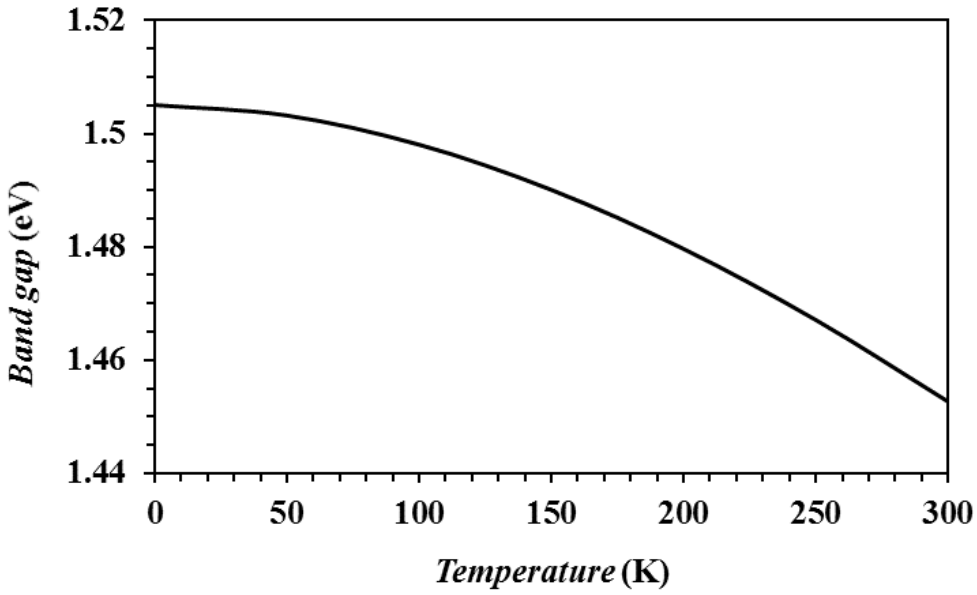

Figure 5.33: *Eg* of $CuSbS_2$ as a function of temperature *T*.

$CuSbS_2$ has been identified as an intrinsically p-type semiconductor due to the dominating presence of copper vacancies [11]. As shown in Section 5.2.3, the sulfurized samples exhibited p-type conductivity, this being consistent with extensive reports in the literature on $CuSbS_2$ as-deposited films. The sulfurized films under optimal conditions presented mobilities around 10 $cm^2\ V^{-1}\ s^{-1}$. The effective mobility generally depends on the grain size – this being related to the deposition method and growth conditions. Wubert and Kuo reported mobilities up to 20 $cm^2\ V^{-1}\ s^{-1}$ for $CuSbS_2$ "bulks" deposited by reactive

sintering at 400°C [12]. Welch et al. reported mobilities up to ~1 $cm^2\ V^{-1}\ s^{-1}$ for Sb-rich $CuSbS_2$ films grown by co-sputtering [13]. Bo-Yang et al. described the properties of highly crystalline $CuSbS_2$ films grown by hydrazine-based solution with mobilities up to 49 $cm^2\ V^{-1}\ s^{-1}$ [11].

The investigation of the morphological properties of the $CuSbS_2$ films grown by sulfurization showed the existence of voids and impurities in the bulk. Voids are a typical characteristic of sulfurized films with small irregular grains [14]. High sulfurization temperatures can be expected to lead to the formation of surface oxides in samples prepared under the levels of vacuum achievable using a rotary pump [15] – i.e. antimony oxide and copper oxide particles as detected from XPS and suggested by PL. The literature on etching treatments to clean $CuSbS_2$ surfaces, and in particular to remove antimony oxide particles is very limited. Hence several methods have been explored in this work. The most effective wet etching treatment was 20% NaOH solution. A complete removal of the antimony oxide particles was achieved by in-situ cleaning with a 500 eV argon ion beam. Soaking in de-ionized water for 4 hours has been demonstrated to be a valid alternative to etch metal oxides from Cu_2ZnSnS_4 surfaces [2]. The latter method was also effectively extended to $CuSbS_2$ films.

The elements tested for doping the absorber were effective in improving the conductivity of $CuSbS_2$ films. As reported for CIGS [16] the introduction of sodium by NaF enhances the conductivity of the absorber layer. However the interpretation on the role of Na atoms is controversial with different theories having been developed – e.g. some authors claim that Na atoms act as an acceptor while others explain the beneficial effects of Na in terms of passivation of grain boundaries [16]. The incorporation of zinc and antimony in the $CuInS_2$ lattice has been demonstrated to be possible [17]. The present work proved the effectiveness of doping $CuSbS_2$ by both zinc and indium in increasing the conductivity of the absorber without affecting the crystal structure. One possibility is that the mechanism of doping $CuSbS_2$ by indium is similar to that for $CuInS_2$ by antimony as described in ref. 18, i.e. by substitution on the sulfur site (Sb_S) – or in the present case In_S.

$CuSbS_2$ films with desirable properties for photovoltaics were produced by sulfurization. However the as-deposited samples contained impurities and residues of secondary phases. It has been demonstrated that both precipitates of Sb_2S_3 and the presence of the copper-rich phase $Cu_{12}Sb_4S_{13}$ are deleterious for the performance of the $CuSbS_2$

absorber and its application in PV devices [19]. The detection and control of these secondary phases is however arduous. In the initial sulfurized samples (see Section 5.2.3) the presence of residues of Sb_2S_3 was detected by Raman spectroscopy – and this may contribute to the strong band tailing seen in the absorption spectrum. The refined process produced more pure samples, however the sulfurization process introduced impurities and defects in the film which can limit the application of $CuSbS_2$ in solar devices, as seen in Section 3.3.3.

5.7.2 $CuSbS_2$ films deposited from a single target

Section 5.5 described the development of thin films from single target $CuSbS_2$ by rf sputtering. In principle the one-step process presents the following advantages compared to the sulfurization technique – a) simplicity: the number of parameters to control significantly decreases, b) purity: the incorporation of impurities into the as-grown film can be reduced, c) scalability: the full device can potentially be fabricated by sputtering in a single chamber. In addition, with this method the absorber layer can be deposited at low temperature and this has a potential benefit for the fabrication of the devices.

$CuSbS_2$ films 1 μm thick sputtered from the single source were crystalline and presented optical characteristics similar to those of the samples fabricated by sulfurization under optimal conditions – i.e. a distinct band gap of ~1.5 eV and absorption coefficient of 10^5 cm^{-1} above the band gap energy.

The thinner films grown from single target were amorphous, with their band gap energies decreasing with the thickness. This characteristic may be related to the grain size of the different samples: under the same deposition conditions it may be the case that thinner films should grow with very small grain size (this was not measured in the present thesis) and the charge carriers should be by the grain boundary potentials, i.e. a quantum confinement effect [8]. Rabhi et al. observed an apparent decrease of the band gap energy with the substrate temperature for crystalline $CuSbS_2$ films deposited by thermal evaporation [20]. However that paper contained no physical characterization and therefore a systematic variation in for example the chemical composition cannot be excluded.

From the white light photoconductivity test the $CuSbS_2$ films 1 μm thick grown at RT showed a photoactive response – this proving the applicability of the one-step approach for PV applications. However the presence of secondary phases, the high resistivity of the layers

and the reproducibility of the process are the main issues for the utilisation of this method in solar device fabrication.

5.7.3 Cu_3BiS_3 sulfurized films

Cu_3BiS_3 films showed optical band gap of ~1.4 eV and absorption coefficient of 10^5 cm^{-1} above the band gap with large band tailing – this being in good agreement with other work for Cu_3BiS_3 films deposited by sulfurization of a sputtered metal stack [21].

Optimized Cu_3BiS_3 samples exhibited p-type conductivity and mobility of 3 cm^2 V^{-1} s^{-1} – consistent with the study conducted from Mesa et al [22]. The authors attributed the relatively low mobility to the high density of point defects and grain boundaries. The authors identified a potential passivation method with a buffer layer of indium sulfide on the surface of as-deposited Cu_3BiS_3 films.

The optical and electrical properties of optimized Cu_3BiS_3 sulfurized films are promising for the utilisation of the material in PV devices. However the presence of defects and impurities in the absorber may strongly limit is application in practice.

5.8 Conclusions

A thorough study on the properties of $CuSbS_2$ and Cu_3BiS_3 films for PV applications was conducted.

Two different methods were investigated for the deposition of $CuSbS_2$ films – i.e. sulfurization (by using sulfur powder rather than the toxic H_2S) and rf sputtering from single source. It was demonstrated that both the techniques led to $CuSbS_2$ films ~1µm thick with optical characteristics suitable for utilization as absorber layer in PV devices – i.e. absorption coefficients of approximately 10^5 cm^{-1} and band gaps of ~1.5 eV.

The synthesis of $CuSbS_2$ films by sulfurization of a metal precursor stack was complex due to the large number of processing variables and the secondary phases involved. The optimal synthesis conditions were found after the analysis of several samples grown under different deposition combinations. Optimized samples were grown from a Sb-rich precursor stack with 5 periods of Cu/Sb by sulfurizing at 400°C and atmospheric nitrogen

pressure for 1 hour with ~20 mg of sulfur. Under these conditions the samples displayed desirable optical characteristics, p-type conductivity and mobility of ~10 $cm^2\ V^{-1}\ s^{-1}$. It was found experimentally that the resistivity of the sulfurized $CuSbS_2$ films changed with the sputtering and sulfurization conditions. Doping the material with an extrinsic element – such as indium or zinc – enhanced the conductivity of $CuSbS_2$. The surface analysis on as-grown $CuSbS_2$ sulfurized films showed the presence of copper and antimony oxides, but these were effectively removable by etching treatments – the most effective being in-situ cleaning by argon ion beam, 20% NaOH solution and soaking in de-ionized water. The $CuSbS_2$ films grown by sulfurization presented defects and impurities, with consequent limitations for their applications as absorber layers. Furthermore the properties of the sulfurized films were generally very sensitive to small changes in the growth conditions – this being therefore a potential limitation to the reproducibility of the process.

Conversely the synthesis of films by the one-step technique was less laborious and led to photoactive $CuSbS_2$ films with the desirable optical characteristics for PV. However the control of the electrical and structural properties was limited, due to the small number of processing parameters. This one-step method presents some disadvantages for upscaling, such as: a) high resistivity of the as-deposited $CuSbS_2$ films, b) lack of control of the stoichiometry of the samples, c) very slow growth rate with deposition times up to 12 hours for the 1 μm thick films, d) reproducibility – since it is expected that the properties of the ternary target will change in the long term – and e) the high cost of the ternary target.

A smaller number of sulfurization experiments were conducted with the Cu-Bi system. The optimal growth conditions were found for nearly single-phase Cu_3BiS_3 films – i.e. sulfurization of a Bi-rich multistack with 5 periods of Cu/Bi conducted at 450°C and atmospheric nitrogen pressure. The best samples exhibited absorption coefficients of $\sim 10^5$ cm^{-1} with band gaps of ~1.4 eV and p-type conductivity with mobilities of ~3 $cm^2\ V^{-1}\ s^{-1}$. The SEM analysis highlighted the main limitation of sulfurized Cu_3BiS_3 films presenting defects and impurities in the bulk and on the surface.

Chapter 6 presents the development and characterization of devices based on the $CuSbS_2$/CdS heterojunction, both in the superstrate and substrate configurations. For this study both the sulfurized $CuSbS_2$ films and the samples deposited by the one-step technique have been considered.

5.9 References for Chapter 5

[1] T. Delsol, M. C. Simmonds and I. M. Dharmadasa, "Chemical etching of Cu(In, Ga)Se_2 layers for fabrication of electronic devices", *Solar Energy Materials and Solar Cells*, vol. 77, pp. 331-339, 2003

[2] H. Katagiri, K. Jimbo, S. Yamada, T. Kamimura, W. Maw, T. Fukano, T. Ito and T. Motohiro, "Enhanced conversion efficiencies of Cu_2ZnSnS_4-based thin film solar cells by using preferential etching technique", *Applied Physics Express*, vol. 1, 2008

[3] C.L. Yaws, "Antoine coefficients for vapor pressure of the elements", *Chemical Engineering*, vol. 113, no. 12, pp. 52-54, 2006

[4] D. Colombara, "Investigation of chalcogenide absorber materials for photovoltaic applications", PhD thesis, Department of Chemistry, University of Bath, 2012, Bath, United Kingdom

[5] E. Peccerillo and K. Durose, "Control of Cu-Sb-S phases in thin film materials for sustainable PV", *PVSAT-9 Conference Proceedings*, pp. 187-190, 2013

[6] M. Dimitrievska, A. Fairbrother, X. Fontane, T. Jawhari, V. Izquierdo-Roca, E. Saucedo and A. Perez-Rodriguez, "Multiwavelength excitation Raman scattering study of polycrystalline kesterite Cu_2ZnSnS_4 thin films", *Applied Physics Letters*, vol. 104, no. 2, pp. 021901-1 - 021901-5, 2014

[7] N. Tigau, "Preparation and characterization of Sb_2O_3 thin films", *Romanian Journal of Physics*, vol. 51, no. 5-6, pp. 641-647, 2006

[8] P. Poulopoulos, S. Baskoutas, S. D. Pappas, C. S. Garoufalis, S. A. Droulias, A. Zamani and V. Kapaklis, "Intense quantum confinement effects in Cu_2O thin films", *The Journal of Physical Chemistry C*, vol. 115, pp. 14839-14843, 2011

[9] C. Tablero, "Microscopic analysis and applications of the Cu(Sb,Bi)S_2 high optical absorption", *The Journal of Physical Chemistry C*, vol. 119, no. 16, pp. 8857-8863, 2015

[10] D. Colombara, L. M. Peter, K. D. Rogers, J. D. Painter and S. Roncallo, "Formation of $CuSbS_2$ and $CuSbSe_2$ thin films via chalcogenisation of Sb-Cu metal precursors", *Thin Solid Films*, vol. 519, no. 21, pp. 7438-7443, 2011

[11] B. Yang, L. Wang J. Han, Y. Zhou, H. B. Song, S. Y. Chen, J. Zhong, L. Lv, D. M Niu and J. Tang, "$CuSbS_2$ as a promising earth-abundant photovoltaic absorber material: a combined theoretical and experimental study", *Chemistry of Materials*, vol. 26, no. 10, pp. 3135-3143, 2014

[12] W. Wubet and D. H. Kuo, "Process limitation for p-type $CuSbS_2$ semiconductor with high electrical mobility of 20 cm^2 V^{-1} s^{-1}", *Materials Research Bulletin*, vol. 53, pp. 290-294, 2014

[13] A. W. Welch, P. P. Zawadzki, S. Lany, C. A. Wolden and A. Zakutayev, "Self-regulated growth and tunable properties of $CuSbS_2$ solar absorbers", *Solar Energy Materials and Solar Cells*, vol. 132, pp. 499-506, 2015

[14] S. M. Pawar, A. I. Inamdar, K. V. Gurav, S. W. Shin, Y. Jo, J. Kim, H. Im and J. H. Kim, "Growth of void free Cu_2ZnSnS_4 (CZTS) thin films by sulfurization of stacked metallic precursor films", *Vacuum*, vol. 104, pp. 57-60, 2014

[15] M. Dehghani, A. Behjat, F. Tajabadi and N. Taghavinia, "Totally solution-processed $CuInS_2$ solar cells based on chloride inks: reduced metastable phases and improved current density", *Journal of Physics D: Applied Physics*, vol. 48, no. 10, pp. 115304 1-8, 2015

[16] F. H. Pianezzi, "Electronic transport and doping mechanisms in $Cu(In,Ga)Se_2$ thin film solar cells", PhD thesis, Department of Physics, E.T.H. Zurich, 2014, Zurich, Switzerland

[17] M. Ben Rabeh, N. Chaglabou, M. Kanzari and B. Rezig, "Structural and optical studies on antimony and zinc doped $CuInS_2$ thin films", *Proceedings of the JMSM 2008 Conference*, vol. 2, no. 3, pp. 745-750, 2009

[18] M. Ben Rabeh, N. Chaglabou and M. Kanzari, "Effect of antimony incorporation on structural properties of $CuInS_2$ crystals", *Nuclear Instruments and Methods in Physics Research Section B-Beam Interactions with Materials and Atoms*, vol. 268, no. 3-4, pp. 273-276, 2009

[19] A. Welch, L. Baranowski, P. Zawadzki, C. DeHart, S. Johnston, S. Lany, C. Wolden and A. Zakutayev, "Accelerated development of $CuSbS_2$ thin film photovoltaic device prototypes", *Progress in Photovoltaics: Research and Applications, in press*

[20] A. Rabhi, M. Kanzari and B. Rezig, "Optical and structural properties of $CuSbS_2$ thin films grown by thermal evaporation method", *Thin Solid Films*, vol. 517, no. 7, pp. 2477-2480, 2009

[21] N. J. Gerein and J. A. Haber, "Synthesis of Cu_3BiS_3 thin films by heating metal and metal sulfide precursor films under hydrogen sulfide", *Chemistry of Materials*, vol. 18, no. 26, pp. 6289-6296, 2006

[22] F. Mesa, A. Dussan, B. A. Paez-Sierra and H. Rodriguez-Hernandez, "Hall Effect and transient surface photovoltage (SPV) study of Cu_3BiS_3 thin films", *Universitas Scientiarum*, vo. 19, no. 2, pp. 99-105, 2014

6 Development of prototype devices based on $CuSbS_2$

6.1 Introduction

This Chapter describes the development and characterization of prototype devices based on the absorber material $CuSbS_2$. As discussed in Chapter 5, $CuSbS_2$ has characteristics making it suitable for thin film solar cell fabrication – including high optical absorption, a band gap of 1.5 eV and p-type conductivity with relatively high mobility. In this work a total of ~400 samples were grown for device analysis and characterization. For the development of prototype devices based on the heterojunction $CuSbS_2$/CdS the two typical configurations for thin film solar cells were considered: the superstrate structure glass/TCO/CdS/$CuSbS_2$/Au and the substrate structure Mo/$CuSbS_2$/CdS/TCO – the latter being the most investigated device type in this thesis.

The individual layers grown under the conditions described in Section 4.6.2 were characterized by XRD, optical spectroscopy, van der Pauw method and profilometer. The properties of the layers are discussed in Section 6.2.

Devices based on $CuSbS_2$ grown both by sulfurization and rf sputtering from the single target were fabricated into devices. Section 6.3 analyses the device performance by *J-V*, *EQE*, *J-V-T* and impedance analysis. Four types of devices were characterized: (i) superstrate configuration based on sulfurized $CuSbS_2$, (ii) superstrate configuration with $CuSbS_2$ from single target, (iii) substrate structure with sulfurized $CuSbS_2$ and (iv) substrate structure based on $CuSbS_2$ from single target. The effects on the device performance of the post-growth treatments applied to the as-grown absorber layer are also discussed.

The first prototype devices were analysed by impedance and *J-V-T* in order to determine the dominant transport mechanism in the junction. Different strategies were adopted in order to enhance the efficiency of the devices and this is discussed in the Section 6.3.4.

A discussion and summary on the main findings including the limitations of the device performance are reported in Sections 6.4 and 6.5.

6.2 Properties of the individual layers for the device fabrication

This Section describes the structural, optical and electrical characteristics of the various device layers.

(a) Molybdenum

The conductivity of the Mo sputtered films generally increased with the deposition time, the substrate temperature, the power and with decreasing chamber pressure. Figure 6.1 shows in details the calibration curves of the sputtered Mo films with (a) time, (b) substrate temperature, (c) power and (d) pressure.

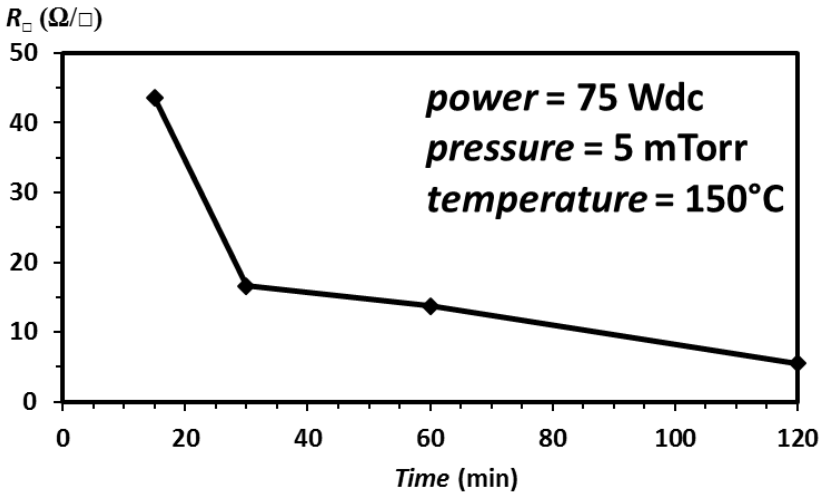

(a)

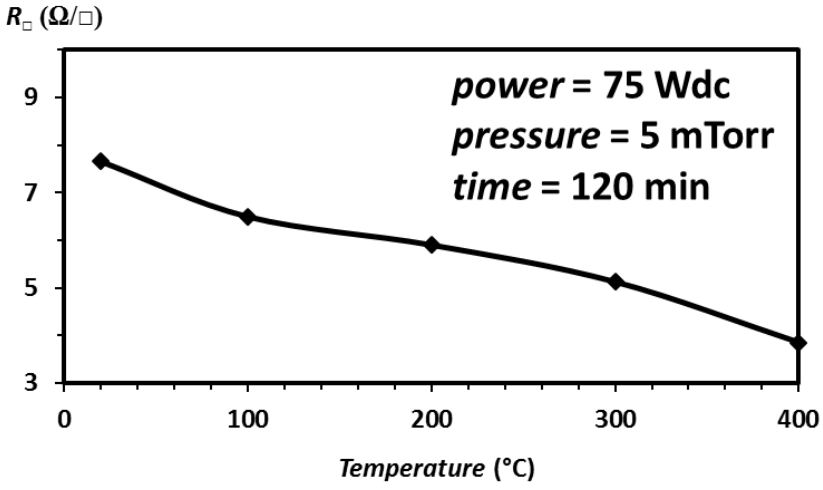

(b)

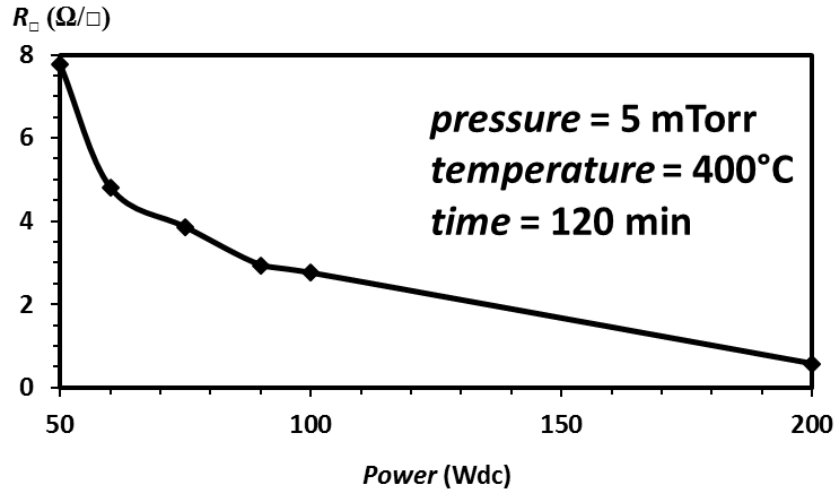

(c)

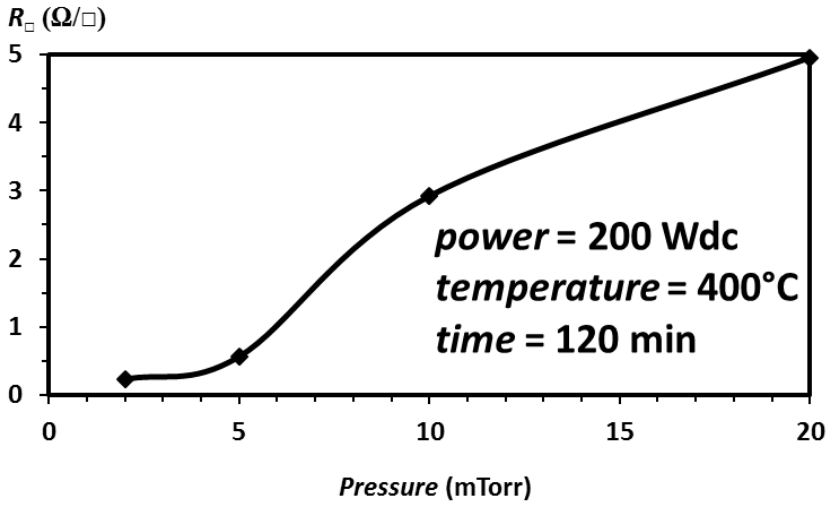

(d)

Figure 6.1: Sheet resistance of molybdenum films grown by dc sputtering as function of the growth parameters: (a) time, (b) substrate temperature, (c) power and (d) pressure.

The most conductive films with good coverage were obtained at maximum power (400 Wdc) and 2 mTorr with a substrate temperature of 400°C. Under these conditions the molybdenum films exhibited sheet resistances of ~10 mΩ/□. Further increase in the substrate temperature did not produce any enhancement in the conductivity of the Mo films. Measurements were limited to below 400 Wdc to maintain target stability. However in the experiments for the development of prototype devices the dc power was normally limited to

75 Wdc. The resulting Mo films were very conductive with sheet resistance typically below 3 Ω/□.

(b) $MoSe_2$

Several Mo-coated glass samples and molybdenum foils were selenized under different conditions in order to find the optimal growth conditions to deposit $MoSe_2$ films. According to the XRD measurement shown in Figure 6.2 single-phase $MoSe_2$ films were fabricated by selenizing the precursor Mo layer at 580°C and atmospheric nitrogen pressure for 2 hours with 20 mg of selenium powder.

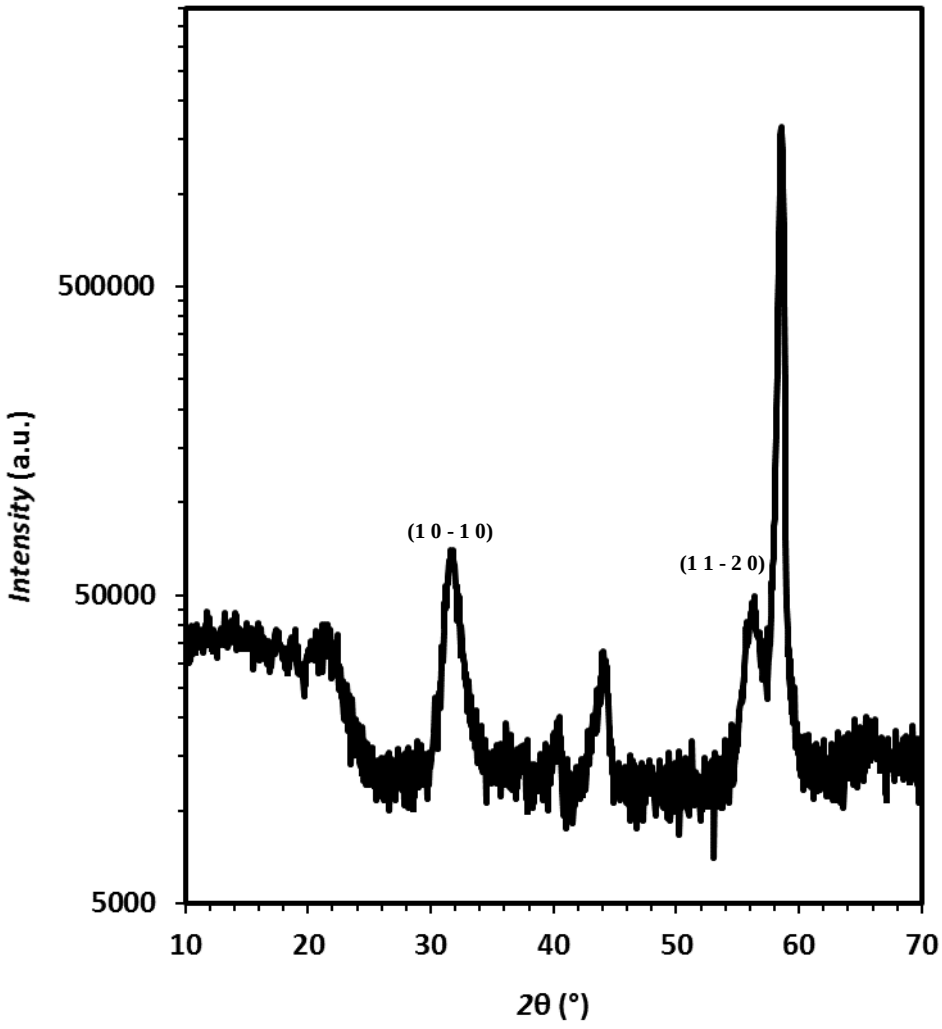

Figure 6.2: XRD pattern of sample grown on Mo-coated glass by selenization at 580°C for 2 hours at atmospheric nitrogen pressure with 20 mg of selenium powder. The main peaks of the XRD pattern match the target phase $MoSe_2$ [1] in θ.

(c) Cadmium sulfide

The CdS films grown by rf sputtering under the conditions specified in Section 4.6.2 c were single-phase CdS with strong (111) orientation, as shown in Figure 6.3.

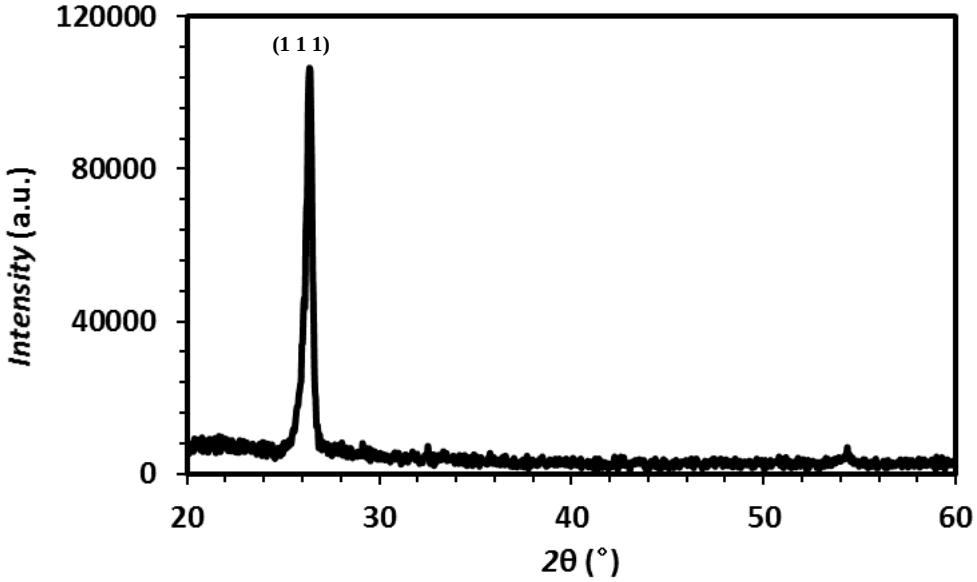

Figure 6.3: XRD pattern of CdS film deposited by rf sputtering. The samples were crystalline with (111) preferred orientation.

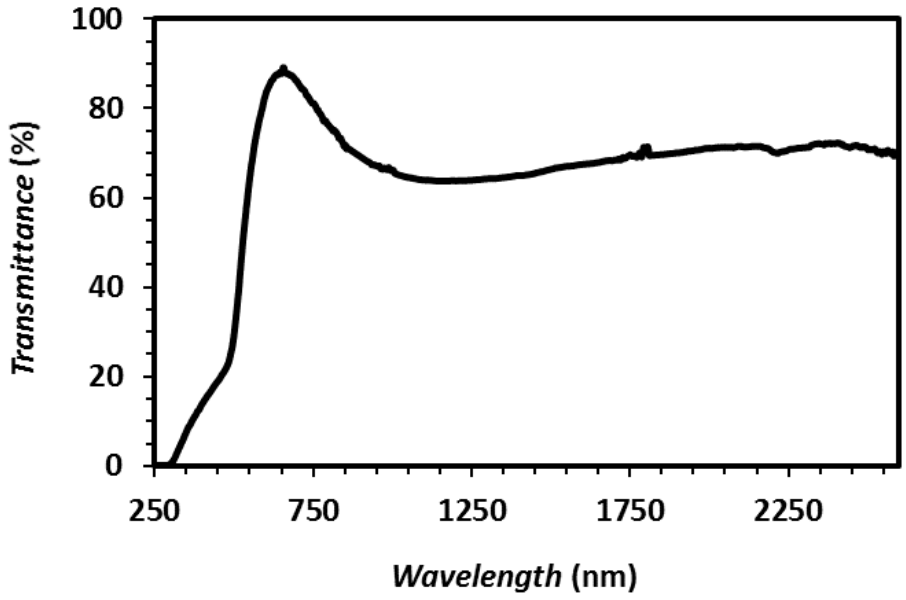

Figure 6.4: Transmittance spectrum of a sputtered CdS film. The samples exhibited relatively high transmittance at high wavelengths and band gap around 2.4 eV.

Figure 6.4 shows the transmittance spectrum of a 110 nm CdS layer grown by rf sputtering with a sharp band gap at about 2.4 eV. In the development of prototype devices the effect of the window layer thickness on the device performance was explored.

(d) Aluminum-doped zinc oxide and gallium-doped zinc oxide

Table 6.1 reports the calibration data of the AZO films deposited by ALD with the sheet resistance and the transparency as functions of the growth conditions for various samples.

Sample ID	ZnO:Al	ALD cycles	*Temperature* (°C)	Notes	*visible T* (%)	$R_{\square}$ (Ω/□)
1235	17:1	648	150	in air from 150 °C	>70	1400
1236	17:1	648	200	in air from 200 °C	>70	240
1245	17:1	1296	200	in air from 200 °C	>70	95
1606	17:1	1296	300	in air from 80 °C	>80	75
1625	20:1	1365	300	in air from 80 °C	>80	50

Table 6.1: Calibration data of AZO films deposited by ALD. In the first five columns the details of the depositions are reported. The optical and electrical characterization of the films is summarized in the last two columns with transmittance T (%) and sheet resistance $R_{\square}$ (Ω/□) respectively.

AZO films with high transparency and sheet resistance of the order of 50 Ω/□ were obtained by ALD from a Zn:O precursor ratio of 20:1 with a substrate temperature of 300°C and after 1365 ALD cycles. The samples were allowed to cool down in the growth chamber to 80°C. Under these conditions the resulting film displayed high visible transparency and a band gap of ~3.5 eV, as shown in Figure 6.5.

GZO films were deposited by ALD under different conditions in analogy with the results from the AZO samples. The optimal films of GZO with transmittance above 80% in the visible and sheet resistance of about 42 Ω/□ were produced from a ZnO:Ga precursor ratio of 20:1 and ALD run of approximately 2 hours with the substrate temperature set at 300°C for all the process.

AZO films with transmittance above 75% in the visible and band gap of ~3.5 eV with sheet resistance of about 28.7 Ω/□ were produced by rf sputtering with the following

conditions: power - 46 Wrf; chamber pressure - 5 mTorr; substrate temperature - 300°C; time - 6 hours. The transmittance spectrum of the resulting AZO film is shown in Figure 6.5.

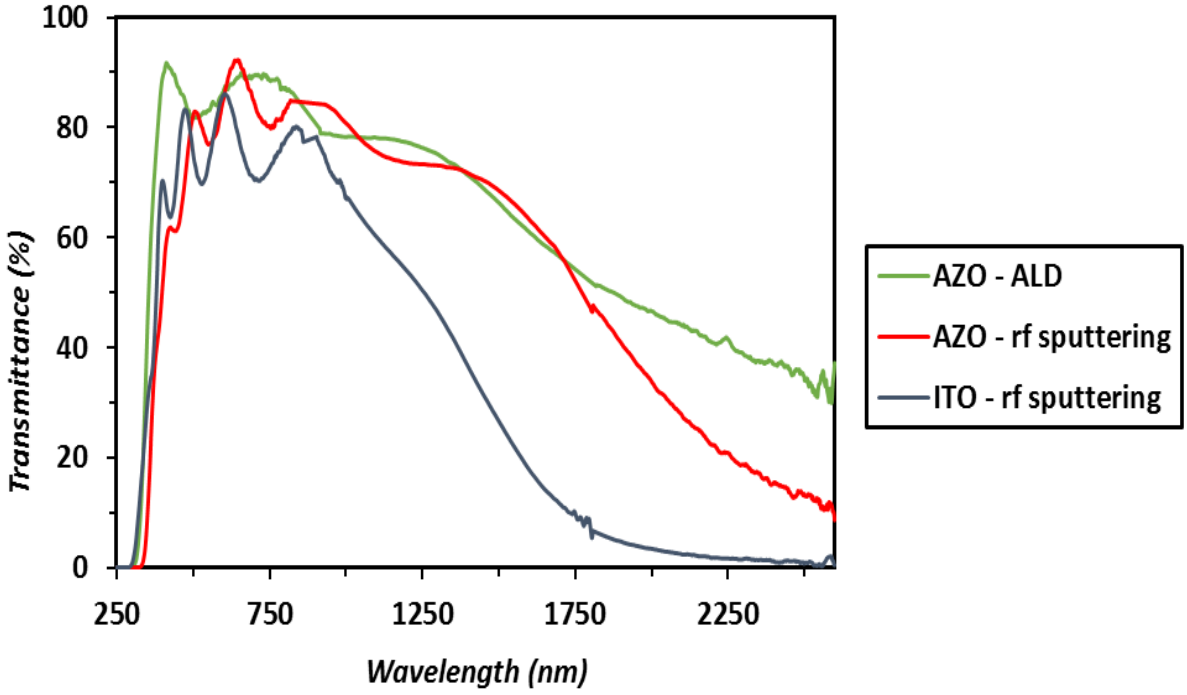

Figure 6.5: Transmittance spectra of optimized AZO films grown by ALD and rf sputtering and sputtered ITO films. The AZO samples exhibited high transparency and band gap of ~3.5 eV. The ITO films grown under optimal conditions showed lower transmittance and band gap of ~3.5 eV.

(e) Indium tin oxide

ITO films with optimal characteristics for TCO applications were obtained by rf sputtering under these conditions: power - 46 Wrf; chamber pressure - 3 mTorr; substrate temperature - 200°C; deposition time - ~3 hours. The as-deposited samples exhibited sheet resistances of ~6 Ω/□ and, as shown in Figure 6.5, high transparency with band gaps of ~3.5 eV.

The conductivity of the films was furthermore enhanced by increasing the substrate temperature to 400°C. However for the fabrication of the devices this strategy was not considered to avoid any decomposition of the underlying $CuSbS_2$ absorber at high temperature.

In comparison with the sputtered AZO films, the ITO films generally were much more conductive by using lower substrate temperatures and shorter deposition times. The high conductivity however was achieved only with slightly lower visible transmittance.

(f) Intrinsic zinc oxide

The sputtered ZnO films were deposited by using: 46 Wrf, 1.8 mTorr at RT for about 24 minutes. According to the van der Pauw measurements the resulting samples exhibited sheet resistances of ~5 MΩ/□.

Conversely the ZnO films deposited by ALD presented relatively high conductivity – i.e. sheet resistances generally below 1 kΩ/□.

6.3 Characterization of the prototype devices

This Section describes the full characterization of the devices in the various configurations. The device efficiency ŋ, fill factor *FF*, open circuit voltage *Voc* and short circuit current density *Jsc* were extracted from *J-V* curves under AM 1.5 illumination. The electrical characterization was completed by external quantum efficiency (*EQE*), impedance measurement and temperature-dependence *J-V* analysis (*J-V-T*).

6.3.1 Superstrate cells with sulfurized $CuSbS_2$

Devices were fabricated as described in Section 4.6.1 using $CuSbS_2$ layers grown from metal precursors from the two batches A and B (as described in Chapter 5). However devices made by this method suffered from delamination and although this was less severe for batch B than A, most of the devices did not have the physical integrity required for meaningful electrical measurements. Most of the resulting samples showed straight line *J-V* responses through the zero and resistance variable with the deposition conditions.

6.3.2 Superstrate cells with $CuSbS_2$ grown from a single-target

The absorber layer can be deposited at room temperature by the one-step process from the ternary target, as seen in Chapter 5. This in principle offers the potential advantage to prevent interdiffusion in the superstrate configuration. The absorber layer was deposited at RT by rf sputtering as described in Chapter 5 on glass/SnO_2/CdS. The gold back contact (0.3 mm^2) was subsequently thermally evaporated. The resulting devices exhibited generally a clear if weak photovoltaic effect, as shown in Figure 6.6. The maximum *Voc* measured was 0.22 V and the *FF* was up to nearly 39%. However the efficiency of the solar cells was usually below 0.01% due to the extremely low *Jsc*. This could be related to recombination and physical defects in the absorber layer. Indeed the as-grown sample had visible pinholes. It is also possible that the room temperature deposition simply failed to form a good p-n junction.

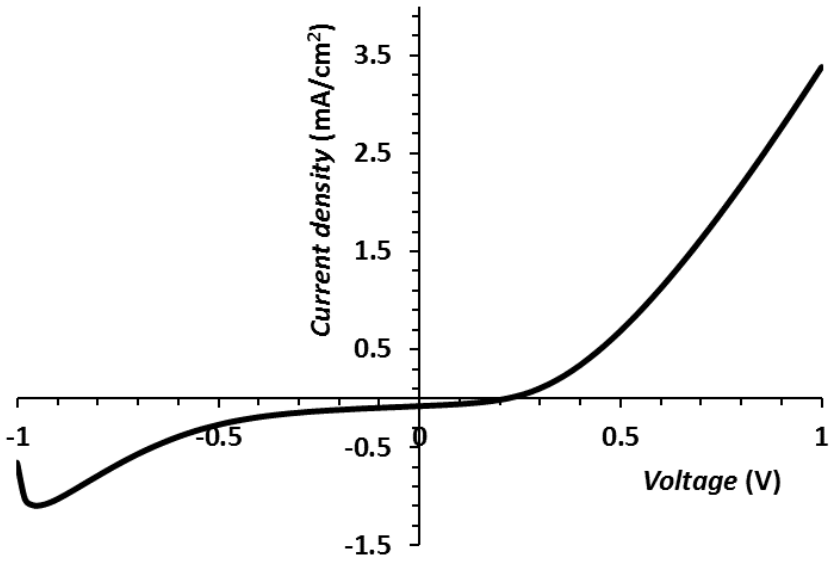

(a)

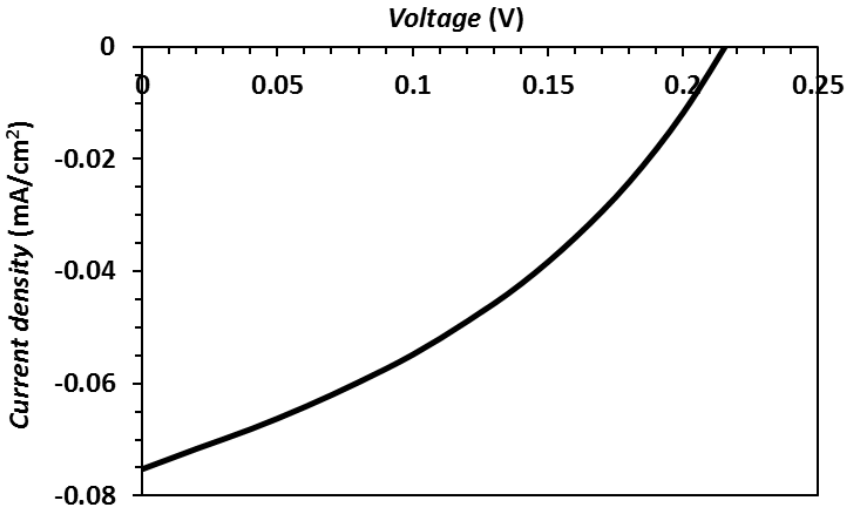

(b)

Figure 6.6: (a) *J-V* curve of superstrate cell based on $CuSbS_2$ grown by sputtering from a single target at RT and (b) fourth quadrant.

The absorber material was also deposited by one-step process at 400°C. This improved the efficiency of the solar cell to a maximum of 0.025%. However as shown in Figure 6.7 the *J-V* curve was quite leaky with low *FF*, low shunt resistance and high reverse bias current. This could be caused from pinholes and defects and interdiffusion at high temperature and it confirmed the findings for the superstrate configuration with the sulfurized absorber layer.

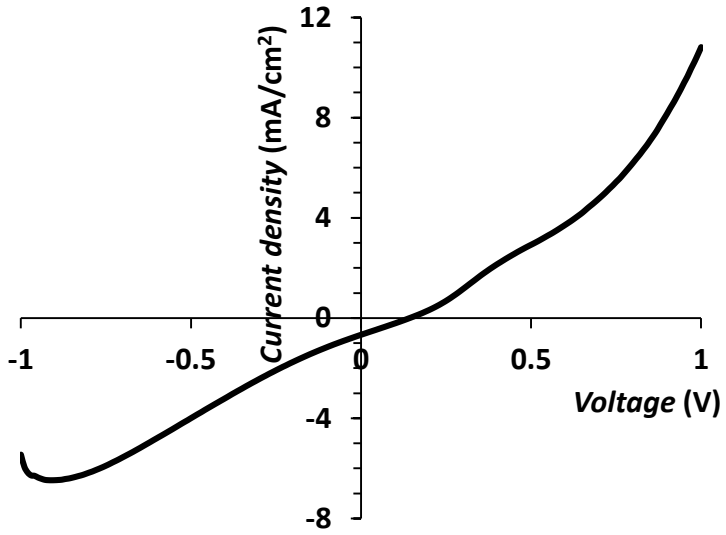

(a)

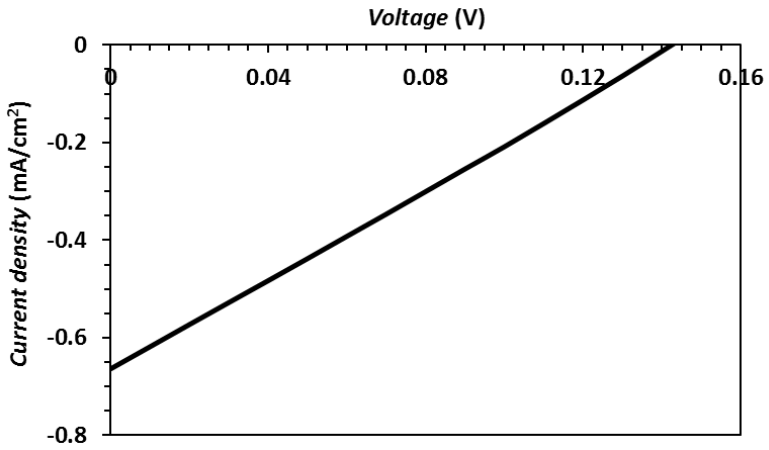

(b)

Figure 6.7: (a) *J-V* curve with (b) fourth quadrant of the superstrate cell based on $CuSbS_2$ grown by the one-step process at 400°C.

A post-growth sulfurization treatment at 150°C applied to the sputtered $CuSbS_2$ enhanced *Voc* to 0.36 V but ŋ did not improve significantly.

6.3.3 Substrate cells with $CuSbS_2$ grown by sulfurization of metal precursor - First devices and analysis of the properties of the junction

(a) *J-V* and *EQE* – The first devices fabricated in the substrate configuration with sulfurized $CuSbS_2$ layers were made from samples series A (see Chapter 5) and used chemical bath deposited CdS and ALD deposited GZO for front contact.

These devices based on the $CuSbS_2$/CdS heterojunction exhibited a photovoltaic effect however, as shown in Figure 6.8, the efficiency of the cells was generally of the order of 0.1%.

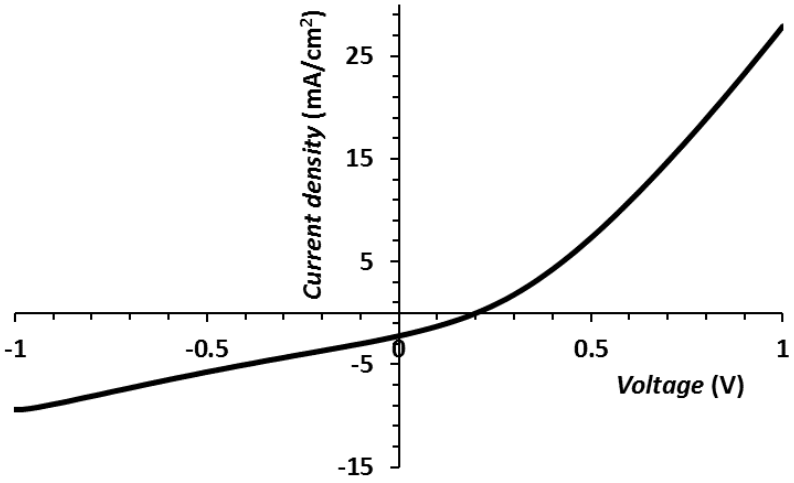

(a)

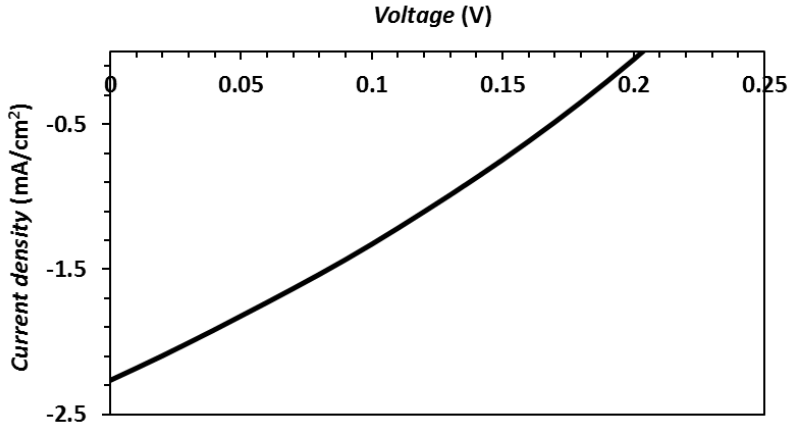

(b)

Figure 6.8: Illuminated *J-V* curve of the early substrate device based on sulfurized $CuSbS_2$ series A with (a) the scan from -1 V to +1 V and (b) fourth quadrant.

In the *EQE* of the sample (Figure 6.9), the cut-off edge from the absorber (~800 nm) is not very sharp – i.e. this confirmed the outcomes from Chapter 5 on the band gap of $CuSbS_2$ samples of type A. The *EQE* was generally low, this being potentially related to recombination in the absorber layer with impurities and defects.

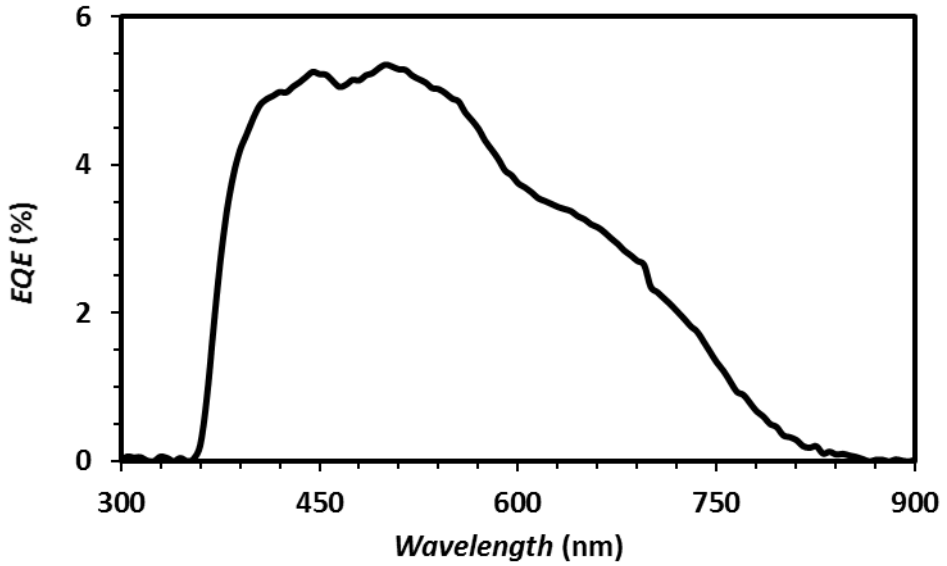

Figure 6.9: *EQE* of the early substrate device based on sulfurized $CuSbS_2$ series A. The *EQE* was below 6%. The cut-off edge at ~800 nm associated to $CuSbS_2$ type A was not sharp.

(b) Impedance analysis – An extensive study by impedance and *J-V-T* on the early devices was undertaken in order to investigate the properties of the junction between CdS and sulfurized $CuSbS_2$. The impedance magnitude and phase of the device were measured as functions of frequency at different voltage bias.

In principle the device can be schematized as shown in Figure 6.10 from an equivalent circuit represented by a parallel resistor-capacitor network connected with a series resistance.

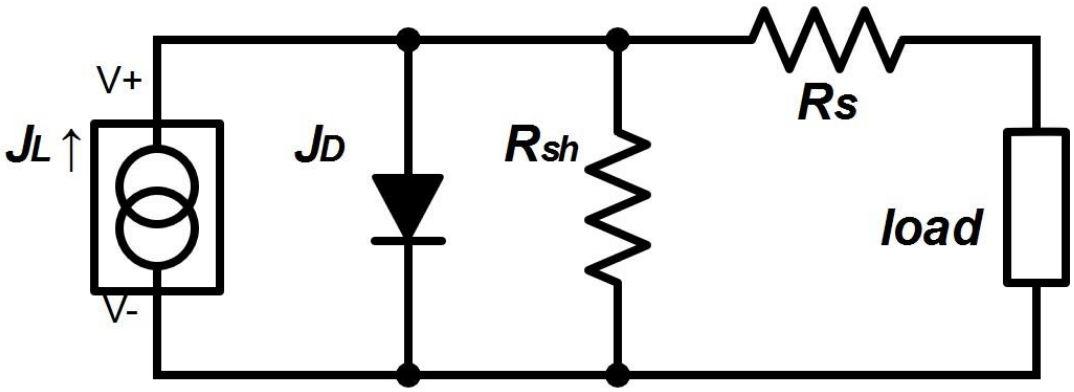

Figure 6.10: Equivalent circuit model of the device where *Rs* represents the series resistance, *Rsh* the shunt resistance and *Csh* the equivalent capacitance.

The impedance magnitude $|Z|$ of this proposed circuit is given from Equation 4.8. It can be demonstrated that at low frequency the impedance magnitude $|Z|$ tends to $Rsh + Rs$ and at high frequency to Rs. In Figure 6.11 it is shown the log-log plot of the impedance magnitude $|Z|$ as a function of the frequency.

Figure 6.11 indicated that the value of series resistance Rs did not change with the applied bias. This suggested that the back contact effects were insignificant and the potential applied to the device acted mainly on the junction interface at the temperature and voltage range considered. On the other hand Rsh decreased with the applied bias – this being normally expected in solar cells.

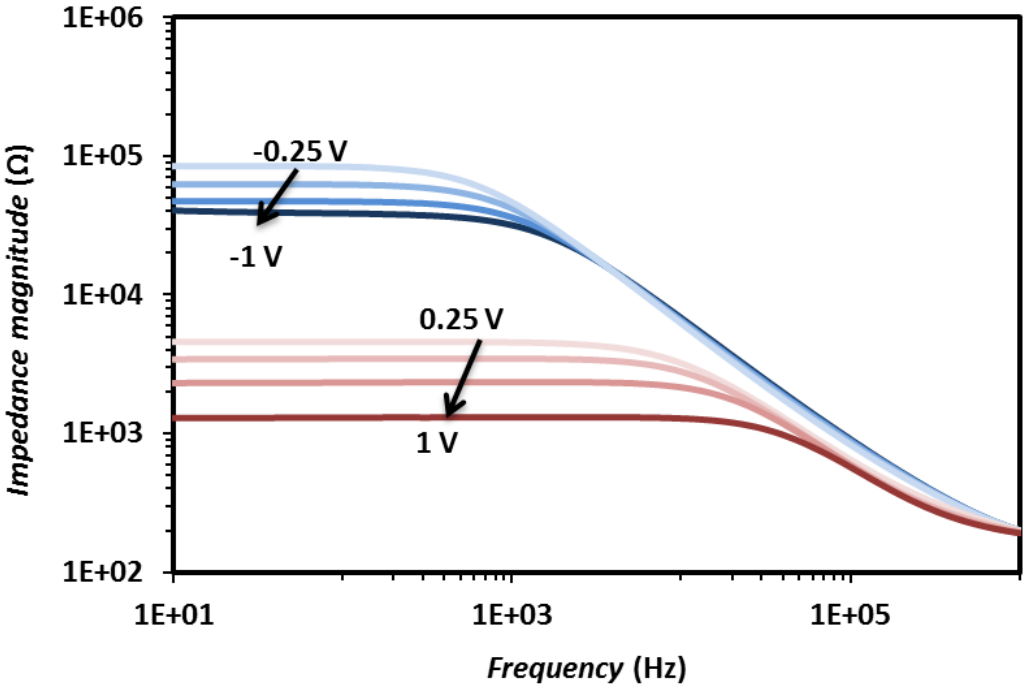

Figure 6.11: Experimental data for the impedance magnitude as a function of the frequency at different voltage bias for the early devices (with sulfurized $CuSbS_2$ series A) based on the substrate structure.

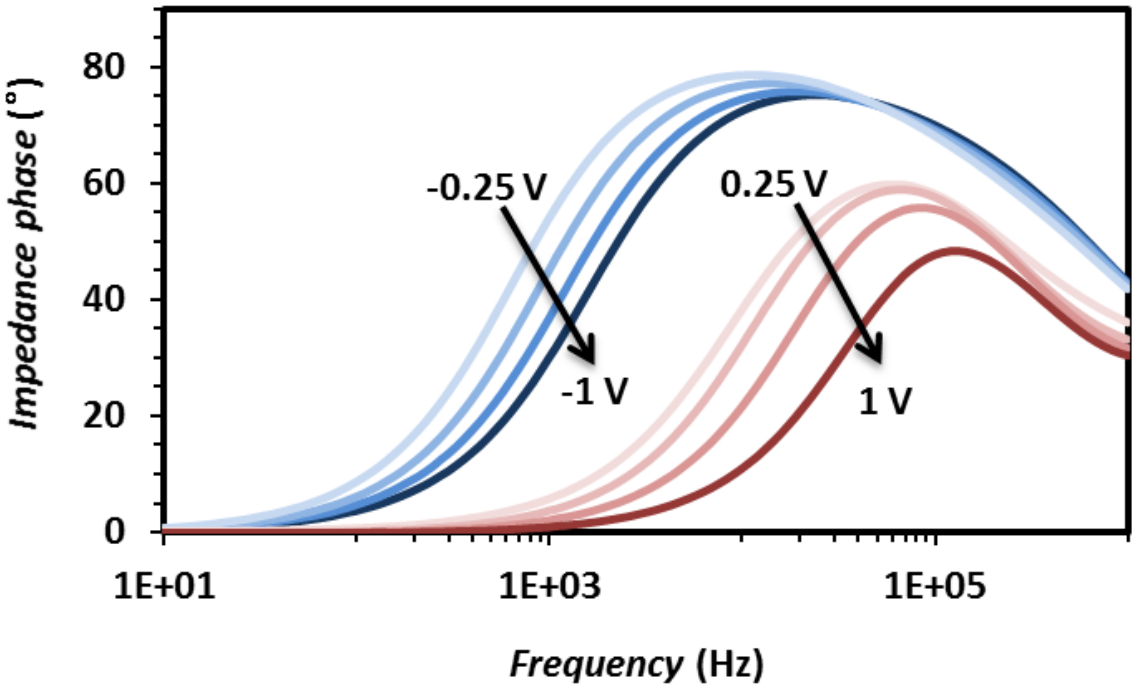

Figure 6.12: Experimental data for the impedance phase as a function of the frequency at different voltage bias for the early devices (with sulfurized $CuSbS_2$ series A) based on the substrate structure.

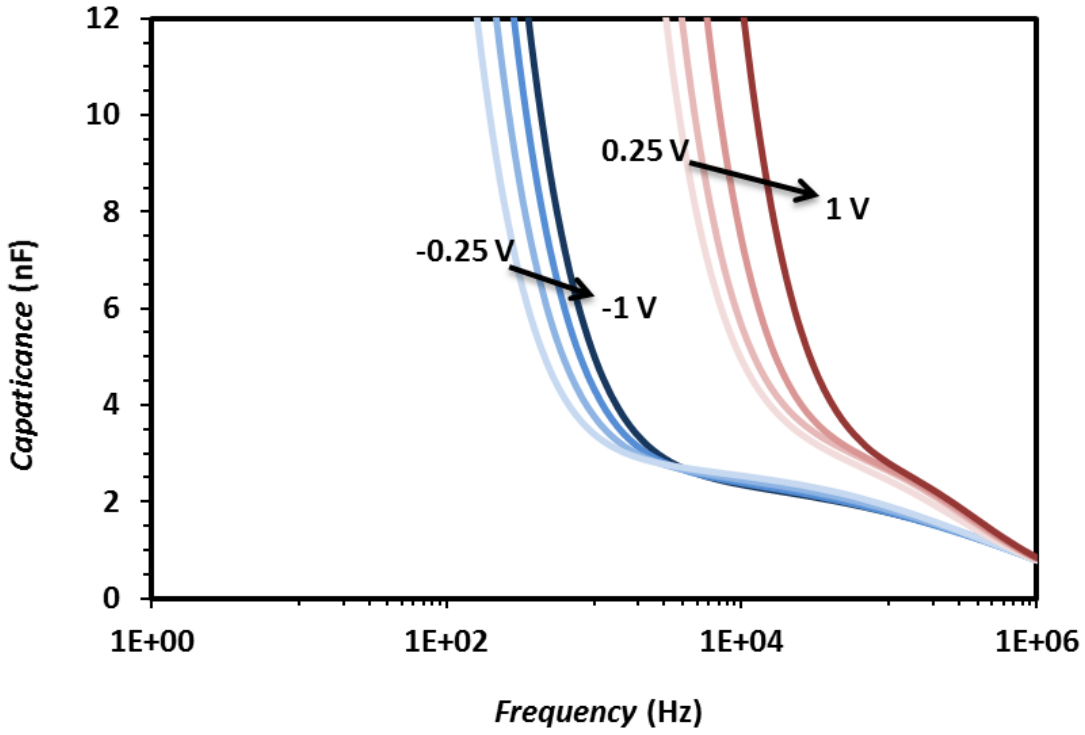

Figure 6.13: Experimental data showing the capacitance as function of the frequency at different voltage bias for the early devices (with sulfurized $CuSbS_2$ series A) based on the substrate structure.

Figure 6.12 shows the phase angle θ as a function of the frequency for different dc bias.

The single peak in all the plots in Figure 6.12 indicated the effective role of a single interfacial region for the experimental conditions considered.

In conclusion the impedance study indicated the presence of a p-n junction between $CuSbS_2$ and CdS with no Schottky barrier issue with the Mo back contact.

Finally Figure 6.13 shows the capacitance *C* as function of the frequency *f* for different biases.

(c) *J-V-T* – A thorough investigation by *J-V-T* on the device was made in order to identify the transport mechanism in the junction. The sample was analysed by *J-V-T* from 120 to 300 K with steps of 10 K, as shown in Figure 6.14.

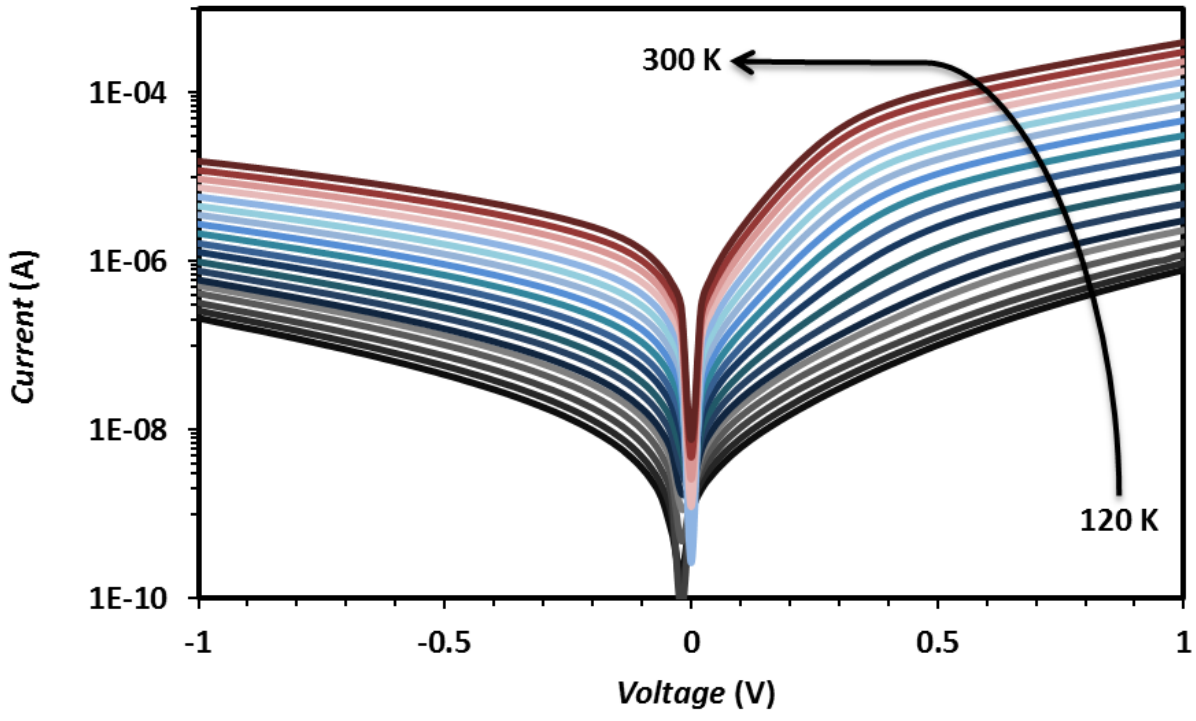

Figure 6.14: *J-V-T* analysis on the early substrate cells. The samples were grown in the substrate configuration with $CuSbS_2$ grown by sulfurization (type A). The samples were analysed from 120 to 300 K with step ΔT of 10 K.

From the *J-V-T* measurement it was possible to extract the dark saturation current I_o and the ideality factor *n* as functions of the temperature, as shown in Figures 6.15 and 6.16 respectively.

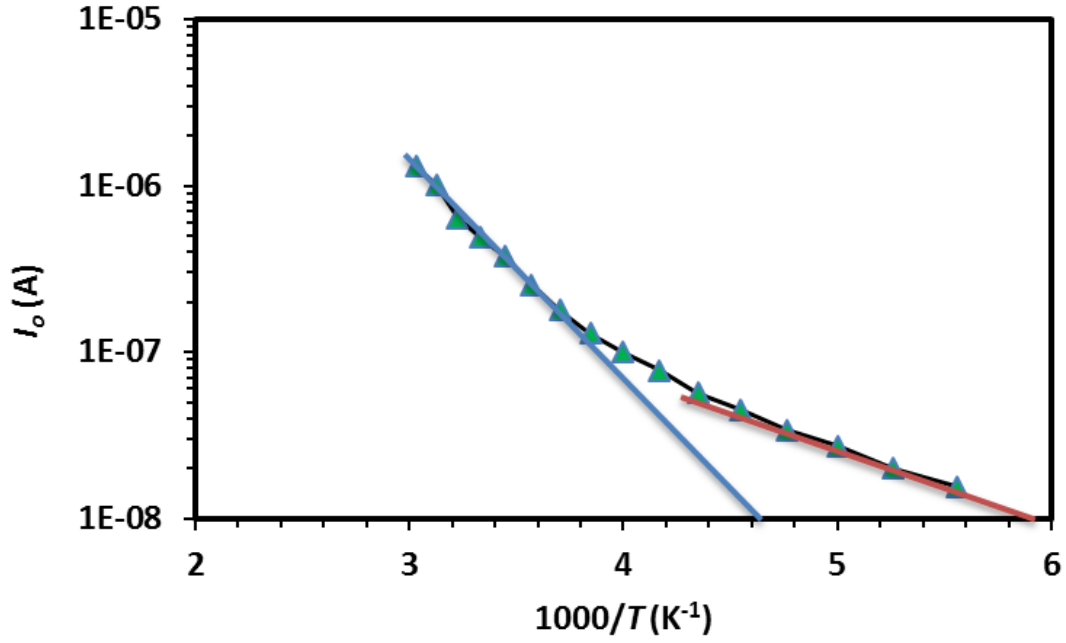

Figure 6.15: Dark saturation current I_o as function of temperature for the devices with sulfurized $CuSbS_2$ series A in the substrate structure.

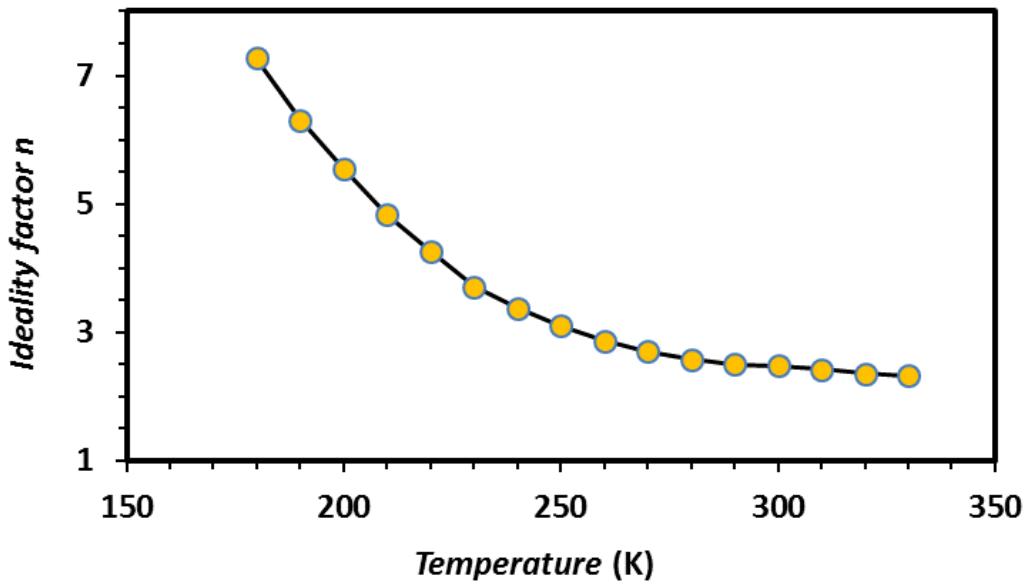

Figure 6.16: Ideality factor *n* as function of temperature in the substrate cells with sulfurized $CuSbS_2$ of type A.

The blue and red lines in Figure 6.15 evidence two different regimes with turning point at about 250K. The regimes are ascribed to two different transport mechanisms with specific activation energies.

As shown in Figure 6.16 the ideality factor *n* decreased smoothly with temperature but was much higher than the value of $1 < n < 2$ expected for typical diodes. This could be due to the high density of defects at the $CuSbS_2$/CdS interface.

From the *J-V-T* analysis it was found that the slope of the *J-V* curve in the linear forward region was approximately invariant with temperature. In addition – as shown in Figure 6.16 – the ideality factor *n* decreased with temperature. These trends implied that the dominant transport mechanism in the p-n junction was tunneling [2].

6.3.4 Substrate cells with $CuSbS_2$ grown by sulfurization of metal precursor - Further development

(a) Substrate device trials with improved, etched and doped $CuSbS_2$ – In the second part of the development of solar cells in the substrate structure different strategies to optimize the performance of the absorber layer were undertaken. In this stage $CuSbS_2$ was deposited by process B and both CdS and AZO by rf sputtering.

All the samples grown without CdS with the $CuSbS_2$/AZO junction were not photoactive. In this case the *J-V* curves generally exhibited diode response with the characteristics as follows: rectification at voltages above 0.4 ± 0.1 V, breakdown below -0.4 ± 0.1 V; zero current between the rectification and breakdown regions.

In a series of experiments the absorber layer was doped with different elements, including sodium fluoride, indium and zinc. Different etching treatments were tested to clean the surface from impurities, as described in Chapter 5. The Cu:Sb precursor ratio and the sulfurization conditions were slightly changed to evaluate the effects on the device performance. In this part a large number of samples were grown by different combinations of the deposition parameters in order to find the optimal growth conditions.

Most of the devices grown with $CuSbS_2$ of type B were in general photoactive with performance parameters varying with the deposition conditions. Sodium fluoride, indium and zinc enhanced the photoactivity of the device. The best devices exhibited efficiencies of

nearly 0.1%. The absorber layer was grown under the optimal conditions described in Chapter 5 – i.e. multistack precursor slightly Sb-rich and reactive annealing at 400°C for 1 hour with 20 mg of sulfur – and was doped with a thin layer of indium by thermal evaporation. It was observed that soaking the absorber in de-ionized water generally was beneficial for the performance of the solar cell.

The *EQE* spectrum in Figure 6.17 shows a sharper edge for the absorber at about 750 nm. However the *EQE* was still low – this being probably related to recombination.

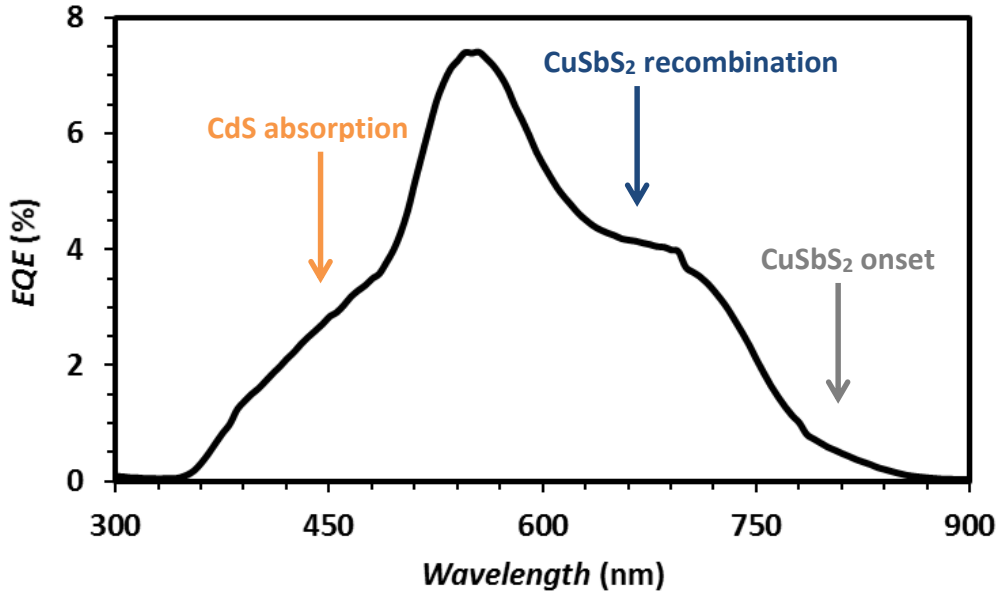

Figure 6.17: *EQE* of device in the substrate structure from sulfurized $CuSbS_2$ of type B. The *EQE* was generally below 10%. The curve is characterized by a distinctive peak at ~550 nm and a band gap related cut-off between 750 and 900 nm.

(b) Devices with i-ZnO and ITO – In the third part of the development of substrate cells based on sulfurization the growth of the absorber and the device was refined. An intrinsic layer of ZnO between the window layer and the front contact was included, and AZO was replaced with ITO. At this stage the as-grown absorber was normally soaked in de-ionized water for 10 minutes and then deposited consequently CdS, ZnO and ITO by rf sputtering without breaking the vacuum in the sputtering chamber.

The resulting cells exhibited efficiencies up to 0.3% with *Jsc* high but *FF* and shunt resistance normally very low as illustrated in Figure 6.18. This was a sign of shunt paths in the device between the electrodes. Figure 6.19 shows the *EQE* of the same device.

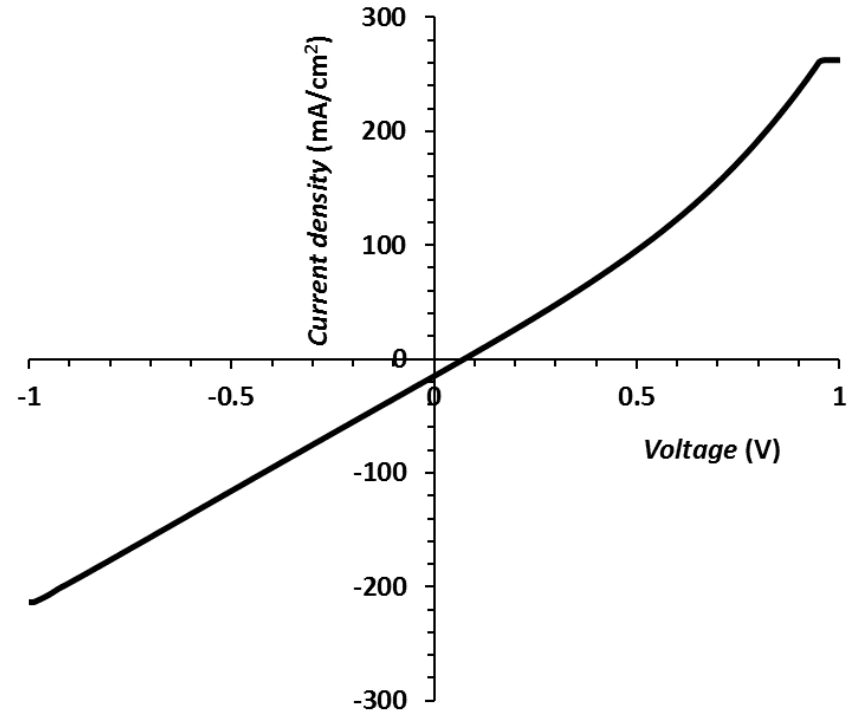

a)

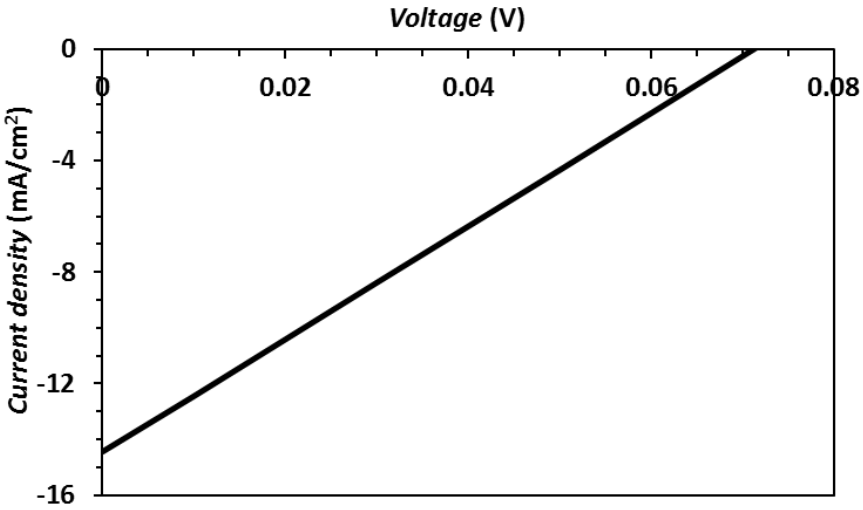

b)

Figure 6.18: (a) *J-V* curve and (b) fourth quadrant of a device in the substrate structure from sulfurized $CuSbS_2$ of type B with CdS, ZnO and ITO deposited without breaking the vacuum in the sputtering chamber.

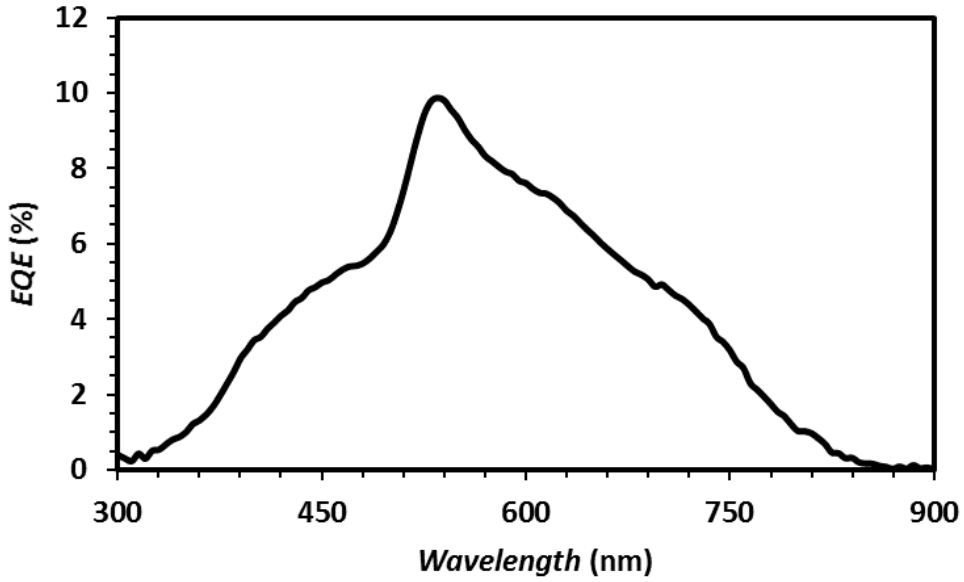

Figure 6.19: *EQE* curve of device in the substrate structure from sulfurized $CuSbS_2$ series B with CdS, ZnO and ITO deposited without breaking the vacuum in the sputtering chamber.

The devices grown using this process were characterized by capacitance measurement. Figure 6.20 shows the capacitance as function of the dc bias.

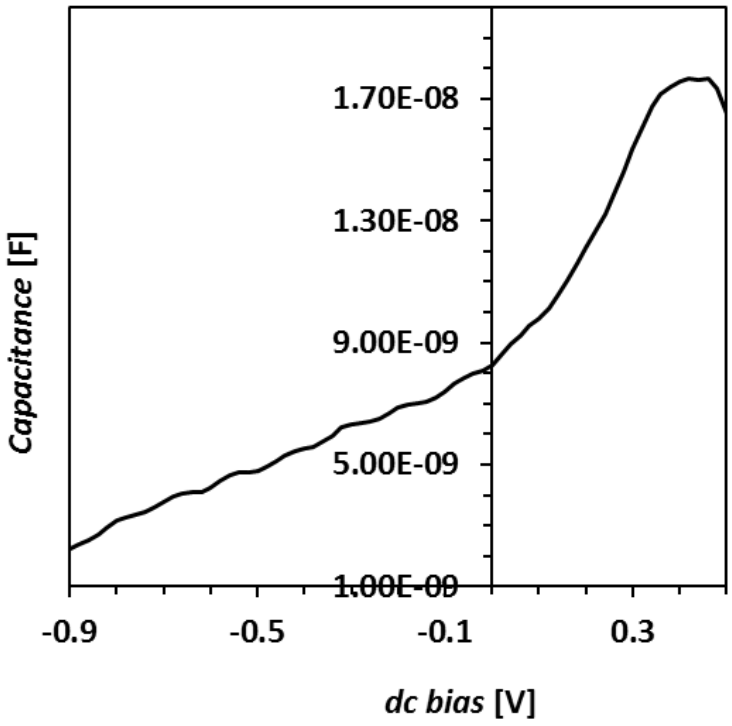

Figure 6.20: Capacitance as function of the dc bias of the device in the substrate configuration based on sulfurized $CuSbS_2$ of type B.

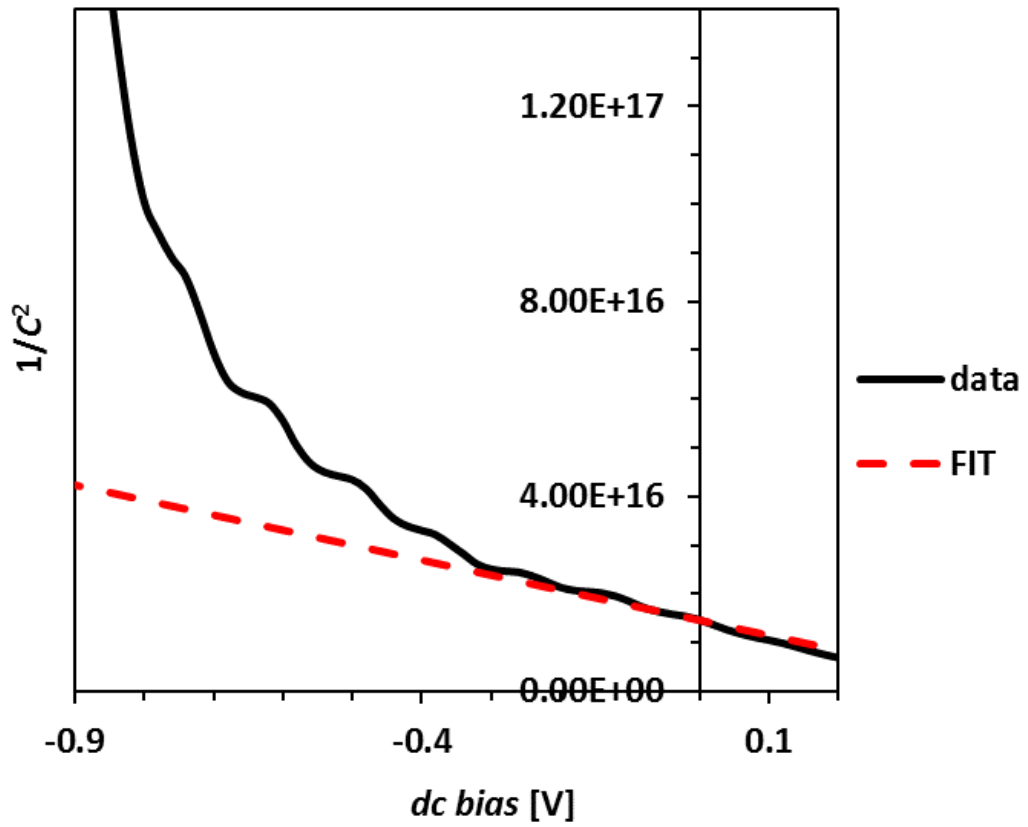

Figure 6.21: Mott-Schottky plot for a substrate cell based on $CuSbS_2$ series B. The black curve represents the inverse of the capacitance squared as function of the dc bias. The dashed red line is the tangent to the curve around zero.

From the capacitance-voltage profiling the graph $1/C^2$ vs. V was calculated as function of the dc bias (Mott-Schottky plot), as shown in Figure 6.21.

The last graph enabled estimation of the doping concentration at the junction, according to Equation (2.13). An approximate value of 10 was used for the relative permittivity $\mathcal{E}_r$ of $CuSbS_2$. From the calculation the device analysed presented a doping concentration N_A at the interface of ~10^{17} cm^{-3} – this being consistent with the value found in Chapter 5 from the Hall effect measurements on the $CuSbS_2$ films grown by sulfurization.

An efficiency of nearly 1% was achieved with Sb-rich precursor layers and with 1 mm^2 contact area cells. The related *J-V* curve is shown in Figure 6.22. The device shows higher current than before but the *FF* remains low at ~25%.

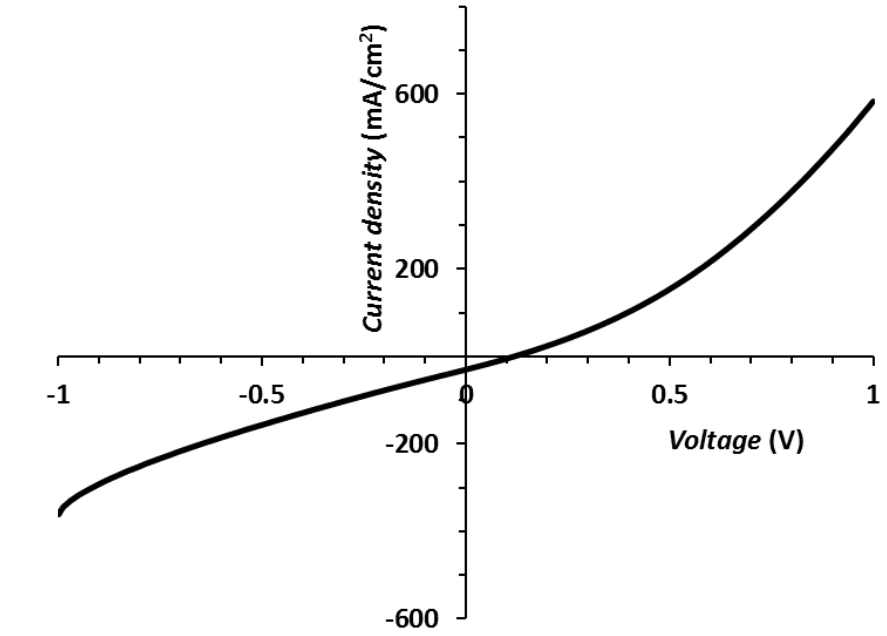

(a)

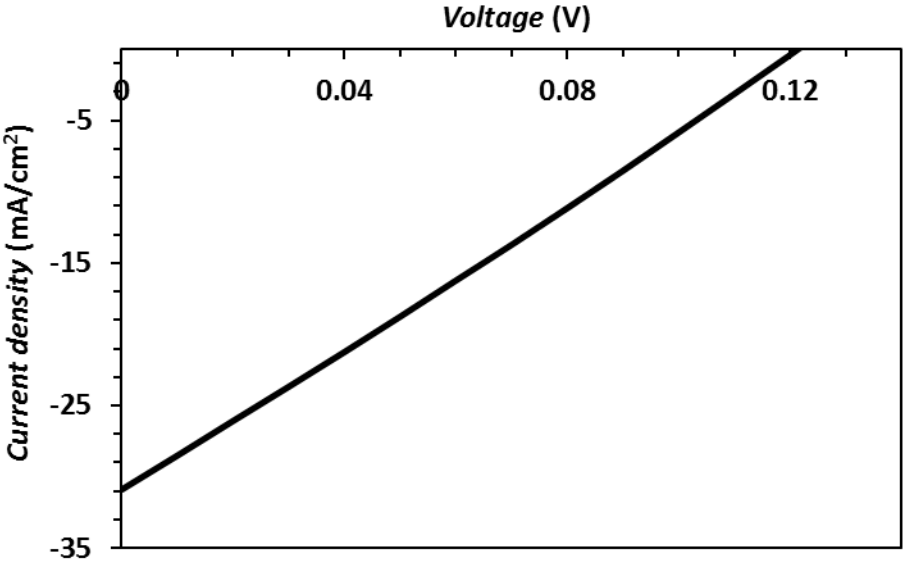

(b)

Figure 6.22: (a) *J-V* curve and (b) fourth quadrant of the optimized substrate device (with sulfurized $CuSbS_2$ series B) with 1 mm^2 contact area.

Finally some devices were fabricated with a thin layer of $MoSe_2$ between the back contact and the absorber. Other devices were grown by including a small amount of selenium powder during the sulfurization of the absorber layer. Both the processes had some beneficial

effects on the performance of the cells exhibiting photoactive response with efficiencies normally below 0.3%. However further work will be required to fully understand the mechanisms.

6.3.5 Substrate cells with $CuSbS_2$ grown from a single target

The last devices grown in the substrate configuration were based on $CuSbS_2$ films deposited by the one-step process. Most of the devices deposited both on molybdenum-foil and Mo-coated glass were short circuited, in particular those with absorber layers sputtered at 400°C. This could be caused by morphology of the absorber. In fact bigger grains grown at high temperature could favour the diffusion of material from the layers sputtered above (normally CdS and ITO) creating shunt paths between the two electrodes. This happened even by sputtering CdS and ITO on the absorber at room temperature. The cells with absorber layer deposited at RT exhibited a *J-V* curve with a clear diode shape but were not photoactive as shown in Figure 6.23.

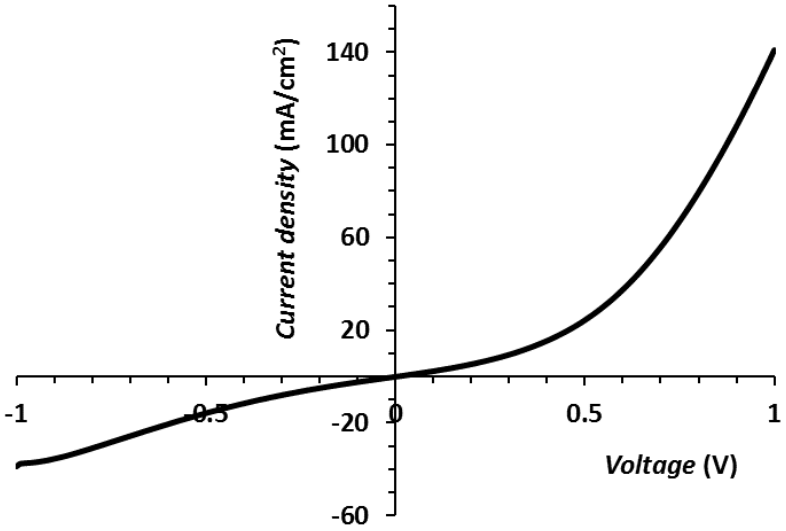

Figure 6.23: *J-V* curve of device in the substrate structure based on $CuSbS_2$ sputtered from the single target at RT and post-sulfurized at 150°C; CdS and ITO deposited at RT.

6.4 Discussion

Table 6.2 shows a summary of the main devices analysed in this Chapter.

Device geometry	Absorber synthesis method	Window layer	Intrinsic buffer	TCO	Doping or etching	*Voc* (V)	*Jsc* (mA/cm^2)	*FF* (%)	η (%)	Section ref.
superstrate	sulfurization of metal precursor, series B	CdS	none	SnO_2	none	0	0	0	0	6.3.1
superstrate	one-step rf sputtering, RT	CdS	none	SnO_2	none	0.22	0.08	39	0.0069	6.3.2
superstrate	one-step rf sputtering, 400°C	CdS	none	SnO_2	none	0.14	0.7	25	0.025	6.3.2
superstrate	one-step rf sputtering, RT + sulf. 150°C	CdS	none	SnO_2	none	0.36	0.1	25	0.009	6.3.2
substrate	sulfurization of metal precursor, series A	CdS (CBD)	none	GZO (ALD)	none	0.21	2.3	27	0.13	6.3.3
substrate	sulfurization of metal precursor, series B	CdS	none	AZO	indium doping, DIW soaking	0.22	1.83	25	0.10	6.3.4
substrate	sulfurization of metal precursor, series B	none	none	AZO	none	0	0	0	0	6.3.4
substrate (4 mm^2)	sulfurization of metal precursor, series B	CdS	i-ZnO	ITO	indium doping, DIW soaking	0.07	15	26	0.27	6.3.4
substrate (1 mm^2)	sulfurization of metal precursor, series B	CdS	i-ZnO	ITO	indium doping, DIW soaking	0.12	32	26	1.00	6.3.4
substrate	one-step rf sputtering, RT	CdS	i-ZnO	ITO	indium doping, DIW soaking	0	0	0	0	6.3.5

Table 6.2: Summary of the principal PV device results obtained with the fabricated $CuSbS_2$-based devices.

As demonstrated in Section 6.3, solar cells based on sulfurized $CuSbS_2$ were produced with a maximum efficiency ŋ of ~1% for dot contact cells. However the high values of current density recorded for dot contact devices – i.e. up to 30 mA/cm^2 – are incompatible with the integrated *EQE* curves. Systematic errors can be caused from overestimated contact areas and edge collection. However, the results presented in this Chapter on the $CuSbS_2$/CdS heterojunction are generally consistent with those found elsewhere.

Welch et al. [3] made devices based on $CuSbS_2$ with a maximum ŋ of ~0.86%. As described in Chapter 3 the authors deposited the absorber by a three-stage co-sputtering process. In particular the highest efficiencies were achieved with a thin layer of MoO_x between the Mo back contact and the absorber working as charge-selective layer in order to enhance the photocurrent [3]. The best *EQE* response among the devices reported from Welch was based on $CuSbS_2$ grown at 400°C and showed a similar shape to the *EQE* spectrum of some substrate cells presented in this Chapter (see Figure 6.17 – i.e. device with absorber layer deposited by sulfurization and ŋ ~0.1%). In particular the plot displayed a peak between 500 and 600 nm and a saddle between 600 and 700 nm. The *EQE* spectrum is characterized by an edge at ~400 nm related to the CdS absorption and cut-off at wavelengths > 700 nm for the effect of the absorber band gap of ~1.5 eV. From Beer-Lambert analysis on the absorption coefficient spectrum Welch indicated that at wavelengths between 600 and 700 nm the number of photons absorbed in the first 100 nm of the absorber layer is much higher than the number of carriers generated measured by *EQE*. This implied that recombination occurred in the absorber and also in the space charge region (a space charge region width W_{SCR} of ~100 nm was measured by *C-V* profiling) – i.e. this explains the saddle observed in the EQE spectrum 600 and 700 nm [3]. Conversely photons at wavelengths between 500 and 600 nm penetrate less deeply in the material, hence with less probability to recombine with defects or impurities in the absorber – i.e. this clarifies the central peak in Figure 6.17.

As discussed in Chapter 3, the maximum efficiency reported for $CuSbS_2$ solar cells is ~3.1% (not certified). The record device was fabricated in the substrate configuration Mo/$CuSbS_2$/CdS/AZO and the absorber layer was produced by sulfurization in H_2S atmosphere of electrodeposited metal stack [4]. Before the sulfurization stage the metal stack was preheated at 510°C in argon atmosphere. The preheating stage at high temperature yielded to the formation of dense $CuSbS_2$ films with strong adhesion to the substrate [5]. The highest efficiency reported from Ikeda et al. [4] could be attributed to the beneficial effects of

using H_2S as sulfurization agent – i.e. the hydrogen atoms could effectively passivate the defects in the absorber with potential increments of the photocurrent.

From the impedance and *J-V-T* analyses it has been demonstrated that the dominant transport mechanism in the $CuSbS_2$/CdS heterojunction is tunneling. The high value of the ideality factor *n* (i.e. > 2) indicated high local density of defects at the $CuSbS_2$/CdS interface [6]. It is plausible to deduce that the minority carriers move in the junction through the defect and impurity levels by multi-step tunneling transport. Therefore the main limitation to the device performance was the high concentration of defects and impurities at the interface – these acting as trap and recombination centers for the carriers.

Another issue was the high density of shunt paths between the front and back contact – this being particularly evident for the cells in the substrate configuration and recurrent for the devices with absorber grown by the one-stage process. The shunt paths could be caused from pinholes and pores in the absorber material, with consequent interdiffusion from the overlying layers.

A further constraint to the development of $CuSbS_2$-based devices is the appropriate selection of the n-type partner material. For the fabrication of prototype devices CdS has been adopted, being the most consolidate material in thin film solar cells. However CdS is not the best partner material for $CuSbS_2$ in terms of band alignment [3]. The basic mechanisms and the investigation of alternative window layer materials are discussed in Chapter 7.

Finally there are a few works on cells based on $CuSbS_2$ in the superstrate configuration. In fact $CuSbS_2$ is normally grown at high temperature and this potentially causes interdiffusion and delaminations induced from the underlying layers. This was consistently observed in the present study. The issue of pinholes and shunt paths in the superstrate cells was prevented by growing the absorber layer at room temperature by the one-stage technique. The resulting samples exhibited *J-V* curves with distinct rectifying shape. The maximum *Voc* observed was ~0.36 V for absorbers post-sulfurized at 150°C. This value is comparable with those reported for the best devices based on $CuSbS_2$ reported in refs. 8 and 9 – i.e. this encouraging the use of the alternative single-stage approach with the superstrate configuration. However the photocurrent was generally poor, this implying that a refinement of the one-step process is required.

The outcomes from the investigation on devices based on the $CuSbS_2$/CdS heterojunction were consistent with those reported elsewhere, with maximum efficiency being ~1%, this being limited primarily from defects and impurities at the interface.

6.5 Conclusions

Devices with ~1% efficiency based on the novel absorber material $CuSbS_2$ were fabricated in the substrate geometry and using the sulfurization process. It was demonstrated that $CuSbS_2$ forms a p-n junction with CdS and the dominant transport mechanism is tunneling. The *EQE* of the cells was generally low – i.e. recombination occurs in the bulk of the absorber and at the interface. The *Voc* was normally low, this probably being due to the selection of CdS as the n-type material for $CuSbS_2$. Finally in many samples the shunt resistance was low, implying the presence of pinholes and/or electrical shunts.

Devices were also fabricated in the substrate configuration by growing the absorber layer with the alternative one-step technique. Most of the samples had short circuits meaning electrical shunts in the absorber. Despite a few experiments having been carried out a better understanding of the microstructure and composition of the sputtered $CuSbS_2$ layers is required.

On the other hand devices grown in the superstrate configuration with single-stage sputtered $CuSbS_2$ exhibited a clear photovoltaic effect with relatively high *FF* (~39%) and *Voc* above 0.2V. In the superstrate devices it was feasible to prevent the electrical shunts by sputtering the absorber at room temperature. However for those samples the photocurrent was generally very low. This could be associated with recombination of the carriers with defects – impurities or secondary phases – either in the absorber or at the interface.

Finally the devices made with absorbers from the sulfurization process in the superstrate configuration were generally not good. This was due to delamination and possibly also due to interdiffusion induced in the samples at high temperature during the sulfurization process.

In conclusion, $CuSbS_2$ has been demonstrated to be a potential candidate as new absorber material. Active heterojunctions with CdS were fabricated with efficiency up to

~1% for very small contact areas. The performance of these devices remains too poor to upscale the $CuSbS_2$ technology at this stage in its development.

The main limitations of the solar cells based on $CuSbS_2$ are:

- defects and impurities in the absorber layer and at the interface
- CdS not a good window layer partner for $CuSbS_2$ [3].

Chapter 7 will explain in detail the latter point and will discuss the development and characterization of devices based on alternative window materials.

6.6 References for Chapter 6

[1] D. Abou-Rasa, G. Kostorz, D. Bremaud, M. Kälin, F. V. Kurdesau, A. N. Tiwari and M. Döbeli, "Formation and characterisation of $MoSe_2$ for $Cu(In,Ga)Se_2$ based solar cells", *Thin Solid Films*, vol. 480, pp. 433-438, 2005

[2] H. M. Al-Allak, A. W. Brinkman, H. Richter and D. Bonnet, "Dependence of CdS/CdTe thin film solar cell characteristics on the processing conditions", *Journal of Crystal Growth*, vol. 159, pp.910-915, 1996

[3] A. Welch, L. Baranowski, P. Zawadzki, C. DeHart, S. Johnston, S. Lany, C. Wolden and A. Zakutayev, "Accelerated development of $CuSbS_2$ thin film photovoltaic device prototypes", *Progress in Photovoltaics: Research and Applications*, *in press*

[4] S. Ikeda, Y. Iga, W. Septina, T. Harada and M. Matsumura, "$CuSbS_2$-based thin film solar cells prepared from electrodeposited metallic stacks composed of Cu and Sb layers", *Proceedings of the 2013 IEEE 39th Photovoltaic Specialist Conference (PVSC)*, pp. 2598-2601, 2013

[5] W. Septina, S. Ikeda, Y. Iga, T. Harada and M. Matsumura, "Thin film solar cell based on $CuSbS_2$ absorber fabricated from an electrochemically deposited metal stack", *Thin Solid Films*, vol. 550, pp. 700-704, 2014

[6] O. Breitenstein, P. Altermatt, K. Ramspeck and A. Schenk, "The origin of the ideality factors n>2 of shunt and surfaces in the dark I-V curves of Si solar cells", *Proceedings of the 21st European Photovoltaic Solar Energy Conference (PVSEC 2006)*, pp. 625-628, 2006

7 Alternative window layers for $CuSbS_2$-based devices

7.1 Introduction

Chapter 6 discussed the properties of prototype devices based on the $CuSbS_2$/CdS heterojunction. As extensively reported in the present study and elsewhere the performances of this type of devices are significantly limited. In particular two main challenges were identified, as follows.

a) Defects and impurities in the absorber and at the junction, according to the measurements presented in Chapter 6 by the impedance and *J-V-T* studies. Devices based on the $CuSbS_2$/CdS heterojunction have been produced with an uncertified maximum efficiency of ~3.1% by Ikeda et al. [1]. The authors ostensibly reduced the defects in the absorber by means of H_2S – i.e. it was assume that the hydrogen atoms had some effects in passivating the defects (e.g. at the grain boundaries). In addition the use of KCN etching removed the $Cu_{2-x}S$ secondary phases at the interface with subsequent improvement in the properties of the junction. Despite the refinement of the fabrication process, the reported conversion efficiencies of devices based on $CuSbS_2$ are clearly inadequate for commercialization.
b) Band alignment of $CuSbS_2$ and CdS as reported in ref. 2. For the development of $CuSbS_2$-based prototype devices CdS was used, this being the window layer material commonly used in thin film solar cells. However Welch demonstrated by surface calculations on $CuSbS_2$ that the material presents electron affinities and work functions incompatible with CdS for PV applications [2]. Figure 7.1 displays the band diagram of the heterojunction $CuSbS_2$/CdS, according to the calculations reported by Welch.

As shown in Figure 7.1 there is no electric field at the interface, which presents abrupt 'cliffs' both at the valence and conduction bands. Welch highlighted the significant limits of the $CuSbS_2$/CdS heterojunction for device applications and suggested the exploration of alternative window layer materials.

The desirable properties of the new compounds to employ as window layer are:

a) high band gap – i.e. $Eg > 2$ eV;

b) relatively low electron affinity in order to avoid the cliff-type band alignment and have strong electric field at the interface.

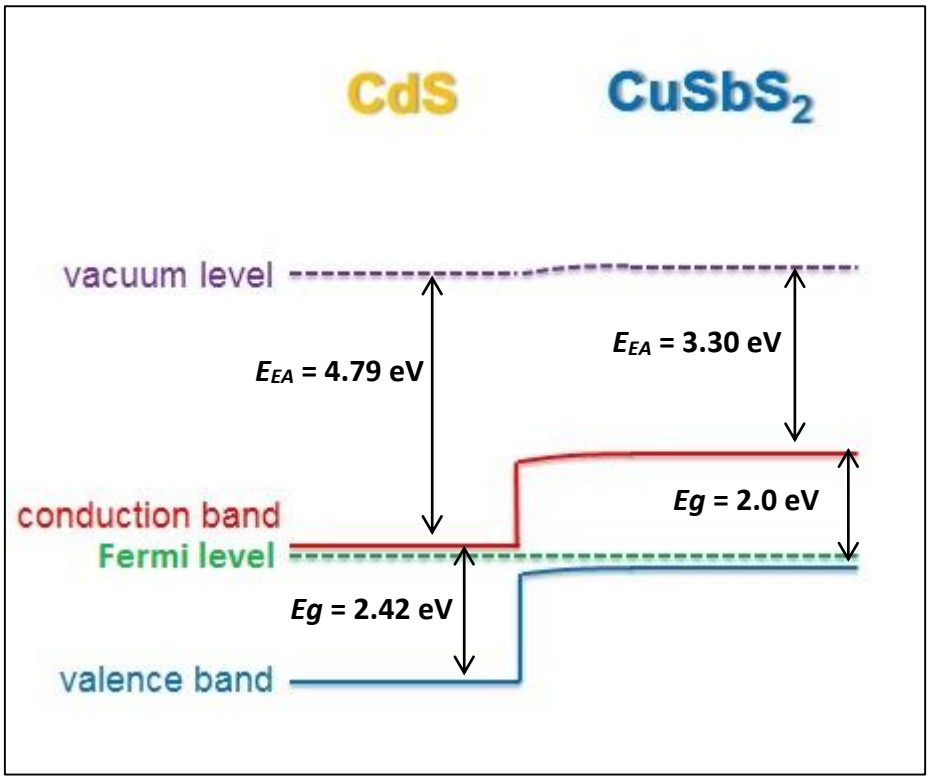

Figure 7.1: Band alignment between $CuSbS_2$ (for the (001) surface in ref. 2) and CdS [3], assuming highly doped semiconductors. The band gap of $CuSbS_2$ estimated by the DFT calculations was ~2 eV.

Three potential candidates for application as window layer were identified:

- zinc sulfide (ZnS), having E_{EA} = 3.9 eV and Eg = 3.54 eV;
- zinc selenide (ZnSe), showing E_{EA} = 4.1 eV and Eg = 2.58 eV;
- zinc telluride (ZnTe) exhibiting E_{EA} = 3.5 eV and Eg = 2.26 eV [3].

The Figures 7.2, 7.3 and 7.4 display the band alignment of $CuSbS_2$ (according to the surface calculations reported in ref. 2) with ZnS, ZnSe and ZnTe respectively.

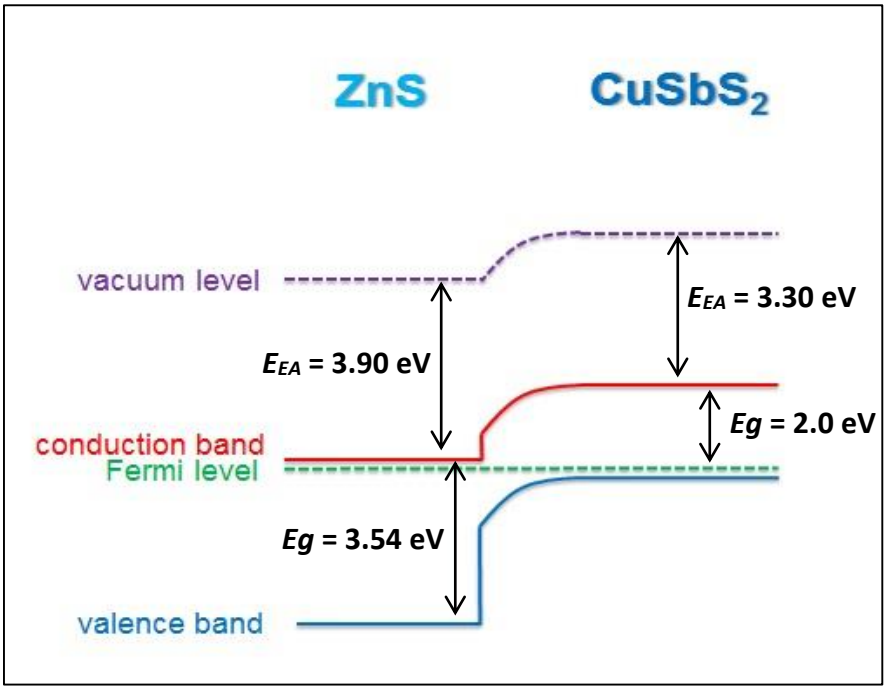

Figure 7.2: Band alignment of $CuSbS_2$ for the (001) surface in ref. 2 and ZnS [3], presuming highly doped semiconductors.

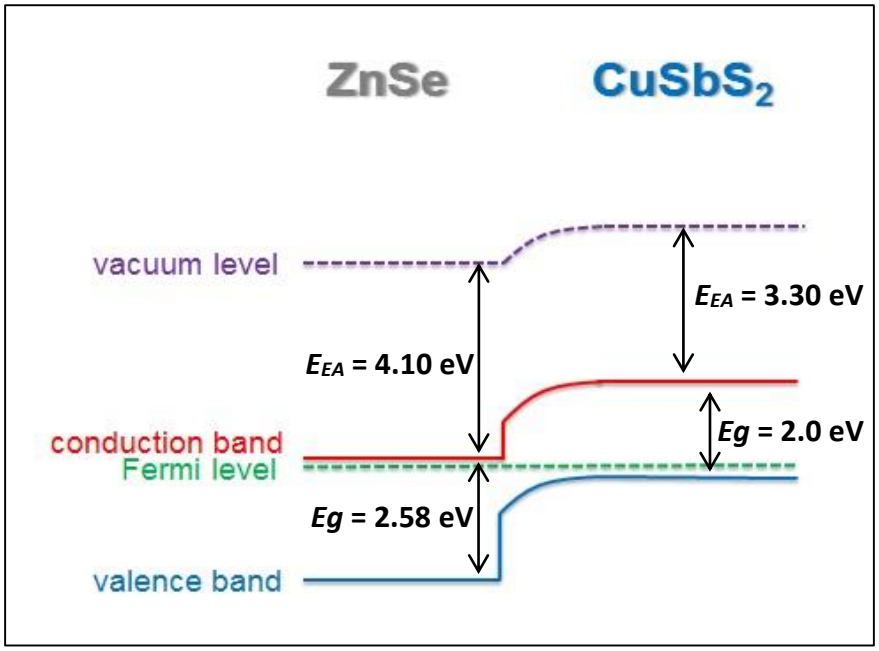

Figure 7.3: Band alignment of $CuSbS_2$ for the (001) surface in ref. 2 and ZnSe [3], with the hypothesis of highly doped semiconductors.

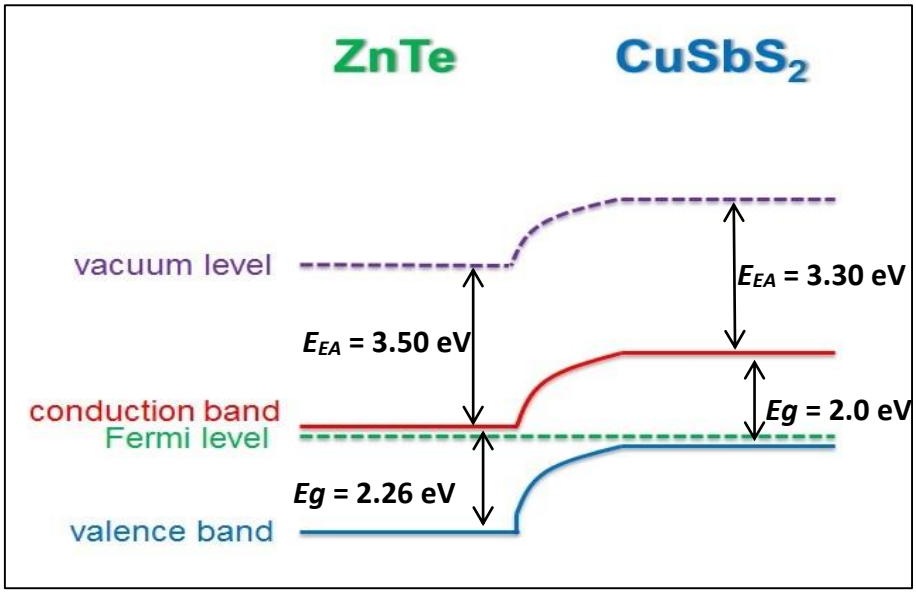

Figure 7.4: Band alignment of $CuSbS_2$ for the (001) surface in ref. 2 and ZnTe [3], assuming highly doped semiconductors.

Figures 7.2 and 7.3 reveal that both ZnS and ZnSe are potentially appropriate materials to be included in $CuSbS_2$-based PV devices as window layers – i.e. a strong electric field is present in the junctions pointing to the desired direction. The same trend is displayed in Figure 7.4 for the $CuSbS_2$/ZnTe interface. However ZnTe exhibits a relatively narrow band gap and grows naturally p-type [4], hence ZnTe was not considered in the experimental study. On the other hand, zinc sulfide and zinc selenide are wide band gap n-type semiconductors normally exhibiting high resistivity – i.e. ρ (ZnS) ~10^7 Ω cm [5]; ρ (ZnSe) ~10^4 Ω cm [6].

The usual techniques adopted for the deposition of zinc sulfide thin films are pulsed-laser- and chemical vapour deposition. The fabrication of ZnS thin films by electrochemical deposition arc and magnetron sputtering are also reported. Zinc selenide thin films can be deposited by a large number of different methods, including: close-space sublimation, MOCVD, hydrochemical-, electrochemical-, pulsed-laser-, chemical bath-, molecular beam-, atomic layer-, photochemical- and chemical vapour-deposition. In this work thin films of zinc sulfide and zinc selenide were deposited by rf sputtering. The structural, optical and electrical properties of sputtered ZnS and ZnSe films are described in Section 7.2.

Prototype devices based on $CuSbS_2$ were fabricated both in the superstrate and substrate configurations by using the alternative window layer materials. For the development of the devices the absorber layer was synthesized by either sulfurization or the single-stage process. Section 7.3 presents the characterization of the prototype devices with either ZnS or ZnSe as window layer. The outcomes from this investigation are discussed in Section 7.4.

7.2 Experimental

Thin films of zinc sulfide and zinc selenide were deposited on 5 x 5 cm^2 SLG by rf sputtering for thickness calibration. The substrates were placed in the sputtering chamber AJA International Orion Phase II with base pressure of ~10^{-7} Torr. The samples were generally fixed at a working distance of 107 mm and rotated at 80 rpm. A series of experiments were undertaken in order to find the optimal conditions to grow ZnS and ZnSe films with suitable characteristics for window layer applications. The samples were characterized by XRD, optical spectroscopy and the van der Pauw technique.

7.2.1 Calibration of ZnS films

Zinc sulfide films were deposited from a 2” x 0.125” ZnS (99.99%) sputtering target supplied from AJA International. The power was usually fixed at 46 Wrf and other sputtering parameters were varied as follows – pressure: 2 - 40 mTorr; temperature: 25 - 400°C; time: 90 - 240 minutes.

The ZnS films grown by rf sputtering were generally amorphous. Films with thickness of ~2 µm were produced under the following conditions: power = 46 Wrf; pressure = 2 mTorr; temperature ~300°C; time ~180 minutes. The XRD pattern of the resulting sample shown in Figure 7.5 presented a small peak at 2θ ~28.5°, this implying that the film was crystalline. However the XRD measurement was insufficient for the phase and crystal structure identification.

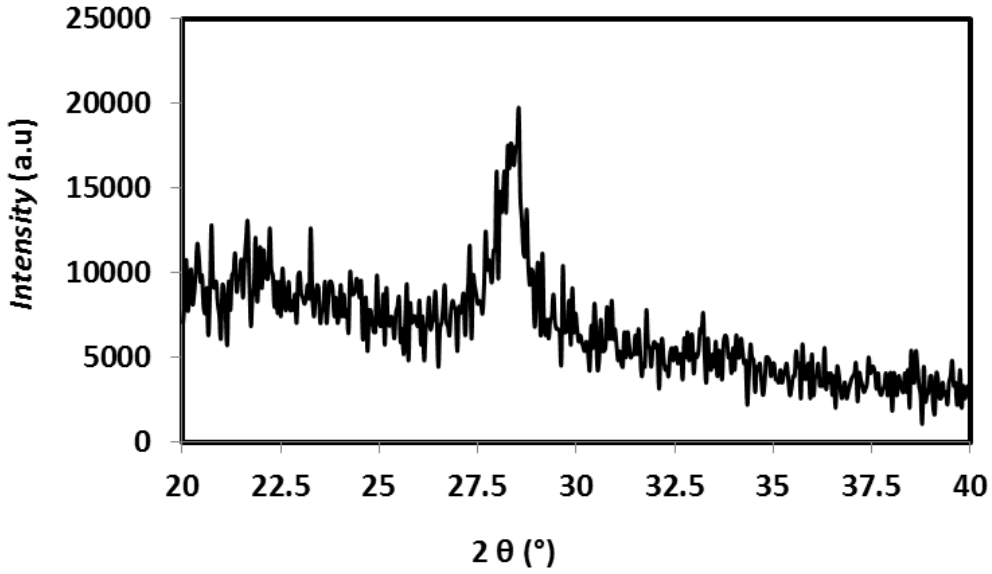

Figure 7.5: XRD measurement of ZnS film grown by rf sputtering by: power = 46 Wrf; pressure = 2 mTorr; temperature ~300°C; time ~180 minutes. The XRD pattern presented a small peak at 2θ ~28.5°. The measurement was insufficient for the phase detection.

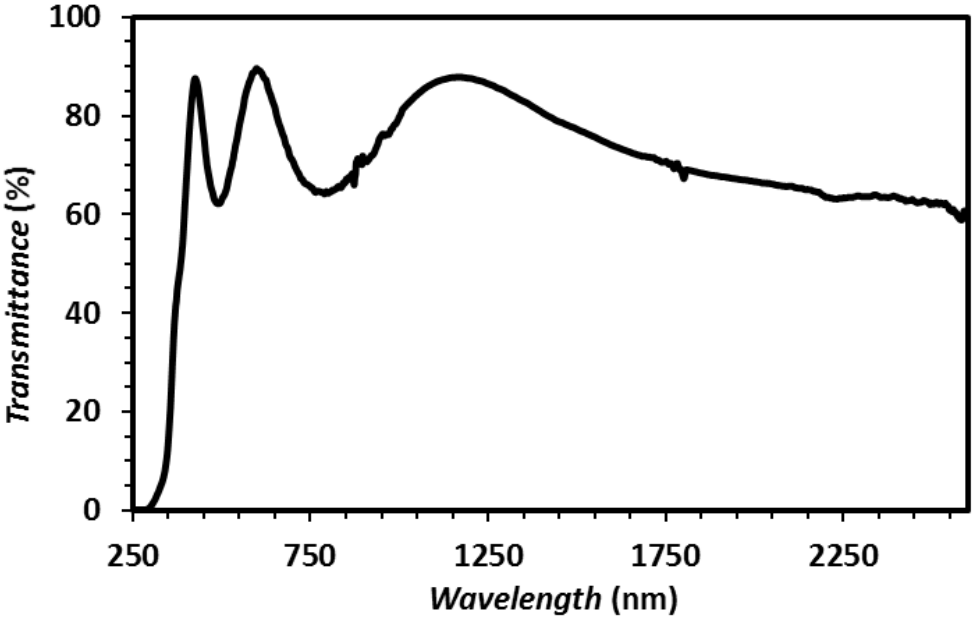

Figure 7.6: Transmittance spectrum of a ZnS film grown by rf sputtering under the following conditions: power = 46 Wrf; pressure = 2 mTorr; temperature ~300°C; time ~180 minutes.

The transmittance spectrum of the sample shown in Figure 7.6 showed the high transparency of the ZnS sputtered films (> 60% in the visible) and having a band gap of ~3.5 eV. The sputtered ZnS films were generally very resistive, exhibiting sheet resistances above 10 MΩ/□ – i.e. beyond the detection limit of the van der Pauw instrument.

7.2.2 Calibration of ZnSe films

Zinc selenide films were grown by rf sputtering from a 2" x 0.125" ZnSe (99.99%) target provided from AJA International. The sputtering parameters were ranged as follows – power = 46 Wrf; pressure: 2 - 10 mTorr; temperature: 200 - 400°C; time 90 - 180 minutes.

Crystalline films were produced by sputtering at 46 Wrf for ~180 minutes under pressure of 2 mTorr and substrate temperature of 400°C. The XRD analysis shown in Figure 7.7 was inadequate for the phase detection or to determine the lattice structure.

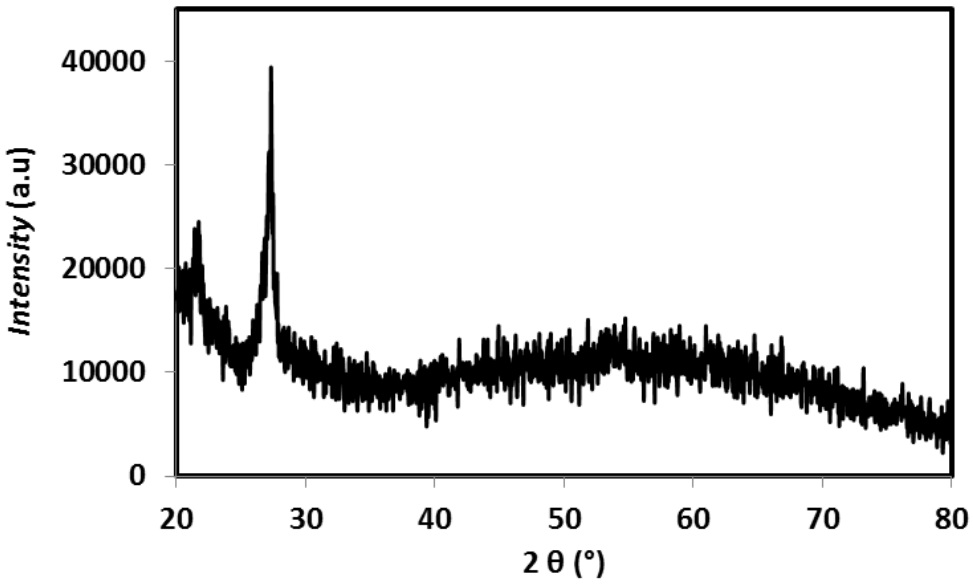

Figure 7.7: XRD analysis of ZnSe film grown by rf sputtering under the following conditions: power = 46 Wrf; pressure = 2 mTorr; temperature ~400°C; time ~180 minutes. The XRD pattern exhibited a sharp peak at 2θ ~27.35° and smaller peak at 2θ ~21.75°.

The ZnSe film grown under these conditions presented thicknesses of ~2 μm and high transparencies (above 60%) with estimated band gaps of ~2.7 eV, as shown in Figure 7.8.

Figure 7.8: Transmittance spectrum of a ZnSe film grown by rf sputtering under the following conditions: power = 46 Wrf; pressure = 2 mTorr; temperature = 400°C; time ~180 minutes.

According to the van der Pauw measurements the ZnSe films exhibited high resistance, having sheet resistances above 10 MΩ/□.

7.3 Results

The sputtered films of ZnS and ZnSe were included in prototype devices both in the superstrate and substrate configurations illustrated in Section 6.2 – i.e. by replacing CdS with either ZnS or ZnSe. For the absorber synthesis both the sulfurization and single-step process were considered. The prototype devices were characterized by *J-V* analysis and *EQE*.

7.3.1 Superstrate cells with sulfurized $CuSbS_2$

The samples grown in the superstrate configuration $Au/CuSbS_2/ZnS(e)/SnO_2/glass$ based on sulfurized $CuSbS_2$ films were generally unsuitable for PV application, presenting visible pinholes and delaminations.

7.3.2 Superstrate cells with $CuSbS_2$ from one-step process

(a) ZnS

The prototype devices were fabricated with the structure Au/$CuSbS_2$/ZnS/SnO_2/glass by depositing ~2 µm ZnS on SnO_2-coated glass (see Section 7.2) and then ~1 µm $CuSbS_2$ sputtered at RT (see Section 5.4).

The *J-V* curve in Figure 7.9 shows that the resulting devices were photoactive, presenting high *Voc* and very low *FF* and *Jsc*. To the best of author's knowledge 0.56 V is the highest value of *Voc* reported for $CuSbS_2$-based devices. However the poor photocurrent limited the efficiency of the cell.

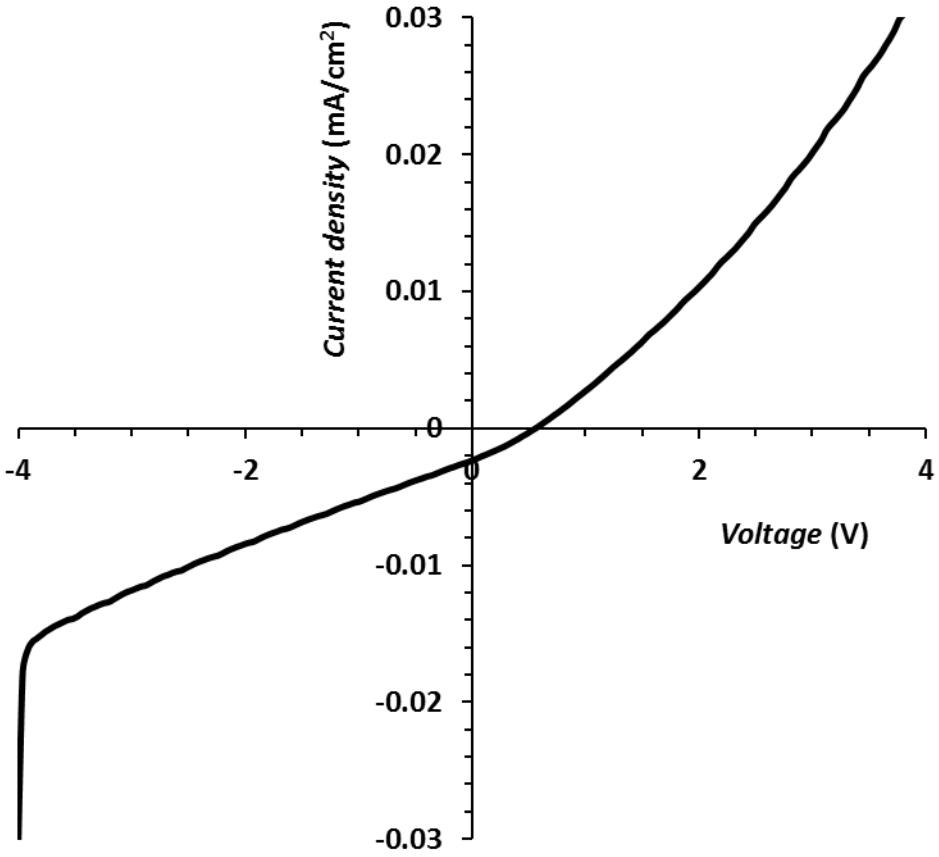

(a)

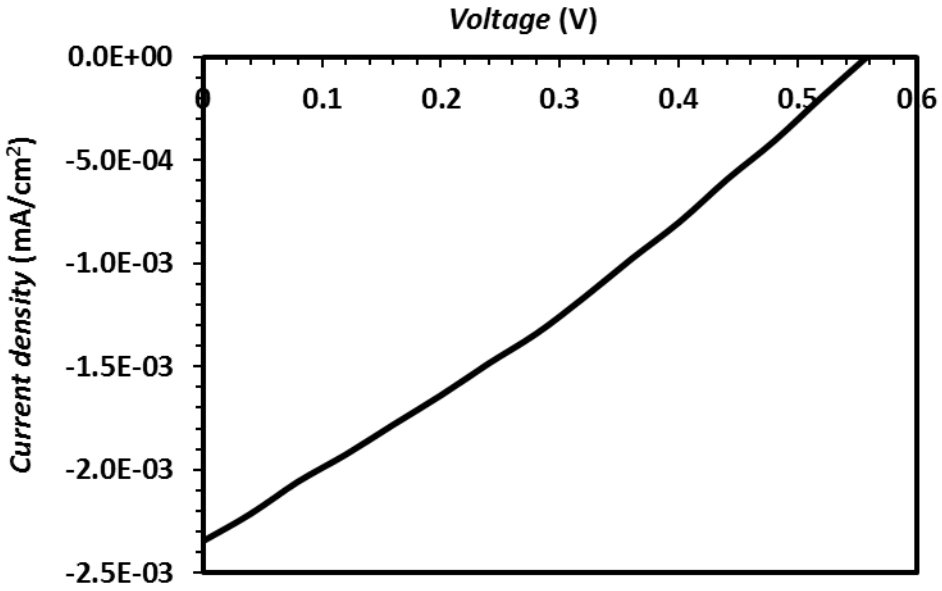

(b)

Figure 7.9: (a) *J-V* analysis and (b) the fourth quadrant for the device in the superstrate configuration based on ZnS and $CuSbS_2$ grown from the single-step process.

The *EQE* analysis reported in Figure 7.10 confirmed the low photocurrent of the device. . This potentially was due to strong recombination in the device.

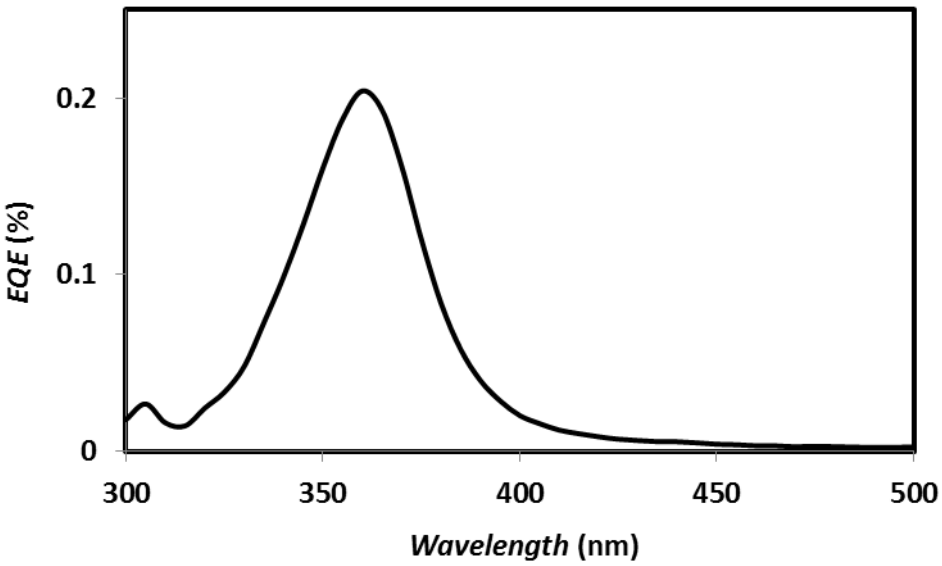

Figure 7.10: *EQE* spectrum of superstrate cell with ZnS and $CuSbS_2$ grown from the single target. The extremely low area under the *EQE* curve is associated to poor photocurrent

Attempts to improve the performance of the devices were made, including, deposition of the absorber at 400°C, post-sulfurization treatment and doping the absorber with NaF. However all these procedure were ineffective in enhancing the efficiency of the cells.

(b) ZnSe

Samples were produced with the structure glass/SnO_2/ZnSe/$CuSbS_2$/Au by depositing ~2 µm ZnSe deposited on SnO_2-coated glass by rf sputtering and ~1 µm $CuSbS_2$ grown at RT by the one-step process.

The resulting devices were photoactive, as shown in Figure 7.11. Although the sample exhibited relatively high *Voc* – i.e. ~0.26 V – the photocurrent and the *FF* were poor and therefore the efficiency of the devices was low. The *J-V* curve for $CuSbS_2$/ZnS in Figure 7.11 (a) is unusual in that shows a diode response for very high forward voltages, ~10V in this case. This value is much greater than the built-in voltage expected from the band diagram in Figure 7.2. Moreover, it is difficult to explain, given that the band gaps and band offsets are all less than several eV. The *EQE* spectrum displayed in Figure 7.12 confirmed the deficiency of photocurrent. The low photocurrent implied potential recombination in the absorber and at the interface.

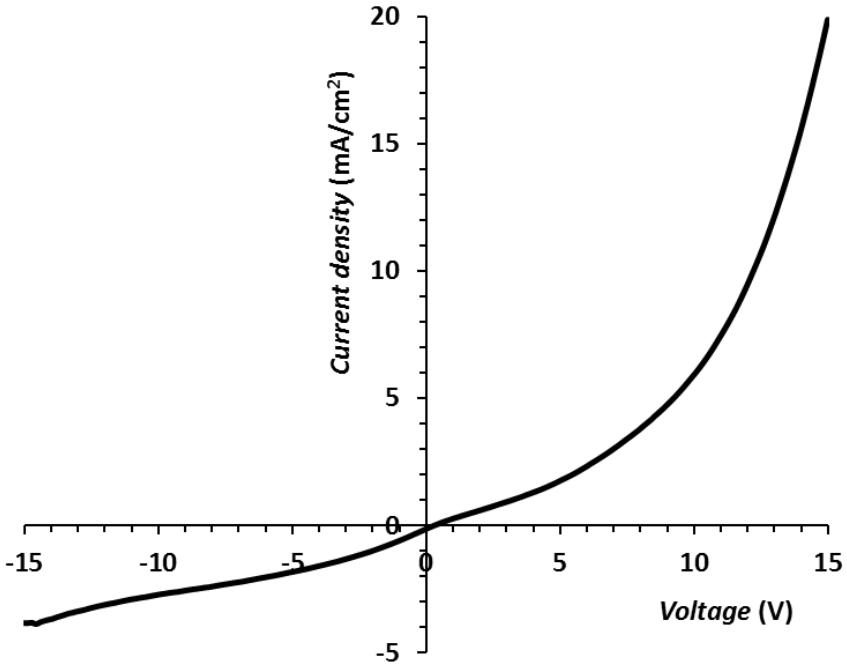

(a)

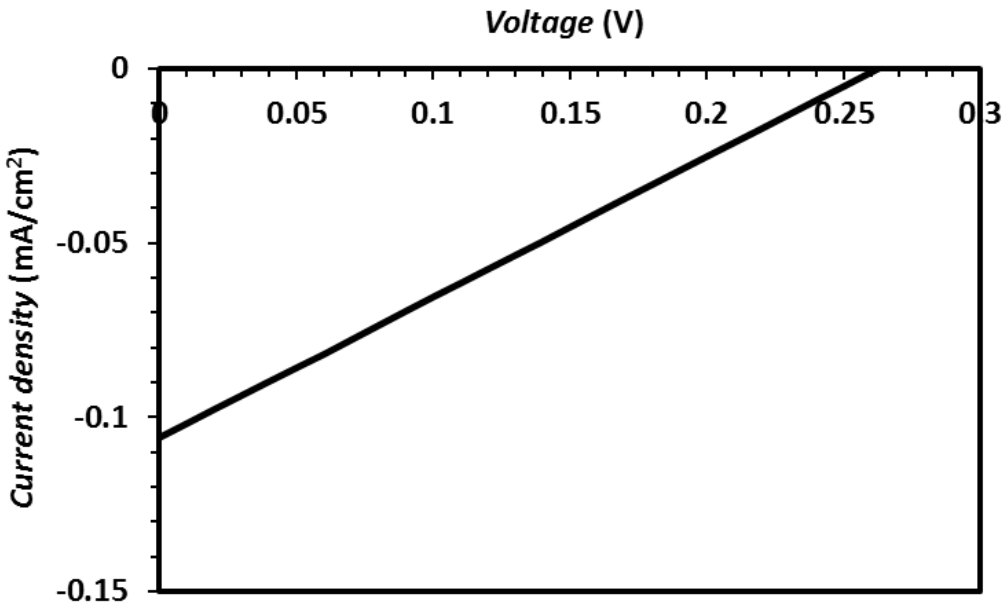

(b)

Figure 7.11: (a) *J-V* analysis and (b) the fourth quadrant for the cell based on the superstrate structure with ZnSe and $CuSbS_2$ deposited from the single-step process.

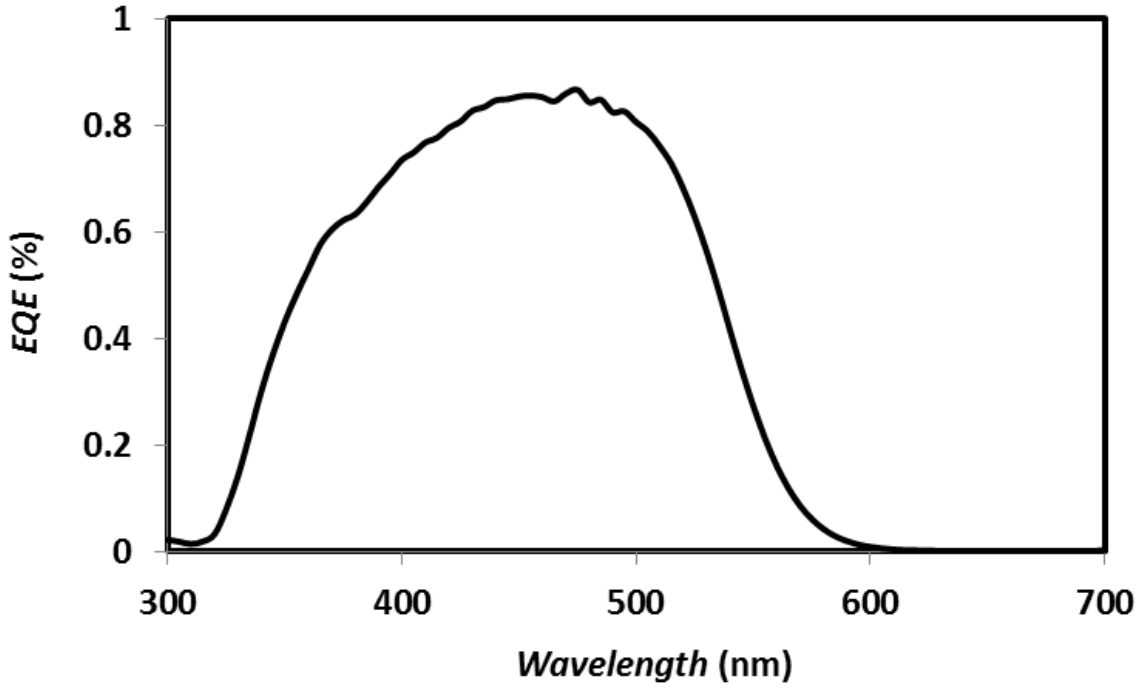

Figure 7.12: *EQE* analysis of the sample in the superstrate structure fabricated with ZnSe and $CuSbS_2$ deposited from the one-step process.

Finally the various experiments undertaken to improve the photocurrent in the cells with superstrate configuration were not effective.

7.3.3 Substrate cells with sulfurized $CuSbS_2$

(a) ZnS

A smaller number of devices were produced with the substrate structure glass/SnO_2/ZnS/$CuSbS_2$/Au with sulfurized absorber. The samples generally exhibited diode response but were not photoactive, as shown in Figure 7.13.

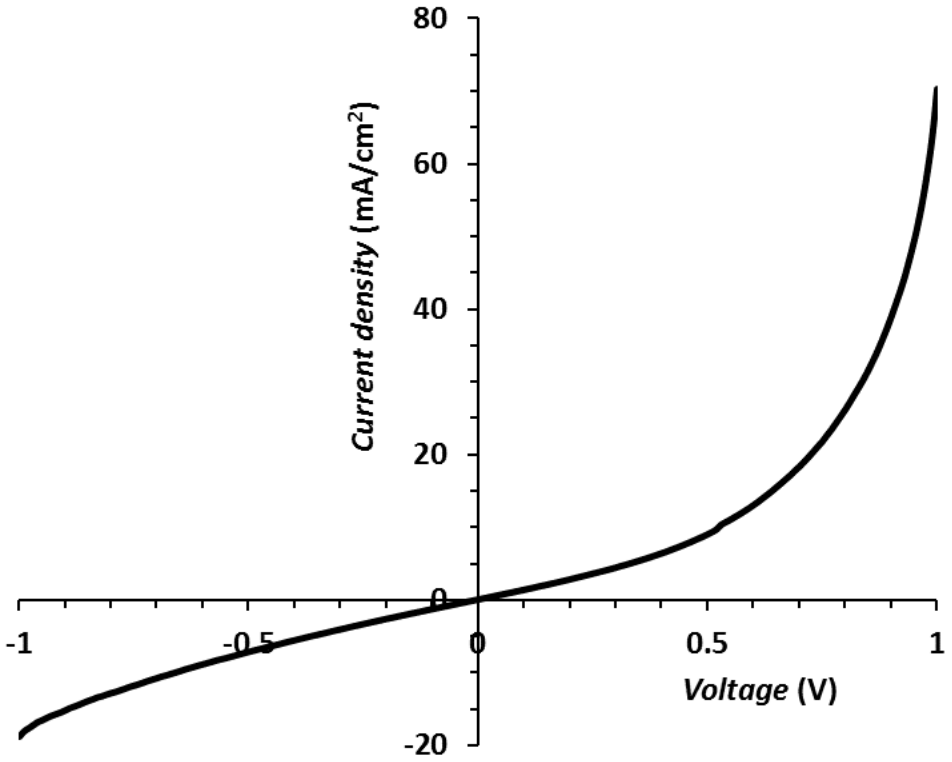

Figure 7.13: *J-V* curve of substrate device based on the $CuSbS_2$/ZnS heterojunction with sulfurized absorber.

(b) ZnSe

The cells were grown in the configuration Mo/$CuSbS_2$/ZnSe/ZnO/ITO. The absorber was sulfurized under the conditions described in Section 5.3.4 and covered with ~2 µm ZnSe. As shown from the *J-V* curve in Figure 5.14, the devices resulted photoactive but with extremely low *Voc* and photocurrent.

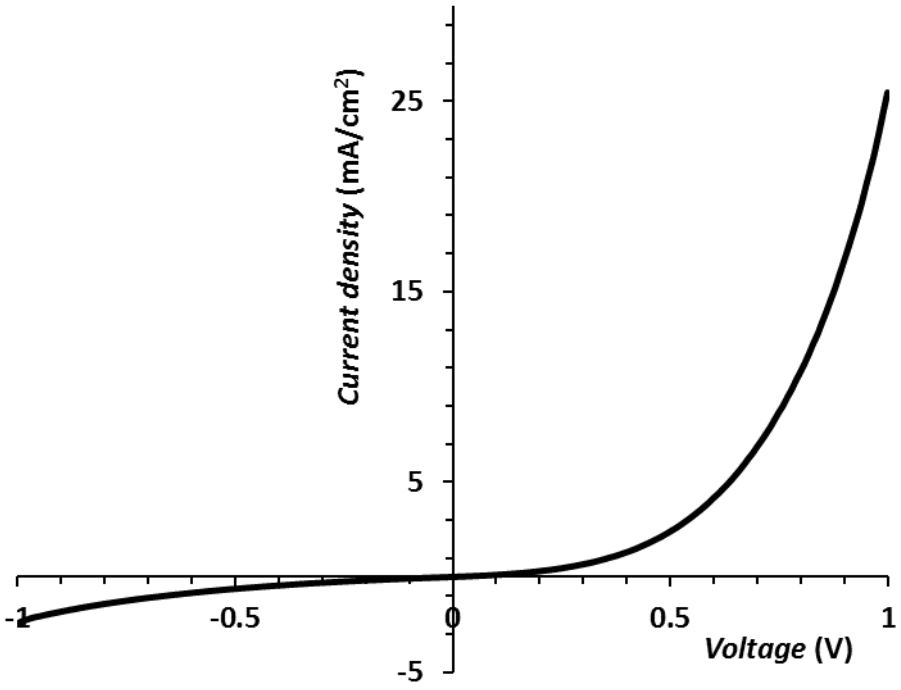

(a)

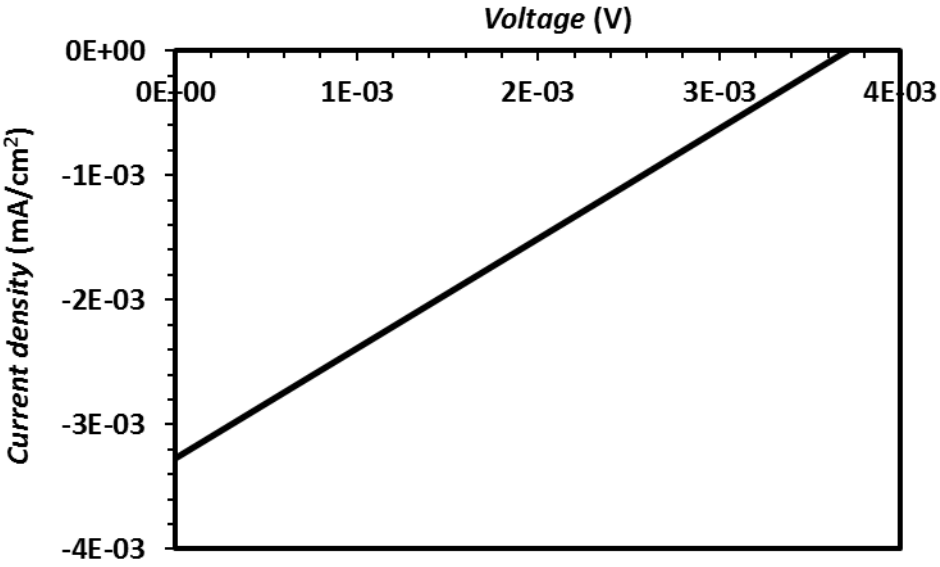

(b)

Figure 7.14: (a) *J-V* analysis and (b) the fourth quadrant for the device grown in the substrate structure based on sulfurized $CuSbS_2$ and ZnSe

7.3.4 Substrate cells from single target

Additional devices in the substrate structure were fabricated by growing the absorber with the one-stage process. The samples were generally not photoactive or very weakly photoactive, as shown in Figures 7.15 and 7.16 respectively for ZnS and ZnSe used as window layer.

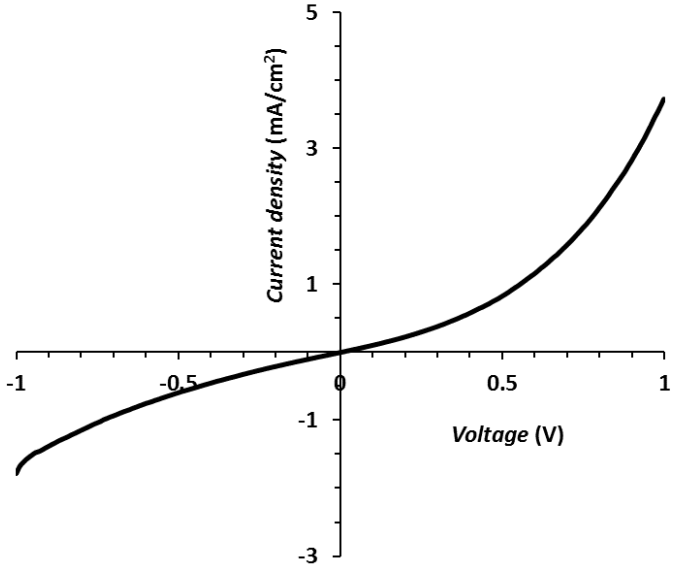

Figure 7.15: *J-V* curve of substrate sample based on the $CuSbS_2$/ZnS with absorber layer deposited by the single-stage approach.

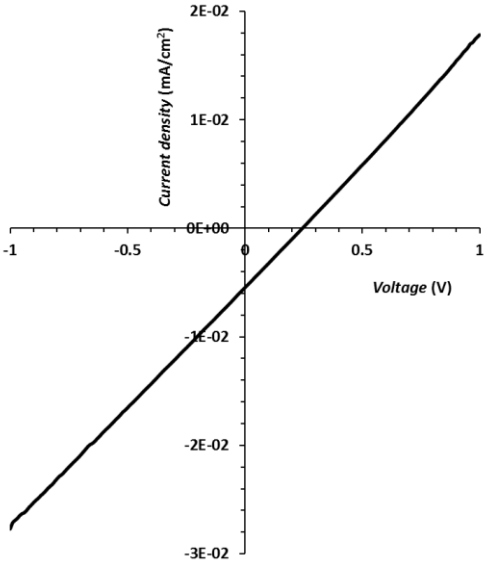

(a)

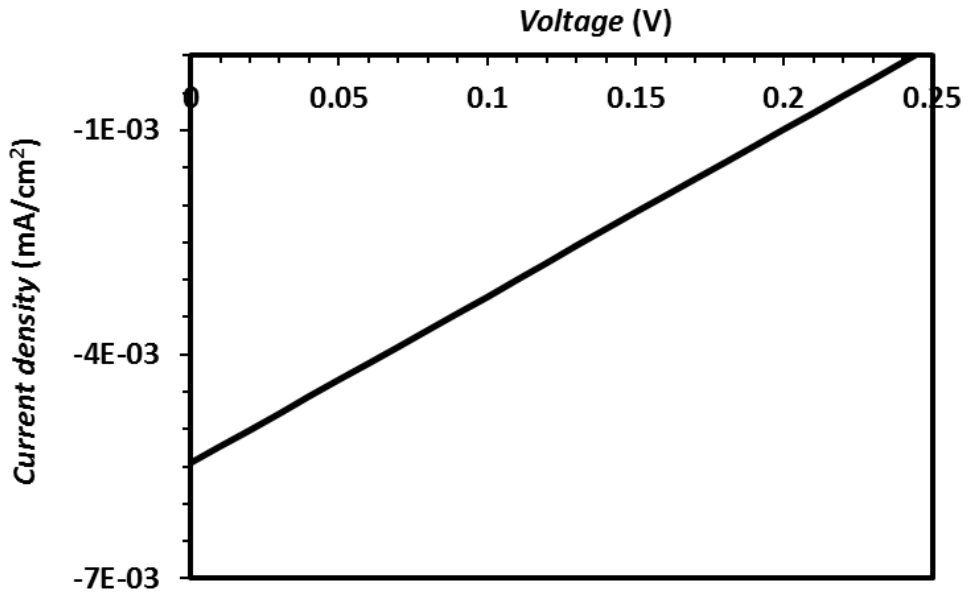

(b)

Figure 7.16: (a) *J-V* analysis and (b) the fourth quadrant for the device grown in the substrate structure based on ZnSe and $CuSbS_2$ grown from the ternary target.

7.4 Discussion and final remarks

The results presented in Section 7.3 demonstrated that both ZnS and ZnSe formed a p-n junction with $CuSbS_2$. In particular with ZnSe the open-circuit voltage increased to ~0.26 V and with ZnS it increased considerably to ~0.56 V. The open-circuit voltage measured in $CuSbS_2$/CdS devices was generally below 0.2 V (see Chapter 6). This proved experimentally the effectiveness of both ZnSe and ZnS in improving the properties of the junction in terms of band alignment with $CuSbS_2$ as compared to CdS. The cells were grown in the superstrate structure with the absorber layer deposited from the single target at room temperature. This approach prevented potential interdiffusion and shunt paths.

However the measured photocurrents were generally very low. This could be related to the high resistivity of ZnSe and ZnS. In fact the photocurrents were particularly low for the devices grown with ZnS – i.e. the most resistive material. In addition to the issues of the absorber layer (e.g. defects and impurities), the high resistivity of the window layers resulted in dramatic decrease of the photocurrent. Furthermore the properties of the p-n junction with the absorber synthesized at RT could be not optimal. However even the devices grown in the

substrate configuration with ZnS and ZnSe generally exhibited *Jsc* values that were very low compared to those with CdS.

The poor photocurrent was also observed from the *EQE* analysis. The unusual *EQE* spectra presenting cut-off at short wavelengths and the low *EQE* values probably implied that recombination occurred in the absorber and at the interface for most of the wavelengths.

Another characteristic of the *J-V* response of the superstrate devices in particular with ZnSe and $CuSbS_2$ produced by the one-stage process was the high forward bias to make a current flow (see Figure 7.11).

Finally this study confirmed a potential increase in the open-circuit voltage of $CuSbS_2$-based devices by means of an improvement in the band alignment of the absorber with the alternative window layer materials. In particular with ZnS open-circuit voltages up to 0.56 V were achieved. However a drop in the photocurrent was observed, as expected from the high resistivity of ZnS and ZnSe. There are not published works on the $CuSbS_2$/ZnS and $CuSbS_2$/ZnSe interfaces, hence comparison is not possible.

More work is required in order to fully understand the properties of the $CuSbS_2$/ZnS and $CuSbS_2$/ZnSe heterojunctions and improve the photocurrent of the PV devices. In particular the main challenge is the optimization of the structure, thickness and conductivity of the window layer.

7.5 References for Chapter 7

[1] S. Ikeda, Y. Iga, W. Septina, T. Harada and M. Matsumura, "$CuSbS_2$-based thin film solar cells prepared from electrodeposited metallic stacks composed of Cu and Sb layers", *Proceedings of the 2013 IEEE 39th Photovoltaic Specialist Conference (PVSC)*, pp. 2598-2601, 2013

[2] A. Welch, L. Baranowski, P. Zawadzki, C. DeHart, S. Johnston, S. Lany, C. Wolden and A. Zakutayev, "Accelerated development of $CuSbS_2$ thin film photovoltaic device prototypes", *Progress in Photovoltaics: Research and Applications, in press*

[3] Y. Nemirovsky and N. Amir, "Surfaces/interfaces of narrow-gap II-VI compounds", *Narrow-gap II-VI Compounds for Optoelectronic and Electromagnetic Applications*, pp. 291-326, 1997

[4] D. B. Laks, C. G. Van de Walle, G. F. Neumark and S. T. Pandelides, "Role of native defects in wide-band-gap semiconductors", *Physical Review Letters*, vol. 66, no. 5, pp. 648-651, 1991

[5] Bo Long, Shuying Cheng, Haifang Zhou, Jie Liao, Hong Zhang, Hongjie Jia and Hongnan Li, "The optical and electrical characteristics of ZnS:In thin films prepared by chemical bath deposition method", *ECS Solid State Letters*, vol. 3, no. 11, pp. 140-143, 2014

[6] E. M. Sofronova, V. V. Starikov, D. S. Sofronov, E. I. Kostenyukova, A. M. Lebedynskiy and P. V. Mateychenko, "Optical and electrical properties of ZnSe films grown by hydrochemical deposition", *Inorganic Materials*, vol. 51, no. 9, pp. 884-890, 2015

8 Discussion

8.1 Preliminary remarks

This Chapter discusses the principal findings of the thesis, with emphasis on the similarities and differences with other experimental works from the literature (Section 8.2), and on the main limitations of the approach to investigation presented here (Section 8.3).

A significant branch of the PV research community is focused on the identification of novel absorber materials based on sustainable elements. The interest in $CuSbS_2$ and Cu_3BiS_3 for PV applications is growing due to their promising optical and electrical characteristics for use as absorber layers in thin film solar cells. Indeed, during the course of this investigation, several new groups have become active in the field and have contributed to the literature.

In the present work $CuSbS_2$ and Cu_3BiS_3 were mainly grown by sulfurization of 'precursor' metal film stacks. The synthesis of single-phase films was not expected to be straightforward due to the complexity of the Cu-Sb-S and Cu-Bi-S phase diagrams and the presence of phases that may compete with the formation of the target phases. Indeed, the deposition conditions had strong impact on the phase composition of the sulfurized samples. $CuSbS_2$ single-phase films were synthesized from a nearly stoichiometric 'precursor' layer by sulfurizing at atmospheric nitrogen pressure – in order to prevent elemental loss of antimony – and by tuning the other sulfurization parameters – i.e. the mass of sulfur, and the annealing temperature and time. Similarly Cu_3BiS_3 single-phase films were produced from a metal stack having Cu:Bi ~3:1 and sulfurizing under atmospheric pressure nitrogen.

Both the $CuSbS_2$ and Cu_3BiS_3 films synthetized in this study presented the optical and electrical characteristics required for photovoltaic applications, these being high absorption coefficients, band gaps in the optimal range, and p-type conductivity, showing relatively high mobility for polycrystalline materials. This is discussed further in Sections 8.2.1 and 8.2.2. The present experimental results are in accordance with both the findings of others [1-24] and are consistent with the materials properties predicted by DFT calculations. However the integration of these materials into efficient solar devices was not straightforward. Prototype devices based on the $CuSbS_2$/CdS heterojunction exhibited efficiencies below 1% – i.e. too low for commercialization.

8.2 Comparison of the results with other reports

8.2.1 $CuSbS_2$ thin films

The $CuSbS_2$ films grown by sulfurization of metal precursor displayed absorption coefficients of ~10^5 cm^{-1}, with optical band gaps of ~1.5 eV – i.e. in good agreement with refs. 1 - 9. The deviations of *Eg* from 1.5 eV reported in refs. 10 - 14 could be attributed to either residues of secondary phases or quantum effects – i.e. the grain size varying with the growth conditions or layer thicknesses. The films were p-type, as extensively reported in the literature (see refs. 1 - 15), and as expected from the theoretical predictions of the dominant effect of the copper vacancies. The best of the films showed mobilities of ~10 cm^2 V^{-1} s^{-1}, this being reasonably consistent with other reports. The resistivities of the films varied with small changes in the sulfur mass included in the sulfurization box in the range 10 - 30 kΩ/□. The typical hole concentration was ~10^{17} cm^{-3} at 400°C, similar to that reported by Welch et al. [6]. Samples grown by single-stage sputtering method exhibited also high absorption and *Eg* ~1.5 eV but were generally more resistive, having sheet resistances of ~800 kΩ/□.

As expected, the material properties of $CuSbS_2$ reported here are broadly consistent with those of other authors. However the exact deposition process and growth conditions affect the micro-structural properties of the film, and in turn the materials and device performance. In particular Ikeda et al. produced $CuSbS_2$-based devices with efficiencies of ~3.1% by sulfurization of a metal layer in a mixture of argon and H_2S atmosphere and with a pre-heating stage at 510°C in purely argon atmosphere [5]. It is reasonable to assume that this process reduced the concentration of defects in the sulfurized films, with consequent benefits on the device efficiency. In particular the pre-heating stage at high temperature could prevent the formation of secondary phases from unreacted metal, improving also the adhesion of the 'precursor' metal layer onto the substrate. In addition it is plausible that the introduction of hydrogen atoms during the reactive annealing – by using H_2S as sulfurization agent – aids the passivation of the defects, although there is no direct evidence for this supposition.

8.2.2 Cu_3BiS_3 thin films

Cu_3BiS_3 sulfurized thin films exhibited high absorption coefficients of ~10^5 cm^{-1} and optical band gaps of ~1.4 eV, these being identical to findings elsewhere [16 - 18]. The

observed p-type conductivity of Cu_3BiS_3 was expected from the theoretical studies and confirmed from other experimental works in the literature [16 - 20]. In this work a variation in the hole concentration of the Cu_3BiS_3 samples from ~10^{16} to 10^{18} cm^{-3} was observed for sulfurization temperatures in the range 350 - 500°C.

8.2.3 Comparison of $CuSbS_2$ and Cu_3BiS_3 with other PV materials

Table 8.1 shows a comparison of the main optical and electrical properties of $CuSbS_2$ and Cu_3BiS_3 grown in this study with those of the most important PV materials. With the exception of c-Si and μc-Si that are indirect semiconductors, all the other materials are direct or direct-like semiconductors. In the Table the band gap variation in a-Si is related to the hydrogen content and that for CIGS is related to the gallium content. Both the conductivity type and band gaps of $CuSbS_2$ and Cu_3BiS_3 are as desired for an absorber material. However, while the established materials have all achieved PV conversion efficiencies of greater than 10 or even 20%, the new materials $CuSbS_2$ and Cu_3BiS_3 investigated in this work have reached at best 3%. The next section discusses the device results.

Material	α (cm^{-1})	band gap (eV)	conductivity
c-Si	10^2 - 10^4	1.1	dopable n and p
μc-Si	10^2 - 10^4	1.1	dopable n and p
a-Si	10^4 - 10^5	1.1 - 1.5	p-type
GaAs	10^4 - 10^5	1.4	dopable n and p
CdTe	10^4 - 10^5	1.5	p-type
CIGS	10^4 - 10^5	1.0 - 1.7	p-type
CZTS	10^4 - 10^5	1.5	p-type
$CuSbS_2$	10^4 - 10^5	1.5	p-type
Cu_3BiS_3	10^4 - 10^5	1.4	p-type

Table 8.1: Comparison of the absorption coefficient α, band gap and conductivity type of $CuSbS_2$ and Cu_3BiS_3 grown in this study with those of the principal PV materials.

8.2.4 Prototype PV devices based on the $CuSbS_2$/CdS heterojunction

a) Devices fabricated using sulfurization-grown $CuSbS_2$ – Substrate-geometry solar cells based on $CuSbS_2$/CdS were fabricated in this work with efficiencies below 1%, with the main cause being the low *Voc* in common with the findings of Welch [6] and Choi [7] who noted that *Jsc* values were quite high in comparison – i.e. 8 - 21 mA/cm^2. The *Voc* for the best cells here ranged between 0.10 V and 0.22 V. However a higher *Voc* of 0.36 V was observed for devices having the same structure, but with the absorber grown by the one-step synthesis approach. The values of *Voc* measured in this study are comparable with those presented elsewhere (see refs. 7, 8 and 21 – 24 and as summarized in Table 3.5), and suggest that an improvement of the quality of the absorber layer and the exploration of alternative device structures and partner materials is required. For example, Choi et al. included $CuSbS_2$ films in a hybrid organic/inorganic device structure, and achieved efficiencies up to ~3% [7]. Work to test alternative inorganic heterojunction partners to $CuSbS_2$ is discussed in Section 8.2.5 below.

Doping the absorber layer was investigated as a means of increasing the efficiency of the devices and to investigate the idea that they were limited by the high resistance of the absorber. It was demonstrated that indium increased the conductivity of $CuSbS_2$ (see Section 5.3.5.2), and indeed, indium doping gave the best performance from $CuSbS_2$/CdS devices in this work, with ~1% efficiencies for 1 mm^2 cells. However further study is required to fully understand the role of indium in the devices. Possibly the indium atoms occupy the sulfur sites in the $CuSbS_2$ crystal lattice to form acceptors, hence increasing the p-type conductivity of the absorber.

In this work the devices fabricated using the alternative superstrate structure were also investigated. Those having $CuSbS_2$ absorbers fabricated by sulfurization were not photoactive, possibly due to delamination of the absorber layer from the SnO_2-coated glass substrate or interdiffusion of the underlying layers during the formation of the absorber.

b) Devices fabricated using single-step sputtered $CuSbS_2$ – Devices based on the one-stage process, showing relatively high *Voc*, were produced in the superstrate configuration. The synthesis of the absorber from a single sputtering target allowed bypassing the annealing stage at high temperature, hence preventing interdiffusion and

delamination of the absorber. The poor photocurrents (i.e. < 1 mA/cm^2) produced from the devices based on the one-step process are consistent with the Al-Saab's findings [25]. In the case of devices based on $CuSbS_2$ films sputtered from ternary target, a post-growth activation step may be necessary to enhance the photocurrent. The activation step by $CdCl_2$ in CdTe/CdS solar cell fabrication is a well-known process used to improve the device performance. CdTe solar cells fabricated without an activation step usually present very low efficiency. The introduction of $CdCl_2$ into polycrystalline CdTe is believed to be beneficial for the recrystallization, passivation of grain boundaries, enhancement of acceptor concentration and minority carrier lifetime [26]. An analogous study on an activating species for $CuSbS_2$-based solar cells could be effective in improving the performance of the devices.

c) Comparison with $CuSbSe_2$ – Welch demonstrated the fabrication of $CuSbSe_2$-based solar cells exhibiting efficiencies above 3% [27] – i.e. significantly higher than the homologous devices based on $CuSbS_2$ reported in ref. 6. Although the optical and electrical properties of $CuSbS_2$ and $CuSbSe_2$ are similar, it might be that the selenium compound contained fewer secondary phases and defects, with consequent beneficial effects in the device. Another reason could be that the $CuSbSe_2$/CdS interface has more favourable band line-ups and hence a stronger electric field than the $CuSbS_2$/CdS heterojunction.

8.2.5 $CuSbS_2$-based PV devices with alternative ZnS and ZnSe window layers

In this study alternative junctions were tested, with ZnS and ZnSe employed as window layer materials. In the experiments a significant enhancement of the *Voc* was observed, this indicating an improvement in the band-alignment of the absorber $CuSbS_2$ with the window layer, as predicted from Welch et al. [6]. In particular devices with *Voc* = 0.56 V based on the $CuSbS_2$/ZnS heterojunction were produced, this being a record *Voc* for $CuSbS_2$-based solar cells. However the photocurrents were usually extremely low and this could be due to the high resistivity of the sputtered ZnS and ZnSe layers. This might suggest the use of more highly doped ZnS and ZnSe films as window layers to enhance the device performance. Further experimental work and characterization will be required to understand the properties of the $CuSbS_2$/ZnS and $CuSbS_2$/ZnSe heterojunctions.

8.3 Opportunities for further developments

For a full understanding of the photovoltaic properties of the novel chalcogenide materials, a detailed knowledge of the following points is required:

a) the compound's microstructure, including the surface morphology, grain structure, impurities and defects;
b) the device's microscopic structure and composition, in order to detect potential interdiffusion, lattice mismatch and recombination centers;
c) kinetics of the growth process – e.g. sulfurization and rf sputtering from ternary target – and the impact of the deposition conditions on the micro-structural characteristics of the absorber layer;
d) band alignment of the absorber for the appropriate integration into devices with alternative window layer and electrode materials.

The investigation presented in this thesis was mainly focused on the optical and electrical characterization of $CuSbS_2$ and Cu_3BiS_3 films. The analyses by SEM/EDX, XPS and photoluminescence evidenced the presence of impurities in the as-grown samples and etching attempts have been presented. However a more in-depth examination of the defect chemistry – including grain structure, impurity types and distribution, deep levels, secondary phases, dislocations, shunt paths – and their influence on the device performance is required for the optimization of the PV devices. In this study voids and impurities were detected by cross-sectional study in the bulk of as-grown films. Further study is required to detect the composition of the impurities, which could be either unreacted metal or secondary phases – e.g. Sb_2S_3 or $Cu_{12}Sb_4S_{13}$ precipitates [24].

$CuSbS_2$ films were included in prototype devices merely by replacing the absorber layer in conventional PV structures, i.e. in designs similar to those used in CdTe and CIGS. Only a few authors have reported detailed studies on the band structure of $CuSbS_2$ and Cu_3BiS_3. However additional work would be beneficial for confirmation and to help further development of the solar cells based on $CuSbS_2$ and Cu_3BiS_3. In addition, as demonstrated from Choi [7], hybrid device configurations have potential for high-efficiency solar cells and should considered for further investigation.

It is clear that the $CuSbS_2$-based devices display limited efficiencies. In most of the cases the photons are absorbed but do not contribute to the photocurrent – i.e. the devices are

electrically limited. There could be different reasons, including recombination in the absorber or at the junction. It might be that the formed junctions are weak or in the wrong position. A potential explanation might be that the new chalcogenide materials are extremely sensitive to defects. Hence their success in becoming high-performance devices could be restricted, even though the materials show promising optoelectronic characteristics. The theoretical predictions of novel absorber materials are generally based on the simulation of their electronic structure and optical characteristic, without considering the influence of the deposition conditions and the integration of the material in a full device. Hence theoretical work on the interface properties of $CuSbS_2$ with the window layer and the electrode materials will be required. It will be also important to find a deposition approach to grow $CuSbS_2$ films free from any trace of secondary phases – at the present there is no simple way of doing this.

8.4 References for Chapter 8

[1] M. T. S. Nair, Y. Rodriguez-Lazcano, Y. Pena, S. Messina, J. Campos and P. K. Nair, "Absorber films of antimony chalcogenides via chemical deposition for photovoltaic application", *Materials for Photovoltaics*, vol. 836, pp. 167-172, 2005

[2] C. Garza, S. Shaji, A. Arato, E. P. Tijerina, G. A. Castillo, T. K. Das Roy and B. Krishnan, "P-type $CuSbS_2$ thin films by thermal diffusion of copper into Sb_2S_3", *Solar Energy Materials and Solar Cells*, vol. 95, no. 8, pp. 2001-2005, 2011

[3] R. E. Ornelas-Acosta, D. Avellaneda, S. Shaji, G. A. Castillo, T. K. Das Roy and B. Krishnan, "$CuSbS_2$ thin films by heating Sb_2S_3/Cu layers for PV applications", *Journal of Materials Science-Materials in Electronics*, vol. 25, no. 10, pp. 4356-4362, 2014

[4] D. Colombara, L. M. Peter, K. D. Rogers, J. D. Painter and S. Roncallo, "Formation of $CuSbS_2$ and $CuSbSe_2$ thin films via chalcogenisation of Sb-Cu metal precursors", *Thin Solid Films*, vol. 519, no. 21, pp. 7438-7443, 2011

[5] S. Ikeda, Y. Iga, W. Septina, T. Harada and M. Matsumura, "$CuSbS_2$-based thin film solar cells prepared from electrodeposited metallic stacks composed of Cu and Sb layers", *Proceedings of the 2013 IEEE 39th Photovoltaic Specialist Conference (PVSC)*, pp. 2598-2601, 2013

[6] A. W. Welch, P. P. Zawadzki, S. Lany, C. A. Wolden and A. Zakutayev, "Self-regulated growth and tunable properties of $CuSbS_2$ solar absorbers", *Solar Energy Materials and Solar Cells*, vol. 132, pp. 499-506, 2015

[7] Y. C. Choi, E. J. Yeom, T. K. Ahn and S. Il Seok, "$CuSbS_2$-sensitized inorganic-organic heterojunction solar cells fabricated using a metal-thiourea complex solution", *Angewandte Chemie-International Edition*, vol. 54, no. 13, pp. 4005-4009, 2015

[8] B. Yang, L. Wang, J. Han, Y. Zhou, H. Song, S. Chen, J. Zhong, L. Lv, D. Niu and J. Tang, "$CuSbS_2$ as a promising earth-abundant photovoltaic absorber material: a combined theoretical and experimental study", *Chemistry of Materials*, vol. 26, no. 10, pp. 3135-3143, 2014

[9] C. Yan, Z. Su, E. Gu, T. Cao, J. Yang, J. Liu, F. Liu, Y. Lai, J. Lia and Y. Liu, "Solution-based synthesis of chalcostibite ($CuSbS_2$) nanobricks for solar energy conversion", *RSC Advances*, vol. 2, no. 28, pp. 10481-10484, 2012

[10] A. Rabhi, M. Kanzari and B. Rezig, "Optical and structural properties of $CuSbS_2$ thin films grown by thermal evaporation method", *Thin Solid Films*, vol. 517, no. 7, pp. 2477-2480, 2009

[11] R. Suriakarthick, V. N. Kumar, T. S. Shyju and R. Gopalakrishna, "Effect of substrate temperature on copper antimony sulphide thin films from thermal evaporation", *Journal of Alloys and Compounds*, vol. 651, pp. 423-433, 2015

[12] S.A. Manolache, L. Andronic, A. Duta and A. Enesca, "The influence of the deposition condition on crystal growth and on the band gap of $CuSbS_2$ thin film absorber used for solid state solar cells (SSSC)", *Journal of Optoelectronics and Advanced Materials*, vol. 9, no. 5, pp. 1269-1272, 2007

[13] S. Liu, L. Chen, L. Nie, X. Wang and R. Yuan, "The influence of substrate temperature on spray-deposited $CuSbS_2$ thin films", *Chalcogenide Letters*, vol. 11, no. 12, pp. 639-644, 2014

[14] A. C. Rastogi and N. R. Janardhana, "Properties of $CuSbS_2$ thin films electrodeposited from ionic liquids as p-type absorber for photovoltaic solar cells", *Thin Solid Films*, vol. 565, pp. 285-292, 2014

[15] L. I. Soliman, A. M. A. El Soad, H. A. Zayed and S. A. El Ghfar, "Structural and electrical properties of $CuSbTe_2$, $CuSbSe_2$ and $CuSbS_2$ chalcogenide thin films", *Fizika A*, vol. 11, no. 4, pp. 139-152, 2002

[16] D. Colombara, L. M. Peter, K. Hutchings, K. D. Rogers, S. Schafer, J. T. R. Dufton and M. S. Islam, "Formation of Cu_3BiS_3 thin films via sulfurization of Bi-Cu metal precursors", *Thin Solid Films*, vol. 520, no. 16, pp. 5165-5171, 2012

[17] N. J. Gerein and J. A. Haber, "One-step synthesis and optical and electrical properties of thin film Cu_3BiS_3 for use as a solar absorber in photovoltaic devices", *Chemistry of Materials*, vol. 18, no. 26, pp. 6297-6302, 2006

[18] F. Mesa and G. Gordillo, "Effect of preparation conditions on the properties of Cu_3BiS_3 thin films grown by a two-step process", *Journal of Physics*, vol. 167, no. 1, 2009

[19] P. K. Nair, L. Huang, M. T. S. Nair, H. L. Hu, E. A. Meyers and R. A. Zingaro, "Formation of p-type Cu_3BiS_3 absorber thin films by annealing chemically deposited Bi_2S_3-CuS thin films", *Journal of Material Research*, vol. 12, no. 3, pp. 651-656, 1997

[20] V. Estrella, M. T. S. Nair and P. K. Nair, "Semiconducting Cu_3BiS_3 thin films formed by the solid-state reaction of CuS and bismuth thin films", *Semiconductor Science and Technology*, vol. 18, no. 2, pp. 190-194, 2003

[21] Y. Rodriguez-Lazcano, M. T. S. Nair and P. K. Nair, "Photovoltaic p-i-n structure of Sb_2S_3 and $CuSbS_2$ absorber films obtained via chemical bath deposition", *Journal of the Electrochemical Society*, vol. 152, no. 8, pp. 635-638, 2005

[22] R. E. Ornelas-Acosta, S. Shaji, D. Avellaneda, G. A. Castillo, T. K. Das Roy and B. Krishnan, "Thin films of copper antimony sulfide: a photovoltaic absorber material", *Materials Research Bulletin*, vol. 61, pp. 215-225, 2015

[23] W. Septina, S. Ikeda, Y. Iga, T. Harada and M. Matsumura, "Thin film solar cell based on $CuSbS_2$ absorber fabricated from an electrochemically deposited metal stack", *Thin Solid Films*, vol. 550, pp. 700-704, 2014

[24] A. Welch, L. Baranowski, P. Zawadzki, C. DeHart, S. Johnston, S. Lany, C. Wolden and A. Zakutayev, "Accelerated development of $CuSbS_2$ thin film photovoltaic device prototypes", *Progress in Photovoltaics: Research and Applications, in press*

[25] F. Al-Saab, "Chalcogenides for solar applications", PhD thesis, Faculty of Physical and Applied Sciences, University of Southampton, 2015, Southampton, United Kingdom

[26] J. D. Major, R. E. Treharne, L. J. Phillips and K. Durose, "A low-cost non-toxic post-growth activation step for CdTe solar cells", *Nature*, vol. 511, no. 7509, pp. 334-337, 2014

[27] A. W. Welch, L. L. Baranowski, P. P. Zawadzki, S. Lany, C. A. Wolden and A. Zakutayev, "$CuSbSe_2$ photovoltaic devices with 3% efficiency", *Applied Physics Express*, vol. 8, no. 8, pp. 1-4, 2015

9 Conclusions and future work

9.1 Summary of main conclusions

This thesis explored novel chalcogenide materials with prospective solar cell applications. Since the demand for energy is growing considerably, as presented in Chapter 1, the discovery of sustainable and efficient photovoltaic materials will be essential in the near future in order to meet the demand for the global PV manufacturing. Organic and more recently hybrid materials have emerged as sustainable and innovative technologies – in particular perovskite solar cells with ~20% have been produced at the lab scale. However these materials suffer from instability and hence their capacity for upscaling may be strongly restricted. Of the inorganic thin films, amorphous silicon suffers from low efficiency and poor stability, and both CdTe and CIGS contain relatively rare elements making them unsustainable for TWp production. CZTS is the most advanced inorganic PV technology among the novel sustainable PV materials, with efficiencies above 12%. Although it comprises Earth abundant elements, it has a complex crystal structure, with many possible secondary phases, and has compositional band gap fluctuations. It is perhaps for these reasons that it has restricted PV performance at present. Hence the research community recognized the necessity to explore alternative inorganic PV materials. Theoretical simulations and experimental works identified some chalcogenides based on copper, antimony/bismuth and sulfur having the desired optical and electrical characterization for solar cell integration.

Chapter 2 provided the fundamental notions of inorganic solar cells, based on the theory of semiconductors and p-n junction, while Chapter 3 reviewed the publications on some novel chalcogenides, emphasizing the relevant properties for PV applications. From the complex Cu-Sb-S and Cu-Bi-S systems the phases $Cu_x(Sb,Bi)S_y$, having either $x = 1$, $y = 2$ or $x = y = 3$, were recognized as potential absorbers. From the literature review, $CuSbS_2$ and Cu_3BiS_3 emerged as the most promising compounds, both exhibiting absorption coefficients of ~10^5 cm^{-1}, band gaps in desired range 1.4 - 1.5 eV and p-type conductivity (see Table 3.2).

A growing number of authors have recently reported the development and analysis of prototype devices based on $CuSbS_2$ thin films and nanostructures synthetized by different methods (see Table 3.3). In particular solar cells with ~3% efficiency were fabricated at the

lab scale, both in the hybrid configuration TiO_2/$CuSbS_2$/PCPDTBT/Au [1] and with the substrate structure glass/Mo/$CuSbS_2$/CdS/ZnO:Al [2].

The phase Cu_3SbS_3 also presents good characteristics for PV applications, however a limited number experimental studies are reported, due to the difficulty in synthetizing phase-pure Cu_3SbS_3 films [3]. In spite of the high optical absorption coefficient and the band gap of ~1.7 eV, the phase $CuBiS_2$ was not considered in the experimental part of the thesis since this phase is usually n-type [4]. Finally $CuSbSe_2$ is the most interesting selenide for solar cell applications, with efficiencies achieved of ~3% [5]. However the synthesis of $CuSbSe_2$ was outside the scope of this thesis.

Chapter 4 reviewed the methods of thin film growth, materials and device characterization used to fabricate the materials and devices. In particular the method of sulfurizing metal films to form chalcogenide layers was acknowledged to feature heavily in the published reports of these materials. This reflects the difficulty in containing the sulfur in the material in order to obtain stoichiometric phase pure material – a problem common to other chalcogenides including CIGS.

Chapter 5 described the synthesis and characterization of $CuSbS_2$ and Cu_3BiS_3 films. The films of $CuSbS_2$ were deposited by two methods: (i) the sulfurization of a metal precursor comprising copper and antimony; (ii) one-stage process by rf sputtering from a ternary target.

The initial sulfurized samples were characterized from the presence of metallic and secondary phases and loss of elemental antimony at low annealing pressure. $CuSbS_2$ single-phase films 1.2 μm thick were produced from a multistack precursor layer having a 1:1 Cu:Sb ratio, by sulfurizing under atmospheric pressure nitrogen– this reduced the antimony loss – and 400°C for 1 hour, with sulfur mass in the range 10 - 80 mg.

The optical transmission characterization showed the films to have high absorption coefficients but only poorly defined band gaps of ~1.45 eV. This was possibly caused from residues of secondary phases coexisting with the main phase $CuSbS_2$ (e.g. Sb_2S_3, as shown from the Raman analysis). Optimized $CuSbS_2$ films were formed from a Sb-rich (Cu:Sb ~4:5) precursor multistack and by an improved control on the vacuum and sputtering process. The resulting samples displayed absorption coefficients of $\alpha \sim 10^5$ cm^{-1}, with sharper band gaps of 1.5 eV and p-type conductivity.

The film resistivity was tuned either by varying the chalcogen mass during sulfurization or by doping with either sodium fluoride or indium or zinc. From the experiments indium was the most effective element in increasing the p-type conductivity of the $CuSbS_2$ films. It is reasonable to assume that the indium atoms occupy the sulfur sites forming acceptors in the $CuSbS_2$ lattice.

The surface analysis indicated the presence of oxides and impurities on the as-grown samples, especially of antimony oxide. Several methods were tested as means of removing this unwanted impurity, and a detailed discussion was given in Chapter 5.

As an alternative to sulfurization, $CuSbS_2$ films with thicknesses in the range 80 - 1000 nm were deposited by the one-step approach from the ternary sputtering target. A shift in the band gap from ~3 eV for the thinnest (yellowish) samples to ~1.5 eV for the thickest (dark grey) samples was observed, this possibly being due to quantum effects associated with grain sizes. Similar unusual behaviour had been reported from other authors. The ~1 µm thick samples exhibited the desired optical characteristics for photovoltaics.

The Cu_3BiS_3 films were produced by sulfurization of a multistack containing copper and bismuth and the main findings on the sulfurization method that were successful for $CuSbS_2$ were exploited in this study. Single-phase films exhibited $\alpha \sim 10^5$ cm^{-1} with *Eg* ~1.4 eV and p-type conductivity, having μ_p ~3 cm^2 V^{-1} s^{-1}.

Chapter 6 described the fabrication and analysis of prototype devices based on the $CuSbS_2$/CdS junction, with different configurations. The solar cells produced by sulfurization of the absorber showed a maximum efficiency of ~1% for a 1 mm^2 contact area. The cells generally displayed relatively high *Jsc* (32 mA/cm^2 for the 1 mm^2 samples), *Voc* between 0.12 and 0.22 V, and low *FF* – i.e. ~25%. The study by *J-V-T* and impedance spectroscopy on the prototype $CuSbS_2$/CdS devices emphasized the recombination issues at the interface, where multi-step tunneling was the dominant transport mechanism of the junction, instead of thermally activated diffusion.

$CuSbS_2$ ~1 µm thick films grown by rf sputtering from single source were also included in prototype devices. These devices exhibited higher *Voc* (in the range 0.22 - 0.36 V), and *FF* (till 39%), but *Jsc* was significantly lower (generally below 1 mA/cm^2), this being possibly caused by the higher resistivity of the films produced from the ternary target, or perhaps due to a the higher concentration of secondary phases and recombination centers.

Welch et al. proved by DFT calculations that CdS is not necessarily the best choice of window layer material for $CuSbS_2$-based solar cells in terms of band alignment [6]. Chapter 7 explored ZnS and ZnSe films for use as alternative window layers with $CuSbS_2$. Sputtered films of both materials usually displayed sheet resistances above 10 MΩ/□, and this high resistance contributed to the poor *Jsc* of the resulting devices fabricated with ZnS and ZnSe. An encouraging increase in the *Voc* to 0.56 V was observed in solar cells based on the $CuSbS_2$/ZnS junction, and having the absorber synthesized by the one-step process. However the poor photocurrents generally limited the efficiencies of the cells made with either ZnS or ZnSe, and hence further optimization work is required.

Finally a discussion of the main findings and the limitations of the study presented in the thesis were given in Chapter 8. A comparison of the principal results with information from the literature proved the consistency of the present study with the findings of others. According to the literature (much of it generated during the period of this study), the main factors limiting the performance of $CuSbS_2$-based device are: (i) recombination centers at the interface and in the absorber layer; (ii) inadequate window layer material. These findings are consistent with the present results.

9.2 Suggestions for future work

This Section proposes future and ongoing studies in order to identify and resolve the main issues of the $CuSbS_2$-based solar cells. In principle the results and approach can be extended to similar investigations on Cu_3BiS_3.

(a) Defects analysis – A detailed knowledge about the defect chemistry of the absorber and about the junction properties are required in order to determine the limiting mechanisms on the efficiency of $CuSbS_2$-based devices. The localisation and compositional analysis of the impurities and residues of secondary phases in the absorber layer and at the interface can be analytically determined by SEM/EDX and TEM.

A microscopy study of the influence of the growth conditions on the grain structure and on the formation and distribution of defects in the absorber layer is recommended. The EDX analysis could aid to detect potential interdiffusion in the device and the dependence on the device growth parameters.

Both deep and shallow electronic states are likely to be responsible in determining both the carrier concentration and recombination behaviour of the material. Some studies to evaluate the levels would be valuable. The temperature-dependence photoluminescence spectroscopy is a powerful tool to examine the nature of shallow defects in the absorber layer. Thermal admittance spectroscopy or deep level transient spectroscopy would give information on the deep levels.

Finally the passivation of the defects (e.g. grain boundaries) is likely to be important as for all thin film PV devices. Usage of hydrogen or oxygen during the growth process could perhaps be beneficial to passivate the defects in the absorber layer. The highest efficiency $CuSbS_2$-based solar cell has been produced by means of H_2S [2]. Possibly hydrogen played a crucial role on the high quality of the absorber films, exhibiting low density of defects, as reported from the authors. The use of oxygen has been reported to effectively passivate the interface defects in CIGS [7] and silicon, and could be extended to $CuSbS_2$.

(b) Band structure – A combined theoretical-experimental study on band structures of $CuSbS_2$ and Cu_3BiS_3 is essential for their optimal integration in PV devices with appropriate window layer and electrode materials. A restricted number of articles indicated that CdS is a bad option as window layer material for $CuSbS_2$ – however further confirmation is required.

Experimental confirmation of the band line-ups could come from IPES (inverse photoemission spectroscopy) and UPS (ultraviolet photoelectron spectroscopy) – these are typical techniques used to determine the band parameters of semiconductors, including electron affinity, work function, electronic band gap. However these techniques are very sensitive to the surface states and hence samples having cleaned surfaces would be necessary for accurate determinations of these parameters. Comparison with theory may well indicate the choices of heterojunction partners that are likely to succeed.

Although in this work ZnS and ZnSe were investigated as alternatives to CdS, high efficiencies were nevertheless not realized. Further optimization may yet give better results.

(c) Alternative device structures – The efficiency of $CuSbS_2$ solar cells based on the ordinary superstrate and substrate configurations is likely to be strongly limited by defects and band alignment issues. The work proposed from Choi [1] suggested the exploration of

the alternative hybrid organic/inorganic structures for $CuSbS_2$ and this could be investigated experimentally.

(d) Further study on the one-step process – The one-step approach of using a single sputtering target is attractive for the convenient synthesis of $CuSbS_2$ films with promising optical properties and for the potential integration of the absorber layer in full devices by a continuous fabrication process. However this innovative method requires further study, as follows. (i) In-depth investigation by XRD and Raman spectroscopy on the phase composition of the as-grown films. (ii) Microscopy and photoluminescence study on the samples fabricated with different thicknesses in order to establish whether the band gap variation is caused from either coexisting secondary phases or quantum effects. (iii) Influence of the sputtering conditions, including power, pressure, substrate temperature and gas mixture (e.g. Ar, N_2, H_2, O_2), on the grain structure of the as-deposited $CuSbS_2$ films. The formation of absorber layers with large grain size at the bottom covered with small grains could minimize the shunt paths, with consequent benefits on the device performance. (iv) A possible activation step to enhance the photocurrent in the solar devices.

To conclude both $CuSbS_2$ and Cu_3BiS_3 thin films display the desired optical and characteristics for absorber applications, but further analysis is required for their integration in efficient devices.

9.3 References for Chapter 9

[1] Y. C. Choi, E. J. Yeom, T. K. Ahn and S. Il Seok, "$CuSbS_2$-sensitized inorganic-organic heterojunction solar cells fabricated using a metal-thiourea complex solution", *Angewandte Chemie-International Edition*, vol. 54, no. 13, pp. 4005-4009, 2015

[2] S. Ikeda, Y. Iga, W. Septina, T. Harada and M. Matsumura, "$CuSbS_2$-based thin film solar cells prepared from electrodeposited metallic stacks composed of Cu and Sb layers", *Proceedings of the 2013 IEEE 39th Photovoltaic Specialist Conference (PVSC)*, pp. 2598-2601, 2013

[3] P. Maiello, G. Zoppi, R. Miles, N.Pearsall and I. Forbes, "Investigations of ternary Cu_3SbS_3 thin films as absorber in photovoltaic devices", *The 7th Photovoltaic Science Applications and Technology Conference and Exhibition (PVSAT-7)*, 2011

[4] S. H. Pawar, A. J. Pawar and P. N. Bhosale, "Spray pyrolytic deposition of $CuBiS_2$ thin-films", *Bullettin of Material Science*, vol. 8, no. 3, pp. 423-426, 1986

[5] A. W. Welch, L. L. Baranowski, P. P. Zawadzki, S. Lany, C. A. Wolden and A. Zakutayev, "$CuSbSe_2$ photovoltaic devices with 3% efficiency", *Applied Physics Express*, vol. 8, no. 8, pp. 1-4, 2015

[6] A. Welch, L. Baranowski, P. Zawadzki, C. DeHart, S. Johnston, S. Lany, C. Wolden and A. Zakutayev, "Accelerated development of $CuSbS_2$ thin film photovoltaic device prototypes", *Progress in Photovoltaics: Research and Applications, in press*

[7] D. Hariskos, S. Paetel, W. Witte, L. Bürkert, M. Oertel, W. Wischmann and M. Powalla, "Passivation of interface defects in CIGS-based thin-film solar cells", *EU PVSEC 2015*, 2015

Appendix

List of presentations and publications from the thesis work

- "Control of Cu-Sb-S phases in thin film materials for sustainable PV"*, PVSAT-9*, 10/4/2013, Swansea, U.K.
- "$CuSbS_2$ thin films for PV applications", *Next Generation materials for Solar Photovoltaics Symposium,* 15/1/2014, London, U.K.
- "Characterization of sulfurized $CuSbS_2$ thin films for PV applications", *40th IEEE Photovoltaic Specialist Conference*, 11/6/2014, Denver, U.S.A.
- "$CuSbS_2$ films and prototype PV devices", *E-MRS 2015 Spring Meeting*, 11/5/2015, Lille, France
- "Prototype devices based on sulfurized $CuSbS_2$ films" (*in preparation*)
- "Characterization of Cu_3BiS_3 films for PV applications" (*in preparation*)
- "$CuSbS_2$ films deposited by rf sputtering from single target" (*in preparation*)
- "Literature review on chalcogenide materials for PV applications" (*in preparation*)